Department of Mechanics, Mathematics and Management

MECHANICAL AND MANAGEMENT ENGINEERING

Ph.D. Program

SSD: ING-IND/14–MECHANICAL DESIGN AND MACHINE CONSTRUCTION

Final Dissertation

Non-destructive thermographic methods for quality evaluation of thin joints

By

Giuseppe Dell'Avvocato

Supervisors:

Prof. U. Galietti

Dr. D. Palumbo

Coordinator of Ph.D Program:

Prof. G. P. Demelio

Course n°35, 01/11/2019 - 31/12/2022

Politecnico di Bari

Department of Mechanics, Mathematics and Management

MECHANICAL AND MANAGEMENT ENGINEERING

Ph.D. Program

SSD: ING-IND/14–MECHANICAL DESIGN AND MACHINE CONSTRUCTION

Final Dissertation

Non-destructive thermographic methods for quality evaluation of thin joints

By

Giuseppe Dell'Avvocato

Referees:

Prof. C. Colombo

Dr. R. De Finis

Supervisors:

Prof. U. Galietti

Dr. D. Palumbo

Coordinator of Ph.D Program:

Prof. G. P. Demelio

Course n°35, 01/11/2019 - 31/12/2022

"Ich halte dafür, daß das einzige Ziel der Wissenschaft darin besteht, die Mühseligkeiten der menschlichen Existenz zu erleichtern."

"I believe that the only purpose of science is to alleviate the difficulties of human existence."
(Bertold Brecht)

ABSTRACT

This work aimed to develop non-destructive control procedures, either automated or semi-automated, for evaluating the quality of thin welded joints using active thermography techniques. After a thorough analysis of the state of the art of traditional non-destructive control methods for thin joints, it was found that thermographic techniques can be used both for a quantitative evaluation of the fusion region in RPW welds and for verifying microstructural changes through the measurement of thermal diffusivity. After developing a pulsed thermography testing procedure to measure the fused zone in RPW joints, this was validated using well-established controls such as ultrasound and computed tomography as references. In addition, using finite element models and Design of Experiment (Response surface method) methodologies, a study was conducted on the influence of test parameters on the error in the thermal diffusivity measurement, identifying a testing procedure for selecting the most suitable parameters. It was also found that the pulsed laser thermographic technique can distinguish different microstructures in boron steels through thermal diffusivity, which was subsequently correlated with the ultimate tensile strength, allowing for an estimation of the latter through the measurement of thermal diffusivity.

CONTENTS

INTRODUCTION

In mechanical design, whenever there is a need to connect two components, it is necessary to use a joint. This makes it virtually impossible to obtain any mechanical component without a welded, glued, or bolted joint.

For this reason, joints are one of the dominant processes in all industrial sectors, especially in the automotive and aerospace industries, where there is a strong push towards adhesive and welded joints, as opposed to bolted joints, in order to lighten the structures. In these fields, the use of joints is particularly massive (over 5,000 welds for an automobile frame and over 2.5 million rivets for an airplane). Therefore, they have always been the subject of research and development, both in terms of the manufacturing process but especially in terms of quality controls.

Indeed, the mechanical design of joints is both a fundamental and delicate aspect, as regardless of whether they are made of metal or composite, especially for glued and welded joints, they represent one of the most significant design challenges. In fact, despite the plethora of processes available to connect two components, it is only sometimes possible to transfer knowledge from one family of joints to another, making their design complicated and control vital.

Considering welded joints alone, there are different types of welds, each with different characteristics. However, they are characterized by one common factor: they are processes that take place at high temperatures to fuse metallic materials, often in environments where control of the conditions is complicated and, in most cases, they are processed with a highly manual component. This means that the actual welded joint can deviate significantly from the designed one, with a wide range of possible defects that reduce its static and mechanical fatigue resistance.

Due to these characteristics, welded joints require great attention in controls in production and operation. Currently, various destructive controls are possible, but non-destructive controls are critical.

Welds are subjected to superficial (penetrant liquids, magnetic particles, visual inspection, induced currents) and volumetric (where the main techniques are ultrasonic and radiographic) non-destructive testing. These techniques, although they allow the

advantage of inspecting the joint without compromising its functionality in any way, have some significant disadvantages, the main ones being:

- Long inspection times;
- Difficult to apply in-situ;
- Difficult to automatize;
- Difficult to have a 100% production check;
- Problem on thin joints.

Despite several advances in ultrasonic techniques, these limitations in the most widespread non-destructive tests are of great importance and constitute an important brake on the use of welds and adhesives in the industrial sector. In an economic-production context where crucial goals are lightening structures, reducing processing waste, and continuous improvement, the development of non-destructive testing procedures that allow automatic verification of these types of joints in times compatible with production times is an essential issue.

Active thermography, which originated as a surface non-destructive testing technique and is now increasingly widespread in the industry, therefore has the potential to overcome the limitations mentioned. The use of active thermography presents several advantages, including:

- Full-field inspection;
- Shorter inspection times;
- No contact with the component;
- Possibility of automating the inspection.

Currently, the use of active thermography as a surface technique for thermally high-diffusive components is mainly due to the high energy densities necessary to achieve greater inspection depths, which, in pulsed thermography, would correspond to high power values. However, for thin joints using high-energy density sources, several applications in the literature confirm the possibilities of this technique. Moreover, there are no well-defined procedures that are automatic or semi-automatic. In addition, most of the works in the literature on the control of welded joints aims to identify defects in the joint or quantify the fused region, but, for example, no attempt has been made to identify and quantify the heat-affected zone, which we know is a vital objective in weld control.

In this scenario, therefore, the present thesis work, incorporated into a wider research project, aims to identify thermographic procedures, automatic or semi-automatic, that

allow for a quantitative analysis of the fused region in thin welds and that allow for the detection of microstructure variations in steels to identify the HAZ.

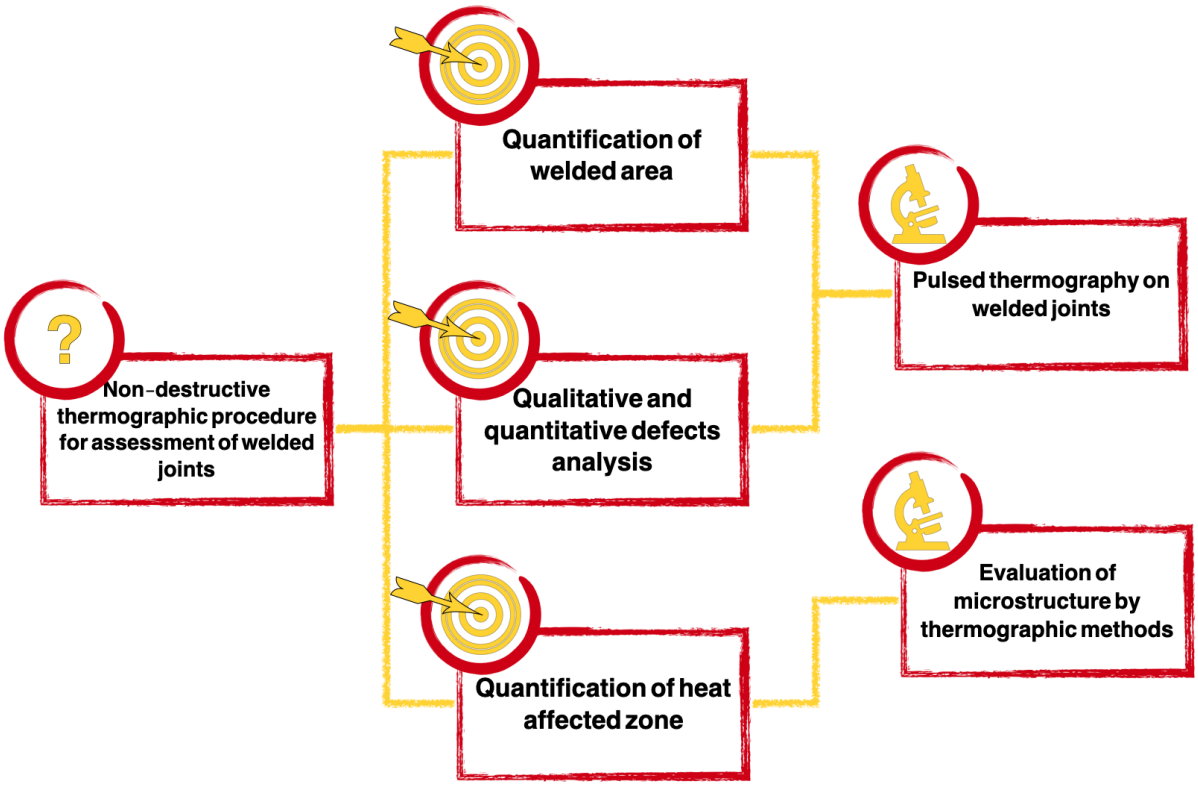

Figure 1 Scheme of research activities conducted in thesis work.

These goals are indeed functional to the long-term goal of developing a unique procedure, followed by a system that automatically verifies the welded zone, checks for defects, and quantifies the HAZ of a thin weld.

The first chapter clarifies the importance of joints in mechanical design, explaining what joint control consists of and with which methods, destructive and non-destructive, it is currently carried out. In addition, the limitations of current non-destructive methods, which we aim to overcome, are highlighted.

In the second chapter, after an introduction to the thermographic technique with a mention of its physical principle, the most common analysis algorithms are treated to clarify the potential of this technique applied to thin joints. Finally, this chapter is concluded with an explanation of why active thermography could also be used to measure microstructure variations following a heat treatment by exploiting thermal diffusivity variations.

In the third chapter, after an analysis of state of the art on non-destructive controls on thin joints, with a focus on thermographic ones, case studies on resistance spot welds (RPW) are presented. In the first case, from the analysis of 12 RPWs obtained with different

process parameters according to a factorial design, a procedure was developed to relate some thermographic features to the set of welding parameters used, using flash thermography. In the second case, carried out in collaboration with the *Bundesanstalt für Materialforschung und -prüfung (BAM)* at their site, a semi-automatic procedure was developed to quantify the fused area of RPWs, comparing it with established techniques such as ultrasonics and computerized microtomography.

In the fourth chapter, two case studies are addressed after a significant review of thermographic methods for measuring thermal diffusivity in opaque materials. First, after a detailed study on the influence of test parameters on the measurement of thermal diffusivity in the pulsed laser method, including with the aid of FEM simulations, a procedure was identified for selecting test parameters based on the sensitivity required for the diffusivity measurement. In addition, steel plates with different microstructures were analyzed to verify the ability of the thermographic technique to distinguish a martensitic structure from a ferritic-pearlitic one, finally identifying, through destructive tests, a correlation between thermal diffusivity and ultimate tensile strength. In the second case study, other microstructures with three different grades (bainite - bainite/martensite - martensite) were analyzed to analyze the resolution of the thermographic technique used to recognize different microstructures.

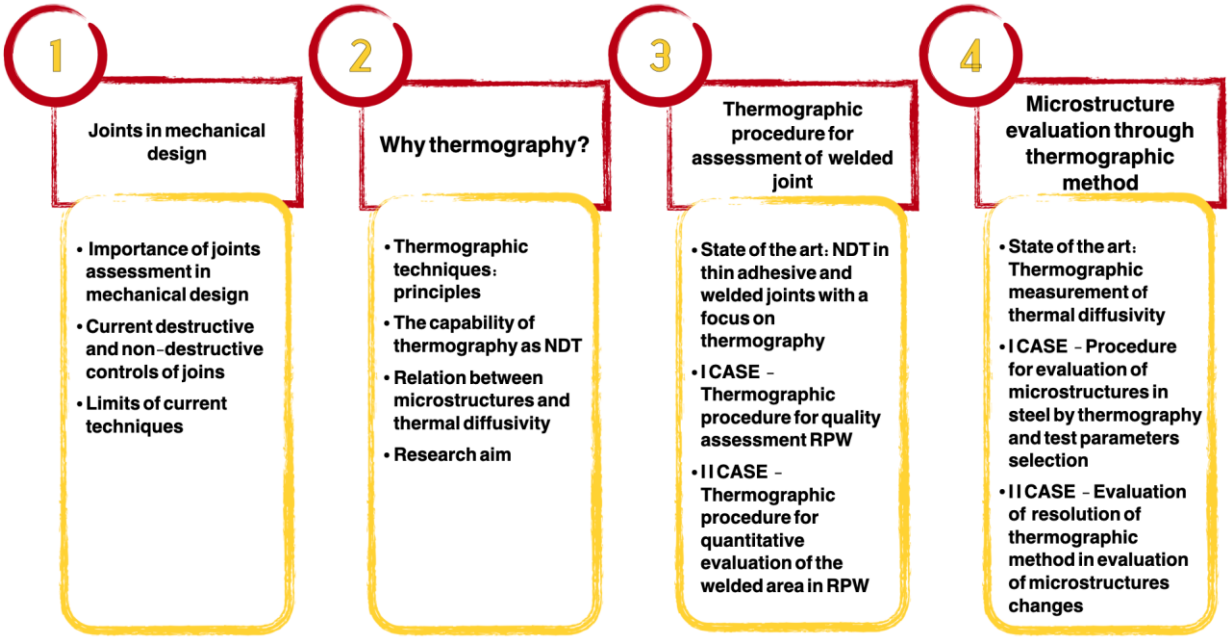

Figure 2. Executive summary scheme.

CHAPTER 1

Joints in mechanical design

The design of mechanical joints and fasteners has traditionally focused on individual structural components and their specific requirements. However, there are numerous models and formulas based on fundamental principles that can improve upon this traditional "rule of thumb" approach. Through continued study and use, these formulas have become increasingly reliable and efficient. In recent years, finite element methods and numerical analysis have further enhanced these formulas. The design of mechanical joints presents a unique challenge because the behavior of a joint is often complex and cannot be accurately predicted by a single formula. This can lead to defects in the overall design if critical material characteristics of the joint components are ignored. The main goal of a mechanical joint is to hold parts together and transfer a load from one structural component to another. The joint must transfer this load across a mechanical boundary without creating a detrimental stress gradient.

One disadvantage of a welded joint is that it can fail due to the propagation of cracks across the heat-affected zone (HAZ). However, welded joints do not experience a high level of stress concentration because the transition from one side of the joint to the other is smooth [1].

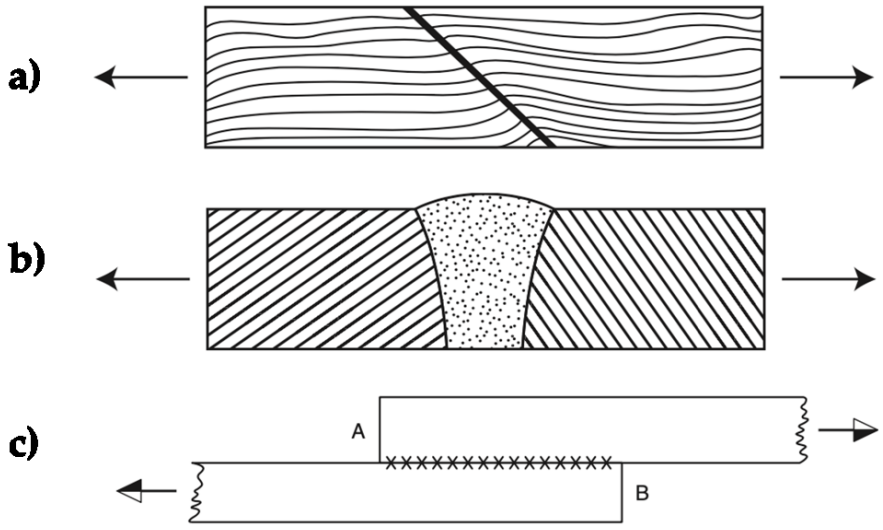

Figure 3. (a) A scarf joint. (b) A butt joint. (c) A lap joint with stress concentration.[1]

When a mechanical joint has a lap configuration, as shown in **Figure *3***, it is impossible to avoid stress concentration. The bonded length is AB, with the highest stresses likely to occur at points A and B. The type of fastener used in a lap joint (such as a rivet, bolt, weld, screw, nail, or glue) does not matter as long as the joint is rigid and secure and does not need to be replaced [1].

The initial consideration to be analyzed by the engineer is to determine if the subject joint is to be either a permanent or a detachable joint. A *detachable joint* is defined as a joint that can be assembled and disassembled without any structural or geometric change to the fastener.

A brief overview of the primary joining approaches is reported below [1].

Adhesive bonding. Adhesive technology allows for the joining of a wide range of materials. Adhesive bonding involves bonding materials at the intermolecular or interatomic level, enabling the joining of dissimilar materials such as ceramic to metal, plastic to metal, and metal to metal. The aerospace industry has played a significant role in various industries' growing use and application of adhesive bonding.

Brazing and soldering. Brazing and soldering are mostly used for oil coolers and radiator seams. These methods are cheaper than welding and are suitable for low-stress and low-temperature environments. Solder has a melting point below 840°F, while braze has a melting point above 840°F. Soldered joints often use formed metal edges to transfer loads across the joint.

Riveting. This involves using a rivet, a mechanical fastener with a head on one end and a stem on the other, to join materials. The stem is inserted through holes in the materials to be joined, and then the head is formed on the stem to secure the joint.

Threaded fasteners. The primary function of most threaded fastener joints, such as bolts and screws, is to hold two or more objects together. Some bolting systems are used to bring objects together during assembly, while others are used to resist shear forces. Threaded fastener joints can be modelled as a series of springs. However, the stress distribution in the fastener spring system is non-uniform, making the joint an unstable system where long- and short-term effects can modify the distribution of stress and stored energy. In this context, "bolt" refers to threaded fasteners typically used with a nut or in a tapped hole. In contrast, "screw" refers to threaded fasteners with a sharp end, such as self-drilling screws for metal or wood screws.

Welded joint. Welding is a popular method of joining materials. Although it is being replaced by adhesive bonding in some cases, there are nevertheless many applications for which welding is the preferred and sometimes the only joining approach available. Many types of welding techniques are available, including electron beam welding, MIG welding, TIG welding, and friction welding. Another type of welding is resistance welding, which uses heat from the resistance to electric current to fuse the welded materials. Resistance welding is often used in manufacturing industries because it is fast, efficient, and can be automated. Despite the emergence of alternative joining methods, welding is still the preferred choice for many applications and is sometimes the only viable option. However, an overview of the welding process advantages/disadvantages will provide insight into the applications of all welding processes, as show in **Table *1***.

Advantages	**Disadvantages**
When properly formed, welds have strength equal to materials being joined.	Special equipment is necessary to detect weld defects, e.g., voids or occlusions and this approach is often not successful.
Temperature changes do not affect strength and rigidity within joint service range.	Residual stresses may be introduced.
Provides good thermal and electrical conductivity.	Welding may cause joined objects to warp.
When properly formed, joints are fluid tight.	Heat treatment of the metals being joined may change especially in the "heat affected zone."
Typically lighter than bolted joints.	Number of dissimilar metals that can be joined is limited. Disassembly of welded joints is very difficult if at all possible.
May be utilized to build-up or construct configurations other processes cannot form.	Welding requires: skilled (certified) operator and relatively expensive equipment.

Can be designed to introduce no additional stress concentrations by properly grinding weld beads.	Pre-welding surface treatment may be required.

Table 1. Advantages and disadvantages of welded joints [1].

Welded connections offer advantages over mechanical fasteners, including strength, stiffness, load-carrying capability, and cost-effectiveness. Modern welding techniques include submerged arc welding, shielded metal arc welding, and gas metal arc welding. However, controlling heat input during the welding process can be challenging. Residual stresses in the heat-affected zone (HAZ) can lead to brittle failure. There are two main types of welded joints: fillet and groove configurations. Groove or butt-type welds are typically stronger. Welded joints can be designed using either elastic or plastic methods, with a plastic design allowing for higher stress capacities. Welding can cause changes in the microstructure of the metal in the HAZ, leading to reduced fatigue resistance. Factors contributing to weld zone cracking include metallurgical and process variables, which must be carefully controlled. Fatigue life is influenced by the initiation and growth of critical cracks, and the fatigue strength of a joint can be reduced by intermittent longitudinal and transverse welds. The design of butt joints is relatively straightforward, but the sizing of fillet welds is mainly empirical. Weld line formulas are convenient and accurate for design purposes. The design of lap joints depends on the rigidity of the connected members, and regulatory bodies provide recommendations for lap joint design to ensure good fatigue resistance. Beam-to-column connections can be stiffened or unstiffened, and simplified formulas and design guidelines are available for selecting the optimal dimensions of the joint components. The design of column base plates involves bearing pressure allowable and plate bending criteria, and plastic hinge methodology can also be used. Cover plates can be welded to form entire girders or to increase the strength of existing structural shapes, using the same design formulas for both cases. New developments in welding technology include explosive seam welding, explosive cladding, diffusion welding, and other techniques that are superior to traditional joining methods. These types of welded joints should be based on empirical data [1].

1.1 Welded joints assessment

Quality assessment in welding is an essential aspect of mechanical design, as the quality of the weld can significantly affect the performance and reliability of the welded joint. Various

factors, including the type of welding process, the welding parameters, the quality of the base material and filler material, and the welder's skill determines weld quality.

Poor weld quality can lead to various problems, including reduced strength and stiffness, increased deformations under load, and reduced fatigue resistance. It can also lead to premature failure of the welded joint, which can be costly and dangerous in specific applications. Therefore, it is crucial to ensure that the welds meet the required quality standards to ensure the welded structure's overall performance and reliability.

By regularly assessing the quality of welds and implementing appropriate quality control measures, it is possible to ensure that the welded joint is of high quality and can withstand the expected loads and environmental conditions.

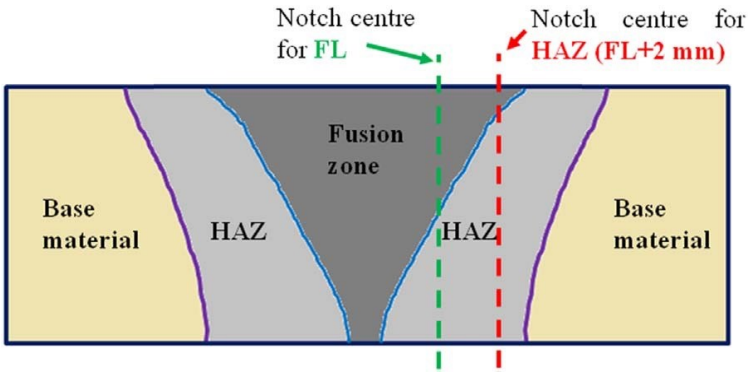

Figure 4. Scheme of different areas in a welded joint [2]

In addition to testing the welds after they have been completed, it is also essential to monitor the welding process to ensure that it is performed correctly. This may involve automated weld inspection systems or implementing quality control checks during welding. By taking a proactive approach to quality assessment in welding, it is possible to reduce the risk of defects and improve the overall performance and reliability of the welded structure [1].

1.1.1 Heat affected zone (HAZ)

The heat-affected zone (HAZ) in welding refers to the area of the base material that has been heated to a high enough temperature to cause a change in its microstructure but not enough to melt it (**Figure *4***). The extent of the HAZ depends on the welding process, the heat input, the material's thickness, and the base material's chemical composition.

During welding, the temperature at the weld interface can reach up to several thousand degrees Celsius. In comparison, the temperature in the HAZ can be several hundred degrees lower. The cooling rate in the HAZ is much slower than at the weld interface, leading to a longer time for the microstructure to transform. The microstructure in the

HAZ can be affected by the formation of new phases or the precipitation of carbides or other intermetallic compounds, which can alter the material's mechanical properties, such as its strength, ductility, and fatigue resistance. This can significantly impact the welded joint's overall performance, particularly under dynamic loading conditions.

One of the main problems with HAZ is that it can be a source of residual stresses. These stresses can be caused by the difference in thermal expansion between the weld and the base material, the formation of new phases or compounds, or the difference in cooling rates between the weld and the base material. These residual stresses can lead to distortion, deformation of the welded structure, or even brittle failure.

To minimize the negative effects of the HAZ, it is crucial to control the heat input during the welding process and to choose the appropriate welding parameters and filler material. The use of pre- or post-weld heat treatment can also help to reduce residual stresses [1].

1.1.2 Welded area

In welding, the effective melted area refers to the region of the base material that has reached the melting temperature and has been fused with the filler material. The effective melted area is an essential factor to consider in mechanical design, as it plays a significant role in the overall performance of the welded joint.

One of the main reasons for measuring the effective melted area is to ensure that the weld is sufficient to transfer the expected loads across the joint. The size and shape of the effective melted area can affect the strength and stiffness of the welded joint and its ability to resist deformation under load. A larger effective melted area will generally result in a more robust and stiffer joint. However, the size of the melted area should also be balanced against other factors, such as the base material's thickness and material properties, the welding process's type, and the weld's desired aesthetic appearance.

Another reason for measuring the effective melted area is to ensure that the weld is free of defects, such as porosity, slag inclusions, or incomplete fusion. These defects can weaken the welded joint and reduce its reliability and durability. By measuring the effective melted area, it is possible to identify and correct any defects that may have occurred during the welding process [1].

1.1.3 Defects in welded joints

Defect detection in welding is a vital aspect of mechanical design, as defects in welds can significantly affect the performance and reliability of the welded joint. Defects can occur

during the welding process due to various factors, including incorrect welding parameters, contamination of the base or filler material, or operator error.

Some common types of defects in welds include porosity, slag inclusions, incomplete fusion, and underfill or overfill **Figure *5***. Porosity refers to small voids or bubbles in the weld that can weaken the joint and reduce its fatigue resistance. Slag inclusions are non-metallic materials that can become trapped in the weld and create stress concentrations, leading to premature failure. Incomplete fusion occurs when the base material and filler material do not fully bond, creating a weak point in the weld. Underfill or overfill occurs when too little or too much filler material is used, resulting in a weld that needs to be properly sized to transfer the expected loads.

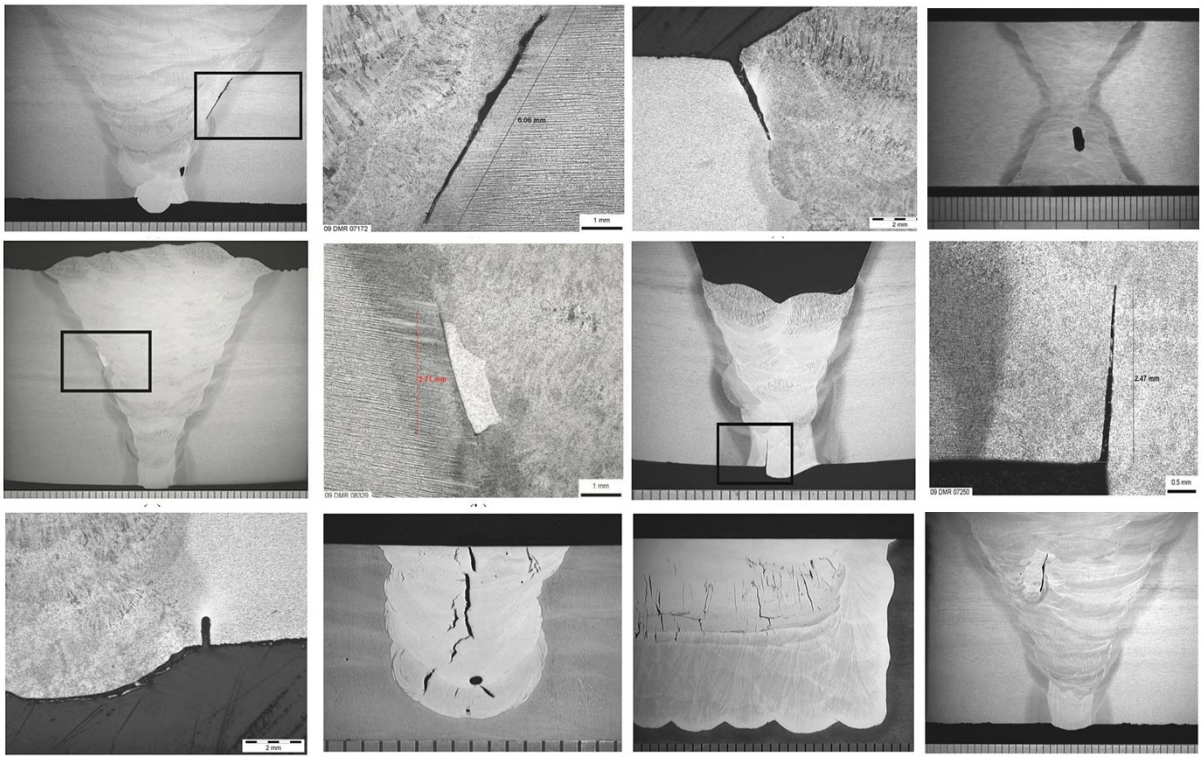

Figure 5. Several examples of typical defects in welded joints[3].

Defects in welds can lead to various problems, including reduced strength and stiffness, increased deformations under load, and reduced fatigue resistance. They can also lead to premature failure of the welded joint, which can be costly and dangerous in specific applications. Therefore, it is essential to detect and correct defects in welds to ensure the welded structure's overall performance and reliability [1].

Various methods for detecting defects in welds include visual inspection, radiographic inspection, ultrasonic inspection, and magnetic particle inspection. These methods can be used individually or in combination, depending on the type and location of the defects and

the material being welded. Regularly inspecting welds for defects and implementing appropriate quality control measures can ensure that the welded joint is of high quality and able to withstand the expected loads and environmental conditions.

1.2 Adhesive joint assessment

Quality assessment in adhesive joints is a crucial aspect of mechanical design, as the quality of the adhesive joint can significantly affect the performance and reliability of the structure. Adhesive joints are often used to join dissimilar materials, and the quality of the adhesive bond is influenced by a variety of factors, including the type and surface preparation of the materials being joined, the type and amount of adhesive used, and the curing conditions. One of the critical points of quality assessment in adhesive joints is ensuring that the adhesive has adequately wetted and bonded to the surfaces of the materials being joined.

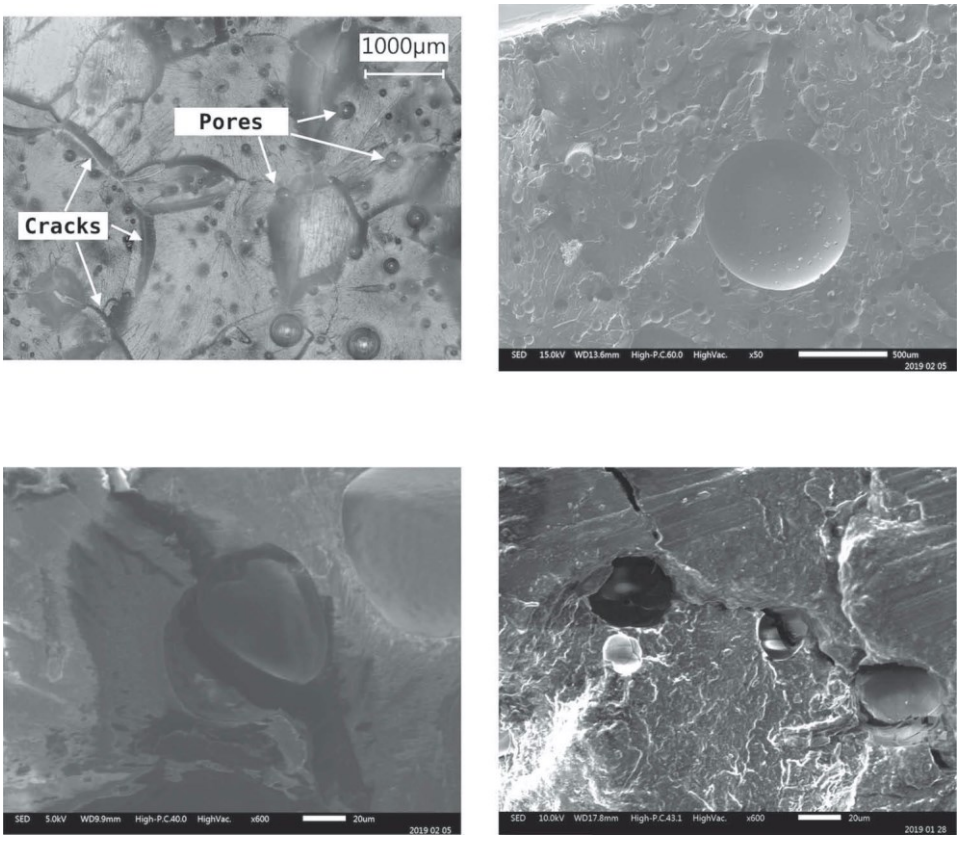

Figure 6. Examples of typical defects in adhesive joints[4]

This is important because a poor bond can lead to reduced strength and stiffness, increased deformations under load, and reduced fatigue resistance. In addition, poor bond quality can result in premature failure of the adhesive joint, which can be costly and dangerous in specific applications.

Another critical point of quality assessment in adhesive joints is ensuring that the adhesive has been adequately cured. Adhesive joints typically require a certain amount of time and temperature to reach their full strength. If the adhesive is not cured correctly, it may not achieve its full potential. This can lead to reduced performance and reliability of the adhesive joint.

There are several ways in which adhesive joints can fail. One common failure mode is a cohesive failure within the adhesive itself. A variety of factors, including excessive stress, temperature changes, or the presence of chemical contaminants, can cause this.

Another mode of failure is an adhesive failure, which occurs at the interface between the adhesive and one of the materials being joined. This can be caused by poor bonding between the adhesive and the material, inadequate surface preparation, or improper curing of the adhesive.

A third failure mode is an interfacial failure, which occurs at the interface between the two joined materials. This can be caused by mismatched coefficients of thermal expansion, differential movement between the two materials, or the presence of contaminants at the interface.

The importance of adhesive joints in mechanical design cannot be overstated. They are used in various applications, including aerospace, automotive, and construction, and play a crucial role in the integrity and performance of many structures and systems. Therefore, it is essential to understand the mechanisms of adhesive joint failure and to design and manufacture adhesive joints that are reliable and resistant to failure. This requires careful consideration of factors such as material selection, surface preparation, adhesive properties, curing conditions, and thorough testing and quality control measures.

There are various methods for assessing the quality of adhesive joints, including visual inspection, peel test, tensile test, and shear test. These methods can be used individually or in combination, depending on the type of adhesive and the materials being joined. By regularly assessing the quality of adhesive joints and implementing appropriate quality control measures, it is possible to ensure that the adhesive joint is of high quality and able to withstand the expected loads and environmental conditions.

1.3 Traditional destructive and Non-destructive methods

1.3.1 Destructive test for joints

Destructive testing methods are widely used to assess the quality of adhesive and welded joints, including their fatigue performance and the effect of defects on their strength and performance. These methods involve physically breaking or cutting the joint to examine its internal structure and properties. They can provide valuable information about the joint's performance under various loading conditions and the presence of defects.

1.3.1.1 Metallographic test

One standard method is the metallographic method which is widely used for evaluating the quality of welded joints. It involves preparing a cross-section of the welded joint and examining its internal microstructure and properties under a microscope.

The first step in the metallographic method is to prepare a sample of the welded joint for examination. This usually involves cutting or grinding the sample to a thin section and polishing it to a mirror finish. The sample is then mounted on a microscope stage, and a thin layer of contrasting material, such as a metal oxide or dye, is applied to highlight the microstructural features of the sample.

The sample is then examined under a microscope, typically at magnifications of around 100-500 times. This allows the examiner to observe the microstructure of the weld, including the grain size, the presence of defects such as porosity or inclusions, and the distribution of elements within the weld.

The metallographic method is a valuable tool for identifying and characterizing defects in welded joints and evaluating the weld's quality.

1.3.1.2 Tensile test

Tensile testing is a widely used method for assessing the quality of welded and adhesive joints. It involves applying a tensile load to the joint until it fractures, allowing to determine the strength and ductility of the weld and to identify any defects or weaknesses that may be present.

The tensile testing process typically involves mounting the joint in a testing machine and applying a tensile load to the joint using a set of grips or fixtures. The load is applied gradually, at a constant rate, until the joint fractures or deforms beyond a specified limit. The load-displacement behavior of the joint is recorded throughout the test. Various properties, such as yield strength, tensile strength, and elongation, are determined from the load-displacement curve.

Tensile testing is a useful tool for evaluating the strength and ductility of welded joints, as it allows to assess the ability of the weld to withstand tensile forces and to deform without breaking. It is also useful for identifying defects such as cracks, inclusions, or porosity that may be present within the joint.

1.3.1.3 Bending test

Bending tests are a widely used method for evaluating the quality of welded joints. They involve subjecting the welded joint to bending forces, either in a three-point or four-point configuration, until it fractures or deforms beyond a specified limit.

The bending test process typically involves mounting the welded joint in a testing machine and applying a bending load to the joint using a set of fixtures or loading points. The load is applied gradually, at a constant rate, until the welded joint fractures or deforms beyond a specified limit. The load-displacement behavior of the welded joint is recorded throughout the test. Various properties, such as yield strength, tensile strength, and ductility, are determined from the load-displacement curve.

Bending tests is used for evaluating the strength and ductility of welded joints, and to assess the ability of the weld to withstand bending forces and deform without breaking. Identification of typical defects such as cracks, inclusions, or porosity that may be present within the weld, can be provided too.

1.3.1.4 Chisel test

Chisel tests are a destructive method used to assess the quality of spot-welded joints. They involve applying a chisel-like force to the spot welded joint, typically in a shear or tensile configuration, until the weld fractures or deforms beyond a specified limit.

The chisel test process typically involves mounting the spot welded joint in a testing machine and applying a chisel load to the joint using a set of fixtures or loading points. The load is applied at a constant rate until the spot weld fractures or deforms beyond a specified limit. The load-displacement behavior of the spot weld is recorded throughout the test, and various properties, such as yield strength, tensile strength, and ductility, are determined from the load-displacement curve.

Chisel tests are useful for evaluating the strength and ductility of spot welded joints, as they allow to assess the ability of the weld to withstand shear or tensile forces and to deform without breaking. It is also used 1 for identifying defects such as cracks, inclusions, or porosity that may be present within the weld.

1.3.1.5 Peel test

Peel tests are a destructive testing method used to evaluate the quality of adhesive and welded joints, including their fatigue performance and the effect of defects on their strength and performance. These tests involve peeling the joint apart to measure its peel strength, which is the maximum force required to separate the two materials being joined.

The peel test process typically involves mounting the joint in a testing machine and applying a peel load to the joint using a set of fixtures or loading points. The load is applied gradually, at a constant rate, until the joint fractures or separates. The load-displacement behavior of the joint is recorded throughout the test, and the peel strength is determined from the maximum load or force required to separate the materials.

It is used to identify defects such as voids, inclusions, or contaminants that may be present within the adhesive or weld.

In fatigue testing, the adhesive or welded joint is subjected to repeated peel cycles, typically at a constant amplitude and frequency, until it fractures. This allows for determining the fatigue strength of the joint in the peel, which is the maximum stress it can withstand before failing due to fatigue.

1.3.1.6 Shear test

Shear tests are a destructive testing method used to evaluate the quality of adhesive and welded joints, including their fatigue performance and the effect of defects on their strength and performance.

The shear test process consists in mounting the joint in a testing machine and applying a shear load to the joint using a set of fixtures or loading points. The load is applied gradually, at a constant rate, until the joint fractures or deforms beyond a specified limit. The load-displacement behavior of the joint is recorded throughout the test, and the shear strength is determined from the maximum load or force required to cause failure.

The strength and performance of adhesive and welded joints, as they allow to the assessment of the joint's capability to resist shear forces and deform without breaking, can be evaluated by shear test. Moreover is used to identify defects such as voids, inclusions, or contaminants that may be present within the adhesive or weld.

1.3.2 Non-destructive tests for joints

Non-destructive testing (NDT) offers a valuable alternative to destructive tests to assess the quality of joints. Several methods are present, and the most suitable for this thesis's scope

will be discussed later. Below is only a short description of the traditional NDT method used to assess joints.

1.3.2.1 Visual test

Visual inspection is a widely used non-destructive testing (NDT) method for evaluating the quality of welded joints. It involves examining the surface of the welded joint with or without optical aids, such as hand lenses or borescopes, to identify defects or imperfections that may affect the joint's strength or performance. Gross surface defects, such as severe undercut or incompletely filled grooves, can be rejected immediately before further testing. The appearance of the weld surface can also provide information about the weld quality. Metallographic examination using a replica technique may be used to examine the structure of the weld metal and the surrounding area. Visual inspection may also include measuring various weld parameters, such as surface contour, and should be performed before welding to check the form of preparation, cleanliness, and fit-up. Optical aids, such as borescopes and closed-circuit television cameras, can be used to examine welds on internal surfaces or in otherwise inaccessible areas[5].

1.3.2.2 Magnetic particles

Magnetic particle testing is a non-destructive method used to detect surface and near-surface defects in ferromagnetic materials such as steel. The principle of the method is that a specimen is magnetized, producing magnetic lines of force within the material. Suppose these lines of force encounter a discontinuity, such as a crack. In that case, secondary magnetic poles are produced at the faces of the crack. These poles can be revealed by applying magnetic particles to the surface as a powder or liquid suspension. The best direction for crack detection is when the crack is at right angles to the magnetic flux and when it reaches the surface so that there is a local leakage of flux out of the specimen. The specimen can be magnetized in several different ways, such as by using it as a keeper across a permanent or electromagnet's poles or by passing a current through the specimen or a bar threaded through it. Magnetic particle testing is useful because it does not require special surface preparation and can detect cracks down to a few microns wide. However, it is limited to ferromagnetic materials and may require several tests on complex shapes to ensure complete coverage. The sensitivity of the method may also vary on complex shapes due to variations in magnetization

1.3.2.3 Eddy current method

Eddy current testing is a non-destructive method that uses alternating currents to detect flaws in conductive materials. When a coil carrying an alternating current is placed near a conductive metal specimen, eddy currents are induced in the specimen, which produces a current in a secondary search coil or affects the current in the primary coil. The flow of eddy currents in the specimen is disturbed by defects, which can be detected by measuring the current in the search coil. Eddy current testing can be sensitive to flaws. However, its accuracy is often affected by the metallurgical condition and dimensions of the specimen, as well as the geometry of the coils. Differential coil probes are a type of eddy current testing probe specifically designed to examine ferritic welds. These probes are characterized by their minimal dependency on variations in conductivity and permeability and operate at the lower frequency end of the range 100kHz-1MHz. To ensure accurate and reliable results, the equipment is calibrated with a standard reference piece containing slots of specified width and depth. Eddy current testing is also widely used for the automatic and rapid inspection of tubes, wires, and bar stock made of ferrous materials, with BS 3889: Part 2A: 1986 covering the inspection of ferrous pipes and tubes up to an outside diameter of 60mm. One advantage of eddy current testing is that it can be applied to non-metallic coated surfaces. However, the roughness of the surface may hinder efficient examination. Additionally, eddy current testing has the capability for high-speed scanning, provided that the computer has sufficient processing capacity to handle large amounts of data. Eddy current testing can also be applied to non-metallic coated surfaces, but the coating must be sufficiently thin to allow the eddy currents to penetrate. It is used for the rapid inspection of tubes, wires, bar stock, and other products and can be automated for high-speed production lines.

1.3.2.4 Penetrant methods

Penetrant methods involve applying a liquid to the surface of a specimen and allowing it to soak into surface-breaking cracks and cavities. The excess liquid is then removed, and any liquid that has entered cracks is made visible through a developer, fluorescence, or seepage. These methods can be used to detect surface-breaking cracks on all weldments. However, magnetic particle methods are preferred for welds in magnetizable materials. Penetrant testing is commonly used on welds in non-ferrous materials, light alloys, and austenitic and non-magnetic steels. It has the advantage of being able to cover the entire surface area of a specimen in one operation. There are two main types of penetrants:

fluorescent materials, which require a source of ultraviolet light for viewing, and dye penetrants, which produce a coloured indication. Fluorescent penetrants can be further divided into those that deposit material into the crack that fluoresces when dry and those that are fluorescent liquids. Effective cleaning of the specimen is crucial for penetrant testing, as contaminants can prevent the penetrant from entering cracks. Abrasive cleaning methods should be avoided unless followed by an acid etch, as they can close the mouth of a crack. Thixotropic penetrant liquids have been developed for in situ inspections on vertical or overhead surfaces.

The use of post-emulsifiable penetrants has allowed for the automation of the process for small components, resulting in standardized processing cycles. Components, such as turbine blades and castings, are typically loaded into wire baskets and placed on a conveyor rail. The total process time, including drying and development, is approximately one hour. Fluorescent penetrants are more commonly used due to their greater sensitivity, although both fluorescent and dye penetrants can be utilized. Automating the process for components with a known history allows for the pre-cleaning process, a crucial factor in the reliability of penetrant inspection, to be tailored to the contaminants present during manufacture. However, pre-cleaning specimens with unknown histories is a challenge in the penetrant inspection. Some dye penetrant processes can be applied at high temperatures and are useful for examining preheated welds, partially completed welds, and weldments with a slow cooling rate. The procedure for these applications involves soaking at reduced temperatures for shorter periods.

1.3.2.5 X-Ray method

X-rays and gamma-rays are types of electromagnetic radiation that have a shorter wavelength than visible light, infrared, ultraviolet, and radio waves, which allows them to penetrate through many materials to some extent. They are absorbed and travel in straight lines as they pass through a material. Suppose a source of X-rays is placed on one side of a specimen and a sheet of photographic film on the other. In that case, the film will show a darker image area under any cavities in the specimen due to the differences in the intensity of the X-rays that pass through the solid material compared to the cavity. This image will be a "shadow picture" of the internal structure of the specimen, with the image of the cavity being a projection of the three-dimensional cavity onto the two-dimensional plane of the film. However, a simple radiograph will not provide information on the location of the cavity through the thickness of the specimen. To produce a radiograph, a

source of X-rays or gamma-rays, a photographic film, and means of processing the film are required. In addition, the film must be viewed on an illuminated screen of appropriate luminance to "read" it. Gamma rays are similar to X-rays, and the same principles apply to producing a gamma radiograph. Other particles such as neutrons, electrons, and protons can also be used to produce photographic images similar to radiographs for specific applications, and terms like "neutron radiography" are used even though these particles are atomic particles rather than electromagnetic radiation.

1.3.2.6 Ultrasonic method

Ultrasonic flaw detection in welds involves using a small probe known as a transducer, which is moved manually over the surface of the parent metal adjacent to the weld. The transducer produces a beam of ultrasound which is transmitted into the metal and reflected from any flaws or discontinuities present. The reflected ultrasound pulse is then picked up by the same transducer, which acts as both transmitter and receiver in the process, known as the pulse-echo technique. The effectiveness of this technique depends on a thorough understanding of the beam direction, size, and underlying physical principles. The transducer must be coupled to the metal surface using a layer of liquid, such as water, oil, or grease. The results of the ultrasonic inspection are typically displayed on an oscilloscope screen.

There is another application of ultrasound, in which a wide field source transmits an ultrasound beam detected over a large area and is used to create an ultrasound image similar to an X-ray image. This method is attractive because ultrasound can pass through thick layers of fine-grain metal and does not involve ionizing radiation. Several systems have been developed, including ultrasonic image converter tubes, computer reconstruction methods, and acoustic holography. However, it should be noted that the wavelength of the ultrasonic waves used for metal inspection is approximately 1 to 4 millimetres, so high-resolution images cannot be expected. These methods have not progressed beyond the laboratory stage, and methods using automated data collection and processing with multiple probe systems such as SAFT will likely replace imaging tubes. Suppose an ultrasonic transducer is made up of multiple elements, and each element is separately activated by generating pulses. In that case, the ultrasonic beam shape and direction can be controlled by appropriately phasing the pulses. By using similar electronic control of the receiver pulses, an ultrasonic image can be created.

One limitation of ultrasonic testing is that it is highly dependent on the surface finish of the metal plate. If the surface is rough or uneven, obtaining a clear ultrasonic signal can be challenging, making it difficult to detect defects accurately. In addition, ultrasonic testing is not well suited for detecting defects that are oriented perpendicular to the surface of the metal plate, as the ultrasonic waves will not be able to penetrate the material.

X-ray inspection is another standard method for inspecting thin metal plates. It is particularly effective for detecting defects that are oriented perpendicular to the surface. However, X-ray inspection is not suitable for inspecting metal plates that are too thick, as the X-rays will not be able to penetrate through the material. In addition, X-ray inspection requires radiation, which can be hazardous if not properly handled.

While destructive testing methods help identify defects and weaknesses in welded joints, they are not suitable for testing in-service components or structures, as they permanently damage the test specimen. Non-destructive testing methods, such as X-ray inspection or ultrasonic testing, are often used instead to assess the quality of welded joints in these cases.

Most of the non-destructive techniques mentioned above are widely used in successfully controlling welds. However, these techniques encounter significant limitations. Much of traditional control is challenging to automate and often requires the preparation of the specimen surface with long inspection times. This is a significant limitation in the production industry where it is, therefore, necessary to perform sample analysis or, if it were done on 100% of the production, it would require exceptionally prolonged times. Another area for improvement, mainly for UT controls, is the inspection of thin joints/sheets where it is difficult to obtain reliable results. Therefore, there is a need for the development of a reliable control on thin joints, which allows a wide range of inspection, with rapid post-processing and is compatible with production times and that is easily automatable.

CHAPTER 2

Why thermography?

In previous sections, it has been seen that both destructive and non-destructive methods have limitations that prevent their automation or application to 100% of production or have limitations of the technique, especially for thin joints. To overcome these limits, thermography is an up-and-coming technique due to its characteristics, which will be better clarified below in this chapter. Although thermography appears as a surface control method, it is possible to inspect even a few millimetres of high-conductive materials with some precautions. For low-conductive materials, such as composites, thermography has also been used as a volumetric technique for some time. It will be seen that active thermography does not require contact with the component, allows full field control, is easy to use and automate, and especially allows a drastic reduction in analysis times and is also suitable for inline controls

2.1 Basics of thermography

The body's temperature measures the level of agitation of the molecules that make it up; that is, it is an intensive property defined by a scalar physical quantity, indicating a system's thermal state. When two bodies at different temperatures are placed in thermal contact, they will give rise to a flow of heat from the body with the higher temperature to the one with the lower temperature; therefore, heat is one of the possible ways to exchange energy between two bodies. Heat exchange can occur in conduction, convection, and radiation. Since temperature is therefore linked to the molecular state of agitation, that is, to the kinetic energy possessed by the molecule itself, it is easily understandable how heat exchange occurs by conduction: in fact, this is due to collisions between contiguous molecules that, during the impact, acquire or transfer kinetic energy, varying their state of agitation, and therefore their temperature. The quantification of heat exchanged is regulated, under stationary conditions, by Fourier's Law, which shows that it depends on: the thermal conductivity of the material, the surface of thermal exchange considered, and the difference in temperature.

$$q_x = -kA_x \frac{dT}{dx} \tag{1}$$

where x indicates the direction of propagation of the heat flow, k is the material's thermal conductivity, and T is the temperature. The substances considered optimal from the point of view of thermal insulation will be those characterized by very low conductivity coefficients. Convection, on the other hand, is a mode of heat transfer characteristic of fluids and is therefore linked to the motion of these in the vicinity of the surface. In this case, we must consider the movements of mass, fluid density, viscosity, velocity, and fluid flows, which makes it a phenomenon far from trivial to study; for a simplified evaluation, the relationship below is used.

$$q_c = \bar{h} A_s (T_s - T_f) \tag{2}$$

In the above relationship, q represents the heat exchanged by convection, A is the surface of thermal exchange, T_s is the surface temperature, T_f is the fluid under consideration, and $\bar{h}$ is the average convective exchange coefficient. The average convective exchange coefficient considers that the flow can be natural or forced, its direction, Reynolds number, Prandtl number, etc. This makes it difficult to determine the proportion of heat exchanged by convection, which is why it is necessary to consider this aspect for outdoor measurements.

2.1.1 Radiative heat exchange

Energy is transmitted through electromagnetic waves, which do not require a material medium during radiation. A material emits it due to the rotational movements of its atoms and molecules, which are always present in bodies at temperatures above *0 K,* so this will occur continuously. In addition, increasing the agitation of particles increases the temperature and, therefore, the thermal emission. Electromagnetic waves are classified according to their frequency and wavelength, which indicates the energy they carry. Therefore, it is possible to obtain an electromagnetic spectrum that allows classification, taking the narrow visible zone as a reference, which is characterized by a spectrum ranging from red to violet, or vice versa, depending on whether the wavelength or frequency increases, as shown in the figure below.

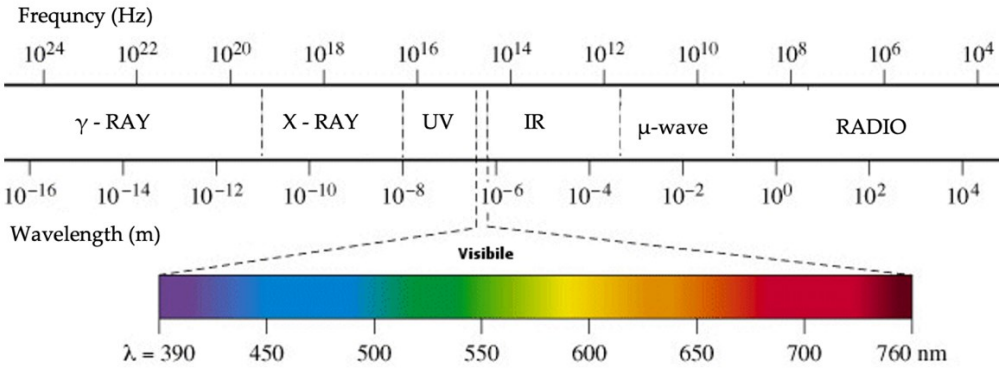

Figure 7. Electromagnetic spectrum classification

Vector quantities that characterize the wave are placed on orthogonal planes. At the same time, in the acoustic field, they have the same direction. However, the relationship between the speed of light, frequency, and wavelength can still be defined analogously as:

$$\lambda = \frac{c_0}{f} \tag{3}$$

The propagation of radiant energy can be considered from another perspective: in the field of physics, it is known that electromagnetic radiation has a dual nature, that is, corpuscular and wave-like, known as the wave-particle duality. In 1924, De Broglie proposed his idea on atomic particles, which therefore possess wave properties in the same way that a photon can be assigned a mass. Using Planck's constant (h = 6.6237 * 10-34 J s) and the momentum of the particles (p = mc), the De Broglie wavelength can be defined as:

$$\lambda = \frac{h}{p} \tag{4}$$

The wave-particle dual nature of radiation forms the basis of Einstein's theory of relativity and the basis of spectroscopy science. In fact, as a consequence of the de Broglie principle, when an electron moves from one energy level to another within an atom, a corresponding (quantum) amount of energy is absorbed or emitted by the atom. However, a body that emits radiation due to its temperature does not emit it throughout the spectrum; in fact, the defined thermal radiation is only in the infrared field, so it is possible to connect infrared radiation to the body's temperature. The relationship for calculating the amount of heat exchanged by radiation is known as the Stefan-Boltzmann law and is reported below:

$$q_r = \sigma \, F_{s-r} \, A_s (T_s^4 - T_r^4) \tag{5}$$

The Stefan-Boltzmann law includes the constant σ, which is the Stefan-Boltzmann constant and is equal to $\sigma = 5.67 \cdot 10^{-8} \left[{}^{W}/_{m^2 K^4} \right]$, $F_{s\text{-}r}$ which is the view factor and takes into account the portion of energy that leaves surface s and reaches surface r, As which indicates the value of the emitting surface, T_s and T_r which indicate respectively the

temperature of the source and that of the lower temperature body. The behavior of a body concerning emitted energy and incident radiation on it varies depending on its state of aggregation. In the case of a gas, it can only emit or receive radiation in specific discrete wavelengths; in fact, a gas does not continuously absorb or emit thermal radiation, so there is a specific "signature" of the gas characterized by a line spectrum. Condensed bodies, that is, liquids and solids, emit in a continuous band, so the spectrum will not be lined, as for gases, but continuous, indicating only the thermal condition of a thin surface layer of the body. When an electromagnetic wave impinges on a body, three phenomena co-occur reflection, transmission, and absorption. This means that, of the energy incident on a body, a portion will be reflected from the surface, and another will be absorbed by the body, increasing its temperature. At the same time, a final part will be transmitted through it. As observed, in real bodies, these phenomena co-occur with different percentages, which makes the study of these phenomena more complex; bodies characterized by this kind of behavior are called: grey bodies. This implies that considering incident radiation with total energy E, the situation described in **Figure *8*** will occur. That is, it will be "divided" between a transmitted portion, a reflected portion, and an absorbed portion, proportional to coefficients that will be characteristics of the struck surface and the body itself. It can then be written that:

$$\alpha + \rho + \tau = 1 \tag{6}$$

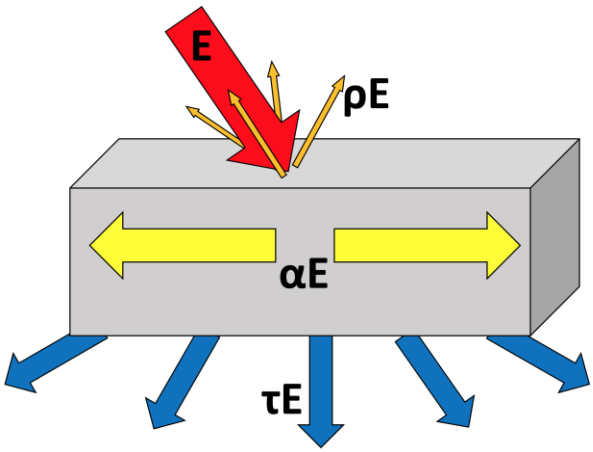

Figure 8. Scheme of the phenomena of reflection, transmission and absorption for incident ray.

2.1.2 Black body

Typically, all three phenomena co-occur reflection, emission, and transmission. Particular bodies have zero reflection and do not transmit anything, only absorbing everything that impacts them. These are known as black bodies. Black bodies do not exist. However, it is

possible to simulate this behaviour with appropriate measures. A cavity can represent a black body with a hole slightly wider than the width of the incoming wave; in this way, once it enters, it will be reflected repeatedly by the internal surfaces until the reflected portion is practically reduced to zero and can exit the orifice (**Figure *9***). This behaviour simplifies the previous relationship because, for a body that behaves as a black body, the reflected portion is zero, and the previous relationship becomes $\alpha = 1$.

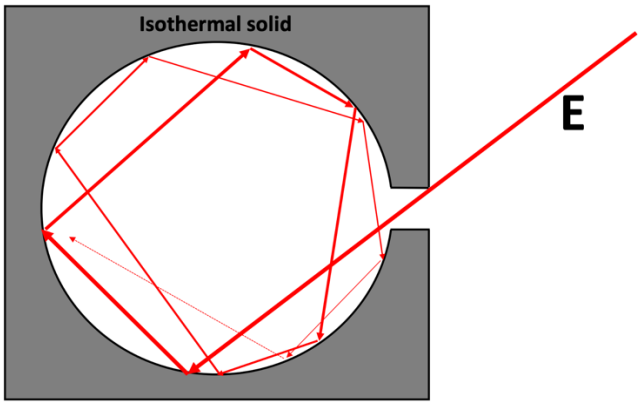

Figure 9. Artificial black body.

A *black body* can therefore be defined as a body with a unit absorption coefficient and a zero-reflection coefficient.

Consider a surface element of a black body, which radiates in all directions with a constant radiance $I\ \left[{W}/{m^2 sterad}\right]$, the radiation flux dW emitted in all directions by the infinitesimal element dA is $dW = \int_{\Omega} I\, dA\, cos\beta\, d\Omega$

For a unit radius hemisphere, the flux density can be defined in the following manner:

$$E = \frac{dW}{dA} = \int_0^{\frac{\pi}{2}} I cos\beta\ 2\pi\ sin\beta\ d\beta = \pi I \qquad (7)$$

It then becomes necessary to define the volumetric spectral density of radiation, which is a function of frequency f and absolute temperature T. This is governed by a specific law known as the Planck law; it is, in fact, possible to derive a significant quantity which is the spectral radiance.

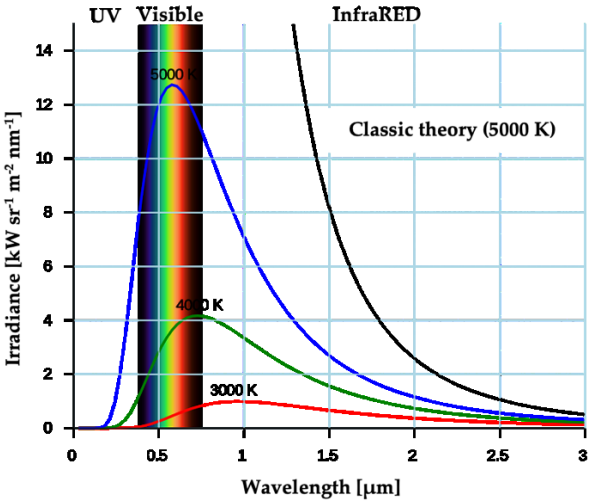

Figure 10. Irradiance of black-body as function of wavelength.

Observing the dependence on temperature is possible because there are different curves, each for a fixed temperature. It can be noted that the maximum value of the spectral radiance varies with temperature. It is obtained at different λ values; as the temperature increases, the radiance curve has a maximum that shifts to the left, that is, to shorter wavelengths. The curve with the maximum radiance in the visible field corresponds to 5000 K, that is, the temperature of the Sun's photosphere. It is possible to obtain a law for the displacement of the maximum radiance value, well known as the Wien displacement law. It can be said that the energy of the black body is not concentrated in any region of the electromagnetic spectrum. However, at each temperature, it has a wavelength at which the emitted radiation has a maximum. This wavelength follows the Wien displacement law: $\lambda_M T = 2.8977685 \cdot 10^{-3} mK$.

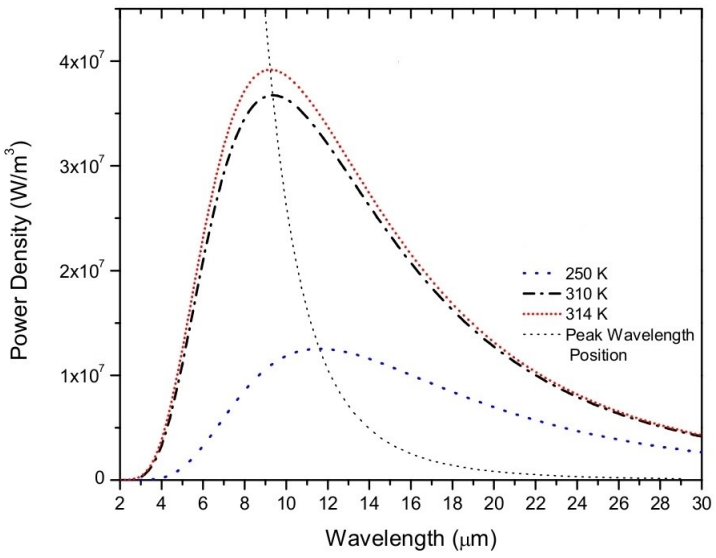

Figure 11. Wien law.

2.1.3 Real surface

It should be noted that the black body is a useful theoretical construct but not a physically realizable object. Real surfaces will exhibit different behaviour. Since a black body is an idealized object that absorbs and emits all incident radiation without transmitting or reflecting anything, it follows that it will correspond to the maximum radiant emission. This is why the black body is considered a reference to the point of defining a critical quantity, the emissivity, which indicates how much energy a body radiates compared to a black body at the same temperature and for the same wavelength.

A body does not have a constant emissivity concerning wavelength (λ). However, it can be considered as such in certain restricted wavelength domains. The emissivity depends on several factors such as:

- Material;
- Wavelength (λ);
- Temperature (T);
- Observation angle (β);
- Surface roughness.

Generally, it can be observed that the emissivity increases with increasing temperature for materials with high thermal conductivity, while it tends to have the opposite behavior, that is, it decreases with increasing temperature, in the case of materials with low thermal conductivity.

Regarding the observation angle (β), it can be observed that it decreases as the observation angle increases. This has significant effects that must be taken into account as for curved surfaces, a different signal could be observed between areas of the same body, although at the same temperature; this variation in the detected signal would not be due to an actual temperature variation on the body, but rather a consequence of the inclination of the surface and therefore a variation in emissivity.

For a natural surface, several considerations can therefore be made that will be fundamental to consider how a body's radiant emission is related to temperature.

The first consideration is Kirchhoff's theorem, which demonstrates that at a given temperature and frequency (or wavelength, given the relationship $\lambda = c/\nu$), the ratio between the emitted power Pem and the absorbed power Pass is the same for all bodies, is, the achievement of thermal equilibrium between two bodies in contact with each other is

possible only if a universal function f (ν, T) results from this ratio, independent of the nature of the bodies themselves:

$$\frac{P_{em}}{P_{ass}} = f(\nu, T) \tag{8}$$

Kirchhoff defined a black body as a body whose absorbed power P_{ass} is equal to 1 at every temperature and frequency: from this, it follows that the function f(ν, T) equals the emitted power Pem. For this reason, it is, therefore, possible to say that for a black body, the emissivity is equal to the absorption, so ε=α. The previously written relationship becomes:

$$\varepsilon + \rho + \tau = 1. \tag{9}$$

For an opaque body, it can also be considered that the portion of the transmitted energy is zero, so the relationship can be further modified and becomes:

$$\varepsilon + \rho = 1. \tag{10}$$

This equation shows how reflective surfaces have a very low emissivity, while rough, oxidized, painted surfaces have high emissivity values.

2.1.4 The media

It must be considered that when making distance measurements between the surface under investigation and the instrument to be used for irradiance, there will be an intermediate medium, the air. In fact, it is impossible to ignore the presence of air between the detector and the object of investigation since, as mentioned before, gaseous substances absorb and emit discreetly, so this must be considered and evaluated in which bands of wavelengths this occurs. Therefore, the atmosphere, which is to be considered a mixture of gases, will have a behavior for which it will emit specific wavelength values. It will be entirely opaque for some λ and transparent only in some windows that will be called atmospheric windows: that is, those values of wavelength for which the atmosphere is transparent, that is, with a unitary coefficient τ. Being able to define areas of "transparency" of the atmosphere, these can be considered as areas for which the effect of the presence of gas between the detector and the emitting surface can almost be neglected, so these will be the areas of main interest in order to make measurements. Similarly, a series of values of λ can be defined for which the atmosphere is completely opaque, so it would be impossible for the waves emitted by the emitting body to reach the detector since the intervening atmosphere would not allow

them to pass. **Figure** ***12*** shows the transmission coefficient's value as a wavelength function.

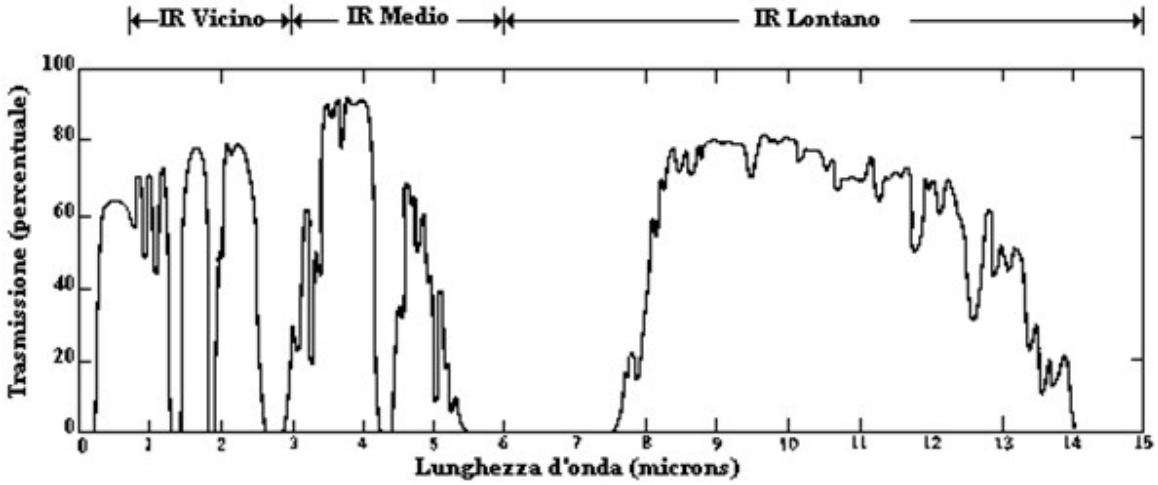

Figure 12. How change the transmission coefficient of atmosphere as a function of wavelength.

It is, therefore, clear that it is possible to consider the atmosphere transparent for wavelengths between 8 μm and 14 μm and between 2 μm and 5 μm. It will be precisely in these ranges that the detectors will work, which will be discussed below. The thickness of the intervening air is relevant: in fact, the transmissibility coefficient varies with the thickness of this. This is synonymous with distance from the object of investigation; that is, for measurements taken at great distances, the atmospheric windows may decrease, so there will be a variation in the transmission coefficient due to the thickness of the air, which must be particularly taken into account for measurements taken at significant distances.

2.1.5 IR Camera

The thermal imaging camera converts incoming information from radiant energy that has struck its sensor into a two-dimensional heat map of the surface being observed. This is accomplished through the use of physical principles. The camera's input is the thermal energy emitted by the target, and its output is a series of electronic signals. These signals are first focused onto the detector by the camera's optics and then amplified and transmitted to the device that processes the video and displays the final two-dimensional information on a screen. The input signal is processed by passing through the optical scan module, which includes a lens, filters, and a chain of mirrors that directs the signal to a series of optical relays equipped with an opening unit and filters. The signal is then focused onto the detector, which converts it from an optical signal to an electronic one. The signal

is amplified by the preamplifier and converted into a 12-bit digital signal by the A/D converter before being transmitted to the microprocessor via optical fibres.

Infrared cameras typically have sensors that are protected by optics that shield them from the environment. In specific applications, filters may also be used to reduce the radiation reaching the sensor at a given temperature and shift the sensor's saturation point to higher temperatures. The optics and filters used in these cameras are transparent only at specific wavelengths. The amount of radiation that reaches the sensor depends on the transmissivity of all the windows through which it passes, as well as on the emission of the optics themselves and the reflection effects caused by the surrounding environment. Common materials used in constructing these optics and filters include fluorocarbons such as silicon and germanium. These materials have good mechanical properties, are not hygroscopic, and can be formed into lenses. Each material is transparent in a particular infrared band but opaque in other electromagnetic spectrum areas. Therefore, the selection of materials for use in IR cameras must be carefully considered to ensure that they are appropriate for the desired range of wavelengths.

2.1.5.1 IR Detectors

Detectors are the primary component of infrared imaging systems. Their function is to detect infrared radiation and convert it into a signal that can be interpreted. Theoretically, any physical property sensitive to temperature can be used as a detector. Herschel created the first infrared image system in 1840, and it used a liquid-filled thermometer with a specially blackened bulb to absorb radiation as a crude monochromator to measure the distribution of energy in sunlight. In 1929, Czerny developed the evaporograph, which used the differential evaporation of a thin film of oil on a dark membrane to detect infrared radiation. Since then, the technologies used for detectors have evolved to include increasingly sophisticated devices with high sensitivity and very high acquisition frequency. Modern infrared cameras use a focal plane array (FPA) as a detector, an array of pixels with micrometre-sized dimensions made of various materials sensitive to infrared wavelengths. Most detectors do not have a response curve that covers the full range of infrared wavelengths, so detectors must be carefully selected to match the range of wavelengths used in a specific application. To evaluate infrared detectors, it is possible to refer to the values of specific characteristic parameters, such as impedance, which is the intrinsic characteristic of the detector that is measured using Ohm's law.

$$Z = \frac{dV}{dI} \ [ohms] \tag{11}$$

The responsivity, that is the transformation ratio of the incident optical flow F:

$$R_v = \frac{\partial V}{\partial F} \ [V \cdot W^{-1}] \tag{12}$$

Other parameters that can be used to evaluate infrared detectors include Noise Equivalent Power (NEP), which is the amount of power induced by an optical signal whose amplitude is equivalent to the intrinsic noise power of the detector. The related incident optical power is called the noise equivalent power flow (FNEP). The Noise Equivalent Temperature Difference (NETD) is another parameter that can be used to evaluate detectors, and it is defined as the change in temperature of a large blackbody in the scene being observed that causes a change in the signal-to-noise ratio of unity in the output of the detector. Detectivity is another parameter commonly used to evaluate infrared detectors. It is defined as the ratio of the NEP to the square root of the detector's bandwidth.

$$D = \frac{1}{F_{NEP}} \ [W^{-1}] \tag{13}$$

To compare the detectivity of different detectors, the detectivity D* is often used. This parameter is measured in units of W^{-1} cm $Hz^{1/2}$ and is obtained by scaling the detectivity D to the unit-sensitive detector area and bandwidth. This allows for a more meaningful comparison of the detectivity of different detectors, as it considers the detector's size and the bandwidth over which it is sensitive.

Infrared detectors can be broadly classified into two main categories: thermal and photonic. Thermal detectors are made of materials whose physical properties vary with temperature, such that they produce a measurable signal when they are heated by incident radiation. The response of these detectors is independent of the wavelength of the incident radiation. Some technologies that have been used as thermal detectors include bolometers, thermopiles, pneumatic detectors, pyroelectric detectors, and liquid crystals. Modern IR cameras with thermal detectors often use an uncooled microbolometer made of a metal or semiconductor material, which operates according to non-quantum principles. The main advantages of these devices are their low cost, wide IR spectral response (limited only by the entry optics and the presence of any filters), and the fact that they do not require cooling (allowing for a compact camera design). However, their disadvantages include a slow reaction to incident radiation (around 12 ms), a limited range of observable temperatures,

detectivity that is only about half as good as that of photonic detectors, and average image quality.

On the other hand, photonic detectors are semiconductors whose free electron states are affected by incident radiation. When the sensor is heated by incident photons, its energy releases electrons, increasing the density of free electrons and thus the detector's electrical conductivity or output voltage. The response of photonic detectors depends on the wavelength of the incident photons, as a certain amount of energy is required to move electrons. Photonic detectors have a faster response than thermal devices, as no temperature increase is required. They react to changes in IR levels with a constant response time of around 1 μs. However, they require cooling, even down to cryogenic temperatures using liquid nitrogen or small Stirling cycle refrigerator systems. The most common materials used as photonic detectors are Si, InAs, InSb, HgCdTe, InGaAs, PtSi, and layered GaAs/AlGaAs. These materials respond to IR by absorbing photons that elevate the material's electrons to higher energy states, causing a change in conductivity, voltage, or current. The sensitivity of these materials to IR increases when they are cooled to cryogenic temperatures. Three leading technologies use photonic detectors in IR cameras: systems equipped with point detectors (single pixel sensors) and mechanical scanning for image formation, systems equipped with SPRITE detectors and mechanical scanning for image formation, and cameras using IR focal plane arrays (IRFPAs) that involve electronic scanning of the image. IRFPAs are the technology used in modern thermal imaging cameras, and their development is currently in flux.

2.2 Active thermography

The previous section briefly described the physical principle of thermography and how it is possible to perform temperature measurements. Nevertheless, when the thermographic technique is adopted as NDT, it usually speaks about active thermography.

Active thermography is so-called because an external heating source is needed to introduce energy to a specimen. In fact, due to local differences in thermo-physical properties between a defective area and a "sound" one, an IR camera can observe a temperature difference on the surface of the specimen. Disparate kinds of sources can be used to generate a heat flux, as resumes the scheme in **Figure *13***, for example:

- Mechanical;
- Optical;

- Electromagnetic.

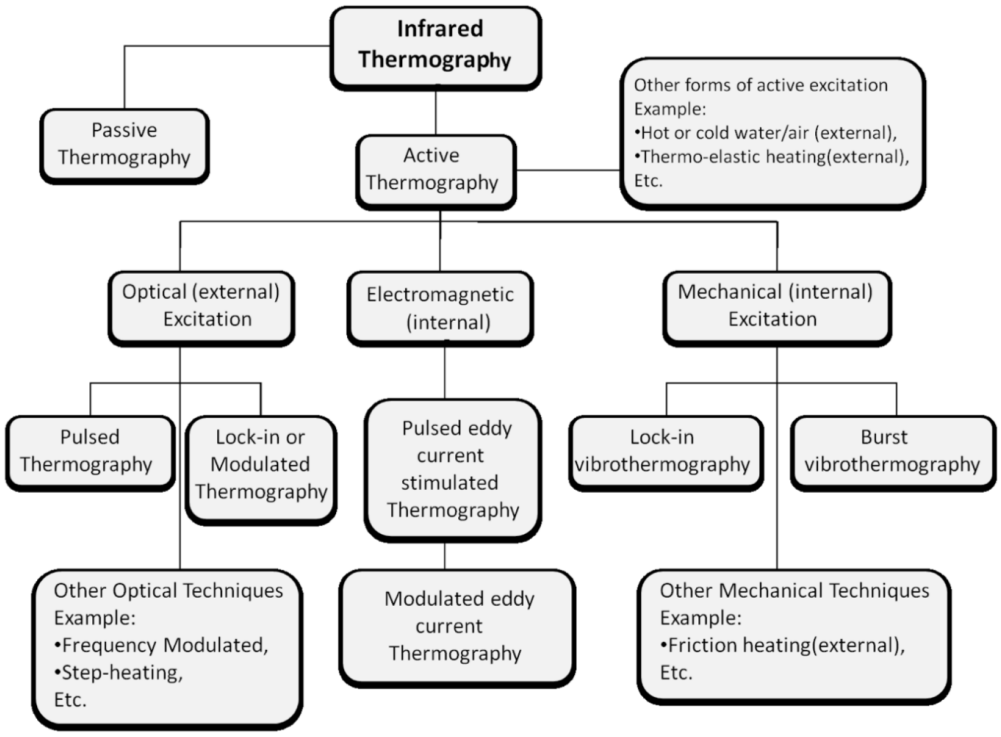

Figure 13. Summary scheme of active thermography.

Optical heat sources are widely used for active thermography because they can be easy to apply and, in cases of halogen of flash lamps, cheap and safe for the user. A preliminary description of the physics of the phenomena and the thermal wave theory will follow, which is necessary to better understand the two main thermographic techniques: lock-in thermography and pulsed ones. A short description of the principal post-processing algorithms will be presented, and the motivation for choosing thermography as NDT for joints will be clarified, discussing briefly the potential application to evaluate HAZ.

2.2.1 Thermal wave theory

When a solid is superficially heated on the surface, a "thermal wave" starts propagating through the material. Thermal waves described the first time by Fourier and Ångström [6] are visible in the infrared spectrum. Thus, it is possible to observe them using by IR camera.

2.2.1.1 Modulated thermal wave

Considering the hypotheses of a homogeneous semi-infinite media with a planar surface heated with a pulse ω, the analytical problem can be reduced in 1D, and it is possible to write the following relation, which describes the temperature *(T)* behavior, through the thickness, as a function of time *t:*

$$T(z,t) = T_0 e^{-\frac{z}{\mu}} \cos\left(\frac{2\pi z}{\lambda} - \omega t\right) = T_0 e^{-\frac{z}{\mu}} \cos\left(\omega t - \frac{2\pi z}{\lambda}\right). \quad (14)$$

where $\omega = 2\pi f$ is in $\frac{rad}{s}$ and, f is the frequency in *Hz* and μ is the thermal diffusion length expressed as reported below:

$$\mu = \sqrt{\frac{2k}{\omega \rho C}} = \sqrt{\frac{2\alpha}{\omega}} \quad (15)$$

Hence, it is possible to write the speed of the thermal wave in material related to thermal diffusion length and the propagation depth.

$$\Phi(z) = \frac{2\pi z}{\lambda} = \frac{z}{\mu} \quad (16)$$

From this relation it is clear the inverse relation between frequency of modulated heating and the inspection depth. It can be observed that μ is inversely proportional to ω, which indicates that high frequencies limit analysis to regions near the surface; lower frequencies, on the other hand, allow for deeper penetration but at slower speeds. For NDT applications, it is interesting to note that thermal waves reflect off surfaces perpendicular to the wavefront, such as defects containing gas or on the bottom surface, and then return to the surface; this allows for the detection of discrepancies between the reflected temperature field corresponding to the intact specimen and the one corresponding to the defect [6]. A reflection coefficient R can then be defined that depends on the material, specifically on the material's thermal effusivity $e = \sqrt{k\rho C}$, as well as that of the defect; it is expressed in terms of $b = \frac{e_2}{e_1}$.

2.2.1.2 Pulsed thermal wave

In the same way as the modulated thermal wave, with appropriate assumptions, it is also possible to write the T trend due to: Dirac pulse, semi-infinite body, adiabatic process, Lambert's surface, 1D flux in an homogenous and isotropic body. So, the solution of Fourier heat equation in this case is [7]:

$$T(z,t) = T_0 + \frac{Q}{\sqrt{k\rho C \pi t}} e^{-\frac{z}{4\alpha t}} \quad (17)$$

in which Q is the energy density absorbed by the surface measured as $[J/m^2]$ and T_0 the initial temperature of the surface ($z=0$):

$$T(0,t) = T_0 + \frac{Q}{e\sqrt{\pi t}} \quad (18)$$

This simple relationship can calculate the cooling curve for isotropic homogeneous materials. Suppose a defect has different thermophysical properties than the base material (air gap, inclusion, interface, etc.). In that case, it is expected that the two cooling curves will diverge when subjected to the same thermal load.

2.2.2 Thermal source

As previously mentioned, it is possible to provide thermal energy to the test specimen in various ways, that is, by exploiting different physical principles depending on the use and the object to be observed. Thermal excitation can be: internal when heat is generated within the material, and the development of this is observed towards the surface, or external when an external source provides it, and the thermal flow goes from the surface towards the core of the material itself. Generally, the sources of thermal excitation are distinguished according to the physical principle as electromagnetic, mechanical, and optical [8–10].

2.2.2.1 Mechanical source

Generally, it is possible to provide heating using mechanical excitation, internally or externally. In the case of external mechanical heating sources, the most common is wear. However, it is more diffused the internal heat production through vibration produced exciting mechanically. In this case, the specimen is called vibrothermography. Using this method, the sample is mechanically excited by sound or ultrasonic oscillations. The excitations of the test sample are generated by coupling an ultrasonic transducer to the sample. The propagation of waves in the material transforms mechanical energy into thermal energy at the tips of the cracks. The energy dissipation between the defect and non-defect areas is significant due to the effects of friction between them. The difference in energy dissipation leads to temperature differences between the two areas, which are then captured using a thermal infrared camera. Vibrothermography is again classified into two categories: *lock-in vibrothermography* and *burst vibrothermography*.

2.2.2.2 Electromagnetic source

In electromagnetic excitation, parasitic currents induce current circulation phenomena within the test specimen, generating internal heat that propagates to the surface. Magnetic induction is governed by the Lenz-Faraday-Neumann law:

$$\varepsilon = -\frac{d\phi_B}{dt} \tag{19}$$

Where ε is the electromotive force, Φ_B is the magnetic field flux through the circuit expressed in Weber. The defective and non-defective areas respond uniquely to the induced

current and show different temperature differences due to magnetic excitation. This temperature difference between the defective and non-defective areas is then detected with a thermal infrared camera. The main disadvantage of electromagnetic excitation is that it only applies to conductive materials.

2.2.2.3 Optical source

Optical sources provide only external heating using source as halogen and flash lamps, lasers, solar hearing, etc. As introduced before, depending on the kind of thermal wave generated, it is possible to define pulsed or lock-in thermography (modulated).

As cited previously, the optical source offers several advantages, like no contact with components or easy application.

Depending on the relative position of the heated surface and IR camera, it is possible to define two setup configurations: reflection and transmission modes. The first describes the situation in which the surface observed corresponds to the heated one. Hence the IR camera and the heating source are frontal to the inspected surface on the same side. This configuration results in a compact setup, clearly indicating the moment at which heating starts. The second one describes the layout where the observed surface is opposite to the heated one. Thus the heat source and IR Camera are on opposite sides of the inspected specimen. This setup has the advantage of permitting homogeneous heating of the specimen because the position of the heat source is completely independent of the IR camera one.

2.2.3 Lock-in thermography

Lock-in thermography (LT) involves generating a thermal wave on a sample through periodic thermal excitation. The resulting temperature field is recorded in a steady state using an IR thermal camera. Therefore, a sinusoidal thermal excitation with a certain amplitude is provided. The material responds with a sinusoid of the same frequency but with a different amplitude. It is strongly attenuated and dispersed out of phase with the excitation. It is possible to determine the characteristics of the thermal wave, i.e. phase and amplitude, by analyzing the temperature field during the application of heat and given the thermo-physical characteristics of the material, which allows, through the relationships previously stated, to link the phase to the depth investigated.

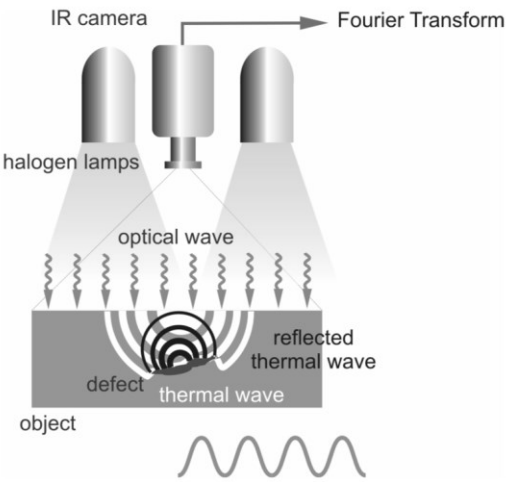

Figure 14. Scheme of lock-in thermography using reflection setup[11]

It is possible to obtain phase and amplitude values for each pixel, obtaining amplitude and a phase map. Phase maps are widely used for defect detection because they are less influenced by inhomogeneous heating of the surface and more sensitive than an amplitude map[6,12,13]. The results can be influenced slightly by the algorithm used to reconstruct the signal [14,15]. Other advanced techniques have been developed based on the periodic wave principle [16–20]. However, they will not be discussed in the present research work.

2.2.4 Pulsed thermography

Pulsed thermography is based on the mentioned principle of the pulsed thermal wave generated by a heat source. Then it analyses the surface during cooling (reflection)/heating (transmission) by an IR Camera. The thermal wave during its path through the component will be interrupted by discontinuities which modify the characteristics of generated wave. Thus, on the observed surface will be possible to observe a locally different thermal behavior due to this inhomogeneities in the material that can be identified and localized. Considering the hypotheses cited in section 2.2.1.2 and the relative equation, considering a reflection setup, the behavior of media in cooling phase can be observed in **Figure *15***.

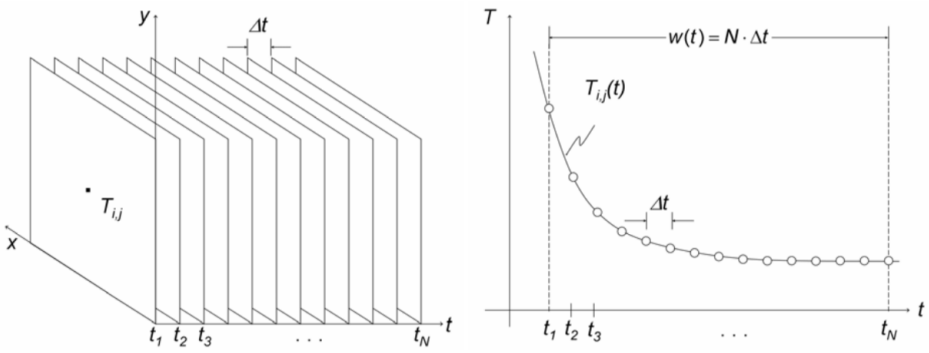

Figure 15. Scheme 3D matrix of temperature in time domain and the cooling curve correspondent to a pixel in a spind area with coordinates (i,j) [21]

In **Figure *15*** only the cooling part has been represented because it is the part that, for pulsed thermography, is analyzed and on which the post-processing procedures are based.

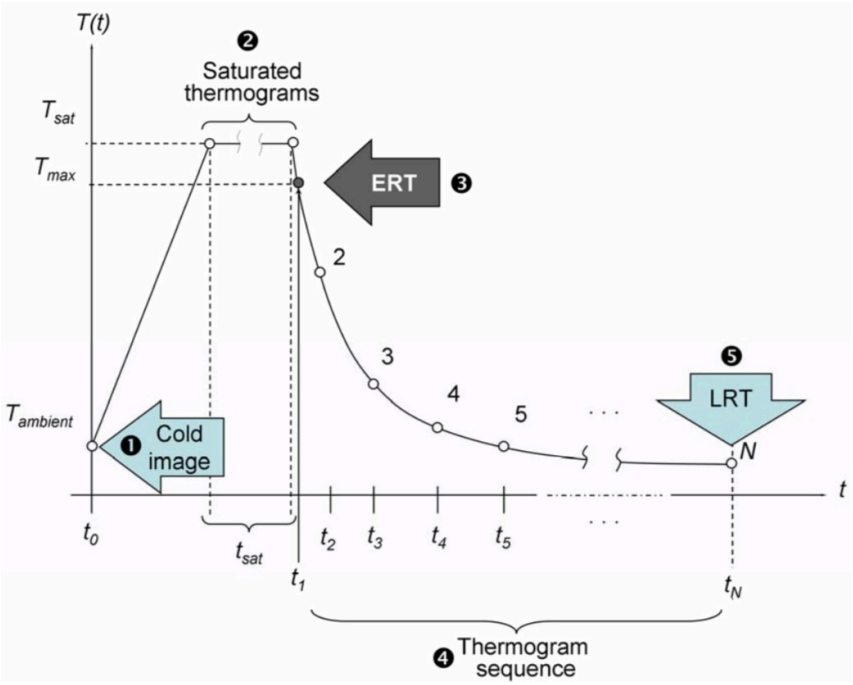

Figure 16. Complete sequence and peculiar points of curve. 1) Cold frame 2) Saturated thermograms 3) Early recorded thermogram 4) Thermogram sequence 5) Last recorded thermogram [21].

In **Figure *16*** are reported the essential parts of the curve. Usually, to reduce the influence of the reflection, the cold frame is subtracted from all the sequences, and the following steps are based on a temperature difference. he saturated thermograms must be avoided if they are present because they have no information about the actual temperature behavior at that time. They occur when the apparent temperature on the surface overcomes the limits of IR camera calibration. The ERT (early recorded thermogram) is the first thermogram that can be used for the analysis and the LRT (last recorded thermogram) is the last one. Between these two thermograms there are all the frames which constitute the thermogram sequence. If a defect occurs, the cooling curve corresponded to a defected are, is different from the ones relative to a sound area. Deeper is the defect and higher is the observing time needed $z \sim t^{1/2}$[6,21].

Several algorithms are present in literarure to highlight the difference between the signal obtained by sound area and the signal due to a defected one, with the aim to identify the defects. The main algorithms will be briefly presented in sections below.

2.2.4.1 Max thermal contrast

The maximum temperature contrast is the most intuitive and immediate of the methods presented for defect detection, consisting in identifying the frame, that is, the moment when the difference between the detected signal value between the sound and the defective zone is maximum. Therefore, the optimal detection time is indicated as the time when this difference is maximum[10,22–24].

$$\Delta T(x,y,t) = T_d(x,y,t) - T_{nd}(x,y,t) \tag{20}$$

More common is the ratio between this temperature difference by temperature in non-defective area:

$$Con = \frac{\Delta T(x,y,t)}{T_{nd}(x,y,t)} \tag{21}$$

The optimal time at which *Con* is maximum does not coincide with the time t at which ΔT is maximum. However, generally, this is found at a value of t that is lower [10,22–24].

2.2.4.2 Principal component thermography (PCT)

Principal Component Analysis (PCA) is a statistical technique used to identify data patterns and present them in a way that highlights similarities and differences. Finding patterns in the data can be challenging when the data size is large. PCA can be used to analyze and visualize such data. After identifying patterns in the data, it is possible to compress the data by reducing its size without losing much information .

The data acquired about the specimen is shown as a 3D matrix of images, with each image made up of N_t frames. Each frame comprises N_x and N_y pixels, representing the horizontal and vertical pixels. PCA is applied by converting the obtained 3D matrix into a 2D image matrix.[22,25–27]

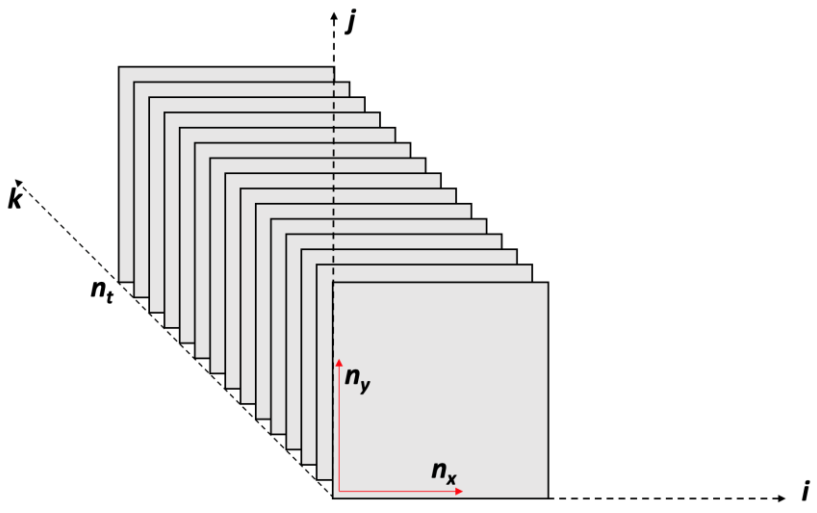

Figure 17. Scheme of recorded thermal sequence.

Each frame with dimensions $N_x x\ N_y$ can be represented as a dimensional vector X with dimension $N_x N_y$.

$$X = \left(x_1 x_2 x_3 \ldots x_{N_x N_y}\right) \tag{22}$$

In this process, the rows of pixels in the image are arranged to form a one-dimensional image. The first N_x elements in the dimensional vector represent the first row of the image. In contrast, the subsequent N_x elements represent the subsequent rows of the image. The values in the vector correspond to the intensity values of the image. This procedure is repeated for all N_t images in the captured image sequence. The resulting 2D image matrix has each row containing information about each image sequence frame and the column containing the number of *Nt* image vectors. This matrix is known as a *raster-like matrix*. After obtaining the 2D matrix of the infrared image sequence, the mean of the data is calculated. The calculated mean is then subtracted from the data set to normalize it. This normalized data is used to calculate the covariance matrix. The covariance matrix can be calculated using the following equation:

$$C = \frac{1}{N} X X^T \tag{23}$$

In the equation above, X is the matrix obtained after normalization, and C is the covariance matrix. Since the data is N_xNy dimensional, the covariance matrix has a size of $N_x N_y \times N_x N_x N_x N_y$. Eigenvalues and eigenvectors can be found by diagonalizing the matrix according to the following equation:

$$C_D = P^{-1} C P \tag{24}$$

Where C is the covariance matrix, C_D is the matrix of eigenvectors diagonalized on the diagonal, and P is the matrix with the eigenvectors as columns. Since the data is of size $N_x N_y$, the covariance matrix has $N_x N_y$ eigenvectors. The matrix CD is reordered to reorder the eigenvalues in decreasing order. The same is done with the matrix P. To reduce the size of the original matrix, the first K columns of matrix P are used to form the matrix PK. The original matrix is converted to the new base using the following equation [22,25–27].

$$C_P = P_K^T C \tag{25}$$

The resulting image will be reconstructs using the matrix C_p. The definition of K is based on the desired ratio r

$$r = \frac{\sum_{i=1}^{K} e_i}{\sum_{i=1}^{M} e_i} \tag{26}$$

As shown above, e_i is the first eigenvalue of the diagonal matrix C_D. In most cases, the first three principal components contain more than 95% variance. To address the issue of calculating a large-size matrix, a method that performs the same operation but with lower computation demands and more manageable data processing must be employed. Thus, PCT based on Singular Value Decomposition (SVD) is utilized to overcome the limitations of PCT [22,25–27].

In PCT using SVD, the initial step is to acquire the dataset for analysis, following which the mean value is computed for the dataset. The calculated mean is then subtracted from the dataset to normalize it. SVD is applied to the normalized data using the following equation to calculate the decomposed matrices U, S, and V to obtain the principal components.

$$A = USV^T \tag{27}$$

The decomposition matrix U is composed of orthogonal empirical functions representing the data set's spatial variation. Each column of U gives the coordinates of the data set in the space of the principal components. The matrix S is a diagonal matrix with singular values on its diagonal, which are the eigenvalues of the corresponding eigenvectors of matrix V. The eigenvalues in S are rearranged in decreasing order. The columns of matrix V or the rows of matrix V^T are the principal components or eigenvectors of the data set, ordered by size in decreasing order. The first columns of matrix U are used to reconstruct the data to reduce the redundancy of the original data set. The thermal image sequence containing information about the sample is processed using SVD-based PCT. The 3D image matrix is converted into a 2D matrix using a similar method described previously to construct matrix A, consisting of N_t as rows and $N_x N_y$ as columns, as shown in **Figure *17***. After obtaining matrix A, the mean of each data point is subtracted to create zero-centred data. Each matrix A column has all the image frame's pixel values. The mean image is the average of the values of each column. After calculating the zero-centered data, the *SVD* transformation is applied to find the eigenvalues and eigenvectors using the equation $A=USV^T$ [22,25–27].

Once the three matrices U, S, and V^T are obtained, the resulting image is constructed using the first columns of matrix U, which are the orthogonal empirical functions giving the coordinates of matrix A in the space of the principal components. This image, constructed using the empirical functions of matrix U, shows good contrast between the defective and non-defective areas, as well as reducing the redundant data of the original matrix A [22,25–

27]. Even though PCT based on SVD is an efficient method for PCT, when dealing with a large amount of data, there remains the issue of processing image sequences of large samples.

2.2.4.3 Thermographic signal reconstruction (TSR)

Thermographic signal reconstruction (TSR) is an algorithm based on the analysis of the cooling curve over time obtained experimentally, considered on a double logarithmic scale [28–33]. The experimental log-log thermogram is then fitted with a logarithmic polynomial of degree *n:*

$$\log_{10} \Delta T = a_0 + a_1 \log_{10} t + a_2 (\log_{10} t)^2 + \cdots + a_n (\log_{10} t)^n \qquad (28)$$

with ΔT, the temperature increase over time t (thermogram) for each pixel (i,j). The curve obtained analytically then replaces the entire sequence of temperature increase images $\Delta T(i,j,t)$ with the series of $(n + 1)$ images of the polynomial coefficients: $a_0(i,j)$, ... $a_n(i,j)$, from which it is possible to reconstruct a complete thermographic sequence. Subsequently to this operation, it is possible to analytically calculate the function's first and second derivatives that approximate the experimentally detected thermogram, clearly reducing the noise derived from the signal recorded by the experimental test [28–33]. This is useful because it is based on the fact that the signal derived from the cooling of a non-defective area of the material has a specific trend. At the same time, as already seen in the method of maximum thermal contrast, in the case of defects, the curve deviates from that of the healthy area, with a substantial variation evident in the analysis, therefore, of the first and second derivatives. There will be a point where the derivatives between the healthy and defective areas will be very different, so a map for the first derivative and a map for the second derivative will be obtained, in which, for each pixel, the value of its derivative is indicated. The fitting and derivatives of thermograms depend on the time domain considered. It is necessary to define a temporal window to consider only the part of the thermograms.

TSR's "classical" use involves selecting the best images from the derivative maps associated with each depth range to detect defects qualitatively or to evaluate their depths based on characteristic times quantitatively. In the latter measure, optimizing the degree of the interpolating polynomial may be necessary. Empirically, it has been found that a degree of 11 may be satisfactory for defects similar to delamination, so it is used to calculate other types of defects [28–33].

2.2.4.4 Slope and coefficient R2

By exploiting the same principle, namely the difference between the sound area's cooling curve and the defective area's cooling curve, the present algorithm has been developed to evaluate the overall slope of the curve and the determination coefficient R^2 [17,34,35]. This algorithm always approximates the cooling curve in a log-log scale, and a linear regression is performed. This means that a regression line with a particular slope will be obtained for the non-defective area. In contrast, a line with a significantly different slope will be obtained in the defective area. Theoretically, by examining the relationship seen in a previous section, the slope of the regression line that should be obtained for the non-defective area would have an angular coefficient of -1/2; this does not happen because the assumptions on which the relationship was obtained are not verified in the actual case, so there will be a deviation from this value.

$$\log(\Delta T) = -\frac{1}{2}\log(t) + \log\left(\frac{Q}{e\sqrt{\pi}}\right) \tag{29}$$

The curve for the sound area will have a much more linear trend compared to the curve for the defective area. It means that the regression lines obtained will have significantly different slopes, with the regression line for the healthy area more accurately approximating the experimental curve. To evaluate this, the determination coefficient R^2 is used, which is the proportion of data variability to the correctness of the statistical model being used. This measure represents the fraction of variance in the dependent variable explained by the regression. In simple linear regressions like the one in question, this is expressed by the square of the Pearson correlation coefficient, which represents any potential linear relationship between two statistical variables and is expressed as follows:

$$\rho_{XY} = \frac{\sigma_{XY}}{\sigma_X \sigma_Y} = R^2$$

where σ_{XY} represents the covariance between variables X and Y, while σ_X and σ_Y represent their respective standard deviations. The value of this coefficient is between 0 and 1, which indicates that the regressors accurately predict the value of the dependent variable in the sample. In contrast, 0 indicates that this is not the case. For the healthy area, values of R^2 close to 1 are expected. This operation, performed on each pixel of the image obtained from the thermal camera, allows the creation of a 3D matrix in which, for each frame, it is possible to have a map of the R^2 coefficient value, allowing for the detection of the defect [36]. In the same way, it is possible to obtain a map indicating the slope of the regression

line related to the thermal signal detected, which, based on the principles mentioned earlier, allows for the detection of the defect.

2.2.4.5 Pulsed phase thermography (PPT)

Pulsed phase thermography (PPT) is a well-known algorithm based on the principle that every signal can be decomposed into individual components, each at a different frequency and with a different amplitude [12,21] The Fourier transform is used to analyse the frequency domain signal. Specifically, it is not possible to apply the continuous Fourier transform (CFT) because the thermal signal recorded by the camera is discrete, so the Discrete Fourier Transform (DFT) is used [12,21]

$$F_n = \Delta t \sum_{k=0}^{N-1} T(k\Delta t) e^{-\frac{i2\pi nk}{N}} = Re_n + Im_n \tag{30}$$

In the equation above, n is the increment of frequency. However, one important term that must be considered is Δt which is the sampling interval. This term is fundamental to reducing the difference between CFT and DFT [12,21] Usually, for the evaluation of DFT, a well-known algorithm is used: the Fast Fourier Transform that reduces computational work to a factor $\mathcal{O}$(N logN) [37].

Phase and amplitude for each frequency can be obtained to have two 3D matrices with frequencies on one axis and phase and amplitude for each pixel [12,21]

$$A_n = \sqrt{Re_n^2 + Im_n^2} \qquad \phi_n = arctg\left(\frac{Im_n}{Re_n}\right) \tag{31}$$

Since thermal profiles are Hermite functions, because the real part is even, but the complex part is odd, in the frequency domain, phase and amplitude are equal and odd;, for a thermal sequence with *N* thermograms, phase and amplitude matrix has only *N/2+1* valuable frequencies.

It is essential to understand that the resolution in the time domain is defined by acquisition frequency because the value of Δ*t* is determined as follows:

$$\Delta t = \frac{1}{f_s} \tag{32}$$

In the frequency domain the resolution is connected to the length of the signal in the time domain: in fact, the value of Δf is:

$$\Delta f = \frac{1}{N\Delta t} = \frac{1}{w(t)} \tag{33}$$

This is why the length of the time window is essential for describing the thermal signal from the back wall of the specimen and improving the resolution in the frequency domain. That is important because the frequency of excitation is related to the depth inspected, as written below, where: α is thermal diffusivity, z is the depth, and f is the frequency of thermal excitation [12,21].

$$z \propto \sqrt{\frac{\alpha}{\pi f}} \tag{34}$$

2.3 Relation between thermal properties and hardness

As seen in the initial chapter of this thesis, to verify the quality of joints, in the case of welds, it is also essential to assess the extent of the thermally altered zone. As already defined previously, the HAZ is a volume of material involved in the welding, which has changed its microstructure, compared to the base metal, because during the joining process, it was subjected to a thermal cycle without reaching melting. It is, therefore, an intermediate zone between the molten zone and the base metal.

As shown in **Figure *18***, where an example of low-alloy steels is shown, different structures are formed in the vicinity of the joint, resulting from a precise thermal cycle. From the same image, it is easy to see that different microstructures correspond to different mechanical characteristics. The thermal cycles suffered by the HAZ lead to different local mechanical characteristics of the joint concerning both the molten zone and the base metal. As mentioned previously, the interfaces of the HAZ are those in which cracks are most easily formed.

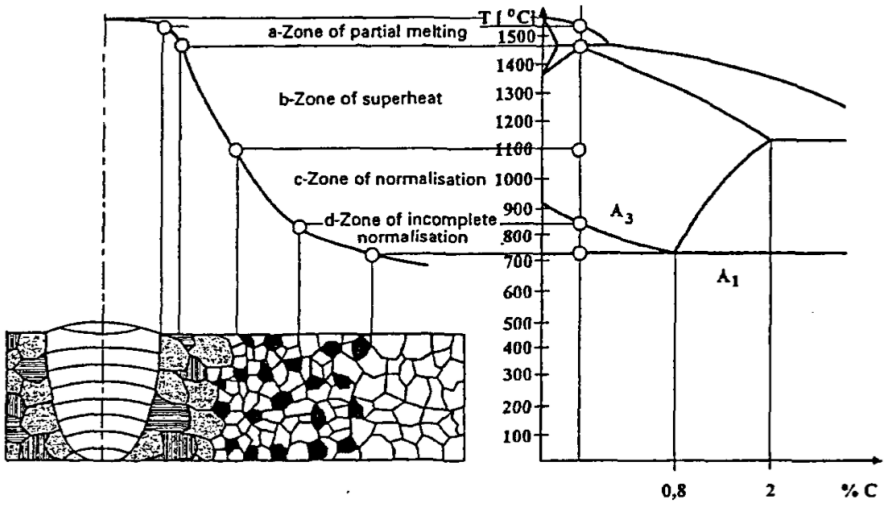

Figure 18. Structural area within HAZ of a joint welded in low-alloy steel plotted as a function of temperature and related to the iron-carbon equilibrium diagram [38].

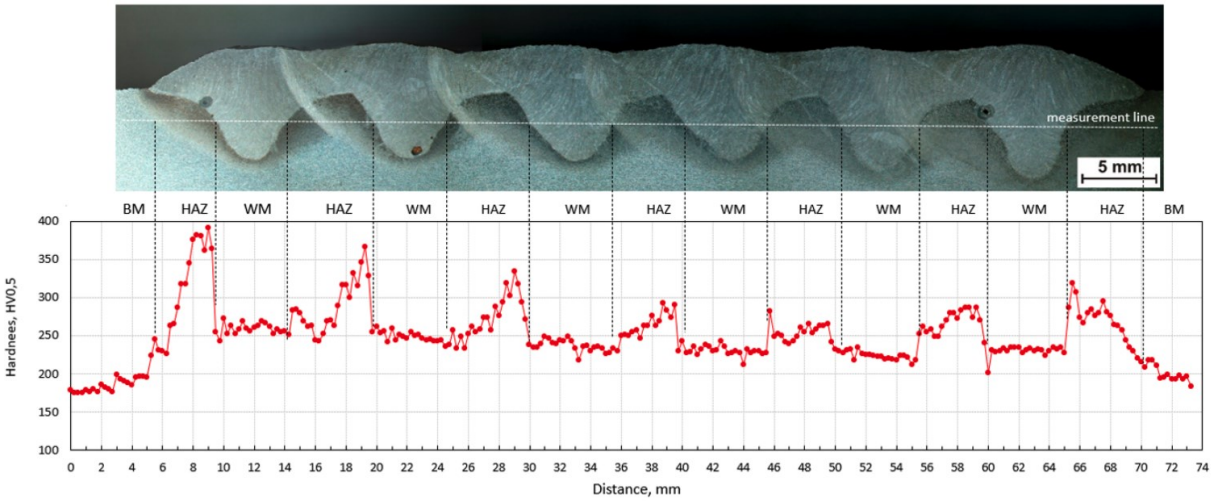

Figure 19. Hardness HV_{05} distribution in plate A; BM-base material; HAZ-heat affected zone; WM-weld metal[39].

The **Figure *19*** above confirms the variation of mechanical properties, specifically hardness, in correspondence with the HAZ. Using the hardness profile, it is possible to identify the extent of the thermally altered zone. However, as the microstructure varies, the mechanical properties and the thermophysical properties change. In order to verify the thermal treatments along the thickness, in Munidasa, Funak, and Mandelis at the beginning an others later[40–46]have studied and verified the variation of conductivity, or thermal diffusivity as the microstructure varies, as well as hardness. The photothermal technique has been used to measure thermal diffusivity in the various works that have followed on the subject. This technique allows for measuring thermal diffusivity in a small and localized area, making it particularly useful for studying heterogeneous materials or materials with a gradient in their thermal properties. The various works [40–46] confirm a relationship between hardness and thermal diffusivity or, more precisely, an anti-correlation between hardness and thermal diffusivity variation. In **Figure *20***, it is possible to observe how the profiles have the same trend but are symmetrical with respect to a horizontal axis.

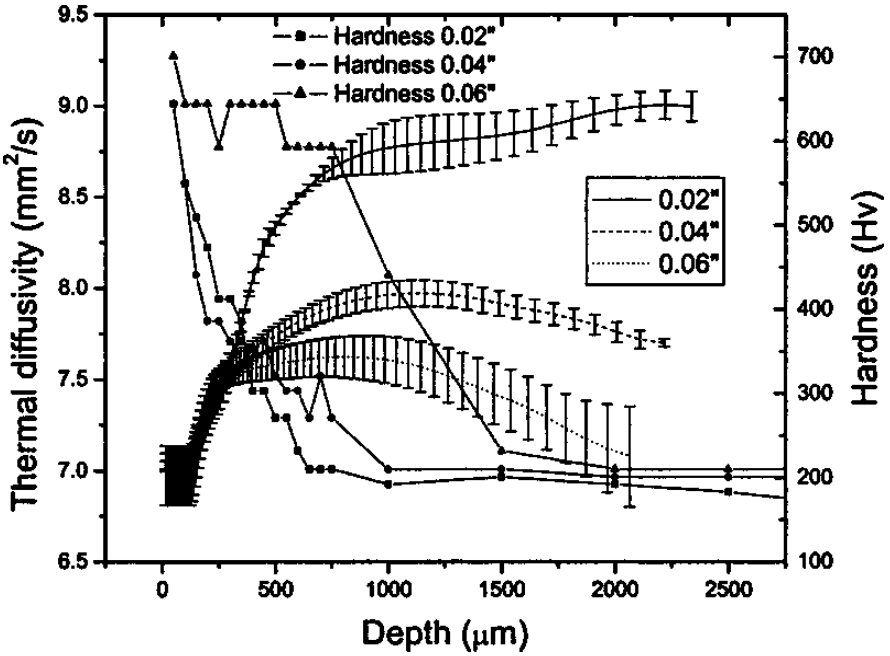

Figure 20. Thermal diffusivity and hardness as a function of depth for quenched 1018 steel samples [40–46].

Using this principle, the questions that have been asked and attempted to answer are:

- Through thermographic measurements of thermal diffusivity, is it possible to trace the same profile?
- Can a single thermographic test quantify both the molten area and the heat affected zone?

In the following chapters, a procedure based on laser thermography will be developed to quantify the molten zone in some welds. On the other hand, various methods for measuring thermal diffusivity through thermography will be discussed, and a study on their potential will be presented.

CHAPTER 3

Thermographic procedure for the assessment of welded joints

In the previous section, a description of the active thermographic methods have been presented, and the reasons why it is promising in assessing thin joints.

In the present chapter, the state of the art of non-destructive methods for assessing thin joints will be presented, followed by a description of the main thermographic methods presented in the literature for the evaluation of adhesive and welded joints. In particular, the application on the resistance spot welded joint of thermographic methods will be considered.

3.1 State of the art: NDT of thin joints

As it easy to deduce and considering that the destructive testing is not a suitable method for continuously monitoring production, so various non-destructive testing (NDT) techniques have been developed to evaluate the quality of thin joints [47].

For thin joints, as described in a previous section, must be considered the joints for which the thickness is lower than *2 mm,* especially for metals. Usually, to obtain these kinds of connections, adhesive and some welding are used; the bolted ones are not so common except the riveting, which is the most used.

To test the quality of glued construction under production and operational conditions, various methods based on the interaction of physical fields or penetrating radiation with the object being tested are used, including acoustic, thermal, optical, electrical, and radiowave methods [48]. Among these methods, acoustic methods are the most prominent for testing multilayered, glued construction made from polymer composite materials (PCMs). These methods rely on the interaction of elastic vibrations and waves with the unit or construction being tested across a wide range of frequencies [48]. Both traditional and unique low-frequency acoustic methods can be used to test glued joints made from PCMs. These methods often involve fluids to establish acoustic contact between the transducer and the tested object. However, dry point contact is used in unique low-frequency methods [48]. The shadow (transit) method, the echo method (including the

principal and reverberation variants), and the stimulated vibration (resonance) method fall into the first group, while the impedance, velocimetric, and free-vibration methods, as well as the vibration-topographic and vibration-thermal methods, fall into the special low-frequency group [48]. The low specific wave resistances of many PCMs make them easier to match acoustically with fluids compared to metals, which can facilitate testing with the first group of methods. Additionally, PCM objects' elastic wave propagation velocity is typically lower than in metals. It is easier to test PCM objects through fluid immersion, where refraction is reduced at the fluid-object boundary. Several factors can hinder using the first group of methods for testing glued joints made from polymer composite materials (PCMs) [48]. These include the high coefficient of elastic vibration damping in the PCM, significant differences in the acoustic properties of the layers in multilayered constructions, and roughness and curvature in the surfaces of the unit and construction. The latter factor is significant in the contact variant of the transmission and reception of elastic vibrations. To reduce the damping in PCM units, it may be necessary to lower the operating frequency, which can decrease sensitivity. It is also often inappropriate or undesirable to wet the surface of PCMs during testing. In such cases, elastic gasket seals or special mixtures may be applied as contact media to establish acoustic contact between the transducer and the material being tested when using the shadow method or the main variant of the echo method [48]. The reverberation and resonance methods involve wetting metal and PCM constructions from the metal side of the layer. If acceptable, surface wetting of PCM surfaces with contact fluids may also be used. Below, we consider the aforementioned acoustic methods in greater detail.

The *shadow (transit) method* [49] is typically implemented in two forms: amplitude and temporal. When testing using the amplitude method, discontinuities can be identified through the attenuation or disappearance of the received signal. On the other hand, the temporal method involves detecting discontinuities through an increase in the duration of the signal transit, as the ultrasound vibration (USV) path is lengthened due to the bending of the material zone with significantly different characteristic impedance. This method can be used to identify discontinuity zones in multilayered structures, as well as to detect stratifications, voids, and areas of high porosity in PCM units and structures [48].

One advantage of the shadow method is its high level of reliability due to the absence of a large uncontrolled zone. However, there are some disadvantages to this method, including the requirement for two-sided access to the structure being tested, which may not always be possible (e.g. during operation). Additionally, the accuracy of the test results can be

affected by issues such as acoustic contact and transducer misalignment, particularly when testing large-dimension objects. To address the issue of transducer misalignment when testing large objects, clamps or specialized orientation systems may be employed [48].

The *echo (reflection) method* [50,51], involves the transmission of an ultrasonic pulse from a transducer to the object under test, followed by the reception of the echo, or the pulse reflected from the nonuniformities in the structure and the opposite side of the object, using the same or a different transducer. By utilizing temporal scanning, the reflected signals can be identified, and their arrival times can be recorded. In this form, the echo method is used to detect areas of non-bonding and stratification in glued PCM structures with thicknesses ranging from 4-10 mm to 100-200 mm [48]. When conducting echo testing on thick non-metallic objects and structures, it is recommended to use lower frequencies (typically 200-1250 kHz) due to the high attenuation of ultrasonic waves in non-metals [48]. However, this shift to lower frequencies can decrease the test's sensitivity.

The *stimulated vibration (resonance) method* [52], used to test multilayered PCM structures, is a variant of the resonance method commonly used for measuring the thickness of metal objects. In this modified resonance method, variations in the resonance frequency of a piezotransducer loaded with the tested structure indicate discontinuities. Additionally, variations in the Q factor of the piezo element system can serve as an additional indicator of discontinuities.

The resonance method can be applied to test glued structures in cases where other methods, such as impedance testing, are ineffective. This method is used to detect discontinuities in two-layered materials with single-sided access from the side of the thicker layer. However, there are some disadvantages to the resonance method, including the difficulty or impossibility of testing curved structures and the requirement for wetting the surface of the structure being tested.

The *free vibration method* involves the application of shock excitation to an elastic structure, causing it to vibrate freely. The resulting vibrations are then analyzed to identify variations in the structure's vibration spectrum within the tested region. These variations, including amplitude, frequency, and phase changes, may indicate the presence of defects or other discontinuities in the structure. A variant of this method involves monitoring variations in the vibration spectrum of a striker element, such as changes in amplitude or width, as indicators of discontinuities. This method is commonly used to test structures that contain rubber-like layers or other materials with high damping and low Young's modulus.

However, it has the disadvantage of generating noise during testing, mainly when applied to non-metal layers [48].

The *acoustic-emission* method involves recording acoustic waves produced during the damage of the test object. This technique has been utilized to evaluate PCM units and multi-layered bonded structures [270]. However, it is not commonly used in industry due to the requirement for loading the test unit or structure and the complexity of the method. In certain situations, specific recommendations for testing methods can only be provided based on the results of tests on samples or on-site structures with artificial or natural defects. The variant of the acoustic impedance method utilized to calibrate the defectoscope for use with standard operative samples (OSSs) allows for the reliable detection of defects. However, this variant also has some drawbacks, the primary disadvantage being the need to produce and standardize a large number of OSSs for calibrating the defectoscope.

Another method which can be considered part of UT techniques, consists in *guided waves* for which a recent example has been presented by Pineda Allen et al. [53], that proposed a method for detecting debonding at adhesive joints using the nonlinear mixing of Lamb waves.

Lamb waves are elastic waves that can propagate through solid materials. They are characterized by their mode of vibration, which determines the shape of the wavefront and the distribution of energy within the material. Nonlinear mixing of Lamb waves occurs when two waves with different frequencies interact and produce new waves with different frequencies. This process can be used to extract information about the material and its properties [53].

This paper [53] examined the interaction between nonlinear Lamb wave mixing and local debonding using experiments and numerical simulations. It was found that the wave mixing technique can detect debonding at adhesive metal joints by observing the creation of a combined frequency wave. The harmonics produced due to the contact effect at the debonding were extracted from the frequency domain of the experimental samples and used to validate a 3D FE model [53]. The presence of the combined harmonic was found to be a reliable indicator of local debonding. In addition, the effect of debonding width on mixed-frequency Lamb waves interacting with damage was studied in the frequency domain. The numerical results indicated that the debonding width could be correlated with the energy produced by debonding. This suggests that the proposed technique is also

sensitive to different debonding widths within a specific range of d/λ. The research also better understood the nonlinear Lamb wave mixing process in adhesive joints.

Another recent study in which several NDT methods are applied to adhesive joints, has been presented by Hean Gan et al [54]. In the presented paper, ultrasonic guided waves, laser shock, high frequency C-scan and computed tomography have been explored to assess the quality of kissing bond joint. The geometry of analyzed composite specimens has been 333999.

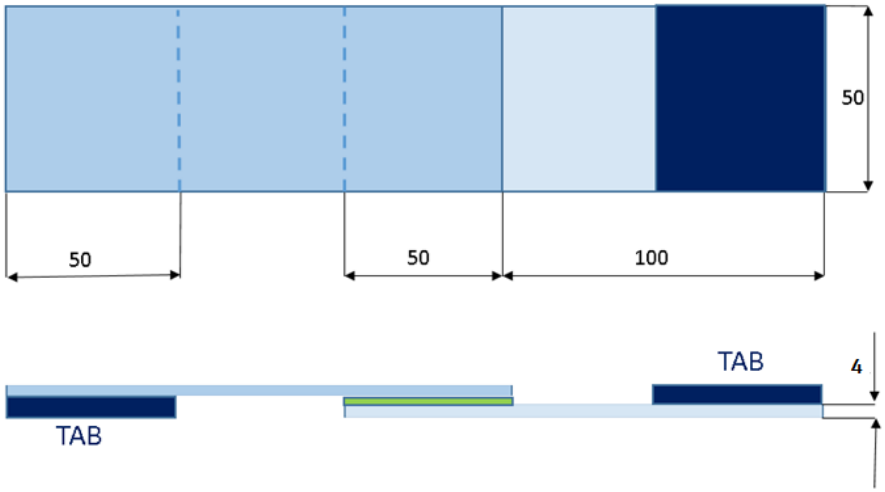

Figure 21. Scheme of the geometry of analyzed adhesive kissing bonds specimens [54]

For using guided waves, a modified geometry was designed to accommodate the inspection of bonded joints while maintaining the dimensions of the joints themselves. **Figure *22***(a) depicts the test samples' dimensions for this inspection technique. **Figure *22***((b) and **Figure *22***(c) show the actual test specimens with transducers attached so that the guided waves traverse the entire length of the sample, including the bonded joint, before measurement. A total of six test samples were used for this NDT inspection, including two without kissing bond defects and four with such defects.

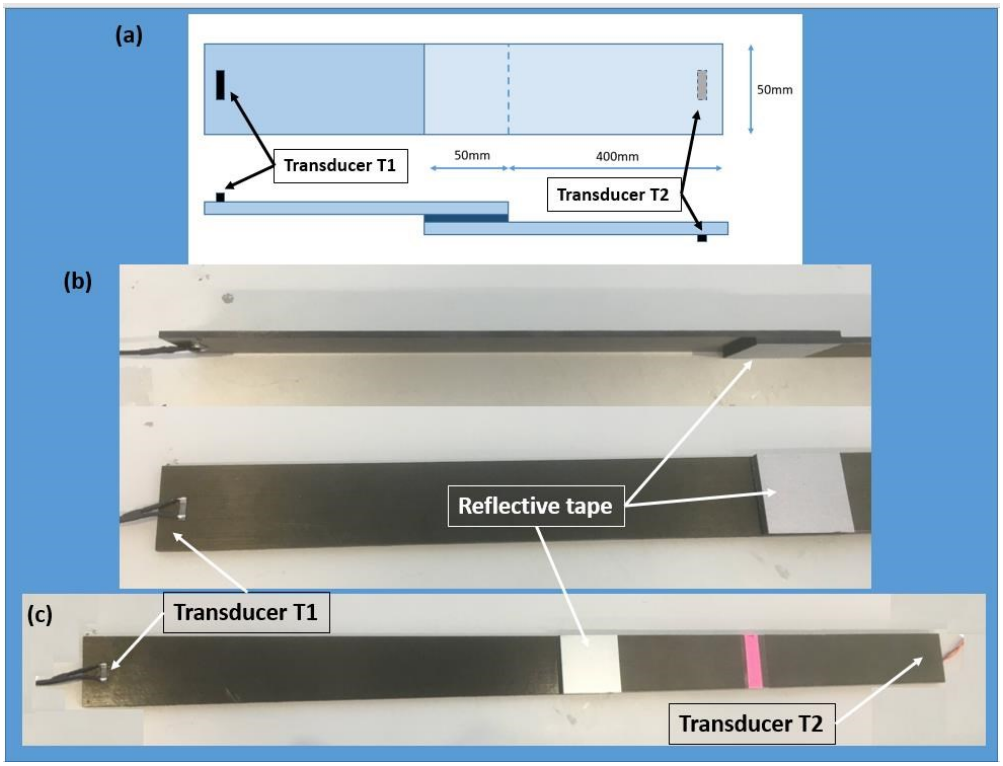

Figure 22. Test sample geometry for guided wave NDT [54]

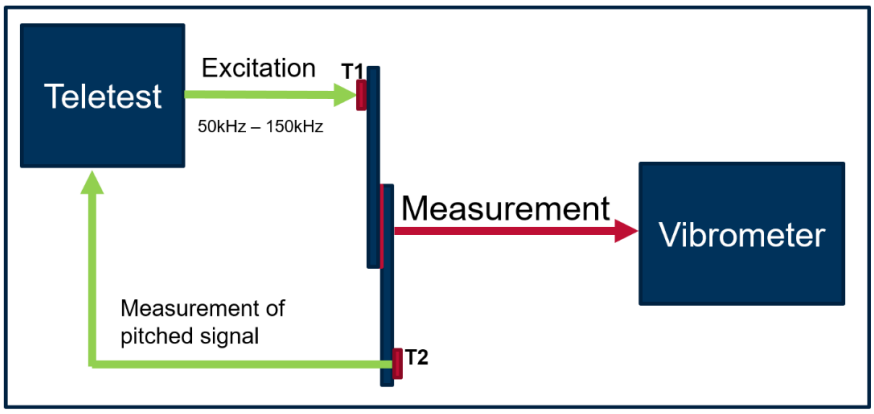

Figure 23. Block-diagram for measurements by guided waves [54]

In **Figure *23***, the scheme of measurement used for guided waves has been reported. It is possible to observe that two different results can be obtained by each test: by teletest and laser vibrometer. By Teletest, measurements are performed in the pitch-catch mode, with transducers attached to the test sample to facilitate the process (see **Figure *23***). Transducer 1 (T1) serves as the input, while Transducer 2 (T2) measures the test sample's response to guided waves [54]. The recorded signals are depicted in **Figure *24***. **Figure *24***(a) displays the amplitude-time plot of the received signal for all test samples. **Figure *24*** (b) presents the power spectral plot of the time signals shown in **Figure *24*** (a). Plots labelled "REF Sample #" represent the response of the test sample without a kissing bond defect. In contrast, plots labelled "Sample #" represents the test sample's response with a kissing bond

defect. Power spectral plots are presented in the amplitude-frequency domain with boxes for improved interpretability of the results.

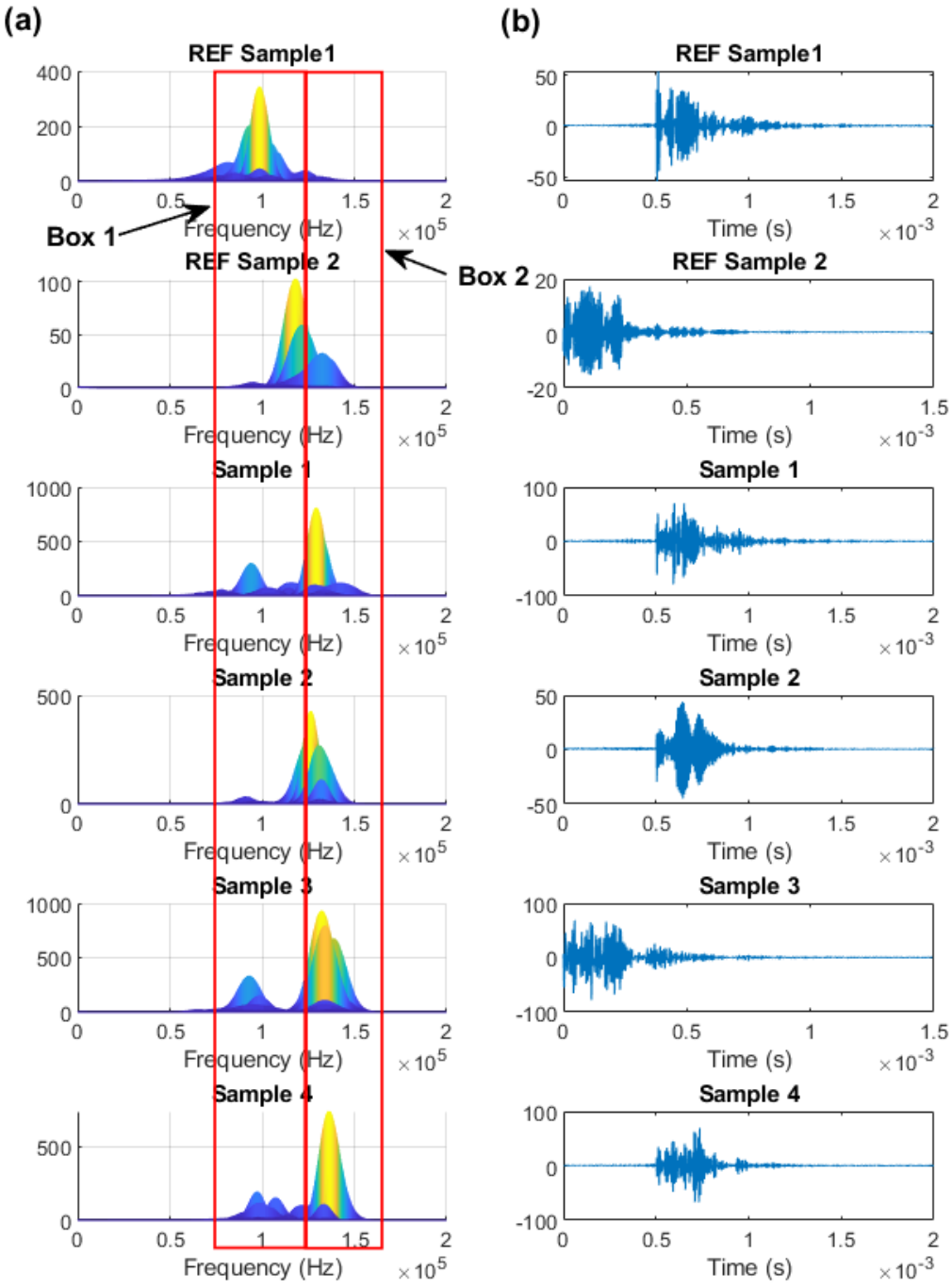

Figure 24. (a) Spectral plot of the time response in frequency domain (b) Time response of the test samples obtained by Teletest [54]

In addition to the Teletest experimental test setup, a capacity laser vibrometer is utilized to measure the test sample's behavior while applying guided waves. The laser-vibrometer is focused on a point on the bonded joint, as shown in **Figure *23***. In this manner, the guided

waves pass through the bonded joint before being measured by the laser vibrometer. The excitation signal applied to T1 is the same as that used in the Teletest experiments [54].

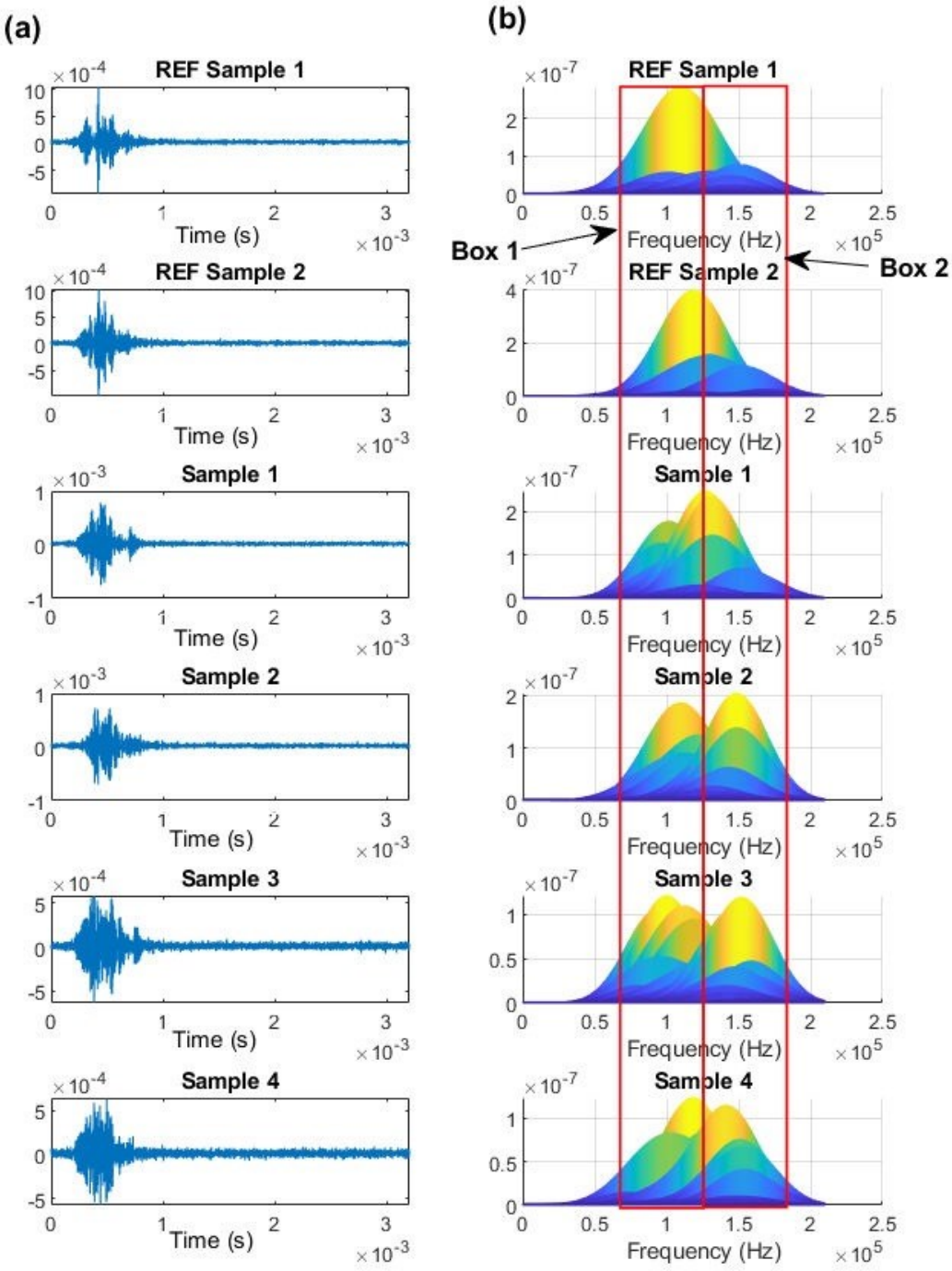

Figure 25. a) Time signal measured at bonded joint (b) Spectrum plot of the time signal measured at bonded joint measured by laser vibrometer [54]

Measurements obtained using the laser vibrometer are depicted in **Figure *25***. **Figure *25*** (a) shows the time signals of the guided waves measured at the bonded joint surface. In contrast, **Figure *25*** (b) presents the spectrum plot of the time signal in the frequency domain. Two boxes are placed on the frequency domain plots in **Figure *25*** (b) for

improving interpretability of the results. It can be observed from the plots that the frequencies of the highest peaks fall within Box 1 for test samples without kissing bond defects. In the case of test samples with kissing bond defects, the frequencies of the highest peaks fall within Box 2.

It is well established, in the literature, that plasma forms on the material surface due to high energy impact within a small area when a material is subjected to laser shock [54]. This plasma generates a shock pulse within the material, which creates tensile and compressive stresses as it reflects back and forth between the material surfaces. The test sample surface vibrates as the shock pulse propagates through the material. This process can be captured to study the material's behavior.

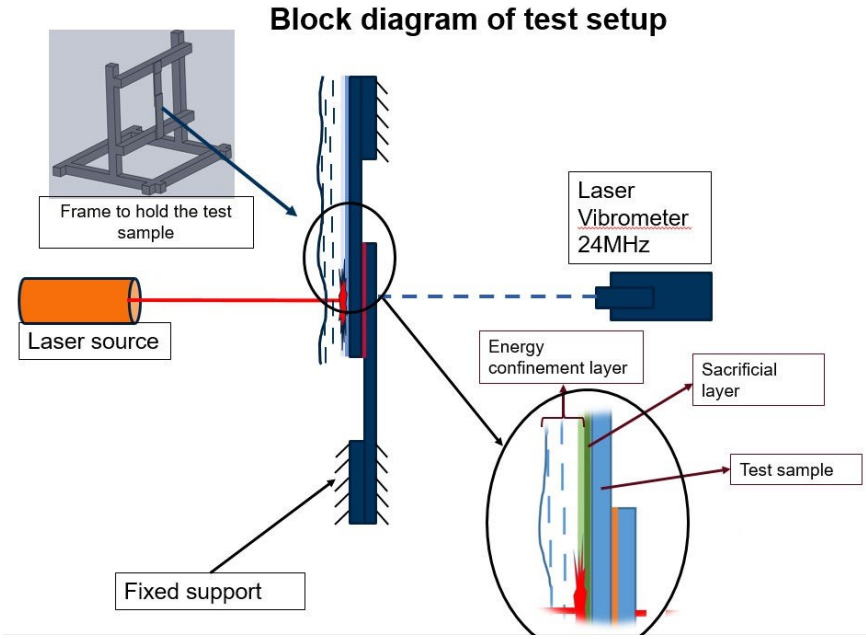

Figure 26. Laser shock test setup used by Hean Gan et al. [54]

The laser-vibrometer is focused on the reflective side of the test sample (**Figure 26**), ensuring that it captures the velocity of the test sample at the same point on the reflective side where it is subjected to the laser shock pulse on the opposite side. The test sample is subjected to one laser shock, and the laser vibrometer records the back-surface velocity. Velocity measurement is continued until the back-surface velocity decreases to pre-shock noise levels. Each sample is subjected to five laser shocks at five-minute intervals to obtain the best results. The tests are repeated five times on each sample because there is no way to obtain an averaged signal. It is necessary to subject the samples to several laser shocks at a time to obtain the averaged back surface velocity but doing so, may damage the test samples.

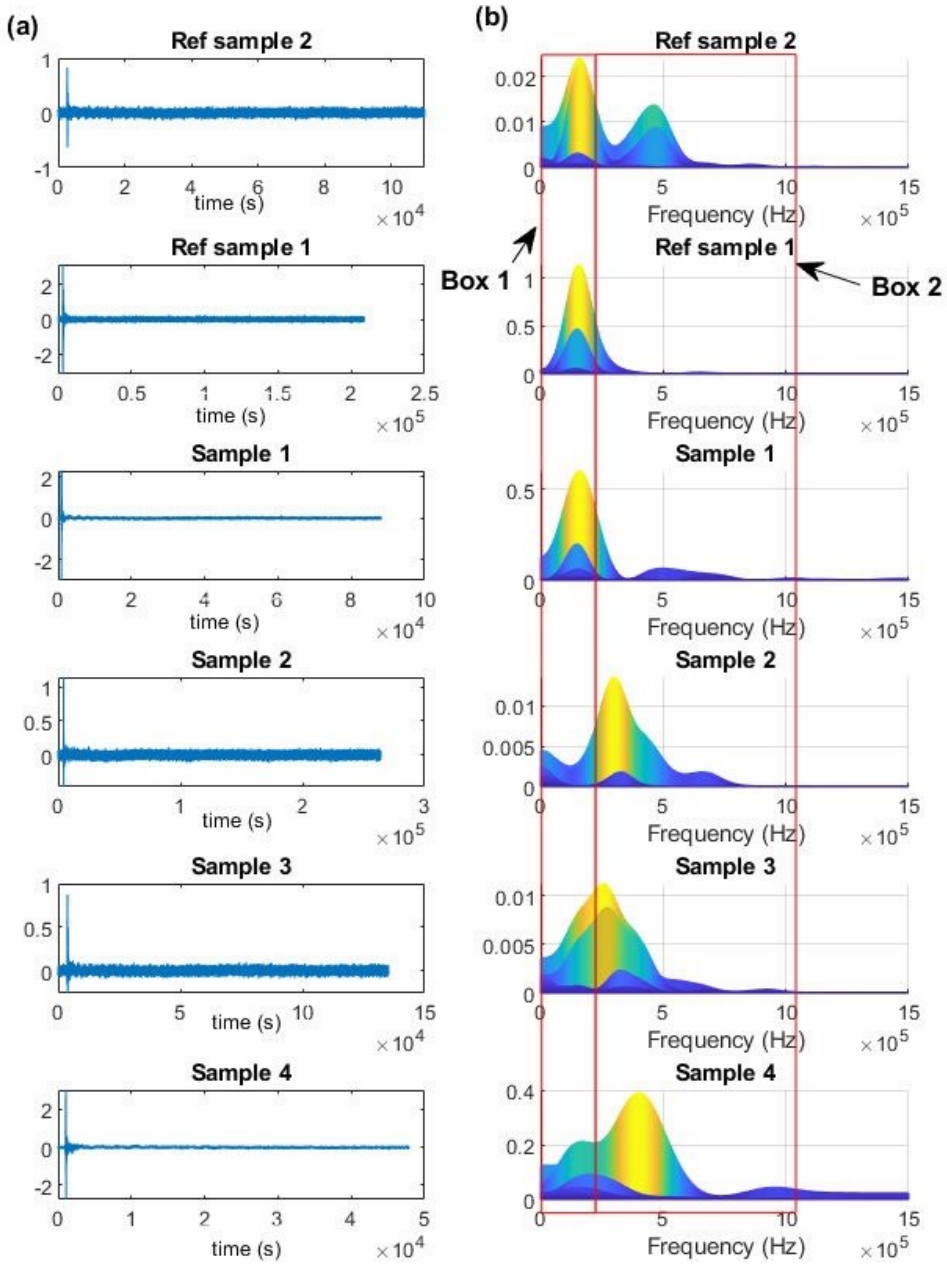

Figure 27. (a) Back surface velocity in time domain (b) Back surface velocity spectral plot on frequency domain [54]

The most favorable result from the five tests on each sample is presented in **Figure *27***. **Figure *27*** (a) displays the back-surface velocity of the test sample in the time domain. A spectral plot of the time signals in the frequency domain is presented in **Figure *27*** (b).

The same specimens by Hean Gan et al. [54], have been analysed through computed tomography (XCT). XCT is a radiographic imaging method used in NDT that produces 2D cross-sectional and 3D volumetric images that can be analyzed to identify internal structures, dimensions, defects, and density. The XCT setup involves an X-ray source on one side of the test sample and an X-ray detector on the opposite side (see **Figure *28***). The X-ray source generates an X-ray beam that passes through the test sample and is detected

by the X-ray detector, which can detect variations in beam intensity caused by internal features of the sample. The test is repeated at various angles relative to the test specimen to create a stacked 2D image. These 2D images can then be further processed by adding grey-scale values to create a 3D image that reflects the test material's density and geometric properties.

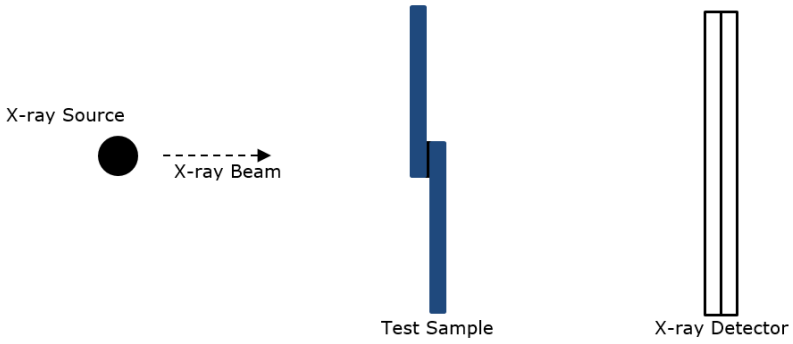

Figure 28. XCT setup scheme used by Hean Gan et al. [54]

The analysis of the generated 3D images involves examining the data in three orthogonal CT slice views: top, right, and front (see **Figure *29***). These orthogonal views enable an analysis of the entire cross-section of each sample.

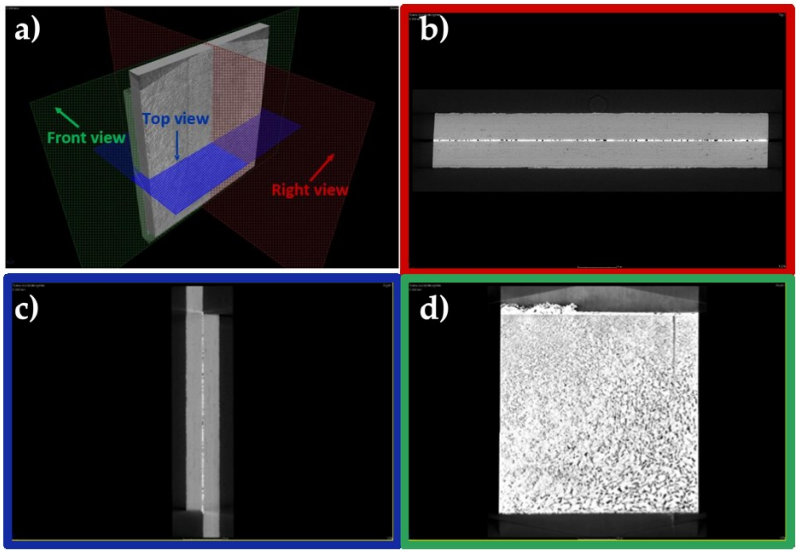

Figure 29. Orthogonal Views of 3D XCT Image [55]. (b) Top-view CT slice. (c) Right view. (d) Front view. [54]

UT C-scanning utilizes high-frequency sound within the ultrasound range to non-destructively test the sample. For the SWAK test, high-frequency probes were used in an immersion setup. Immersion testing involves immersing the sample in a medium, water, and positioning the probe at a set offset before scanning over the surface with a 0° probe (see **Figure *30***). The probe acts as a transducer and receiver in a pulse-echo practice.

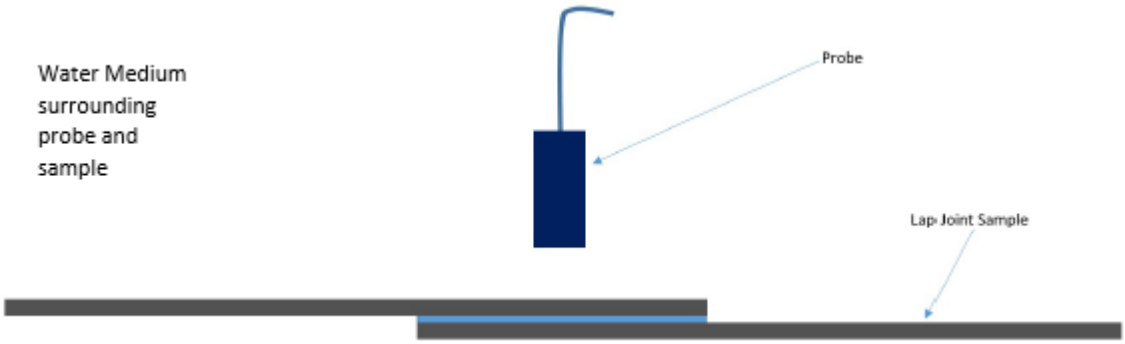

Figure 30. Immersion Tank Set Up [54]

Once the probe receives the reflected sound wave, an ultrasonic A-scan and C-scan can be created to display the data. The ultrasonic A-scan is a conventional NDT technique used to inspect materials and displays the reflected pulse amplitude (in dB) along the Y-axis with time or distance presented along the X-axis. The A-scan presents information at a specific point of interest within the material. In addition, an ultrasonic C-scan can also be created to display information over an extensive range or sample surface (see **Figure *31***). The C-scan representation consists of a two-dimensional scan of a specimen maps parameters, such as reflected wave amplitude, as a function of location over the sample's surface. The C-scan gives a plan view of the sample, including any defects, and is often an automated process used to map out lamination-like indications.

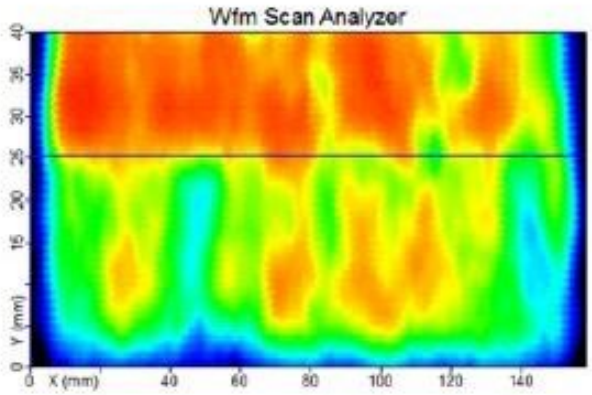

Figure 31. C-scan of reference sample used in described work. [54]

Ultrasonic testing (UT) typically involves a tradeoff between wavelength and frequency. As frequency increases, wavelength decreases, increasing sensitivity and attenuation of the scan [54]. Attenuation refers to the energy lost through scattering and absorption within the material. While increasing frequency can improve sensitivity, the internal fibres of composite samples often result in high attenuation, significantly reducing signal penetration. As a result, lower frequencies are often chosen for the inspection of composites

in order to balance the need for penetration with the desire for sensitivity and resolution [54].

The application of adhesive joints is more common for composite materials than metallic ones, which are widely spread welded joints. For these kinds of joints, which can be very thin, the NDT techniques usually used are visual inspection[56], ultrasonic test [57–65], magnetic particle test[66–70], radiography test[71,72], and liquid penetration test[71,73]. Among all the welding processes, the first part of this research work has focused on resistance welded joints, the most common welding method to join thin metal sheets, particularly in the automotive industry[47,63,74–93]. In fact, for one car frame, an average of 2000 welded spots are present. Thus, the assessment of these joints can be crucial. In the literature, several works based on NDT methods of resistance spot welding are present [47,63,74–93]. Hence, some of them have been summarized below.

Ultrasonic technique (UT) is a promising approach for the quality control of RSW joints in the automotive industry [94], as it allows for cost reduction but requires qualified operators [86], particularly when the complex material microstructure interferes with ultrasonic wave propagation, making it challenging to interpret the results [95]. These results are heavily dependent on the operator's experience [87], and the latter's efficiency may be impaired by the task of repeatedly interpreting ultrasonic oscillograms for an extended period of time [86]. Tools that assist operators in interpreting and classifying ultrasonic oscillograms can contribute to improving the evaluation of RSW joints through ultrasonic technique. The ultrasonic oscillogram obtained through the A-scan technique is a plot of wave amplitude over time [86], where the ultrasonic beam reflects upon reaching an interface, resulting in a series of echoes whose positions indicate the location of the reflecting interface and whose heights are a function of sound attenuation, i.e., of the weld nugget's microstructure [86]. With the aim to semi-automatize the UT procedure, automatizing the classification of welding, in 2006, Martín et al. [96] extracted a ten-component vector from each ultrasonic oscillogram and used a multi-layer feedforward artificial neural network (ANN) trained with the Levenberg–Marquardt algorithm to classify it, i.e., each ultrasonic oscillogram and its corresponding RSW joint, into four possible quality levels [86]: (i) good weld, (ii) undersize weld, (iii) stick weld, and (iv) no weld. To obtain a classification, two parameters of the weld nugget has been considered [96]:

- *Weld nugget microstructure*. In the nugget a cast microstructure with coarser grain than the base metal is present, hence the nuggets produce high attenuation than base material. The HAZ, that is the small area between the weld nuggets and parent material, showed a recrystallized microstructure with fine grains with low attenuation for UT, thus its influence can be neglected (**Figure *32*** a-c).
- *Weld nugget size*. If the weld nugget diameter is smaller than the width of the ultrasonic beam, an echo which is a part of reflections occurs at the interface between the two sheets. A thick nugget produces higher attenuation (**Figure *32*** b-d).

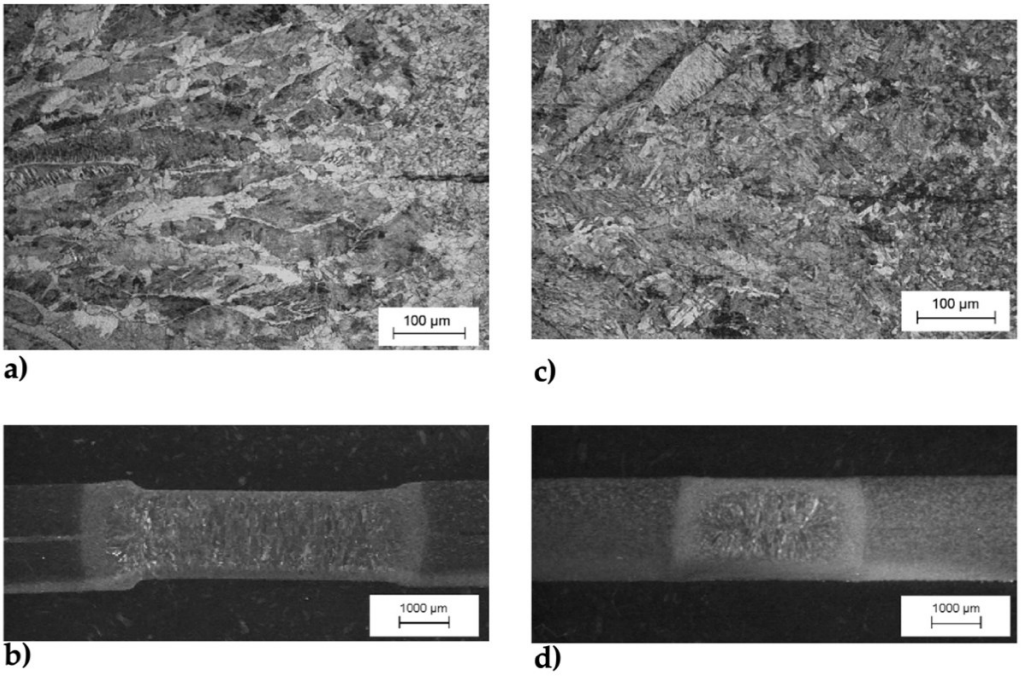

Figure 32. (a) micrograph of a cross-sectioned good weld. (b) Macrograph of a cross-sectioned good weld. (c) Micrograph of a cross-sectioned undersize weld. (d) Macrograph of a cross sectioned undersize weld [96].

Other cases of not-good weld are represented by sticked weld and no welded. The sticked weld presents a cast microstructure but is thinner than the wed nugget of a good-welded joint. In this case, the welded nugget is larger than the width of ultrasonic beam (**Figure *33*** a-b). In no welded joint there is no melting thus the grain is not as coarse as the grain of cast microstructure, as it is evident in **Figure *33*** c-d.

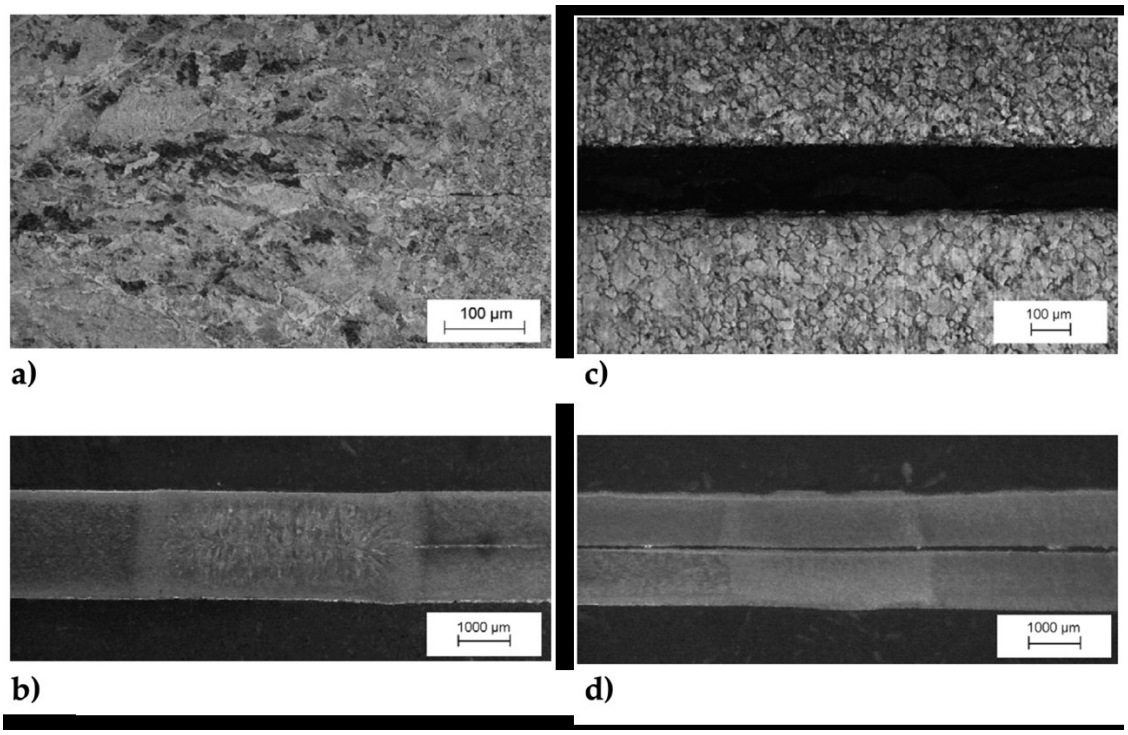

Figure 33 (a) Micrography of a sticked joint and (b) the correspondent macrography. (c) The micrography of a no welded joint and (d) correspondent macrography [96].

Subsequently, and considering that ANNs are "black boxes" and lack explanatory capacity, Martín et al. [88] proposed classification and regression tree (CART) and random forest techniques as pattern recognition models for classifying ultrasonic oscillograms obtained from RSW joints and demonstrated that CARTs resulted in an acceptable error rate with high interpretability. In contrast, random forests reduced the error rate at the expense of reduced decision interpretability compared to CARTs. Intending to save time on 2019, Hua et al. [97] developed an in situ ultrasonic detection system comprising an electrode with an embedded probe, allowing for rapid acquisition of the ultrasonic testing signal from the RSW joint. In the presented work, as respect of previous [96], another classification based on the nugget characteristics is presented and more levels are considered.

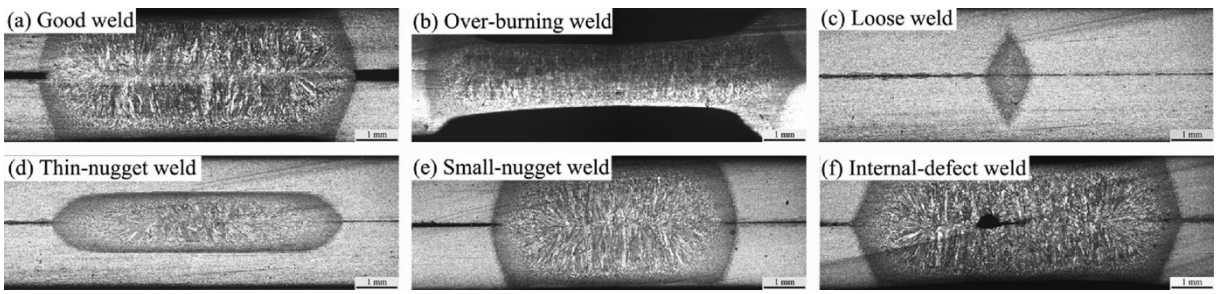

Figure 34. Nugget macro-structures of different welded joints analyzed by Hua et al. 13]

In **Figure** ***34*** different situations are presented, and several cases of ineligibility are showed. To increase the ratio between signal due to defected weld and background noise, a frequency-domain analysis has been used to amplify the signal features.

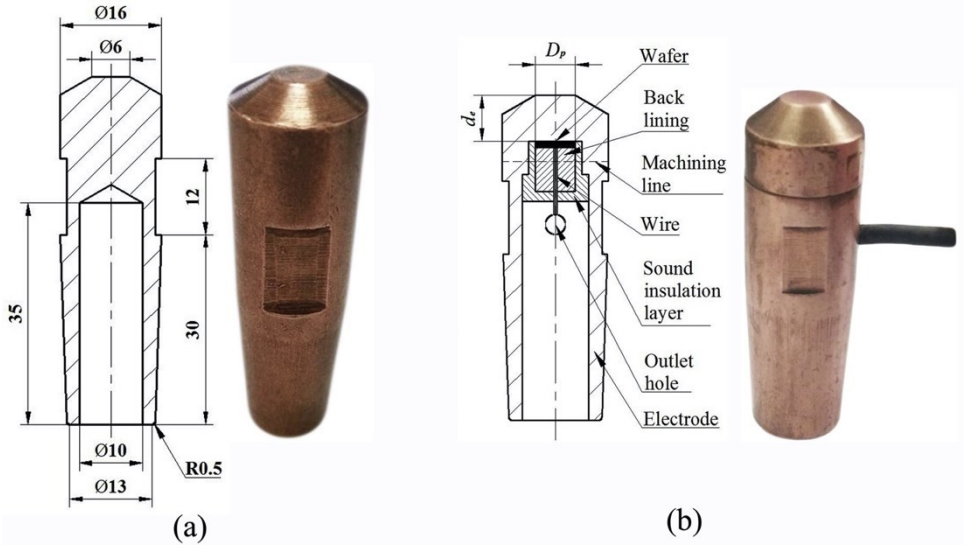

Figure 35. (a) Usual electrode for RSW and (b) electrod with embedded probe developed by Hua et al. [96]

The proposed method guarantees an error of 7% on the measurement of nugget diameter and thickness. Something that must be evaluated as a cons is the increased time to produce and change the electrodes, because of the embedded probe, the less versatility of system that can be used only with that specific equipment and fixed dimensions, moreover the measurements have been obtained only for good condition electrodes. In fact, one factor that can influence the quality of joints in RSW is the wear of electrodes during the process. Wang et al. [98] proposed a particle swarm optimization support vector machine (PSO-SVM) to classify the maximum tensile-shear strength (MTSS) of RSW joints. Signal processing and mathematical statistics methods were utilized to extract the features of ultrasonic detection signals as input variables, and the MTSS of the RSW joints were used as output variables. Wavelet packet analysis was employed by Qiuyue et al. [99], for UT evaluation of the size and location of porosity in stainless steel RSW joints. In this paper, the authors developed a method for detecting and quantifying porosity in spot welds using ultrasonic waves and wavelet packet analysis. To do this, they first performed ultrasonic testing on welded specimens with known porosity levels **Figure** ***36*** [99], and then collected the resulting ultrasonic waveforms and wavelet packet decomposition to analyze them. By examining the decomposed waveforms, they could extract information about the size and location of any porosity present in the welds.

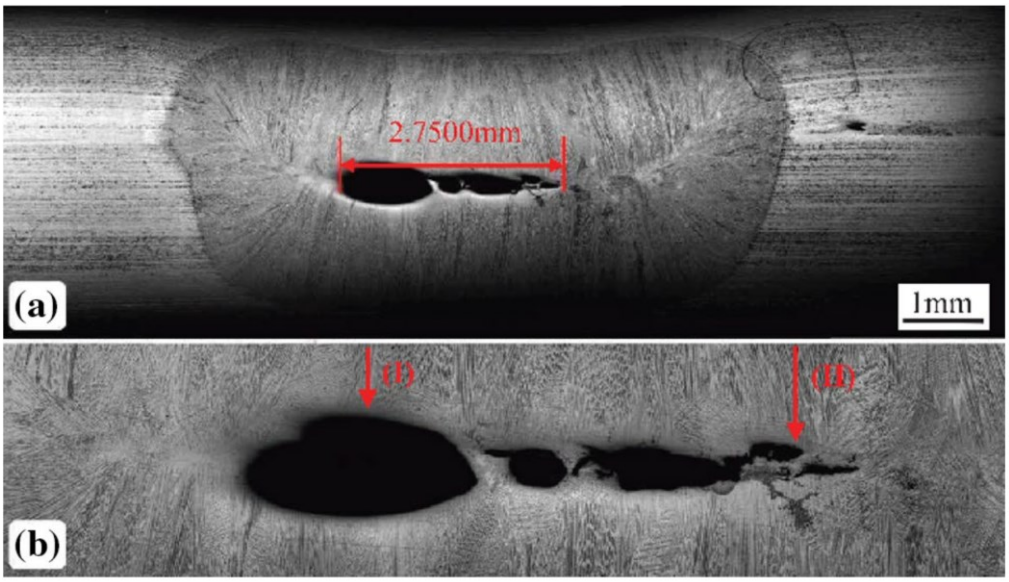

Figure 36. Cross-section metallography along scanning line obtained from Qiuyue et al. [99].

Qiuyue et al. [99], found that their technique could accurately detect and quantify the welds' porosity. They also demonstrated that the method could detect porosity in welds with different geometries and locations within the weld. In addition, they compared the results obtained using their technique with those obtained using conventional destructive testing methods and found good agreement between them.

Overall, it is possible to conclude that the presented method could be used as a non-destructive testing technique for evaluating the quality of spot welds [99]. It could be beneficial for identifying and characterizing porosity in welds, as it allows for the detection and measurement of porosity without damaging the welded material.

Liu et al. [89], for automatic identification and classification of ultrasonic echo signals obtained from stainless steel RSW joints, using back-propagation neural network models.

Moghanizadeh [100], studied the relationship between the attenuation coefficient in low carbon steel RSW joints and microhardness, and in turn, between microhardness and welding quality, in light of the effect of heat input on two microstructural features (grain size and phase content).

In his study, Moghanizadeh [100] introduces a technique for utilizing ultrasonic testing to assess the physical characteristics of spot welds. Ultrasonic testing has been adopted as a method to evaluate the quality of spot welds by measuring the welded material's thickness and the weld nugget's size.

Moghanizadeh [100] starts by discussing the principles of ultrasonic testing and how it can be used to measure the properties of spot welds. Ultrasonic waves are transmitted through

the welded material, and the time it takes for the waves to travel through the material is used to calculate the thickness of the welded material. The size of the weld nugget can be determined by analyzing the reflection of the ultrasonic waves at the weld interface.

The author [100] then presented the results of experiments conducted to test their method's effectiveness. The experiments were conducted on welded specimens with known thicknesses and weld nugget sizes. The results showed that the ultrasonic testing method accurately measured the thickness of the welded material and the size of the weld nugget.

Moghanizadeh [100] discussed the limitations of ultrasonic testing for evaluating spot welds. One limitation is that the accuracy of the measurements can be affected by the presence of defects or inhomogeneities in the welded material. In addition, the method is not suitable for evaluating welds with complex geometries or those that are located at a depth within the material. Overall, it is possible to conclude that ultrasonic testing is a valuable NDE technique for evaluating the physical properties of spot welds. It can provide rapid and accurate measurements of the welded material's thickness and the weld nugget's size, which can be useful for ensuring the quality and reliability of spot welds in manufacturing and other applications.

Amiri et al. [101], investigated the relationship between ultrasonic testing results and the tensile strength and fatigue life of three-sheet RSW joints using a single and dual-objective neural network. However, evaluating the strength and fatigue performance of spot welds can be challenging, as it requires destructive testing methods that can be time-consuming and costly. The authors proposed a method for predicting spot welds' static and fatigue behavior using ultrasonic testing and machine learning techniques. They first conducted experiments on welded specimens to measure the welds' mechanical properties under static and fatigue loading conditions. They also collected ultrasonic data from the welds using pulse-echo testing, which involves transmitting ultrasonic waves through the welded material and measuring the time it takes for the waves to travel through the material.

The authors then used the ultrasonic data and the measured mechanical properties of the welds to train machine learning models to predict the static and fatigue behavior of the welds. They found that the models could predict the welds' static and fatigue strength accurately and that the prediction errors were within acceptable limits.

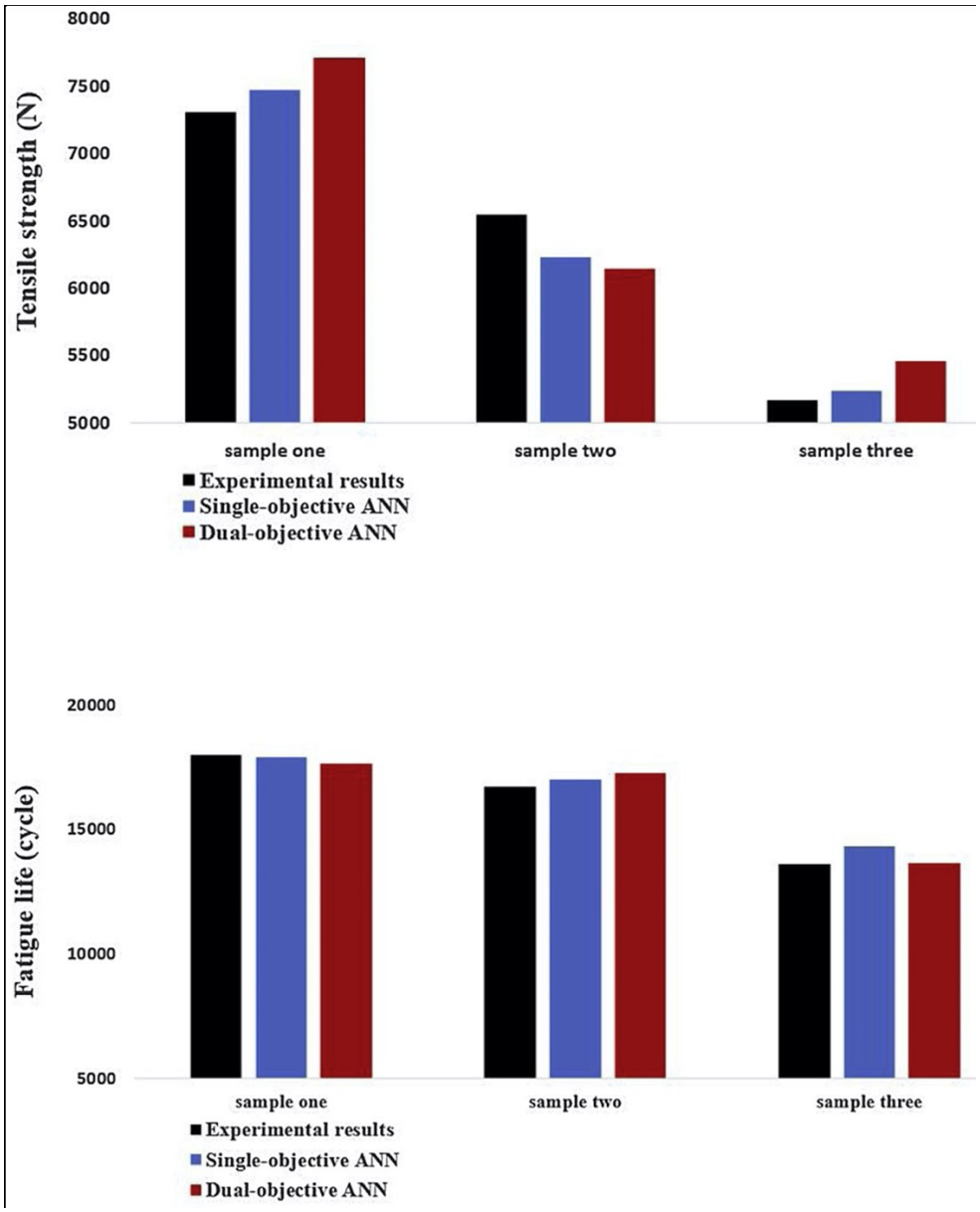

Figure 37. Comparison of the predicted mechanical properties (tensile strength (a) – fatigue life (b)) of spot-welded joint with the actual values

The authors also investigated the effect of different parameters, such as the welded material's thickness and the weld nugget's size, on the models' prediction accuracy. They found that the models were more accurate for welds with larger nugget sizes and thicker welded material and that the prediction errors increased as the nugget size and thickness of the welded material decreased.

Overall, their method can be used as a nondestructive testing technique for evaluating spot welds' static and fatigue behavior. It could be particularly useful for identifying and

characterizing welds prone to failure, as it allows for predicting the strength and fatigue performance of the welds without the need for destructive testing.
Another method consists of *guided waves* for which a recent example has been presented by Pineda Allen et al. [53], that propose a method for detecting debonding at adhesive joints using the nonlinear mixing of Lamb waves.
Lamb waves are elastic waves that can propagate through solid materials. They are characterized by their mode of vibration, which determines the shape of the wavefront and the distribution of energy within the material. Nonlinear mixing of Lamb waves occurs when two waves with different frequencies interact and produce new waves with different frequencies. This process can be used to extract information about the material and its properties [53].
This paper examined [53] the interaction between nonlinear Lamb wave mixing and local debonding using experiments and numerical simulations. It was found that the wave mixing technique can detect debonding at adhesive metal joints by observing the creation of a combined frequency wave. The harmonics produced due to the contact effect at the debonding were extracted from the frequency domain of the experimental samples and used to validate a 3D FE model [53]. The presence of the combined harmonic was found to be a reliable indicator of local debonding. In addition, the effect of debonding width on mixed-frequency Lamb waves interacting with damage was studied in the frequency domain. The numerical results indicated that the debonding width could be correlated with the energy produced by debonding. This suggests that the proposed technique is also sensitive to different debonding widths within a specific range of d/λ. The research also better understood the nonlinear Lamb wave mixing process in adhesive joints.

According to Lindner and Deike [102], radiographic examination is an effective non-destructive testing technique for the intermediate sheet area that is difficult to access and is suitable for use in the large-scale automotive industry. The above-mentioned authors [102], described a method for detecting liquid metal embrittlement (LME) cracks using X-ray. They conducted experiments on welded specimens with known LME cracks and used X-ray imaging to collect data from the welds. They then analyzed the data to identify the presence and location of LME cracks. As results, they found that their method was able to accurately detect LME cracks in the welds, as it is possible to see in **Figure *38***, and then discuss the potential applications for detecting LME cracks in industrial settings.

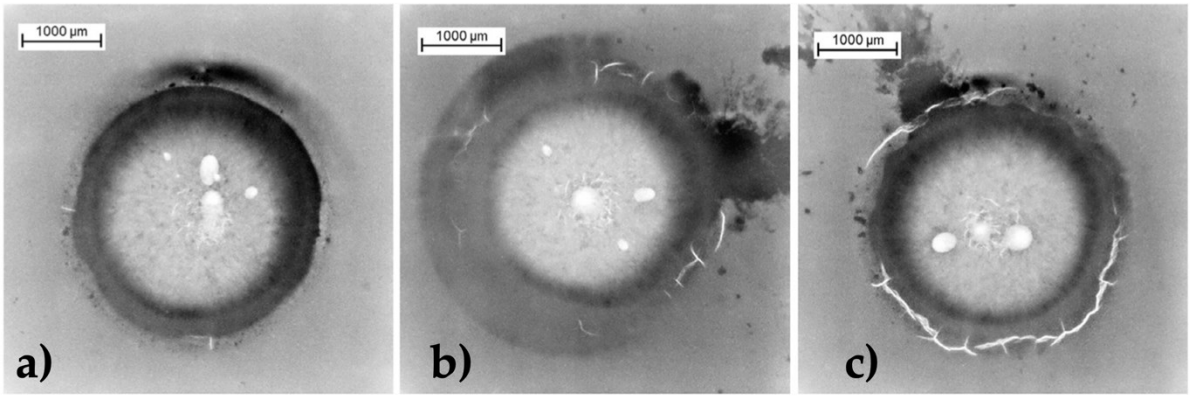

Figure 38. X-ray results [102] of change of crack characteristic depending on the heat input in process

One advantage of using X-ray as a NDT method is that it allows for the detection of cracks without the need for destructive testing, which can be particularly useful in situations where the welds are part of a critical structure or component. In addition, X-ray imaging can provide detailed information about the size and location of LME cracks, which can be useful for identifying and characterizing welds that are prone to failure.

However, there are also some limitations to using X-ray as an NDT method. One limitation is that it may not be suitable for evaluating welds with complex geometries or those that are located at a depth within the material. In addition, the accuracy of the measurements can be affected by factors such as the thickness of the welded material, the size of the weld nugget, and the presence of defects or inhomogeneities in the welded material. Thus, it is important to consider the limitations of the method and to take steps to minimize any potential sources of error when using X-ray imaging to evaluate welds. It is worth noting that the use of radiographic inspection for welding quality control in actual production is limited due to the fact that X-rays are harmful to the human body.

Another method for non-destructively inspecting RSW joints is the magnetic technique, which, although it does not provide as much morphology information as ultrasonic and radiographic techniques, is convenient and low-cost [66,67,69]. Ma et al. [69] describe a method for detecting defects in welds using magneto-optical imaging, which involves the application of a combined magnetic field to the welded material and using a camera to capture images of the resulting magneto-optical effect. They conducted experiments on welded specimens with known defects and used the magneto-optical imaging method to collect data from the welds. They then analyzed the data to identify the presence and location of defects in the welds using the setup showed in **Figure *39***.

The authors found that the magneto-optical imaging method was able to detect defects in the welds accurately, and they discuss the potential applications of their method for detecting defects in industrial settings. They also discuss the advantages and limitations of the method, including its sensitivity to the size and location of defects and its ability to distinguish between different types of defects.

Overall, the authors conclude that magneto-optical imaging is a promising NDT technique for detecting defects in welds. It allows for detecting defects without the need for destructive testing, and it can be used as a tool for ensuring the quality and reliability of welds in manufacturing and other applications.

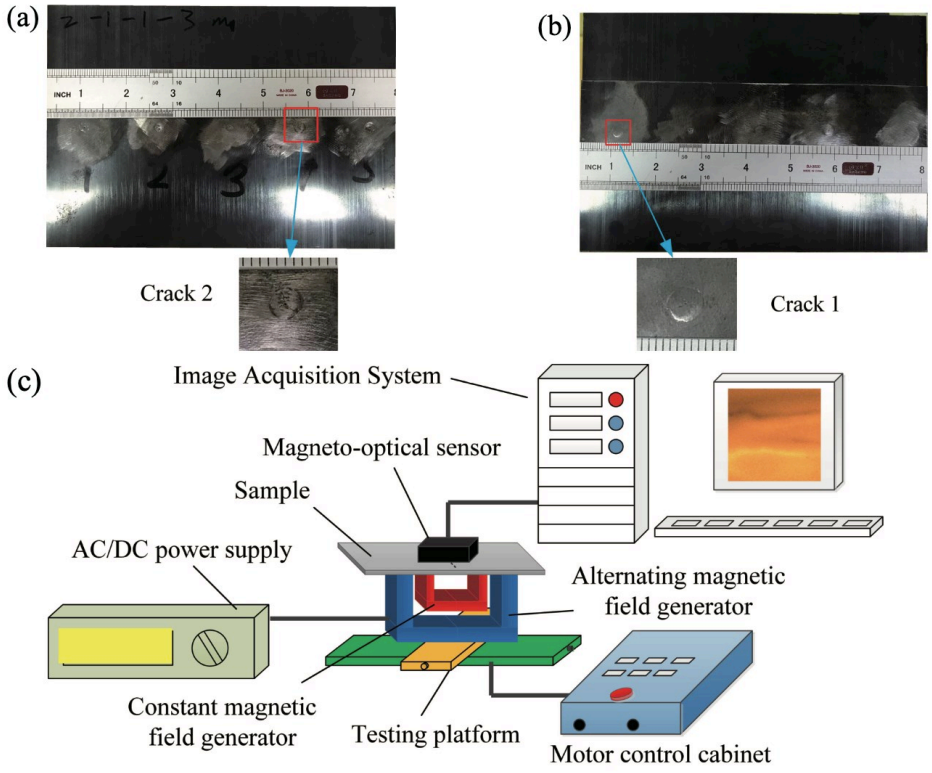

Figure 39. Experimental and schematic diagram of the setup used. (a) Front of sample. (b) Back of sample. (c) Schematic diagram of experimental platform.

According to Tsukada et al. [67], there are two main methods for conducting magnetic-based testing: (i) the magnetic flux leakage test (MFL) (**Figure *40***), which uses the magnetic flux leakage from the sample surface when a low-frequency magnetic flux is induced, and (ii) the eddy current test (ECT) (**Figure *41***), which uses high-frequency electromagnetic induction in conductive materials.

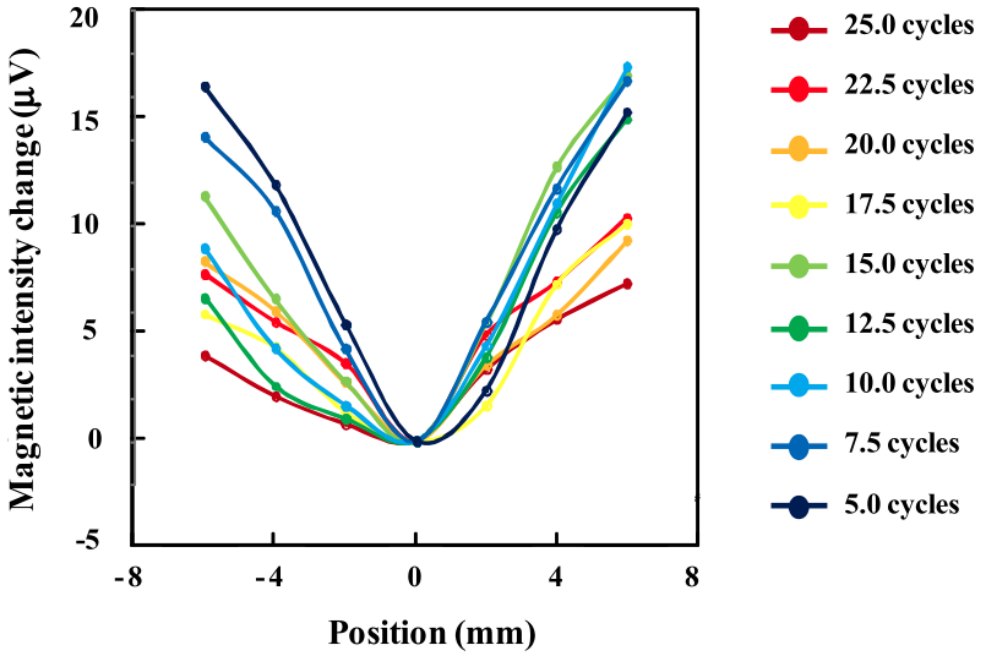

Figure 40. Example of results obtained by Tsukada through flux leakage test. [67]

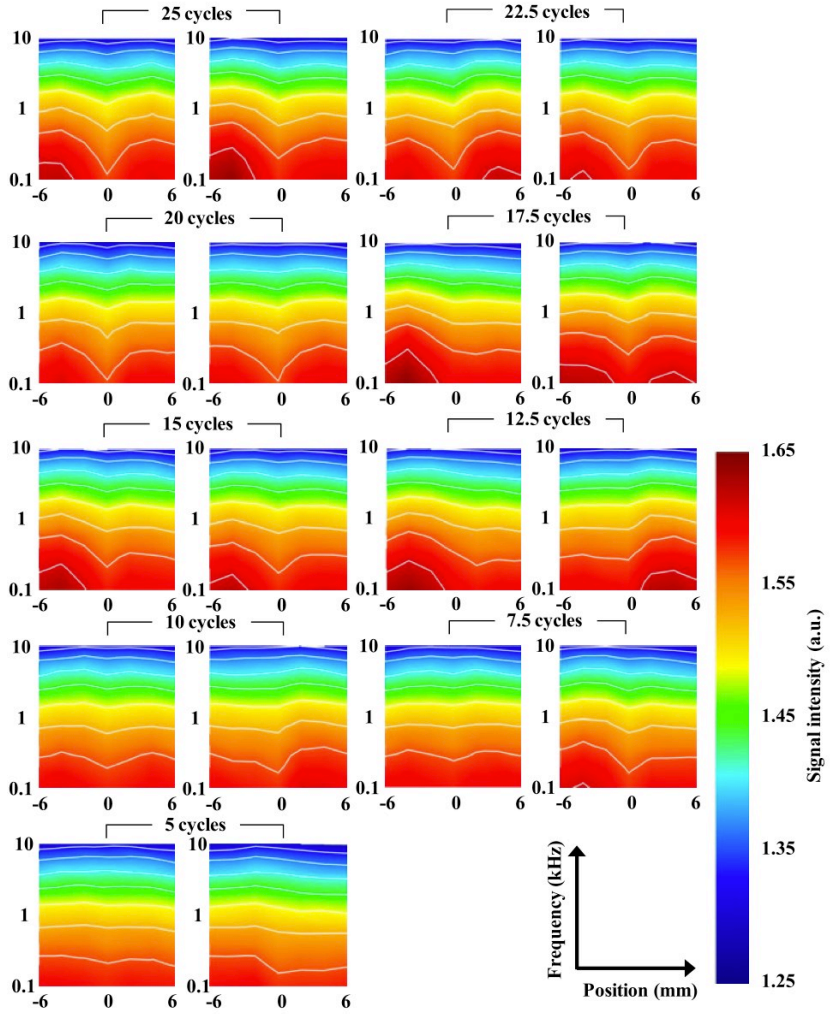

Figure 41. Example of results obtained by Tsukada through flux leakage test. [67]

The authors of the paper [67] conducted experiments to evaluate the performance of the magnetic flux penetration and eddy current methods for the detection of weld defects. They used both methods to inspect welds with various types and sizes of defects, including incomplete fusion, lack of penetration, and porosity. They found that both methods effectively detect these defects, with the eddy current method being more sensitive to minor defects.

The authors also compared the performance of the two methods with the ultrasonic testing method, another commonly used NDT technique for weld inspection. They found that the magnetic methods could detect defects that were not detectable using ultrasonic testing.

Overall, the results of the experiments demonstrate the potential of magnetic flux penetration and eddy current methods for the nondestructive testing of resistance spot welds. These methods can provide valuable information about the quality and integrity of welded joints, helping to ensure the safety and reliability of welded structures.

Tsukada et al. [70], developed an MFL system using a magnetoresistive sensor for non-destructively testing RSW joints. The authors [70] propose a method for evaluating the integrity of spot welds using a magnetoresistive sensor and magnetic flux leakage. The technique involves using a permanent magnet to generate a magnetic field around the weld, with the magnetoresistive sensor used to measure the magnetic flux leakage from the weld. By analyzing the flux leakage patterns, it is possible to determine the presence and location of any defects in the weld.

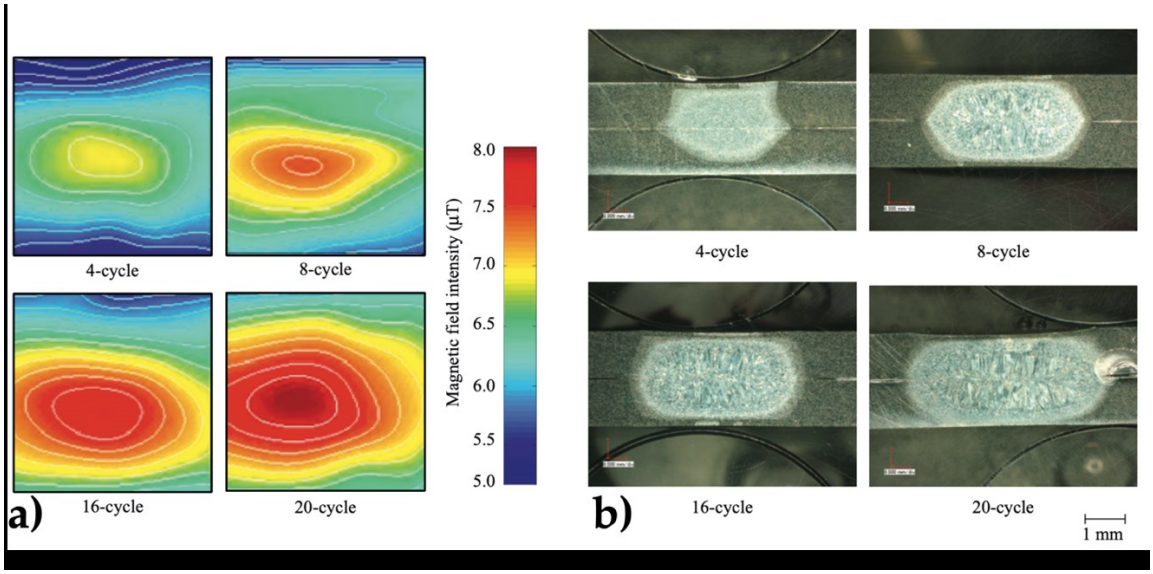

Figure 42. (a) Contour maps of the magnetic field distribution above the spot welds, and its dependence on the cycle time of welding: upper side. (b) Macrograph of cross-sectional spot welds, showing the dependence on cycle time [70].

Tsukada et al. [70] conducted a series of experiments to evaluate the proposed method's effectiveness, using welds with artificially introduced defects and welds taken from actual automotive components. The results in **Figure 42**, showed that the technique could accurately detect the presence and location of defects in the welds with a high degree of sensitivity [70].

Overall, the study [70]demonstrates the potential of the magnetic flux leakage method using a magnetoresistive sensor as a reliable and accurate non-destructive testing (NDT) technique for evaluating the integrity of spot welds.

Song et al. [103], used an imaging method to analyze the internal structure of RSW joints based on the phase of a magnetic field using a wide range of frequencies from high to low. Vértesy and Tomáš [66], presented the adaptive magnetic testing (MAT) method, which is based on the systematic measurement and evaluation of magnetic minor hysteresis loops, as an alternative for characterizing the quality of RSW and found a good correlation between the current welding value and the magnetic descriptors. For the ECT, Harada et al. [68], used it to evaluate RSW joints whose internal microstructure could be visualized using multiple frequencies and obtained a good correlation between the measured magnetic field strength and the tensile-shear load. The ECT method involves the application of a low-frequency alternating current to the surface of a sample and measuring the resulting magnetic field using a series of sensors [68]. By analyzing the magnetic field distribution, it is possible to infer the electrical conductivity of the material within the sample, which can be used to identify defects or variations in the internal structure of the spot weld.

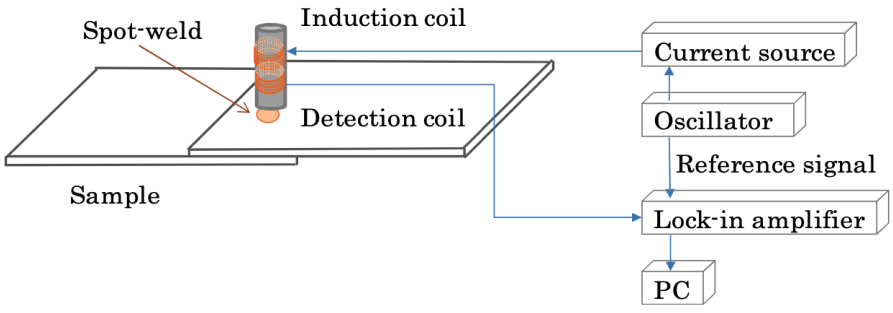

Figure 43. Measurement system for the internal structure analysis of a spot-weld used by Harada et al. [68]

The authors [68], conducted experiments to test the effectiveness of the ECT method for the NDT of spot welds. They used a sample of two sheet metals joined by a single spot weld as it. As showed in **Figure *43***, the sample was placed in a coil, and a low-frequency

current was applied to the sample's surface. The magnetic field produced by the current was measured using a series of sensors arranged in a circular pattern around the sample. The data collected by the sensors were used to reconstruct an image of the internal structure of the spot weld, which was then compared to a reference image obtained from destructive testing of the sample [68].

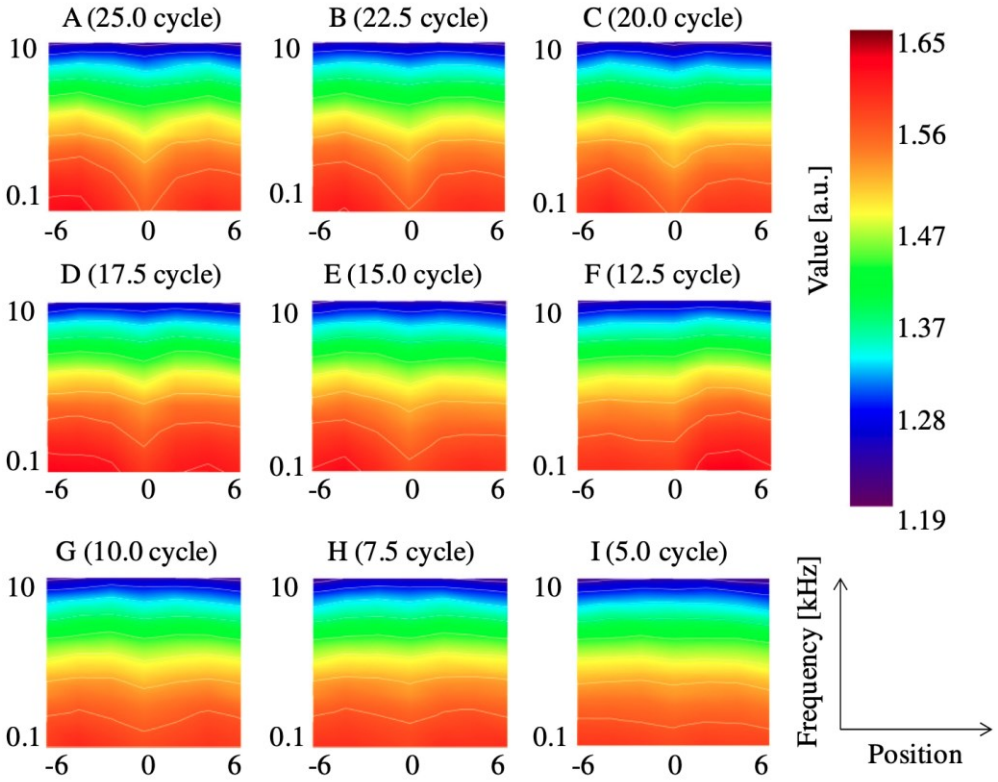

Figure 44. Map of the measured magnetic field strength for different frequency obtained by Harada et al. [68].

The results of the experiments showed that the ECT method could accurately identify variations in the internal structure of the spot weld, including the presence of voids and cracks. The authors [68] concluded that the ECT method is a promising tool for NDT of spot welds, as it allows for the non-destructive evaluation of the internal structure of the weld without the need for physical access to the weld. They also suggested that further research is needed to optimize the ECT method for NDT of spot welds, including developing more advanced sensors and improved reconstruction algorithms.

All the described techniques can be applied to the thin joint as non-destructive methods but, each one presents disadvantages. One of these, is that all the presented techniques need contact with the surface of component, that is not always possible and can be a problem in several industrial application. Another disadvantage that is present in the most of presented works, is that these techniques are time-consuming. In fact, must be

considered that, for example, in automotive industrial applications for a frame of a car more than 1000 resistance welding joints are present thus, if the inspection time is not compatible with the production time, a 100% control cannot be applied avoiding to increase too much time and cost of production. In several cases there is a semi-automatization of the control but is very specific for the kind of joint and process, hence a more versatile control should be developed to fulfill this void in the non-destructive controls.

In this direction, the thermographic technique can represent an opportunity because can overcome several of the limits which are present in other techniques, and be challenging with well-established techniques, which nowadays, are spreadly diffused.

3.1.1 Thermography on thin joints

In previous section, several methods and applications of NDT methods on thin joins have been presented, in particular for adhesive and welded joints. For the peculiarities of thermographic methods described in section 2.2.4, it is evident that this method can be particularly interesting for thin joint. In fact, must be remembered that the thermography is a superficial technique and can be considered a volumetric one only for low thermal diffusive materials. Nevertheless, the principal limit of thermographic techniques for high thermal diffusive material is the quantity of energy that can ensure a signal strong enough to be detected by a thermal sensor after the path in the material (the thickness of specimen in case of transmission configuration and double in case of reflection ones). In case of pulsed thermography, in fact, another limit is the pulse duration that must be applied to consider valid the pulse hypotheses, on which are based the most of algorithms, especially for metal specimens with very low thickness. For these reasons, the thermographic method can be suitable for inspecting thin joints, especially in cases of high energy density heat sources such as the laser source.

In the literature, some uses of thermography as non-destructive testing for joints can be found, both for low-diffusive [104–111] and high-diffusive materials[112–122]. Therefore, some more significant ones will, be reported below.

In 2018 Leicht et al. [123], presented an interesting application of passive and active thermography for defect detection in polymer joints. In the case of passive thermography, the thermographic system has been integrated with the welding process, obtaining an online evaluation. To analyze the data collected during the process, the differential picture method has been applied. Differential pixels (DP) are calculated by determining the

temperature difference between each current measurement (CP) pixel and a reference image. The reference image was generated by averaging a number of thermographic measurements (RPi) of a process with known quality, such as tensile strength. The method is illustrated in **Figure *45***.

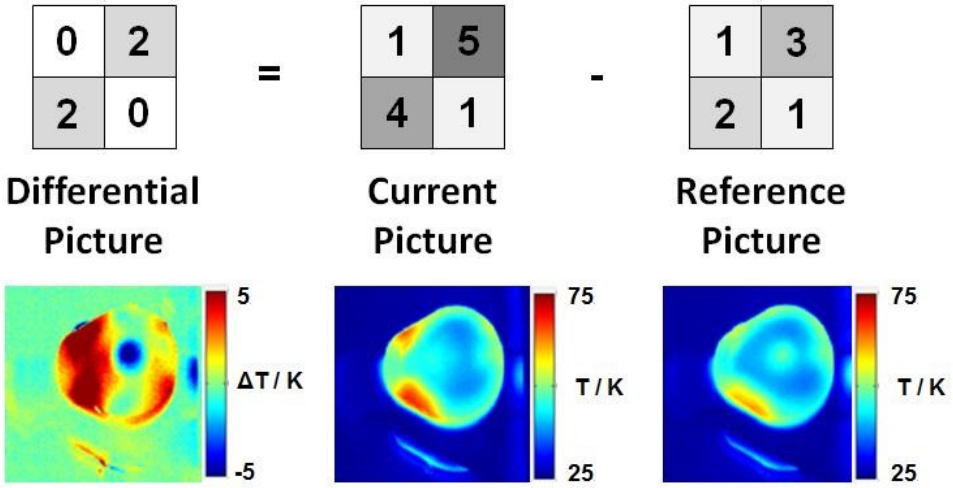

Figure 45. Schematic of the differential picture method illustrated by pictures with four pixels and different grey values (1 to 5; top). Example for the measurement of an industrial part with a defect prior to welding (bottom) [123]

Lock-in thermography has been applied in [124–126] . As described briefly in section 2.2, this method produce results in terms of phase and amplitude maps.

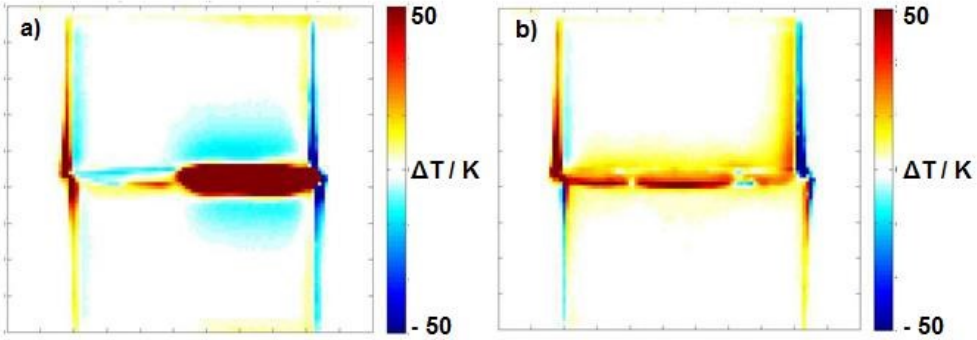

Figure 46. Differential pictures of infrared welded PVDF sheets. Half of the welded area has been blackened with ink (arrows; a) in order gain a higher absorption of the infrared radiation on the surface of the weld area. Additionally, sheets with two notches (indicated by arrows) in the weld area have been prepared to simulate the effect of surface defects (b) [123].

In **Figure *46***, it is shown an example of surface defects revealed by passive thermography, by infrared welding process using a PVDF.

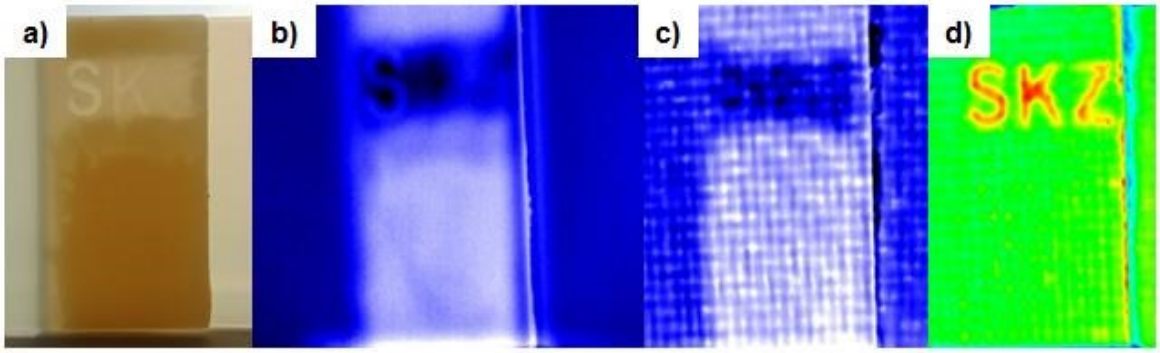

Figure 47. Photograph of an overlapping adhesive bond of PA66 with an air inclusion building the letters 'SKZ' (a) and phase picture of the OLT (lock-in frequency 6.2 mHz) of this specimen (b). The depth of the air inclusions is rising from 'S' (1.0 mm) to 'Z' (3.0 mm). Phase picture (c) and amplitude picture (d) of an equal specimen built from GFRP-PP (lock-in frequency 17.7 mHz) [123].

Air inclusions can be detected to a depth of 1.0 mm (labelled as "S") in PA66. Additionally, the absence of adhesive around the area of the defects, which can be seen in the photograph, is clearly visible in the phase images. In the phase image (**Figure *47***) of GFRP-PP, the inclusion is slightly obscured by the reflections created by the fibreglass structures of the composite, which slightly hinders the identification of the shape of the defects. However, the defects are visible to a depth of 3.0 mm (labelled as "Z") in the amplitude image, and the absence of adhesive application is no longer detectable. Therefore, it is important to utilize both amplitude and phase images in order to detect defects in polymer joints accurately.

Another interesting application of pulsed thermography to adhesive joints has been proposed by Kostroun et al. [108], which examine the possibility of using active thermography to test composite aircraft adhesive joints. After a measurement of thermal diffusivity in thickness direction using the transmission flash method [127], pulsed thermography with a reflection setup has been used to detect defects using a flash lamp as heat source. To be able to calibrate the technique, a reference gauge has been produced with geometry reported in **Figure *48***. In **Figure *49***, several thermograms of reference sample after a pulse heating have been reported. It is possible to observe that, for long time cooling, the image became blurred because of lateral heat flow.

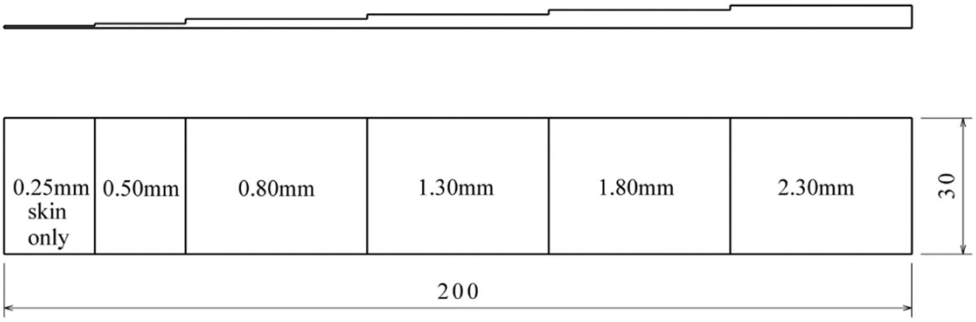

Figure 48. Schematic geometry of reference gauge used [108]

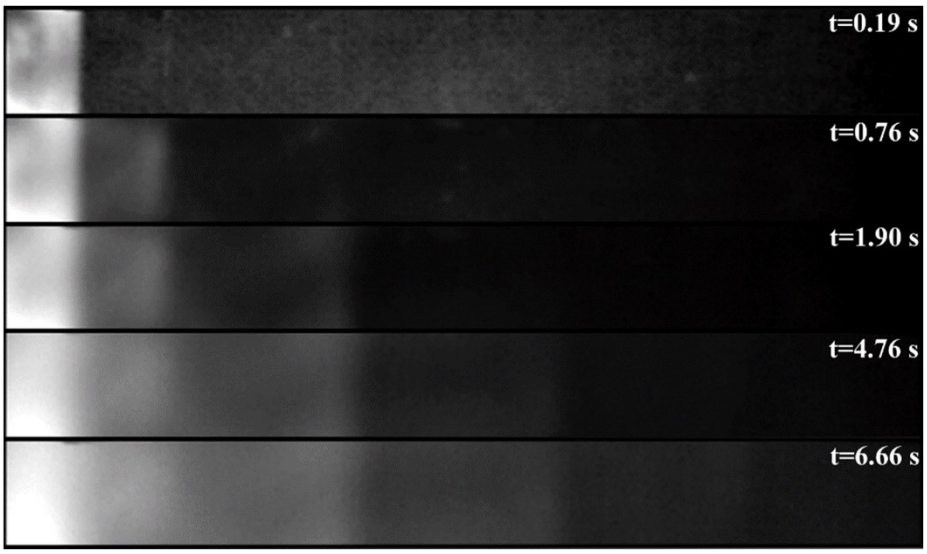

Figure 49. Thermograms obtained after pulse heating by flash lamp for different observation times of reference sample. [108]

The Modified Differential Absolute Contrast (DAC) method has been utilized to process the measured data to partially eliminate unevenness in the heat source, such as reflections from the environment (e.g., IR camera, flash lamps) and variations in emissivity on the surface. The DAC method compares the temperature of the tested area with the theoretical temperature that would exist in the absence of a defect. This theoretical temperature is calculated using the 1D form of the Fourier equation for heat conduction in a semi-infinite medium based on the measured temperature at a point when the temperature defect is not present [128].

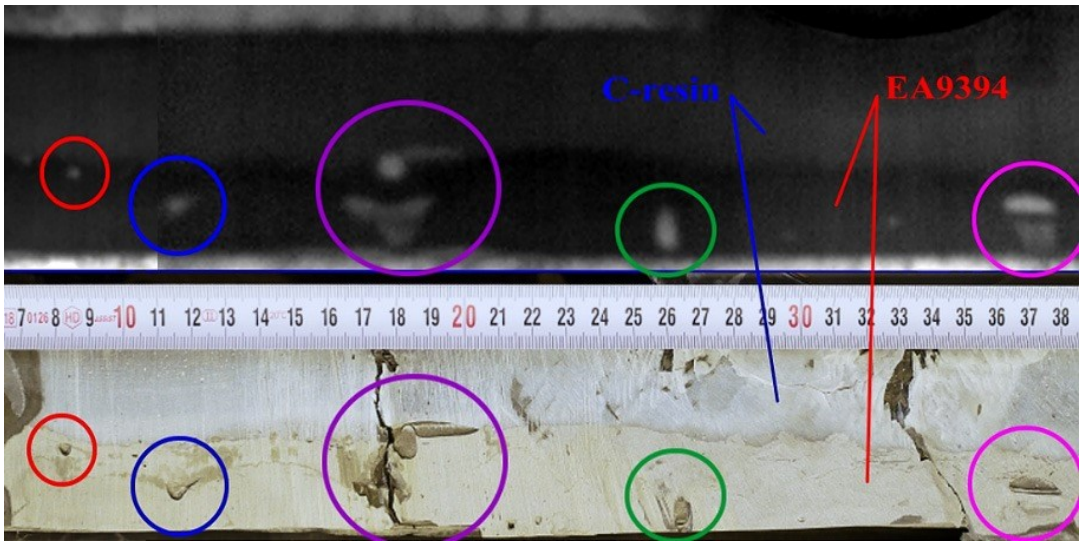

Figure 50. Comparison of NDE findings (top) with the actual condition of the adhesive joint (bottom) [108]

Figure *50* compares the results of the Non-Destructive Evaluation (NDE) and the actual condition of the adhesive joint. The top portion of the image displays an evaluated image of the adhesive joint before the structural strength test. At the same time, the bottom part shows the condition of the adhesive joint after the strength test and the resulting damage to the wing. The colored circles indicate the corresponding defects in the joint. The NDE measurement aligns well with the actual condition of the joint. The tiniest detected defect (marked in red) has a diameter of approximately 3 mm. Given the resolution of the IR camera, this size can be considered the smallest detectable defect in the adhesive joint for the given test configuration. In addition to defects in the adhesive layer, the use of two adhesives (EA9394 and C-resin) are visible in the image. The bottom half of the image also shows two vertical cracks caused by a failure during the strength test of the wing demonstrator [108].

The paper [108], presents a method for testing the quality of adhesive joints in thin-walled composite structures of light sports aircraft using an IR camera. After the use of a reference gauge that simulated an adhesive joint, it demonstrated sufficient depth resolution and sensitivity to detect defects of at least 3 mm in size. The method was effective for detecting defects in adhesive joints of wing skins, ribs, and load-bearing spar structures made from thin CFRP. It can also identify manufacturing defects and inaccuracies such as adhesive overflow, misaligned foam inserts, or overlapped composite layers. The results obtained with this method are useful for both qualitative and quantitative evaluation of adhesive joints. The readability of the resulting images can be improved through the use of higher

resolution IR cameras or IR cameras with greater sensitivity and stability or by using more powerful heat source [108].

Palumbo et al., in 2016 [107], used lock-in thermography for the evaluation of debonding in composite adhesive joints, comparing the results with a well-established method as the UT C-scan.

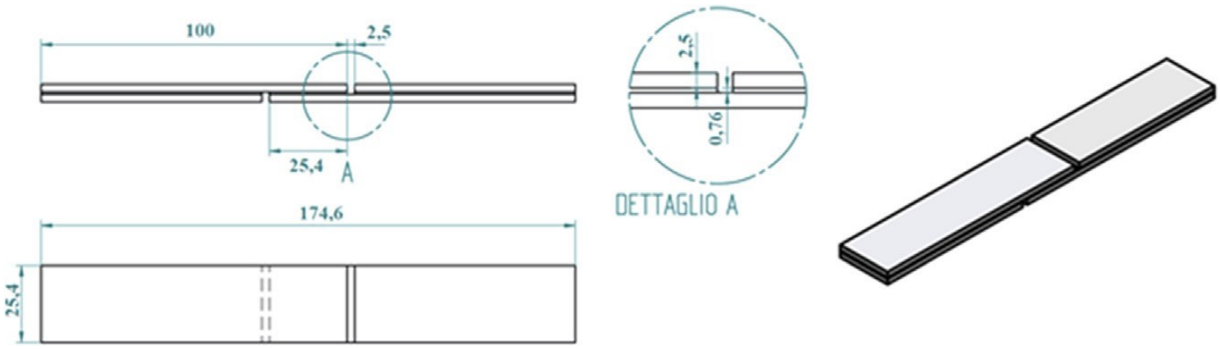

Figure 51. Specimen geometry used by Palumbo et al. [107]

In the research work [107], 12 single lap GFRP joints have been considered and a hygrothermal aging procedure has been applied to simulate natural weather conditions. Secondly, halogen lamps have been used as the heat source for the lock-in thermography, and phase maps have been compared with C-Scan results after the definition of a threshold for segmentation to obtain binarized maps, as showed in **Figure *52***.

In the reported study [107] ,the tests were conducted on single-lap adhesive joints by ASTM D 3165, both before and after accelerated ageing, using both lock-in thermography and ultrasonic testing (UT). The results of these tests indicated the presence of defects that remained unchanged in size and shape. C-scan ultrasonic testing was also utilized to validate the results obtained through thermography, and quantitative analysis was performed using decision threshold values. The lock-in thermography results were consistent with those of UT C-scan inspection and visual inspection after sample rupture. In conclusion, lock-in thermography was demonstrated to be a valuable non-destructive testing tool for evaluating a bonded composite assembly's initial condition and monitoring its performance under various environmental conditions. Additionally, lock-in thermography can provide information about the appropriateness of the manufacturing process and suggest potential areas for improvement [107].

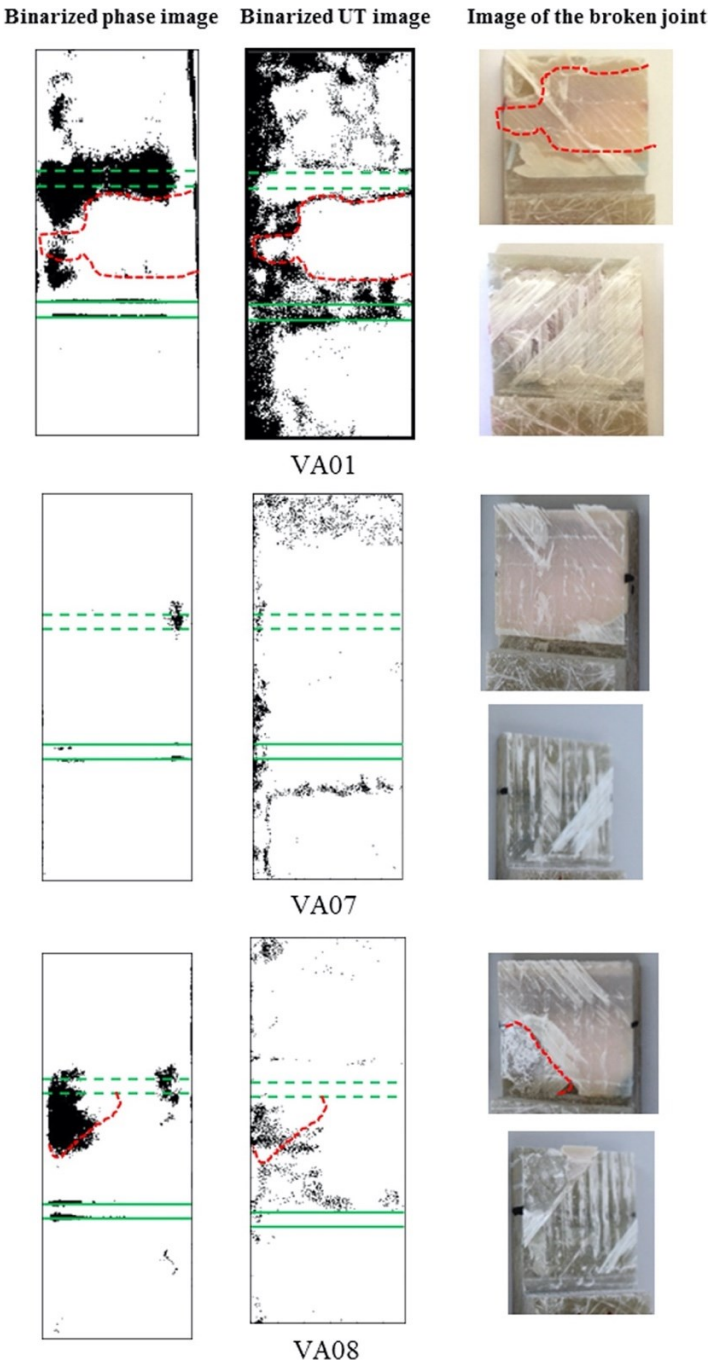

Figure 52. Binarized phase images, binarized UT images and images of the broken joints of three of the analyzed samples [107]

Another recent work by Wu et al. [106], describes an application of active thermography to verify bonded joint structures in CFRP, using the super-resolution thermal imaging [129–132]. The authors conducted experiments to evaluate the performance of the proposed method. They found that it could provide high-resolution thermal images with good accuracy and reproducibility, applying a super-resolution algorithm to the acquired thermal images. The authors also conducted experiments to compare the performance of the proposed method to that of a traditional destructive testing method. They found that

the proposed method could provide similar results to the destructive method but without the need for dismantling the joint.

Overall, the results of this study suggest that the proposed super-resolution thermal imaging method is a promising technique for the non-destructive testing of adhesive-bonded joints. It allows for evaluating the performance of such joints in a convenient and non-invasive manner, with results comparable to those obtained using traditional destructive testing methods.

An interesting work, which presents an application of a Thermoelastic Stress Analysis [133–138] as non-destructive method for a quantitative evaluation of bonded CFRP T-joints, has been presented by Palumbo et al.[139]. This study used the thermoelastic stress analysis (TSA) technique to evaluate debonded regions and analyze the mechanical behaviour of adhesive T-joints under cyclic loading in carbon fibre-reinforced polymer (CFRP) structures. Four T-joint specimens were produced using the Automated Fiber Placement process and subjected to pull-off tests, during which the TSA technique was used to monitor the joints. The TSA results demonstrated a strong correlation between the thermoelastic signal and the elastic stiffness of the joints. They showed that TSA is more effective than other techniques (such as the LT technique) in quantifying the extent of debonded areas as is possible to observe in **Figure *53***. The TSA technique has several advantages, including its ability to provide a full field map of a signal related to the mechanical behavior of the joints and its sensitivity in detecting debonding under operational loading conditions. However, there are some limitations to the technique, including the need for good accessibility of the monitored area with an infrared camera, a sufficient number of cyclic loadings to obtain a significant signal-to-noise ratio, and the ability to detect TSA signal variations in thick composite structures with severe, hidden damages.

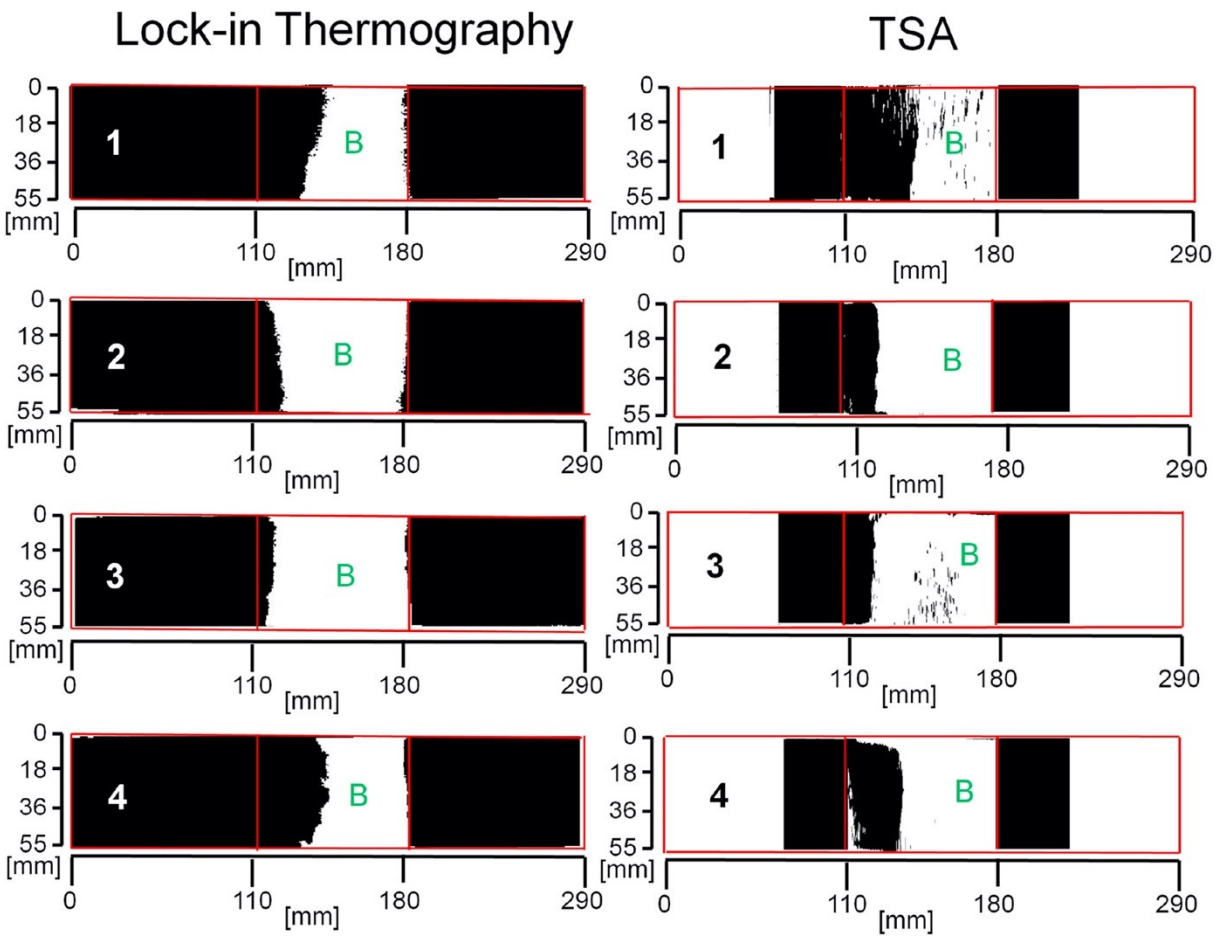

Figure 53. Binary maps of lock-in and TSA data (letter B indicates the bonded area).

The research works reported above, presented thermographic techniques applied to evaluate adhesive joints, mainly in low thermal conductive materials. This aspect must be considered because heat sources like halogen lamps or flash can easily be used in these cases. In fact, for low thermal diffusive materials with reduced thickness, the hypothesis of pulse heating is valid for heating times higher than for the conductive materials, as will be discussed in the next chapter defining thermally thin and thermally thin components.

An interesting application of thermal methods to detect edge debonding in composite patch, has been presented by Moradi et al. [140]. In this paper, to overcome one of the limits described, a long pulsed/stepped heating has been applied to detect disbond defects at the edge of the adhered carbon/epoxy patch on the aluminum plate. Thermal infrared images of the patch, obtained through flash thermography inspection, were analyzed using four widely-used techniques: principle component analysis (PCA), thermal signal reconstruction (TSR), Fourier transform (FT), and one-dimensional wavelet transform (1D WT). A novel method was also utilised to measure the area under temperature-time signals (Thermal Signal Area: TSA). A comprehensive performance evaluation of all post-

processing methods has been performed (**Figure *54***), both quantitatively and qualitatively [140].

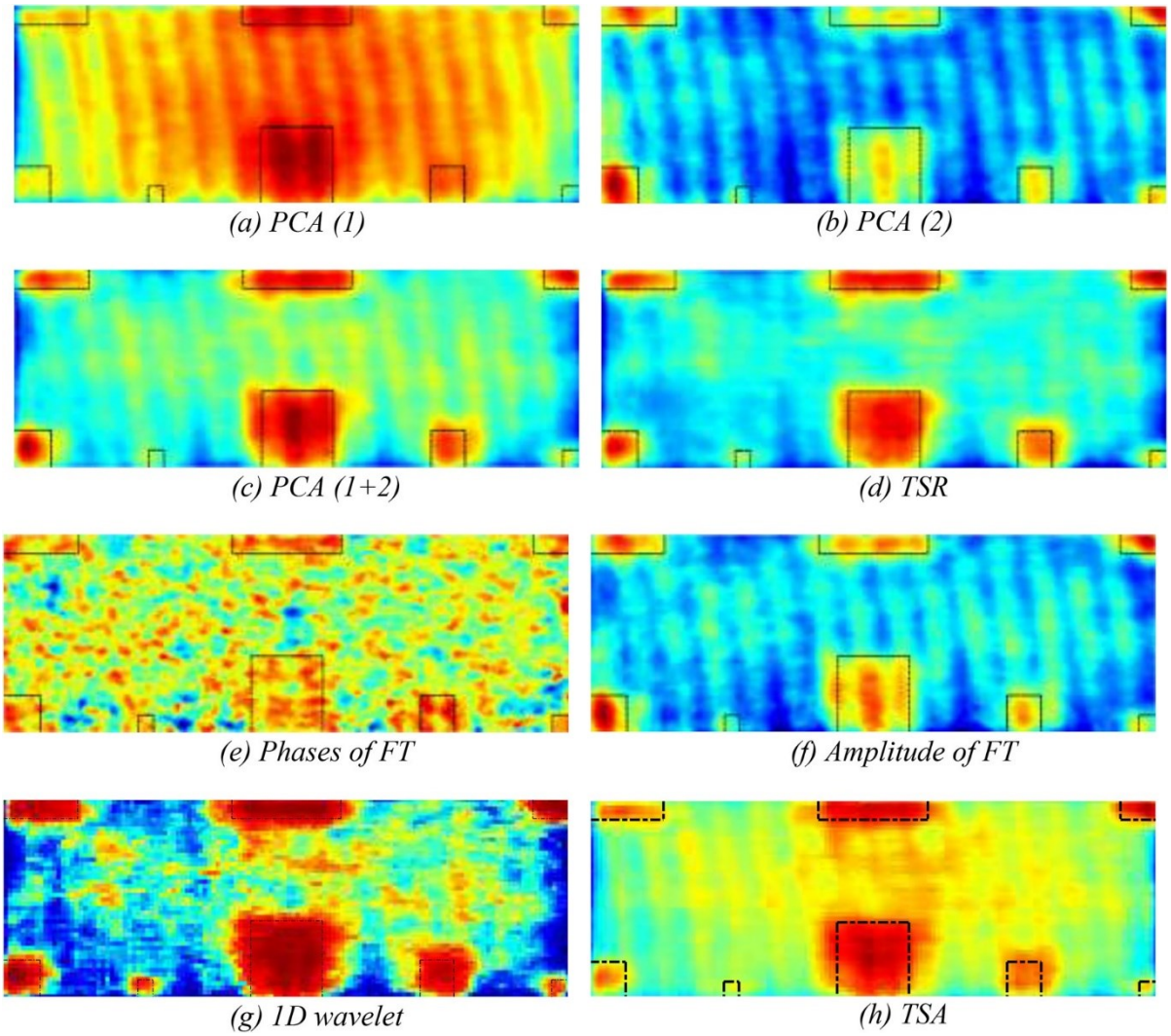

Figure 54. The results of (a) PCA (1), (b) PCA (2), (c) PCA (1 + 2), (d) TSR, (e) phases and (f) amplitude of Fourier transform, (g) 1D wavelets transform (ap- proximation at level 3), and (h) TSA [140].

The binary thresholding method impacted the comparison significantly, and thus two commonly used thresholding methods, global and local, were employed. Results indicated that the local thresholding method was more reliable, as demonstrated by its superior performance measured by the RMSE, NLSE, PSNR, TIR, Ave., and TDR parameters. Based on this, the TSR, PCA (1 + 2), and TSA algorithms produced more accurate results when using the local thresholding method (**Figure *55***). To further improve the results, the proposed method was combined with the one-dimensional wavelet transform, resulting in low noise and a reliability of 96.18% for thermography inspection. The proposed method was found to be particularly effective for minor debonding defects (5 x 5 mm^2) compared to other methods.

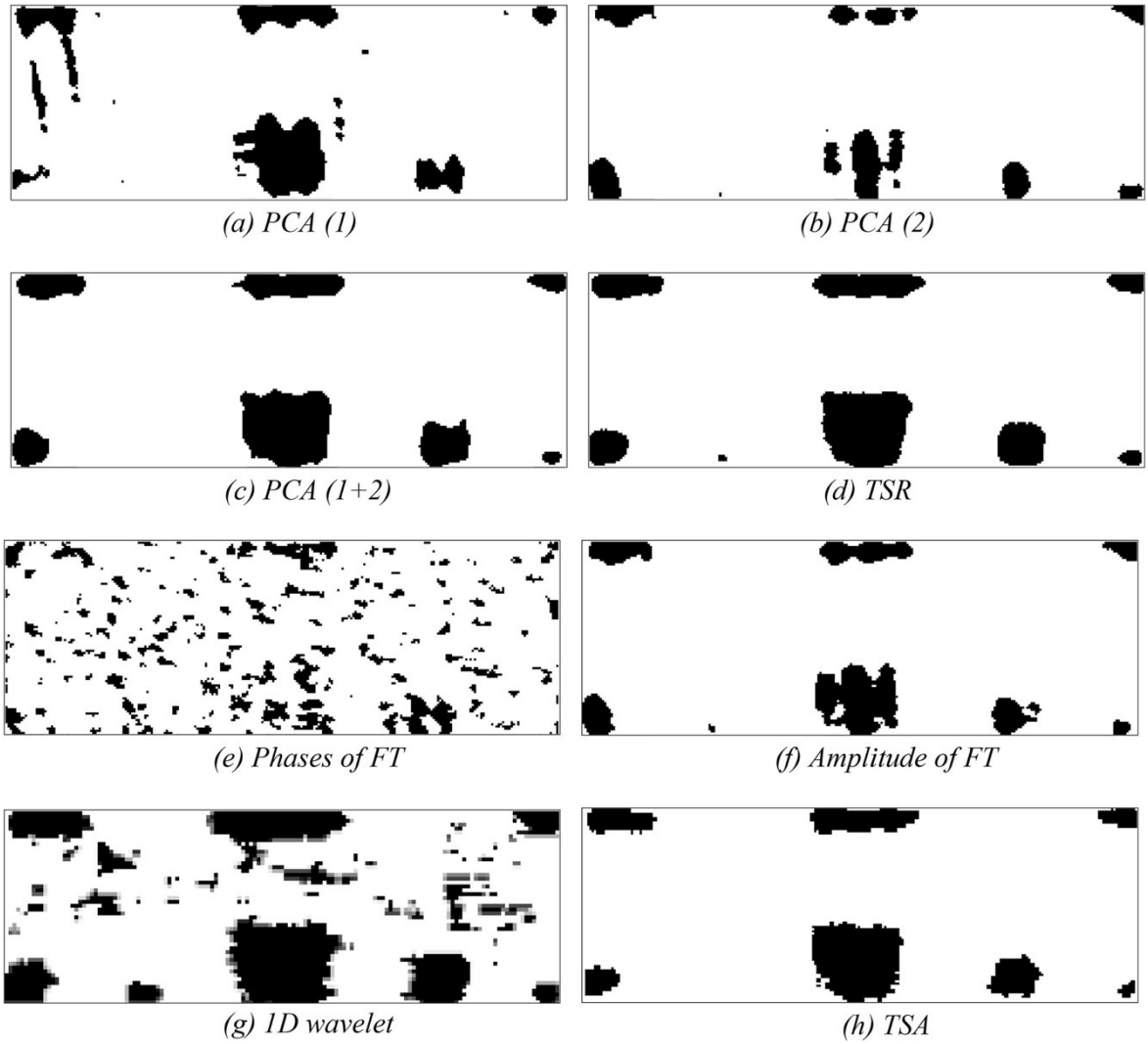

Figure 55. The binary results by local threshold value for (a) PCA (1), (b) PCA (2), (c) PCA (1 + 2), (d) TSR, (e) phases and (f) amplitude of Fourier transform, (g) 1D wavelets transform (approximation at level 3), and (h) TSA [140].

As discussed previously, despite the open issues about applications of active thermography on thin welded joints, several research works are present in the literature that explore the possibility of developing this technique to improve the use of thin welded joints.

Srajbr et al. [141] presented a work in which three different welded joints have been realized by different welding process: two by MAG process and the last by laser powder bed fusion (LPBF). For each one of these specimens some reference methods have been considered among the usual NDT resumed in **Table *2***.

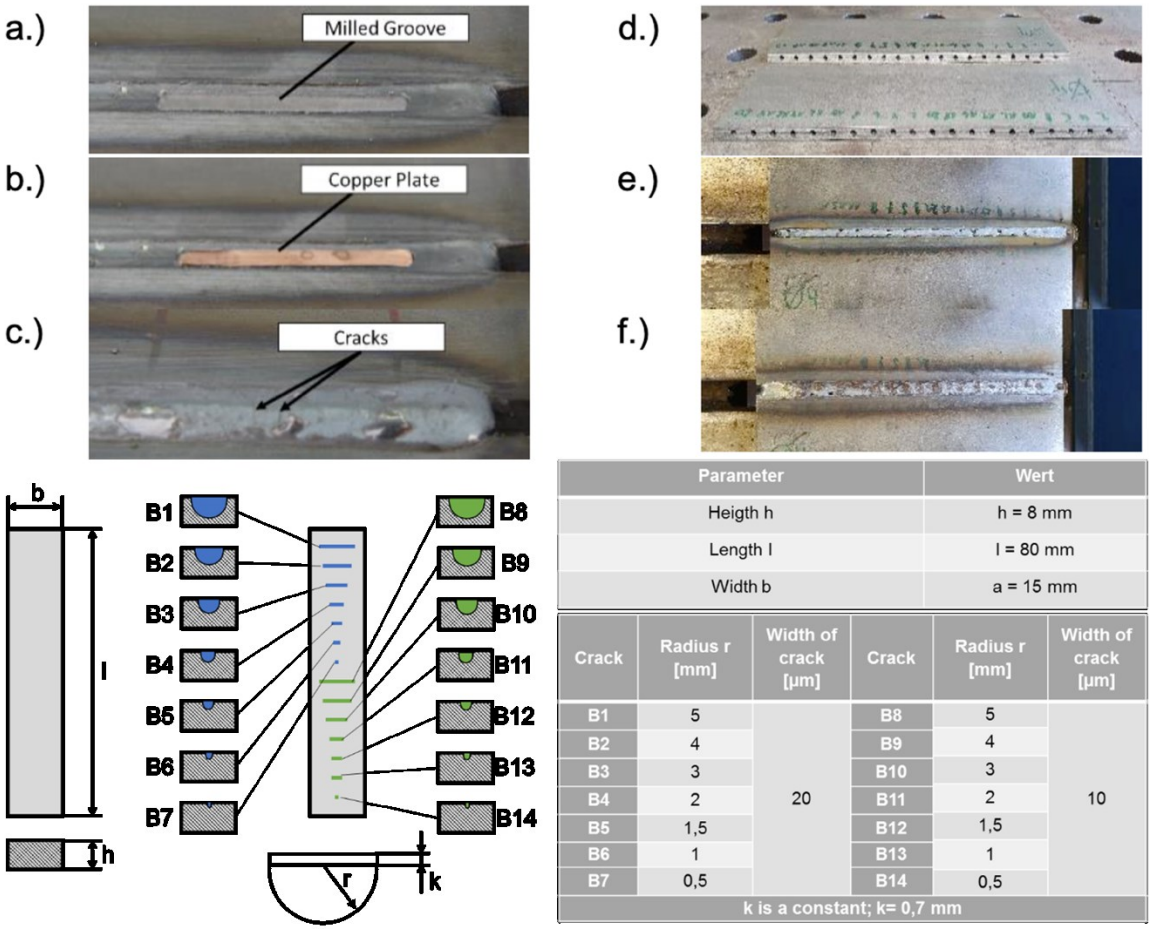

Parameter	Wert
Heigth h	h = 8 mm
Length l	l = 80 mm
Width b	a = 15 mm

Crack	Radius r [mm]	Width of crack [µm]	Crack	Radius r [mm]	Width of crack [µm]
B1	5	20	B8	5	10
B2	4		B9	4	
B3	3		B10	3	
B4	2		B11	2	
B5	1,5		B12	1,5	
B6	1		B13	1	
B7	0,5		B14	0,5	
k is a constant; k= 0,7 mm					

Figure 56. Tested specimens with irregularities and process steps necessary for fabrication – a.)-c.): Manufacturing of Specimen 1 (a.) Mechanical pre-treatment by milling, b.) Insertion of copper plate and c.) Resulting cracks); d.)-f.):Manufacturing of Specimen 2 (a.) Drilled holes, b.) welding of intermediate layer and c.) Welding of top layer. Below the Definition of parameters and nominal crack sizes for Specimen 3 [141].

Specimen number	Manufacturing method	Defects	Reference measurements
1	MAG	Cracks (realistic)	VT, PT, MT, RT
2	MAG	Voids (realistic and artificial)	VT, PT, MT, RT
3	LPBF	Cracks (idealized)	CT-measurements

Table 2. Specimen with different defects and NDT-techniques to detects the defects [141]

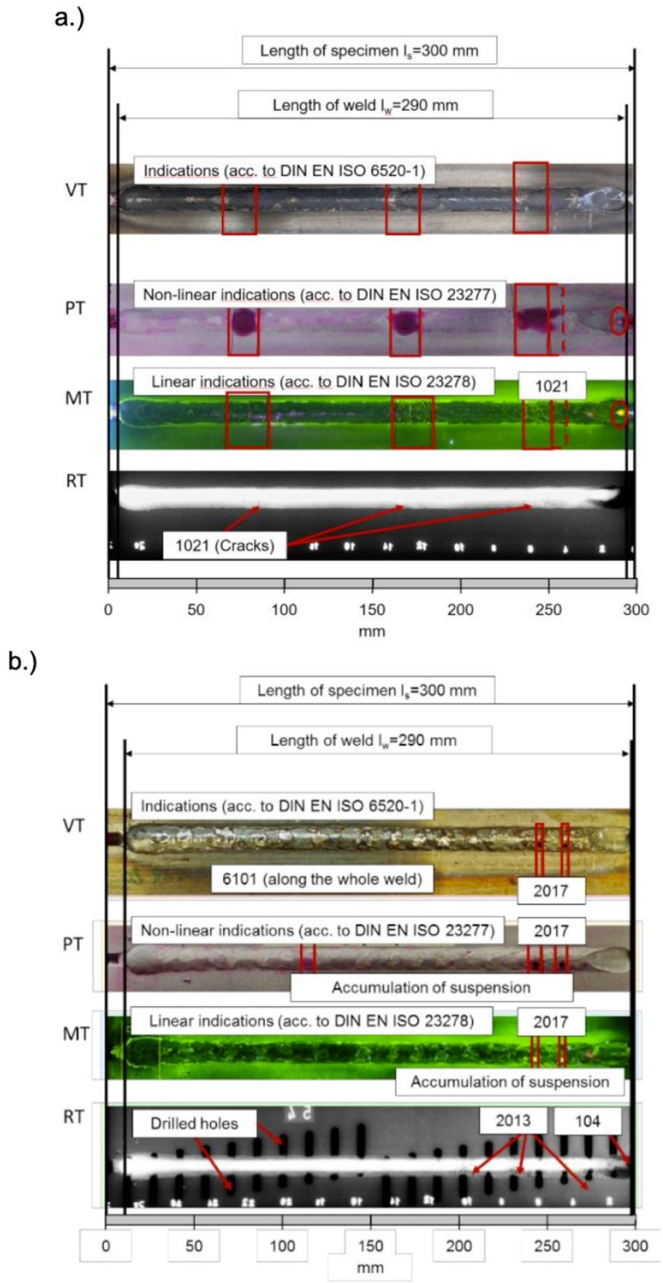

Figure 57. Results of reference measurements - a.) Specimen 1 with cracks and b.) Specimen 2 with inner defects [141].

The photographs in **Figure *57*** illustrate various testing methods, which reveal the presence of several different types of defects in the specimens. Specifically, specimen 1 exhibits predominantly crack-like defects, while specimen 2 exhibits predominantly internal defects.

The visual inspection of specimen 1 (**Figure *57*** a), reveals differences in surface appearance across three areas where copper was applied and the presence of larger cracks on the surface. This is further corroborated by the results of penetrant testing and magnetic

particle testing, which show large colored areas and vertical cracks, respectively. Radiographic testing also confirms the presence of cracks; however, no further inner defects are visible on the radiographic image.

In contrast, the visual inspection of specimen 2 (**Figure *57*** b), reveals discolouration along the entire weld and two surface voids. These voids are also visible in penetrant and magnetic particle testing results. Radiographic testing of specimen 2 shows clusters of pores at the end of the weld, indicating the presence of internal defects. Additionally, the radiographic image reveals the presence of artificially introduced defects in the form of drilled holes, which cannot be detected from the outside. These defects can be used to evaluate the ability of thermographic testing to detect inner defects.

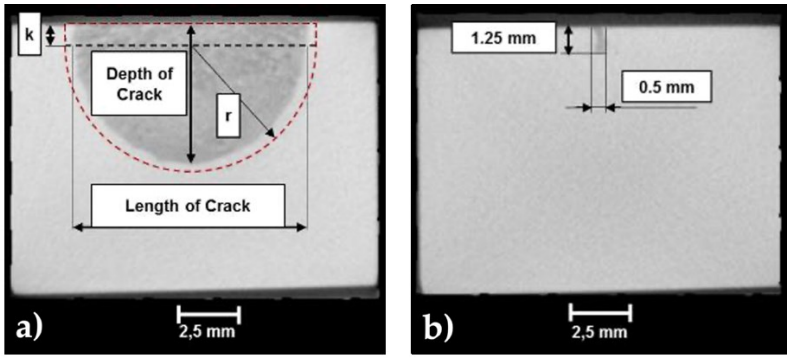

Figure 58. Computer tomographic images of the semi-circular crack structures – a.) Illustration for the determination of the parameters crack depth and crack width using the example of irregularity B8 and b.) illustration of the crack structure and determination of the geometric parameters of irregularity B14 [141]

Computer tomographic measurements were conducted on specimen 3 to evaluate the presence and characteristics of cracks. **Figure *58*** presents examples of the results of these CT scans, including the most extended crack (B8) with a nominal length of 10 mm and the parameters used to describe its contour, as well as the slightest irregularity and sample measurements of its length and depth.

For each specimen, a different thermographic technique has been used and are resumed in **Table *3***.

Specimen number	Manufacturing method	Defects	Reference measurements
1	MAG	Cracks (realistic)	Induction excited pulse-phase thermography, Ultrasonic excited thermography
2	MAG	Voids (realistic and artificial)	Induction excited pulse-phase thermography
3	LPBF	Cracks (idealized)	Laser-excited thermography

Table 3. Specimen with different defects and applied thermographic methods [141]

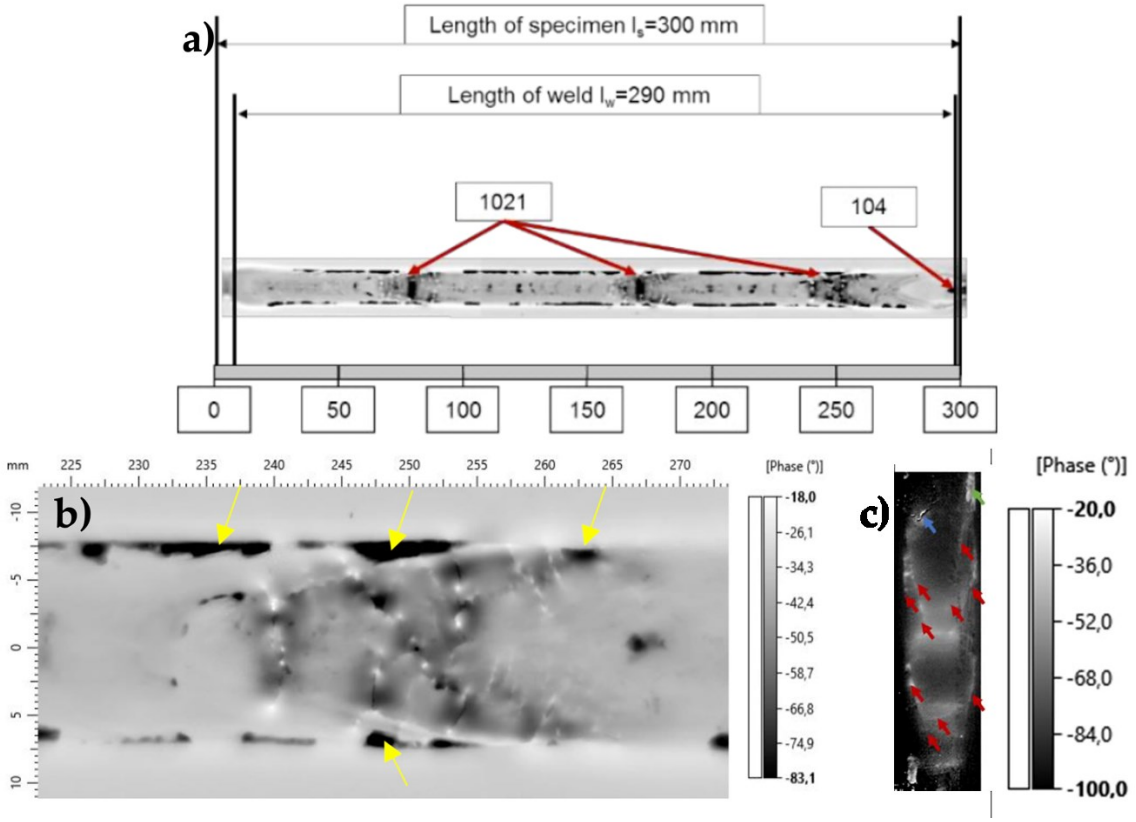

Figure 59. Results of induction excited pulse-phase thermography – a.) Overview of test of the whole weld and b.) enlarged picture of area with cracks. (c) Exemplary results of crack testing on a sample with cracked areas using ultrasound-excited lockin thermography [141]

Figure 59 a shows the results of inductive pulse-phase thermography on specimen 1. The phase image, obtained at a frequency of 5 Hz, reveals clear crack indicators as deviations from the surrounding weld. These indicators appear as white lines crossing areas of the lower phase and are visible in the enlarged image (**Figure 59** b). The cracks are easily identifiable as they stand out significantly from the rest of the weld. It is worth noting that only transverse cracks are visible in the images.

In contrast, longitudinal cracks are not excited by the used test arrangement. In addition to the crack indicators, the images also show black areas, such as those marked with a yellow arrow. These silicate residues from the filler metal used in welding do not represent any relevant flaw [141].

Figure 59 c presents the measurement results using ultrasound-excited lock-in thermography on an area with cracks. This method involves modulating the excitation frequency and power of the ultrasound excitation sinusoidally and applying a discrete

Fourier transform (DFT) to obtain amplitude and phase maps. The phase map shows that the crack contours appear as bright areas (indicated by red arrows). In addition, the image reveals measurement disturbances caused by moving particles on the component's surface (indicated by a blue arrow) and highly reflective areas (indicated by a green arrow). These disturbances are likely due to the high mechanical load on the sample, which causes slag residues and silicate particles to be dislodged and interfere with the measurement. Despite these disturbances, the technique demonstrates its ability to detect cracks in welds [141].

Figure 60 presents the test results for specimen 2, which reveal both artificially introduced defects (drilled holes) and realistic defects (cluster of pores). Both types of inhomogeneities cause an accumulation of heat, as the flow of heat into the sample's interior is hindered. This is indicated by a shift in the phases to lower values. As a result, the fields of pores near the surface can be easily identified. In contrast, the deeper-lying artificial defects are only hinted but can be detected by applying a measuring field and averaging the measured values, as demonstrated in the enlarged section. The resulting diagram clearly shows the individual holes [141].

Exemplary test results obtained through laser excitation of specimen 3 are presented below. The laser had a pulse duration of 0.1 s and a nominal power equivalent to 22.5 W. The measurement results were then processed using a discrete Fourier transform with an evaluation frequency of 1.5 Hz. **Figure *61*** shows the results in the phase representation. As shown in the images, all artificially introduced, idealized cracks are detectable. However, the signature of the cracks decreases in strength as the size of the irregularities decreases. While large cracks (e.g., B8) produce a clear and distinct signature, the measurement signal for small cracks (e.g., B14) is very faint.

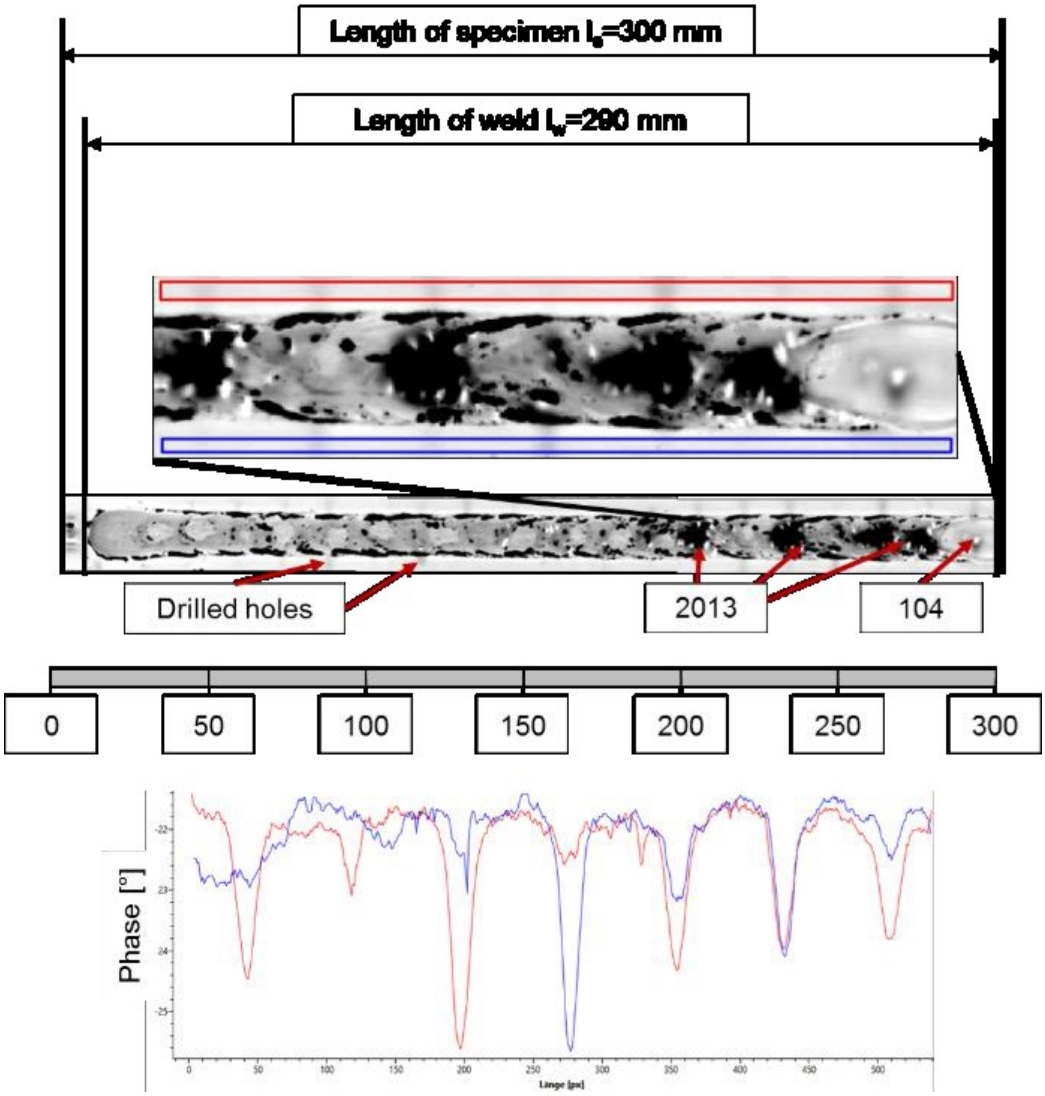

Figure 60. Test result of induction excited pulse phase [141]

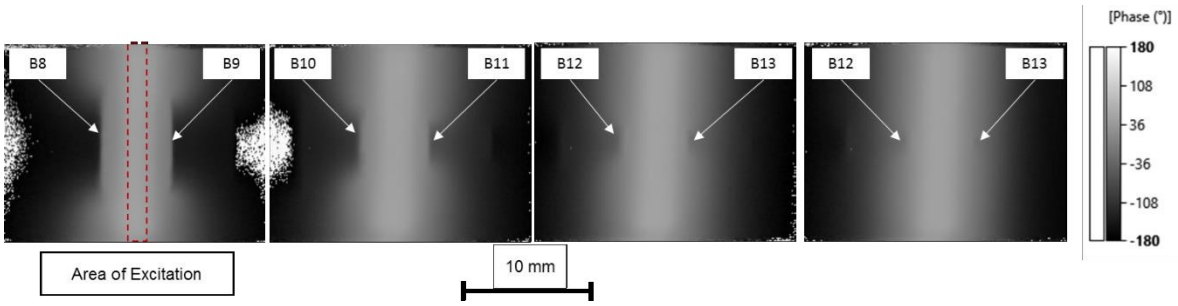

Figure 61. Results of laser heated thermography at Specimen 3 [141]

In the study [141] specific defects have been created specimens and the authors found that thermographic methods can effectively detect these defects. Of these methods, induction-excited pulse-phase thermography was particularly successful in detecting cracks. At the same time, ultrasonic excited thermography could detect lower-resolution cracks. Laser-

excited thermography was able to detect artificial cracks ranging from 0.7-0.8 mm, but further testing is needed to determine its effectiveness in detecting realistic defects. Overall, thermographic testing methods appear suitable for detecting weld cracks. However, their ability to detect inner defects is limited and depends on the excitation source. The promising results of induction excited thermography suggest that it may be a viable alternative for lower quality requirements, as only radiographic testing (RT) can detect such defects.

Another interesting method described by Guo [142], that applied vibrothermography to detect cracks in friction stir welded aluminium joints (**Figure *62***).

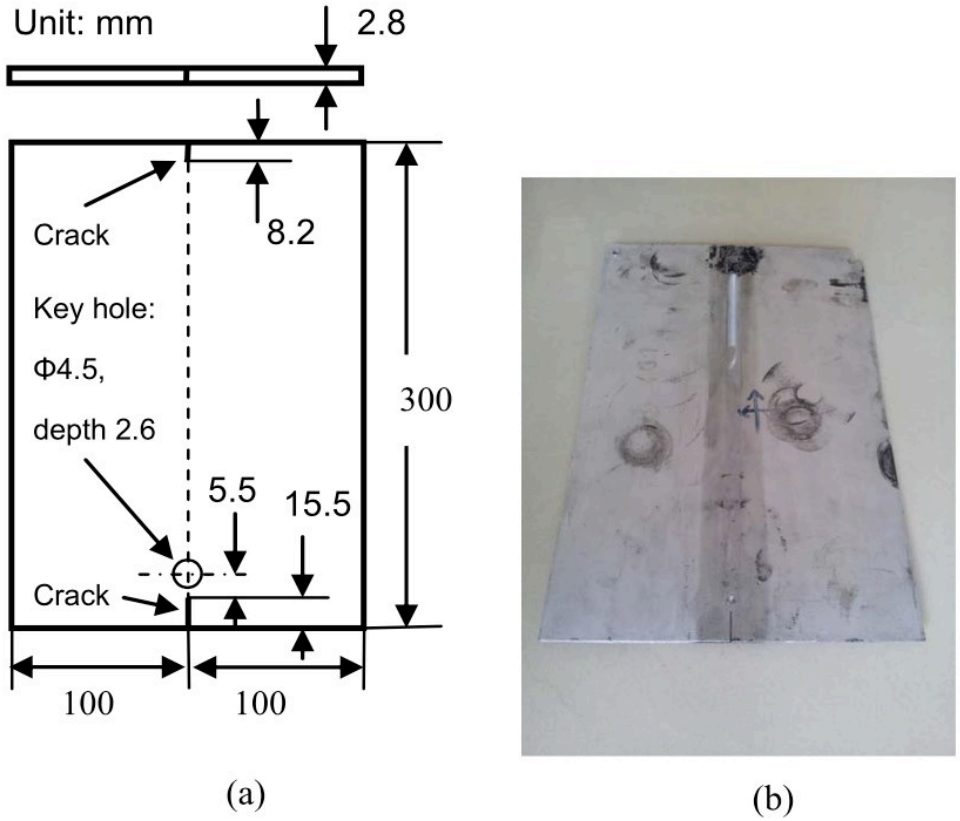

Figure 62. Aluminium alloy plates welded by friction stir welded joint. (a) scheme (b) specimen photo [142]

Three different reflection setups have been used for the described work, with two different positions of specimen, has showed in **Figure *63***

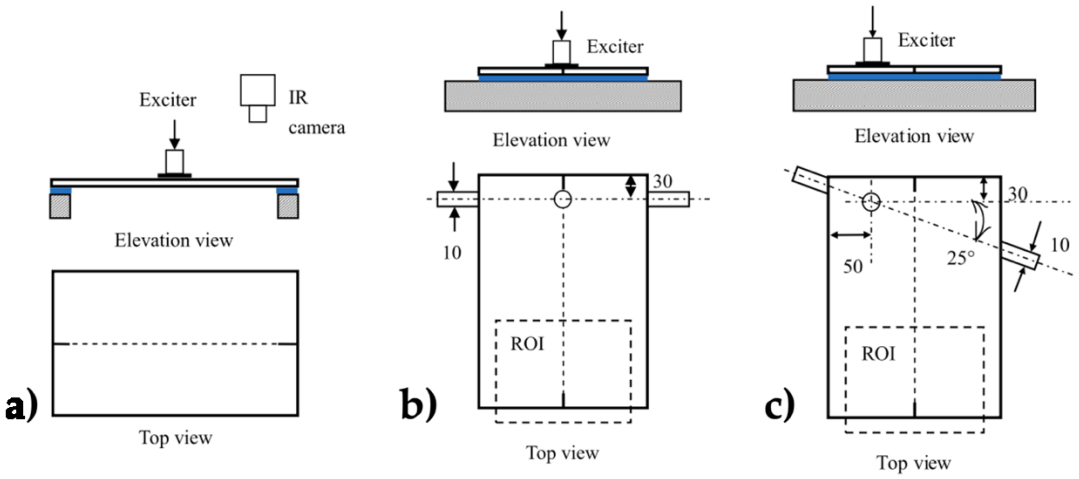

Figure 63. (a)First experimental setup, (b) the second and (c) the third one. [142]

In the first experiment, the plate was supported at both ends and excited at a middle position in the transverse direction, but no crack signatures were detected. In the second experiment, the plate was horizontally clamped in a cantilevered way and excited at one end, but no crack signatures were detected. In the third experiment, the plate was fixed in an unsymmetrical way, and this time crack signatures were detected at the tip and notch of the crack. The author [142], analyzed the resulting thermal images using various information parameters **Figure *64***, including signal-to-noise ratio (SNR) and contrast-to-noise ratio (CNR). They found that the third experiment produced the highest SNR and CNR values.

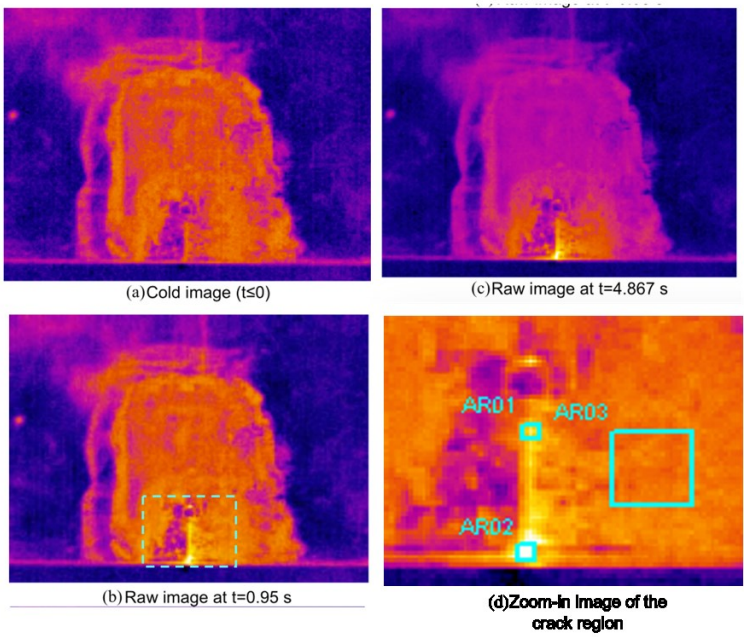

Figure 64. Vibtrothermography results. [142]

The author [142] also applied wavelet image enhancement to the thermal images to further improve the visibility of the crack signatures.

Runnemalm et al. [143] investigate the use of thermographic methods to analyze cracks in welded joints through UV excitation. Thermographic inspections using UV excitation were conducted on a laser-welded titanium plate with a butt weld of 3 mm thickness. The plate contained eight artificial surface defects, referred to as "surface notches," of various dimensions produced via electrical discharge machining in the weld seam and heat-affected zone. The lengths of the notches ranged from 250 to 1030 mm, and the widths ranged from 80 to 400 mm **Figure *65***.

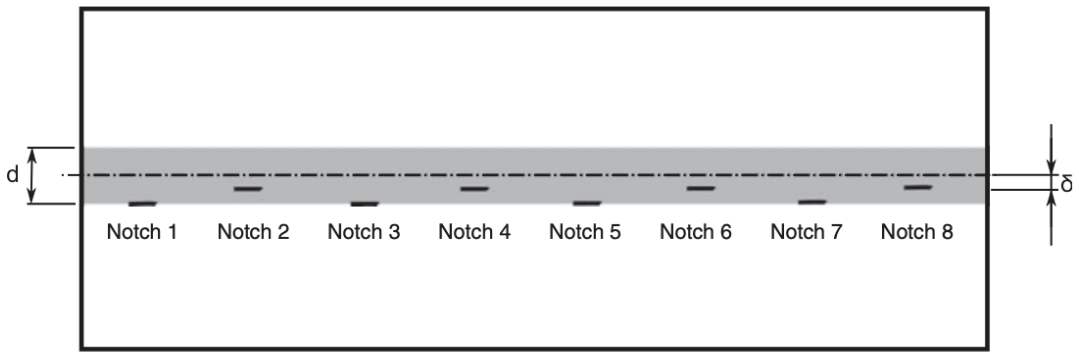

Figure 65. Scheme of the analyzed specimen. [143]

UV light from a mercury lamp was found to be a suitable excitation source for detecting surface defects in welds through thermography due to the reduction in the number of reflections on the surface compared to using a flash lamp excitation. While both excitation sources were comparable for relatively large defects, smaller defects (250 mm in length and 80 mm in width) were only detectable using a mercury lamp excitation. Data for the comparison were acquired 0.02 seconds after the start of illumination. Although a slightly higher signal-to-noise ratio was achieved after 0.25 seconds, the effect of heating from the mercury lamp appeared to reach a stable condition as the signal-to-noise ratio did not change for longer illumination times. Using a mercury lamp as the excitation source was found to provide fast data acquisition suitable for automated processes. The structure of the weld influenced the results, with notches located in the weld seam exhibiting lower signal-to-noise ratios than those located in the heat-affected zone [143].

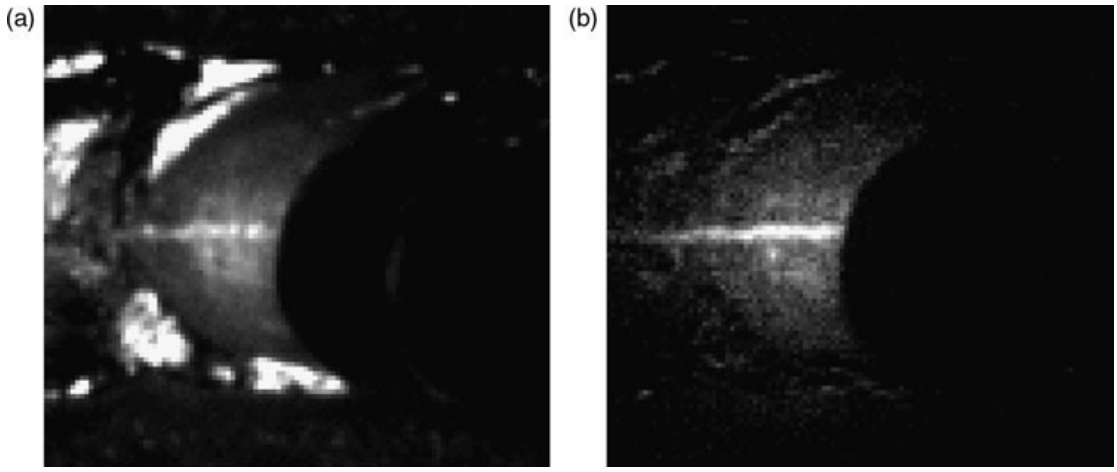

Figure 66. Example of Result of measurement of an MIG-welded steel plate with a long real crack in the weld. The width of the crack is 270 mm. (a) The raw data image captured 0.25 s after start of excitation. The crack is visible as a bright horisontal line in the middle of the image. (b) The raw data image after 0.25 s with the first image subtracted to reduce influence from surface variations. [143]

Further study is needed to determine the effects of surface roughness, weld geometry, and curvature on the results. Tests were performed to validate the method on two real cracks: a 270 mm wide MIG weld crack and a 10 mm wide, 820 mm long fatigue crack. The MIG weld crack was detectable in the raw data image. However, care must be taken to account for emissivity variations due to the MIG weld's surface structure. The fatigue crack was too narrow to be detected in a single image. However, the crack could be detected by studying the time derivative of the image sequence during UV light excitation. UV light sources, such as the mercury lamp used in this study, are commonly used in industrial nondestructive testing applications without operator restrictions. However, safety considerations must be considered during this method's implementation in an industrial setting.

As discussed previously, resistance welding is one of the main processes for welding two thin metal sheets together. In particular, one of the spreadly used in automotive industries is resistance spot welding. For the assessment of quality of these kinds of joints, there are two different control that can be done: on-line process control or NDT, as discussed before. In this regard, [144] presented a work about IR-based NDT for spot weld in automotive industries.

While IR thermography has been explored for offline, post-processing inspections in a laboratory setting, there have been no reports of online, real-time RSW inspection using IR thermography. Previous attempts at using IR thermography for NDT inspection in the automotive industry have been partially unsuccessful due to the requirement of treating the weld surface to eliminate reflections and environmental interference. This step is not

practical for high-volume production lines. The presented method [144] allows for real-time (during welding) and post-processing inspections (after welds have been completed).

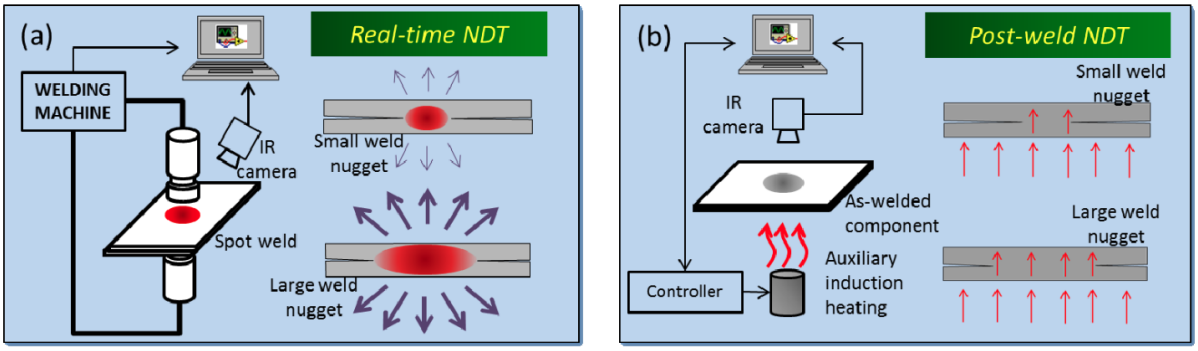

Figure 67. Scheme of setups adopted (a)on-line and (b) active thermography. [144]

A particular IR thermal image processing method was developed that utilizes relative IR intensity changes to reduce the impact of surface reflections and environmental interference. For post-processing inspections, a special induction heater was used in place of a flash lamp, resulting in temperature changes on the order of 10°C and significantly improving the signal-to-noise ratio without needing surface painting. Real-time inspections utilized the heat from the welding process (temperatures exceeding 1000°C). "Thermal features" were identified through computational modelling and testing that corresponded to different weld quality attributes.

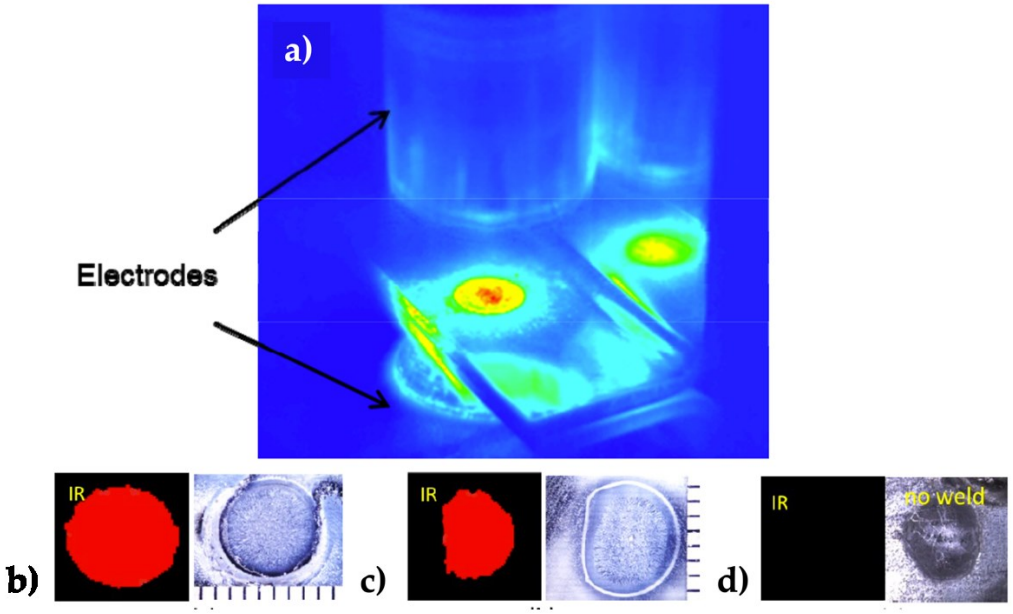

Figure 68. (a) Real-time IR image. B-c-d)Comparison of post-weld IR NDT measured weld nugget shape to the destructive cross-sectional measurements [144].

In 2016 Jonietz et al. [115], presented an exciting research work to determine the size of the melted area in friction spot welded joints, which is usually related to the quality of the final joint. Active thermography has been applied with two different setup configurations: in reflection and transmission mode and used as heating source flash lamps and laser squared shape heating.

One of the main advantages of the proposed method [115] is that, with both setup configurations, no paint on the surface to uniform emissivity is needed except for flash heating in reflection mode, contradicting results obtained by Runnemalm [145]. A normalization of thermal data has been proposed to avoid coated surfaces and is reported graphically in **Figure *69***.

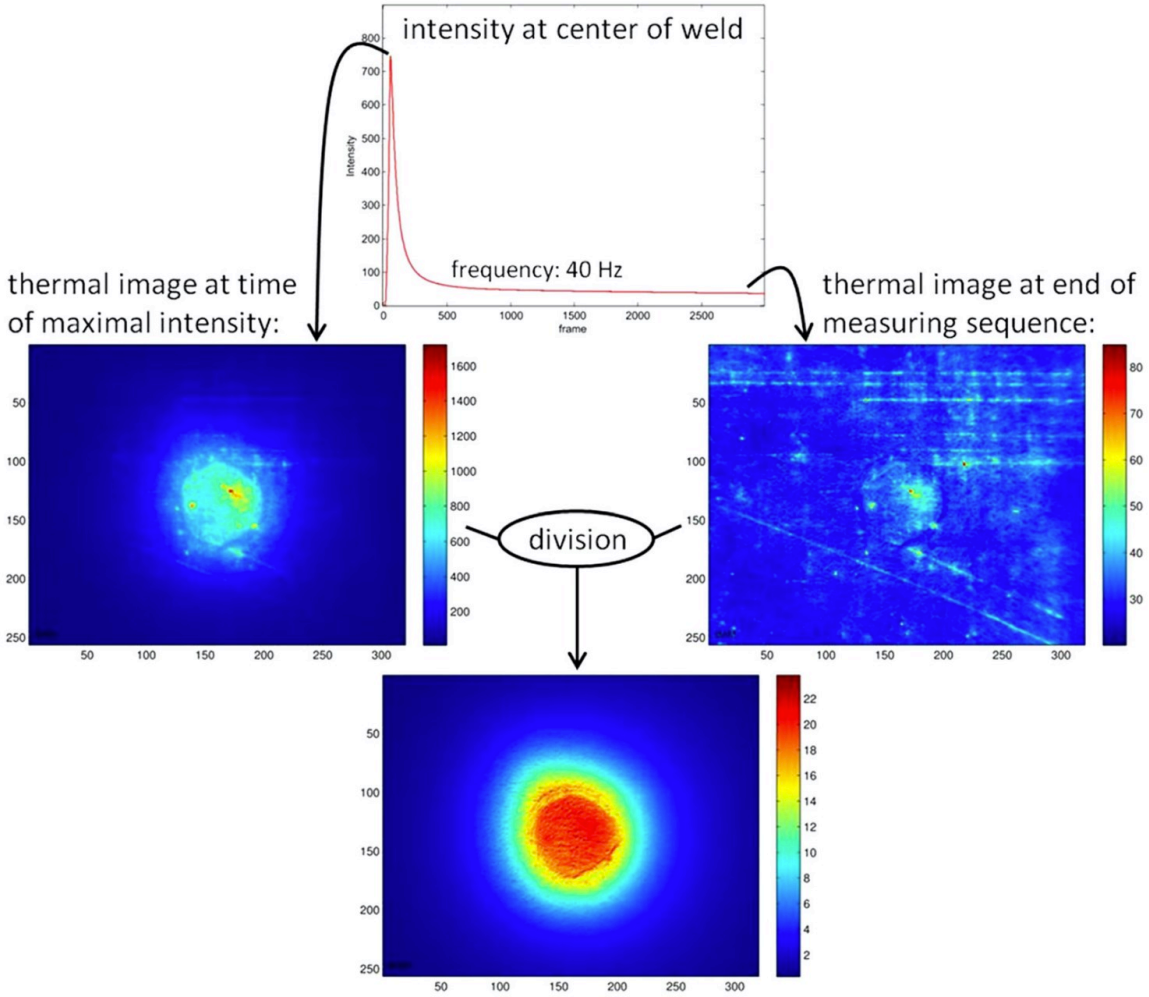

Figure 69. Normalization with transmission setup. Top Heat course at cen- ter of weld (digital camera-values). The frame rate was 40 Hz. Left Thermal image at time of maximal intensity after 1 s of heating with laser radiation. Right Thermal image after 75 s, taken as emissivity image. Bottom Division by the emissivity image delivers emissivity- corrected data [115]

The normalization method proposed is based on an intuitive, simple consideration: that after several instants after the end of the heating, it is possible to see the difference in signal on surface of the specimen that a variation of emissivity must cause because it is reasonable to consider the body temperature homogeneous. Hence, by dividing each frame (after cold frame subtraction) by one after the cooling phase, it is possible to reduce the influence of emissivity in maps **Figure *69*** and **Figure *70***.

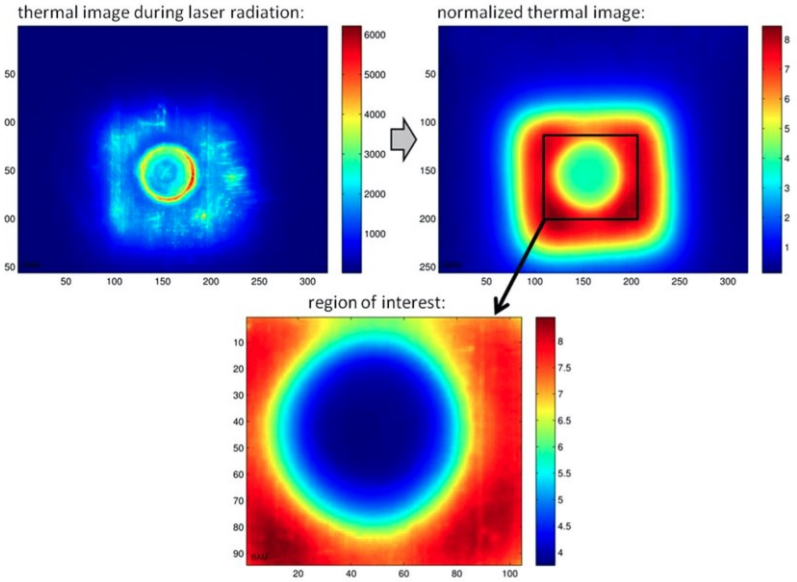

Figure 70. Normalization with reflection setup. Top left Thermal image with maximal intensity at end of laser radiation (digital camera-values). Top right Thermal image after normalization by emissivity image taken 2 s after stopping the laser radiation. Bottom Region of interest around spot weld for further data analysis [115].

Another significant difference is about the heating time used for each heat source. For flash, lamps are *~2 ms,* but for laser heat source until 1 s has been used; hence, in the first case, it could be correct to define it as pulsed thermography, but in the second one must be defined as long pulsed/stepped thermography.

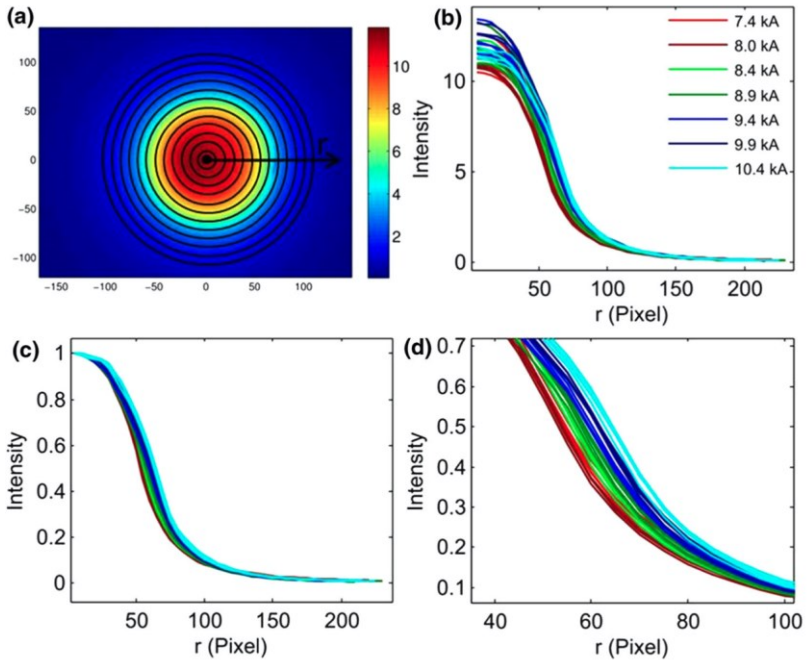

Figure 71. Transmission setup with laser. Data taken during laser radiation 0.7 s after switching on the laser. a Normalized thermal image of one sample with concentric rings. b Radial intensities of all samples, each color represents one welding current. c Radial intensities normalized at r = 0. d Detailed view of (c) (shoulders) [115].

In **Figure *71***, the intensity curves obtained for specimens with different welding parameters are presented and it is possible to observe that is a clear correlation among parameters and curves thus on the diameter of welded area (**Figure *72***)

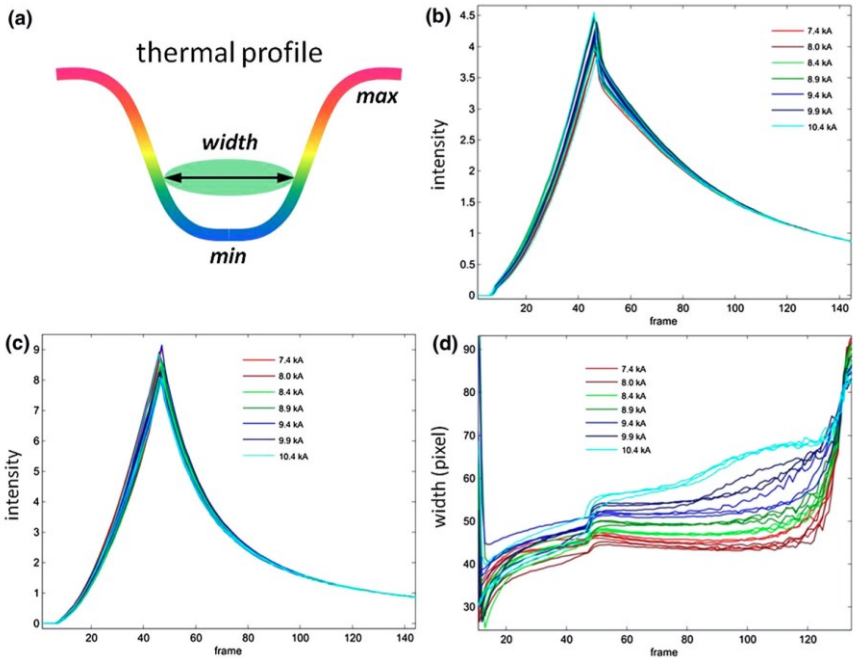

Figure 72. Reflection setup with laser. A) Definition of parameters for analysis of thermal profiles. B) Minima, c) maxima, and d) widths of the thermal profiles

Basing on a similar procedure, the same research activity has been persecute by Kastner et al. [119],with a classification of spot-welded joints using convolutional neural networks.

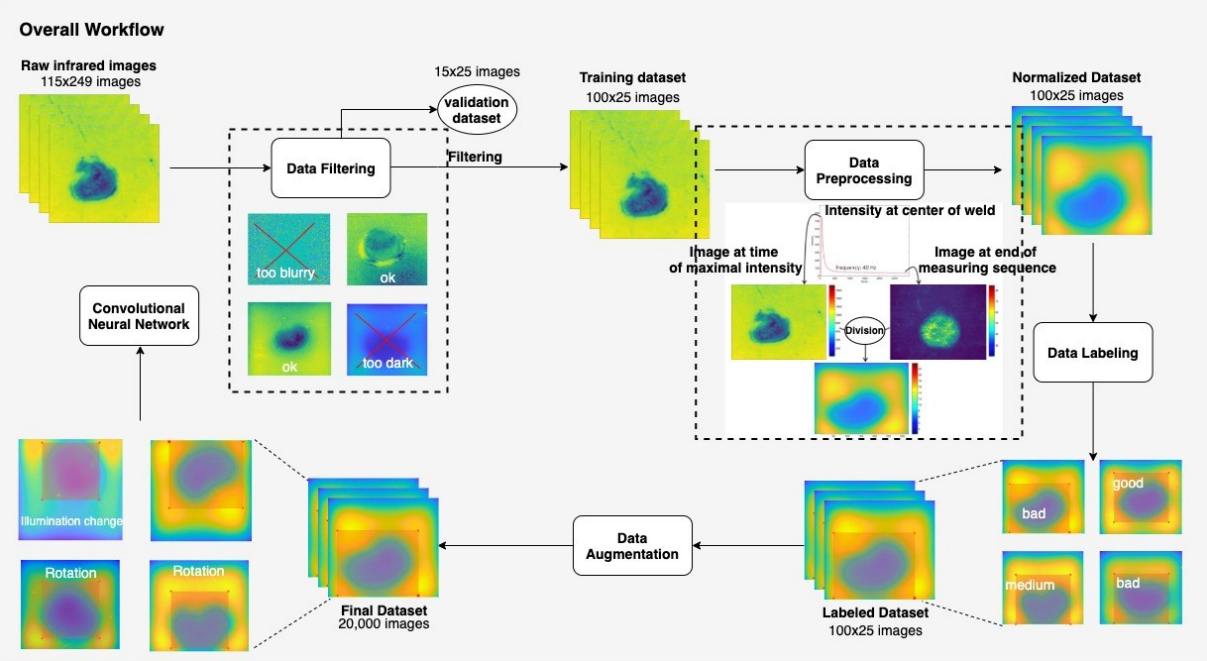

Figure 73. Overall workflow for research work by Kastner et al. [119].

As results, it has been possible to obtain a classification of quality of welded joints, considering three different quality classes [119] as showed in **Figure *74***.

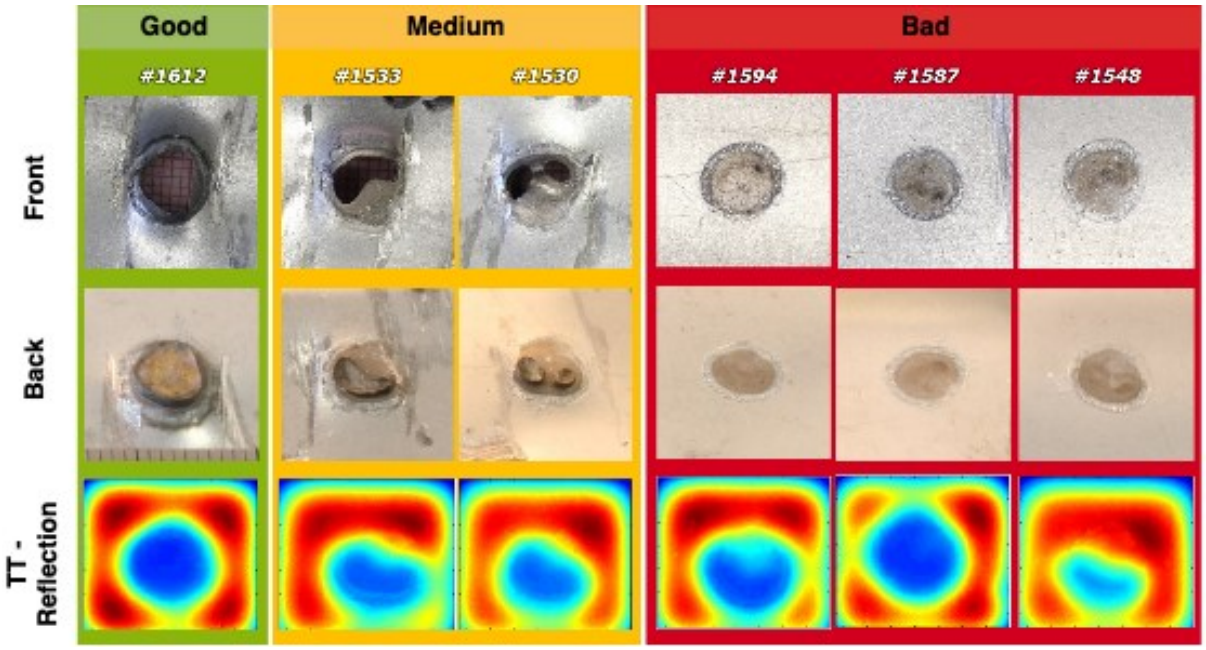

Figure 74. Classification of welding quality. Specimens for the three different quality classes are shown and their respective thermal image after preprocessing steps applied [119].

In 2019 Palumbo et al. [93] presented a thermographic procedure to assess the quality of RSW joints. In the research work, a transmission setup was used, and a flash lamp was used as a heating source. This method presents the same advantage presented in previous

one, which is the possibility to perform experimental tests on the surface as it is. Recording the heating and the consequent cooling phases in the centre of the spot after a fitting procedure, based on the time when the minimum value is achieved by the curve, has been possible to distinguish among three classes: stuck, good and over-welded as it is possible to see in **Figure *75***.

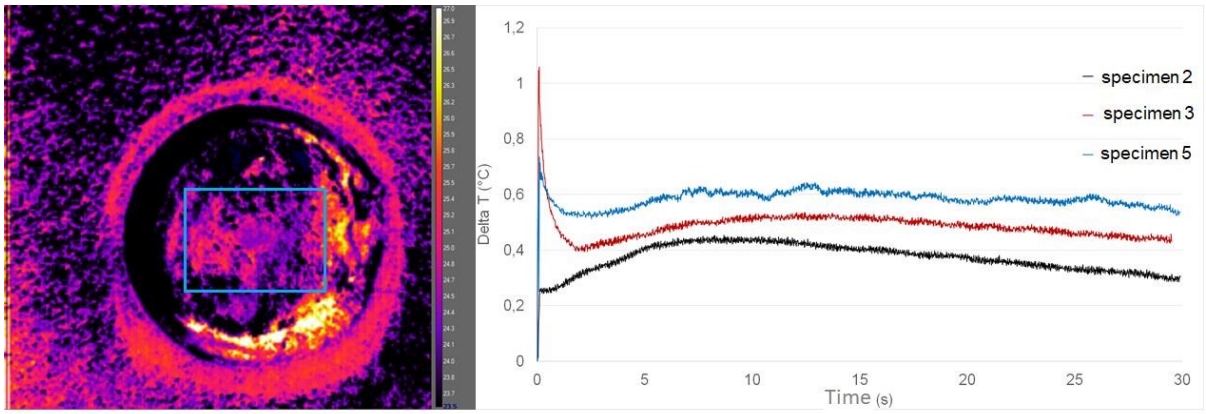

Figure 75. Comparison among the mean value of temperature over time for the three investigated specimens [93].

This method thus, provides to a qualitative evaluation of the quality of the joint and has been proved to be sensitive in changing of test parameters, better to the geometry of welded area, more than mechanical load tests that showed comparable values for ultimate load, for all theexaminated welded joined . The main disadvantage of this method is the transmission setup configuration that imposes to have access to both surfaces of joint.

Recently Verspeek et al. [146], presented another approach to the assess of quality for RSW. In this work [146], nine RSW joints have been inspected using halogen lamps, with modulated and pulsed heating, and induction heating as heating sources. After the heating, the FFT and SVD[147] have been used as analysis algorithms and the induction heating showed best results in term of quality of images and capability to discern a good welded joint (regular circle) from a not good ones (irregular circle). This method seems to be qualitative and no other considerations about the welding are possible but is very easy to automatize, especially reflection heating setup. An interesting result is that the shape of welded area can be a hint to discern between a good or not good RSW joint.

In the next section, two study cases have been reported which are based on another kind of resistance welded joint which is resistance projection welded joint. About this kind of joining process, only rare works are present and involves welding with circular embossing [148–150]. For the first time joints with rectangular embossing have been investigated

developing a procedure for quantitative evaluation of welded area, easy to automatize, applied on "as welded" surface conditions and with results comparable with well-established NDT methods.

3.2 Non-destructive evaluation of resistance projection welded joints (RPW) by flash thermography

3.2.1 Introduction

Resistance welding is widely used in automotive industries, in particular as joint in bodywork [74,76,78,81,83,85,91,93,151–159]. One of the crucial aspects related to the application of welded joints in industries is the possibility to assess their quality. Currently, the only techniques used for quality controls of joints is carried out by traditional destructive tests like Chisel or peeling tests (ISO10447). More important, nowadays, is the possibility to check the quality of welded joints by non-destructive methods. In fact, ultrasound tests (UT) are the most widespread for this kind of weld [57–63,77,82,84,90,92,160–170]. This non-destructive technique is well-established but, for this application, has limits: the control is based on a statistical approach, time-consuming tests, contact between specimens and probe is required, some difficulties with thin specimens may occur and the automatization can be expensive as discussed in previous section.

In the present case, specimens obtained by resistance projection welding process have analyzed. In resistance projection welding process, two plates are forced in contact between two electrodes, with a procedure comparable with RSW. The main difference with respect to the RSW process is that, in case of RPW, one plate has an embossing. This reduces the contact area and thus increases the electrical resistance. Consequently, the applied force during the welding can be reduced. Eventually, the required processing time is shorter in comparison to the traditional RSW. Moreover, localized heating is developed with a reduction of the heat-affected zone (HAZ) because higher temperature than in RSW is reached, but in a smallest area. In **Figure *76*** is reported a qualitative representation that shows the behavior of electric resistance and correspondent temperature distribution in RSW and RPW, where it is evident that the reduced contact area, in RPW, results in a high temperature in a small area, as opposed to the RSW process.

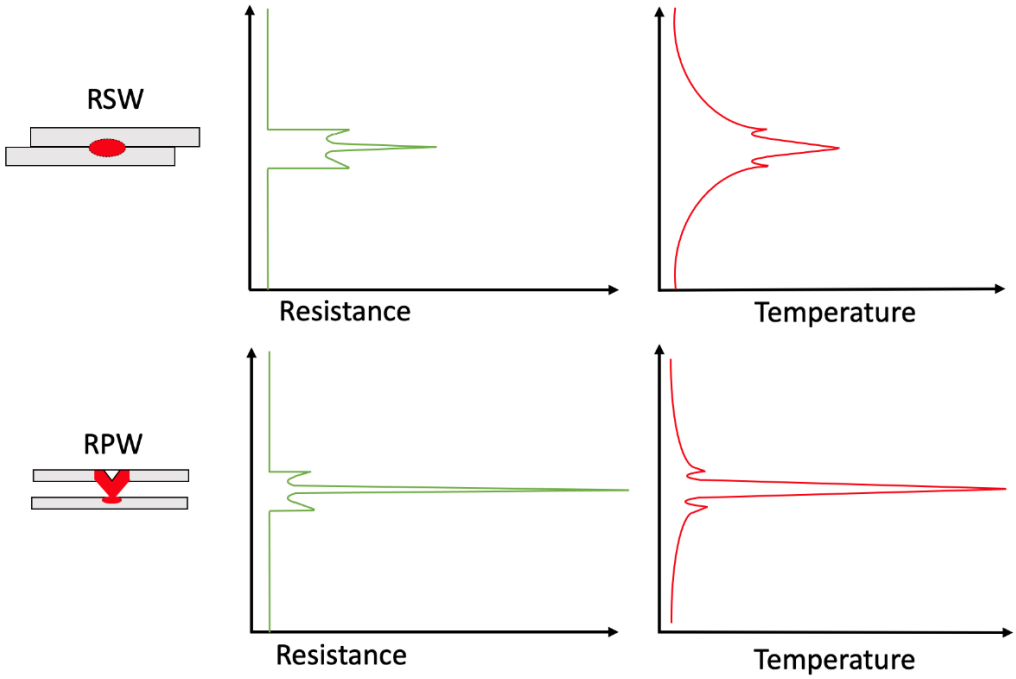

Figure 76. Scheme of difference between RSW joints and RPW joints. Green curves show the resistance as function of the distance from the contact area. Red curve shows the temperature distribution in depth direction during the welding process

Additionally, the RPW joints present a smooth surface on one side with no strongly visible signs of welding that makes it suitable for aesthetic applications. This is one of the biggest advantages of this process for automotive industries.

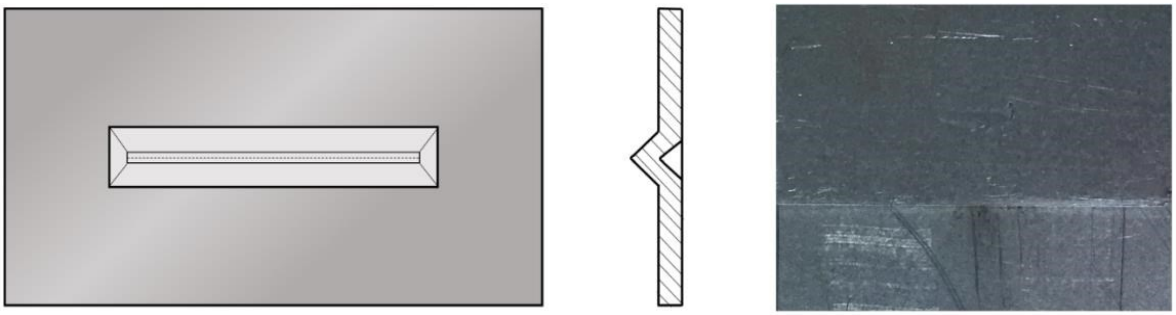

Figure 77. (a) Embossing geometry for the inspected RPW joints (b) Front surface of joints without paint.

In ***Figure 77,*** the investigated joints geometry, the rectangular shape of embossing and also the front side of the welded joint are shown. On the surface there are no scratches that, instead, are typically of RSW joints.

In the present step, the aim is to develop a thermographic NDT procedure to allow the quality inspection of RPW joints, in particular, to identify process welding parameters by pulsed thermography after the application of PPT algorithm [6,12,171–175]. This work is important for the future develop of automatized procedure for assessment of RPW and recognize a correlation between process parameters and thermographic features.

3.2.2 Material and methods

3.2.2.1 Specimens

The present case study investigated 12 welded joints with the same geometry. The specimen has the embossed plate made in FeP04 (0.67 mm) and the smooth plate in FeP05 (0.70 mm), joined by resistance projection welding. The rectangular emboss measures 9 mm x 1.2 mm, as shown in **Figure *78***.

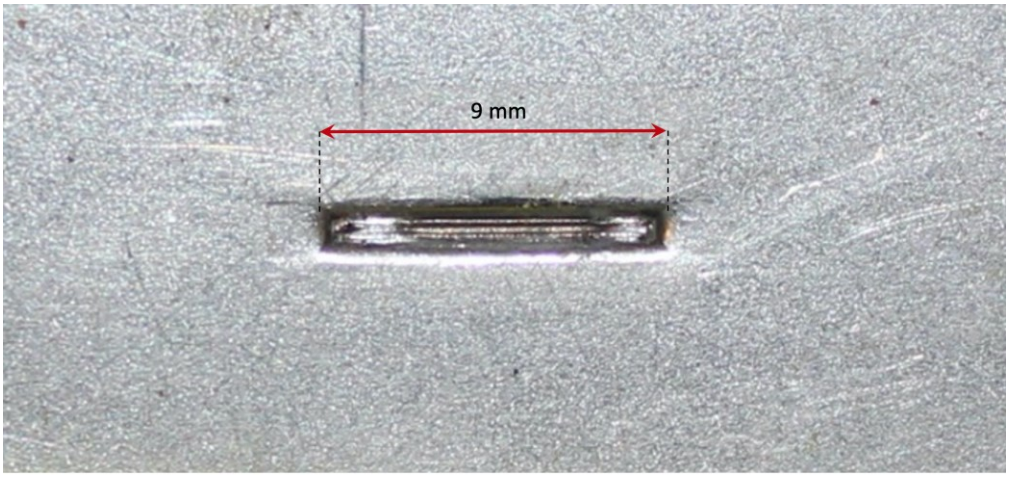

Figure 78. Picture of one of the embossing on the investigated specimens

To evaluate the simultaneous effects of the welding parameters on the joint and the interactions among them, a factorial plan has been used. The adopted design of experiment (DOE) technique allows us to save time and reduce the total number of experiments compared with the traditional procedure where the welding parameters are changed one by one. In the proposed DOE, three parameters change (F, I, t) with two levels for each for a sum of four combinations of parameters. Three replications for each set of parameters have been obtained to evaluate the repeatability of the process too, so the total number of specimens is 12 (**Table *4***).

Unlike RSW, where the surface of the welded joint has the same characteristics on both sides, in RPW, one of the plates is embossed, so it is possible to define the front and rear sides. The back side is where the embossed plate is the first, so the shape of the electrode is evident. The front side is the plate without embossing, and where the surface is completely smooth. This aspect is very important because, in the application of thermography to RSW joints, one of the critical aspects is the difference of emissivity in the welded spot that generates a difference in the signal recorded by the IR camera that does not correspond to a real difference of temperature, so it is necessary to compensate this phenomenon. Instead, in this kind of joints the front surface is smooth and does not

present strong inhomogeneities, which is one of the main advantages of this join technique avoiding aesthetic defects. A thin paint layer with highly known emissivity has been used to cover the specimen surfaces to avoid the influence of emissivity, the difference in absorbed energy and to reduce the reflectivity too. Another important advantage of the use of paint layer, is to increase the emissivity to a value ~95% resulting in a strong signal easier to detect by the IR camera, with lower noise influence.

ID	(I) Current [kA]	(F) Force [kN]	(t) Time [ms]	Replications
J1_DOE_1	15	1.4	10	3
J1_DOE_2	13	1.4	12	3
J1_DOE_3	13	1.6	10	3
J1_DOE_4	15	1.6	12	3

Table 4. Welding process parameters

3.2.2.2 Experimental Setup

The experimental set-up is showed in **Figure *79***. The reflection mode has been used because less space than the transmission mode is needed to fit and better reproduce an industrial application and because the front surface is smooth and guarantees uniform heat absorption. In fact, considered the geometry of inspected specimens, observe from the embossed side can give problems for interpretation of signal because the *"black body effect"* can influence the signal with a complex evaluation. On the other hands, observing the front surface in transmission mode, it can create an inhomogeneous absorption due to the embossing.

Figure 79. Experimental set-up in reflection configuration. **(a)** The front surface of specimen with black coating. **(b)** The back surface of specimen with embossing.

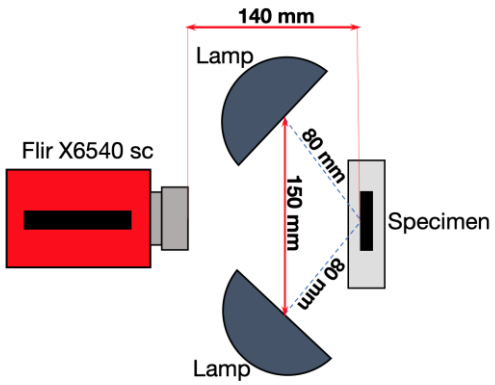

Figure 80. Schematic representation of experimental set-up used.

Two flash lamps (Hensel HP Pro 3000 J) have been used for the pulse heating with a pulse time duration of ~3 ms, which is a good approximation for an instantaneous excitation (Dirac pulse); 5 s after heating pulse have been recorded. As it is possible to see in the diagram of the experimental set-up in ***Figure 80***, the specimen is in the middle of two lamps and in front of the IR camera (FLIR X6540 sc), and the distance of 140 mm between the IR camera lens and the specimen was measured. To have a good spatial resolution, it is necessary to have more pixels as possible on the region of interest (ROI). It is good to put the IR camera closer as possible to the specimen, so a lens of 50 mm with a 12 mm extension ring has been used to have an mm/pixel ratio of 0.055 mm/pixel. On the other hand, to have a good time resolution and describe as well as possible phenomena, such as the cooling down of metal specimens after pulse heating, a high frame rate is needed. To achieve the frame rate of 910 Hz, a reduced acquisition window has been chosen (304 x 104 pixels) with an integration time of 0.5650 ms.

For controlling the thermal excitation and synchronizing it with the IR Camera, the PC, flash lamps and the IR camera have been connected to the MultiDES System®, as is showed in **Figure *81***.

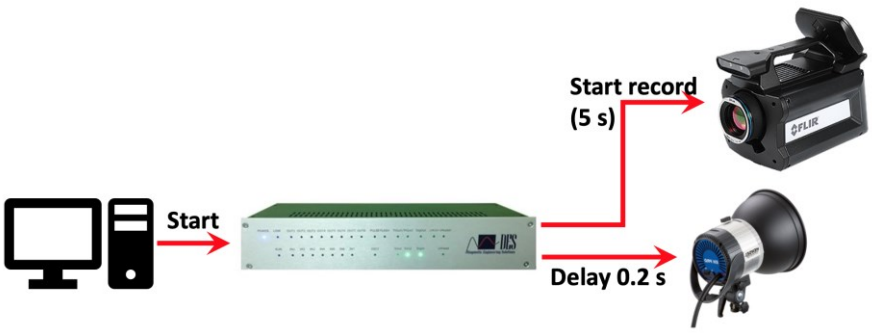

Figure 81. Scheme of system used for the experimental tests.

3.2.2.3 Methods

For each test, a thermographic sequence of 5 s has been recorded that can be represented by a 3D matrix (x, y, t). For all thermographic sequences, the same operations have been carried out. First, a cold frame was subtracted from all the sequences to reduce background noise and the influence of the reflection. Then, after the identification of saturated thermograms, the early recorded thermogram (ERT) was identified, and the time axis was shifted to have at time 0 the ERT; frames before ERT been neglected. The thermographic sequence is needed to define the last recorded thermogram (LRT) that is strictly related to which frequency is possible to have on the frequency axis (for phase and amplitude 3D matrix) and not only depends on the maximum depth that is needed to investigate. In fact, in the frequency domain, the maximum value of the frequency depends on the frame rate ($f_{max} = f_s/2$), but Δf depends on the number of elements between f_{min} and f_{max} that is $^{N}/_{2} + 1$, where $N = LRT - ERT$. For these reasons, it has been decided to use the same fixed number of thermograms in order to be able to have phase and amplitude 3D matrix with the same values of frequencies axis and to have the possibility to compare phase or amplitude maps at the same frequencies, therefore depth, for each test. Because of the characteristics of the fast Fourier transform (FFT) algorithm, $N = 4096$ algorithm, it has been chosen because if $N = 2^k$, $\mathcal{O}(N\log_2 N)$ operations are needed instead of $\mathcal{O}(N^2)$.

Using the MATLAB® software, the algorithm of PPT has been applied, providing two 3D matrices: one for amplitude and one for phase. Attention has been focused mainly on the phase matrix because reflection and inhomogeneous heating problems influence it less than the amplitude map.

In order to evaluate the quality of the joints, and then identify characteristics that are related to the process parameters, it was decided to analyze the trend of the phase signal along a profile passing through the center of the embossing, then the welding. The profile has been selected starting to the rear side where the embossing is clearly visible, considering a line ~12 mm long, passing through the center of the embossing (9 mm long), as shown in the **Figure *82***. To reduce the noise of the signal, an average among 3 lines for 216 pixels has been considered: the pixel array passing through the center of the embossing and the pixel arrays just above and just below. The value of the first element of the array has been subtracted to all other values of the array, for each phase profile extracted. This procedure allows us to have for all profiles *"0"* as the first value and the comparison among results.

To carry out the analysis of the factorial plan by ANOVA, it is needed to identify "features" that will permit to quantify the difference among the phase profiles. Two features have been extracted from the phase profile: the minimum value of phase and the slope of profile in the first part, as it is possible to see in **Figure *83***. A second-order polynomial fitting has been applied to obtain the value of minimum in the profile. In particular, about 70 data have been considered for each profile. From the polynomial equation, the value of the minimum has been calculated. For the second feature, 30 pixels (from 37 to 67) have been considered and a first-order polynomial and the value of angular coefficient has been used as the second feature to quantify the slope of that part of phase profile.

The ANOVA has been performed to investigate the dependence among the features and the welding process parameters since in this way, it is possible to understand if the difference among the value of features can be attributed to the difference of welding parameters or not.

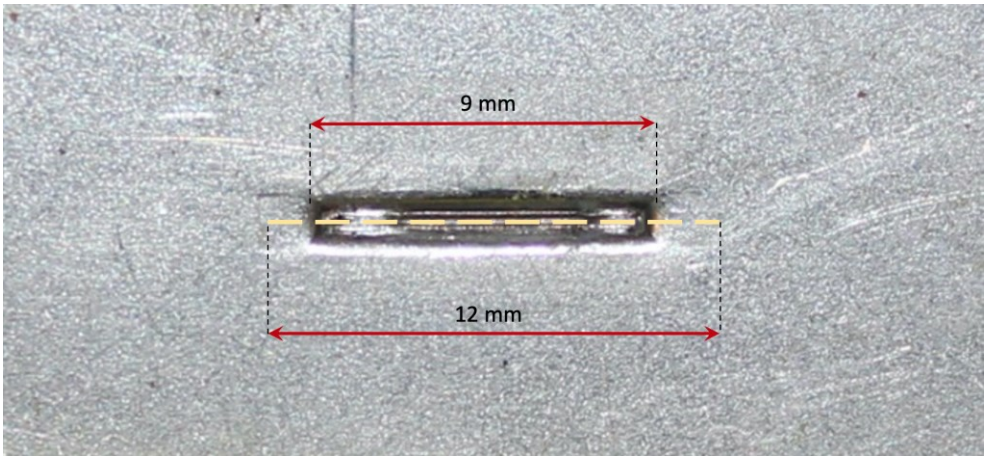

Figure 82. In yellow it is represented the line considered for the profile selection with length 12 mm.

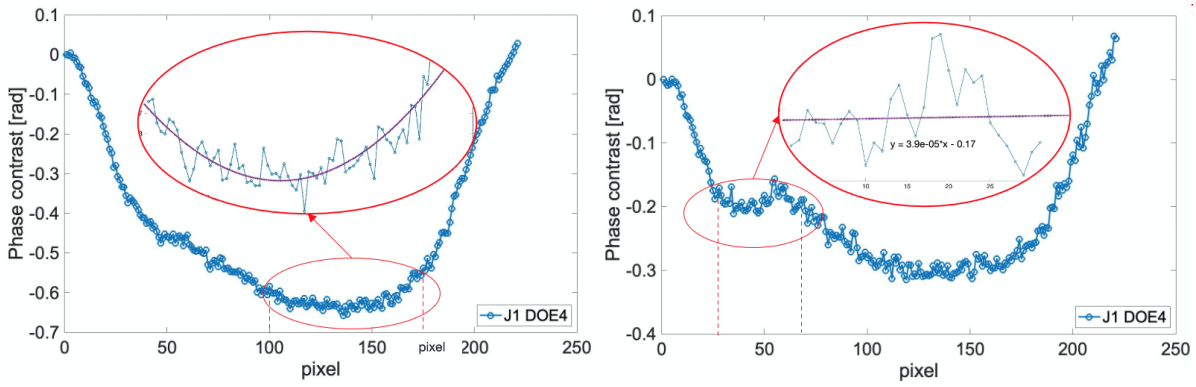

Figure 83. In the pictures it is showed the features selection. To the **(a)** Phase profile for f=0.444 Hz and the selection of minimum between pixels 100 and 170. **(b)** Phase profile for f=4.884 Hz and selection of value of slope between pixels 37 and 67.

3.2.3 Results and discussion

Thermographic results do not show a symmetric thermal map along the weld from left to right, **Figure *84***. In fact, immediately, by thermographic images, it is possible to see that the signal in the left part of thermogram is different from the right side. Observing the welding from the rear side, it is possible to see that the embossed plate is not perfectly symmetric, and this could be caused by not perfect contact between the smooth plate and embossed part and for a non-homogeneous distribution of force for all the length of embossing. It is reasonable to think that, during the process, the heat follows the current flow that starts to go through the plate from the part of embossing in contact and in the part of the surface with a minimum radius of curvature.

As written above in section 2.2, the thermographic sequence has been post-processed by the PPT algorithm, especially to reduce the noise that is present in the thermal image, as it is shown in **Figure *84***. In fact, in **Figure *84(a),*** there is a thermal image after the cold frame subtraction, and it is possible to see that the signal is noisy, and some paint spots are visible as hot spots.

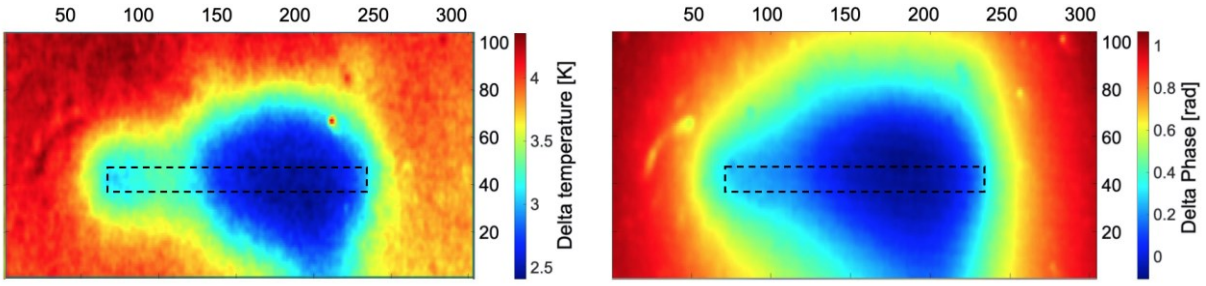

Figure 84. Thermal image for the DOE_1_A at t=27.5 ms after the ERT. (b) after the application of PPT algorithm, phase image for f=0.444 Hz for DOE_1_A.

In **Figure *84*** is possible to see a phase map that corresponds at the same test showed in **Figure *84 (a)*** but, the phase image is sharper than the thermal one, less noisy and that the hot spot is not visible. The reason why the hot spot disappears is that the phase image in **Figure *84 (b)*** corresponds to a low frequency, then to a high depth section; in addition, usually, the phase map obtained by PPT is lower influenced by non-uniform heating [12,173,176] and for this motivation is used more than amplitude data.

For the first 25 frequencies (from 0.444 Hz to 10.108 Hz), as described in section 3.2.2.3, phase profiles have been considered and four of them are shown in **Figure *85(a)***, each one correspondent to a different set of welding parameters (F, I, t) for the frequency 0.444 Hz. It is possible to see in **Figure *85*** that the profiles have the same behaviour but there is a

shift among the curves and the difference among the value of an absolute minimum of the profile curve, can be used to distinguish curves, then welding parameters. In **Figure *85(b)*** are shown four profiles but for a higher frequency of 4.884 Hz, that means closer to the surface than the profiles in **Figure *85 (a)***. For the high frequency, the value of the minimum of the curve, that for low frequencies shows the difference among different specimens, has no relevant difference but, the behaviour of the profiles is different, especially in the first part of profile where the profiles seem to have 2 different behaviours: DOE_1 and DOE_2 shows a different slope from DOE_3 and DOE_4.

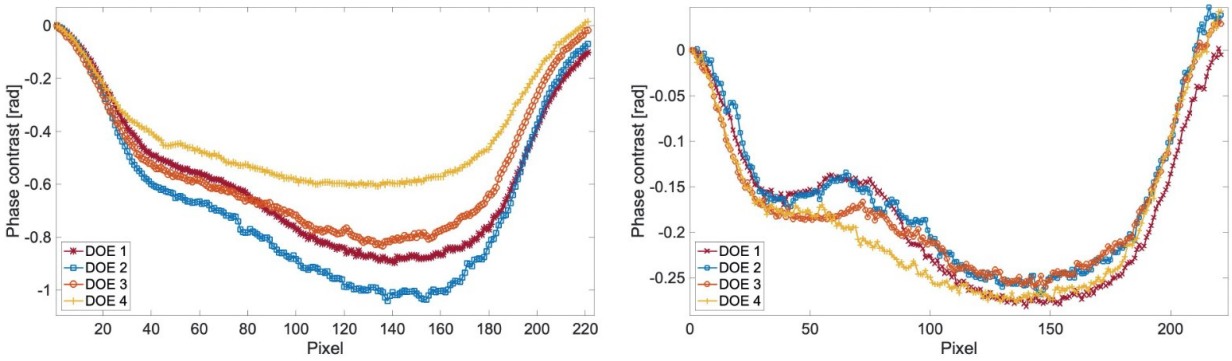

Figure 85. (a) Phase profile for different DOE at f=0.444 Hz. (b) Phase profile for different DOE at f=4.884 Hz.

The values of minimum (P_1) have been assessed for the first 25 frequencies between pixel 100 and 170, while the slope values (P_2) between pixel 37 and 67, as described in section 3.3. For each frequency, the ANOVA was performed for both indexes P_1 and P_2 and the confidence level was fixed to 95%. In **Table *5***, the values of P1 and P2 for each specimen, for the most significant frequencies, are reported. These two frequencies (0.444 Hz and 4.884 Hz) were chosen because they are the two frequencies for which the parameters investigated showed higher significance, therefore P-value lower. The Pareto diagrams in **Figure *86(a)*** shows at frequency 0.444 Hz that the value of P_1 is influenced by the force (F) and the current (I) but only for low frequencies; in fact, results show no significance for higher frequencies. In **Figure *86(b),*** the Pareto diagram for high frequency has been reported: it shows that the value of P_2, that for lower frequency has no dependence on welding parameters, at high frequencies depends on the value of the force. It is interesting that that dependence of P_2 from F starts to be significative from frequency *f=5.332 Hz* until frequency *f=10.220 Hz*, and this could be useful for optimization of PPT parameters. There is no parameter that shows a dependence from *t* but does not mean that there is not. In fact, in developing a factorial plan, it is very important the choice of values used for the two levels of parameters, because, if the values are very close could be possible that the

influence on the process it is not strong enough to be detected. The values of time in welding parameters are 10 ms and 12 ms, which are very close, but the confirmation of this hypothesis will be possible only after comparison with destructive standard testing.

Sample	Current (kA)	Force (kN)	Time (ms)	Min at 0.444 Hz	Slope at 0.444 Hz	Min at 4.884 Hz	Slope at 0.444 Hz
J1_DOE_1_A	15	1.4	10	-0.891	-33.03 E-04	-0.306	11.08 E-04
J1_DOE_1_B	15	1.4	10	-0.735	-28.02 E-04	-0.262	9.616 E-04
J1_DOE_1_C	15	1.4	10	-0.696	-29.19 E-04	-0.263	6.571 E-04
J1_DOE_2_A	13	1.4	12	-0.900	-34.13 E-04	-0.268	1.681 E-04
J1_DOE_2_B	13	1.4	12	-0.881	-26.34 E-04	-0.218	7.228 E-04
J1_DOE_2_C	13	1.4	12	-0.788	-11.26 E-04	-0.287	22.68 E-04
J1_DOE_3_A	13	1.6	10	-0.766	-29.09 E-04	-0.313	-1.878 E-04
J1_DOE_3_B	13	1.6	10	-0.687	-25.56 E-04	-0.210	4.038 E-04
J1_DOE_3_C	13	1.6	10	-0.645	-23.34 E-04	-0.239	-0.620 E-04
J1_DOE_4_A	15	1.6	12	-0.544	-16.51 E-04	-0.226	-10.59 E-04
J1_DOE_4_B	15	1.6	12	-0.560	-31.95 E-04	-0.327	-7.739 E-04
J1_DOE_4_C	15	1.6	12	-0.603	-23.37 E-04	-0.260	0.387 E-04

Table 5. Values of minimum and slope for 2 frequencies f=0.444 Hz and f=4.884 Hz.

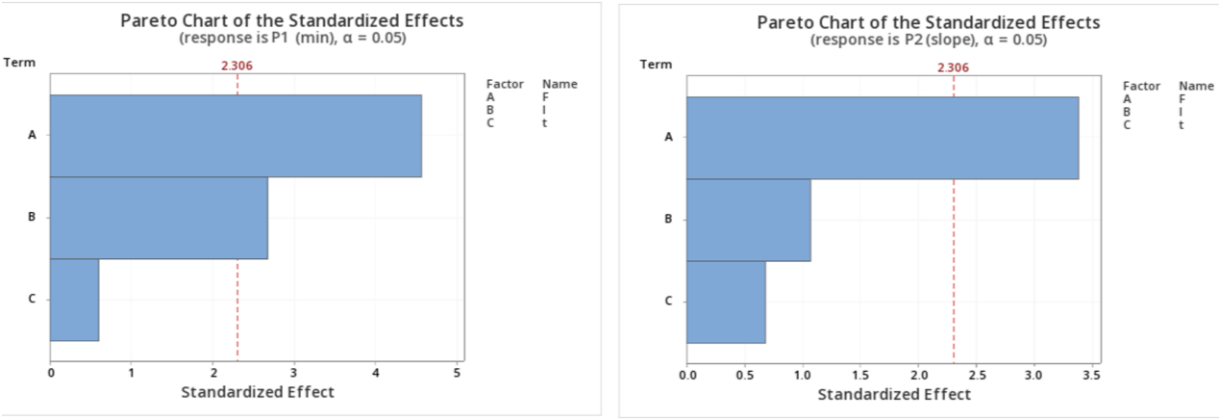

Figure 86. (a) Pareto chart of the standardized effects for values of minumum at f=0.444 Hz. (b) Pareto chart of the standardized effects for values of slope at f=4.884 Hz.

Source	Seq SS	*Contribution*	Adj SS	*Adj MS*	*F-Value*	*P-Value*
Model	0.134	77.93 %	0.134	0.045	9.41	0.005
Linear	0.134	77.93 %	0.134	0.045	9.41	0.005
F	0.098	57.19 %	0.098	0.098	20.73	0.002
I	0.034	19.73 %	0.034	0.034	7.15	0.028
t	0.002	1.01 %	0.002	0.002	0.37	0.562

Error	0.0378	22.07 %	0.0378	0.0378		
Total	0.1714	100 %	0.1715			

Table 6. Analysis of Variance for value of minimum at f=0.444 Hz.

Source	Seq SS	*Contribution*	Adj SS	*Adj MS*	*F-Value*	*P-Value*
Model	0.000005	61.87 %	0.134	0.045	4.33	0.043
Linear	0.000005	61.87 %	0.134	0.045	4.33	0.043
F	0.000005	54.24 %	0.098	0.098	11.38	0.010
I	0.000000	5.43 %	0.034	0.034	1.14	0.317
t	0.000000	2.20 %	0.002	0.002	0.46	0.516
Error	0.000003	38.13 %	0.038	0.037		
Total	0.000009	100 %	0.171			

Table 7. Analysis of Variance for value of slope at f=4.884 Hz

3.2.4 Conclusions

In the present work active thermography has been applied to resistance projection welding joints, in order to evaluate the quality of the joint and to find a thermographic NDT procedure that can be used to identify welding parameters by thermographic features.

To find these features, a well-established algorithm has been used that is the pulse phase thermography and profiles on phase maps have been analysed. It was demonstrated that the pulsed thermography can be used for the evaluation of projection resistance welded joint.

Phase maps for the first 25 frequencies have been analysed and the frequencies that maximize results were chosen (0.444 Hz – 4.448 Hz) but probably will be possible to optimize the parameters used for PPT algorithm. Two different indexes that can give information about current (I) and force (F) used in the welding process were identified and the ANOVA has been performed. Results showed that is possible to recognize two of three welding parameters, with a confidence of 95%. In fact, in the phase contrast profile, the value of min at low frequencies (P_1) and the slope in the first part of welding (P_2) at higher frequencies, are sensitive to the variation of current and force. The considered indexes give information about the two welding parameters (I, F) at different frequencies because they depend on different depths.

Time seems to have no influence on the features P_1 and P_2 but might be due to a too narrow time range chosen but, it can be confirmed only after traditional destructive standard tests. Next steps for the present work are:

- To assess the mechanical characteristics of welded joints with destructive traditional test in order to relate them to welding parameters;
- Optimize the developed procedure to be able to maximize results and reduce computational work more as possible;
- To perform the developed NDT procedure without coating to validate the method on as is joints;
- Apply method to thicker specimens in order to verify that this technique can be applied, and which are the limits.
- Apply different algorithms in order to find new features and evaluate which is more convenient to use depending on applications.

3.3 Quantitative evaluation of the welded area in Resistance Projection Welded (RPW) thin joints by pulsed thermography.

3.3.1 Introduction

With the aim to overcome the limits of current widespread non-destructive tests as UT, Pulsed Thermography (PT) technique may constitute a viable alternative, since it has several advantages: full field and non-contact technique, possibility of 100% of product check instead of statistical approach, faster that UT control and more suitable for automation, as discussed in previous sections.

In literature presented in Section 2.2, several applications of pulsed thermography as a non-destructive method for the detection and quantification of defects in composites and in metals, were reported. Usually, post-processing algorithms are needed to improve the signal to noise ratio and permits to increase the chance to detect and quantify defects and other anomalies. In the case presented, the slope algorithm has been applied, and the slope maps have been analyzed.

Applications of thermographic techniques and procedures for the assessment of resistance spot welded (RSW) joints are present [93,104,105,115,117,119] but, few works e regard the resistance projection welded joints (RPW).

Hereafter, resistance projection (RPW) welded joints have been investigated with the aim to quantify the welded area.

The aim of the case study is to present a thermographic NDT semi-automatic procedure for the quantitative evaluation of the welded area in RPW joints through the pulsed thermography and the slope algorithm. The results were compared with those obtained with well-established methods as UT and μCT techniques, which have been considered as a reference. One of the main strengths of developed method, is the application on the surface of RPW joints 'as it' is.

3.3.2 Materials and Methods

3.3.2.1 Specimens

Two specimens composed by two plates welded together through RPW process have been investigated (**Figure *87***). The front plates are made in steel DC 05 (EN10130) and are 0.67 mm thick while back embossed plates are made in DC 04 steel and have two different thicknesses: the first one 0.70 mm (J1) and the second one 0.90 mm (J2), as resumed in ***Table 8***. In Figure 4 is showed the embossing present on the back plate that has the length of 9 mm and the thickness of 1 mm. One fundamental aspect is that all tests have been performed on the surface as 'it is', without painting, with the goal to develop a procedure that can be applied on situ.

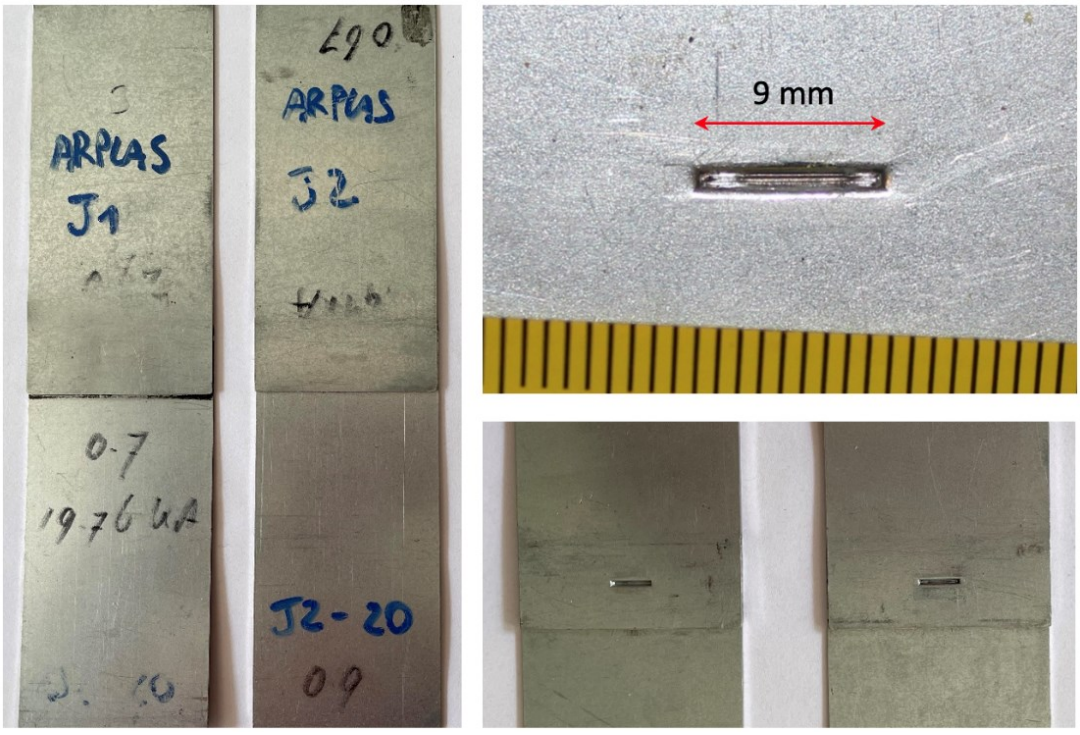

Figure 87. (a) Front view of specimens J1 and J2. (b) Detail of embossing present on the back plate for specimen J1. (c) Back view of specimens J1 and J2.

ID	Material (simple plate)	Material (embossed plate)	Thickness (simple plate)	Thickness (simple plate)	Joint thickness
J1	DC 05	DC 04	0.67 mm	0.70 mm	1.37 mm
J2	DC 05	DC 04	0.67 mm	0.90 mm	1.57 mm

Table 8. Geometrical dimensions of specimens

3.3.2.2 Experimental set-up

Thermographic experiments have been carried out adopting reflection set-up (**Figure *88***). A MWIR – Camera (INFRATEC Image IR 9830) with a cooled sensor and the NEDT of 25 mK has been used. Using extension rings and a 50 mm lens, a spatial resolution of 0.041 mm/pxl has been reached. The frame rate has been set to 480 Hz, using an acquisition window of 304 x 200 pxl2 and an integration time of 640 µs. The thermal camera has been aligned in front of the specimen in order to have best view as possible of area without distortion of images. As heat source, diode laser (900 nm – 1080 nm) with a nominal power of 500 W, equipped with a square shaped optic (19 x 19 mm2) has been used, resulting in a power density of ~ 138 W/cm2. As is possible to see in **Figure *89***(a), the heat source has been positioned with the center in correspondence of the embossing on the back plate. Each specimen has been heated for 40 ms. A dichroic mirror with an angle of 45° has been placed between the thermal camera and the specimen to avoid the spatial distortion of the laser beam square shape, **Figure *89***(b). The cooling after the pulse heating was recording for 3 seconds.

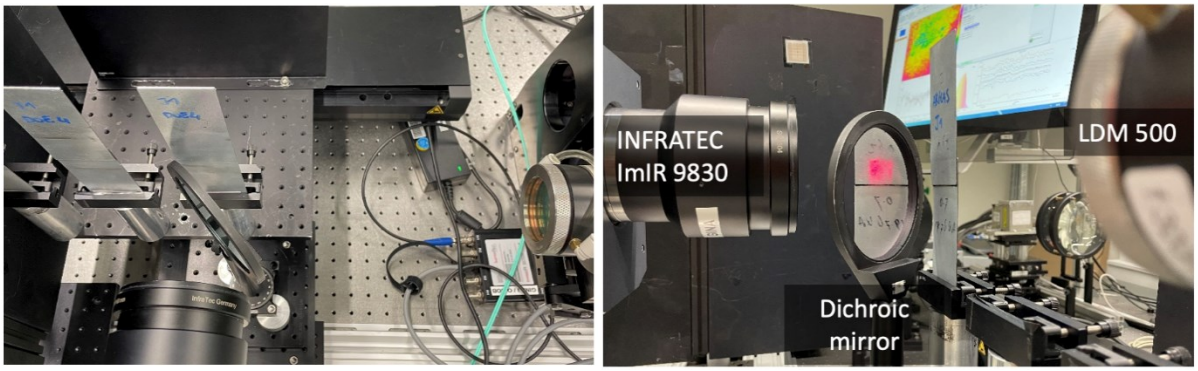

Figure 88. (a) Reflection experimental set-up used for the pulsed laser thermography. (b) Particular of laser excitation on front surface of specimen J1.

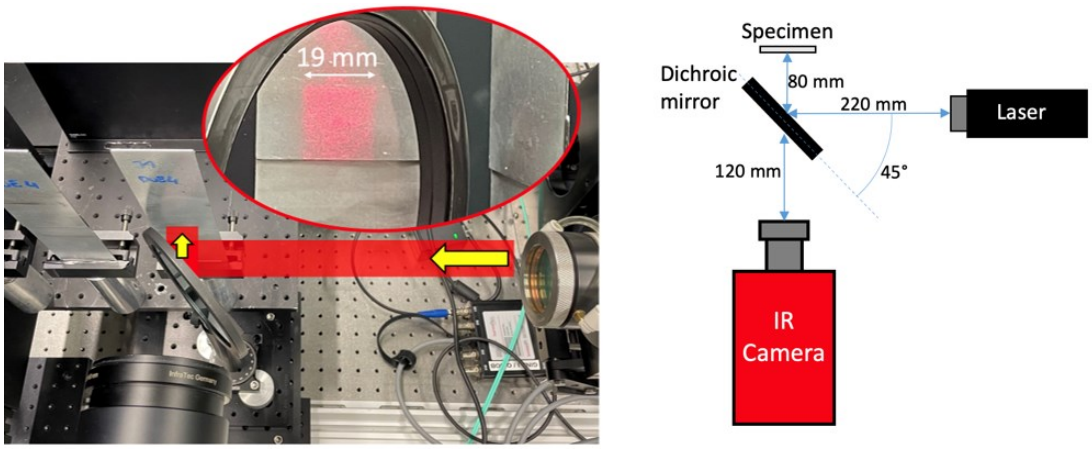

Figure 89. (a) Laser square spot positioning and scheme of laser path. (b) Scheme of set-up used.

For the inspection with the ultrasonic technique (UT), the high-resolution pulse-echo method using water as coupling media, has been adopted. In particular, a focusing ultrasonic probe with a center frequency of 50 MHz and a focal distance of 1 inch (in water) was applied, focusing on the back-wall echo of the upper plate ('smooth plate'). **Figure *90***a shows one of immersion tank system with 7 degrees of freedom (DOF), whereby only 5 DOFs were required to adjust the probe and realize the region of interest. After fine adjusting the ultrasonic probe, a scanning area of 5x13 mm² parallel to the specimen's surface was scanned with a spatial resolution of 20 microns (**Figure *90***b). The raw data (position synchronized A-Scans) is sampled and recorded for each position inside the scanning grid. To avoid influences due to the outer shape of the specimen, the recording of the data was synchronized to entrance echo of the sample. Moreover, D-Scans (depth scans) has been obtained during the post-processing of the data.

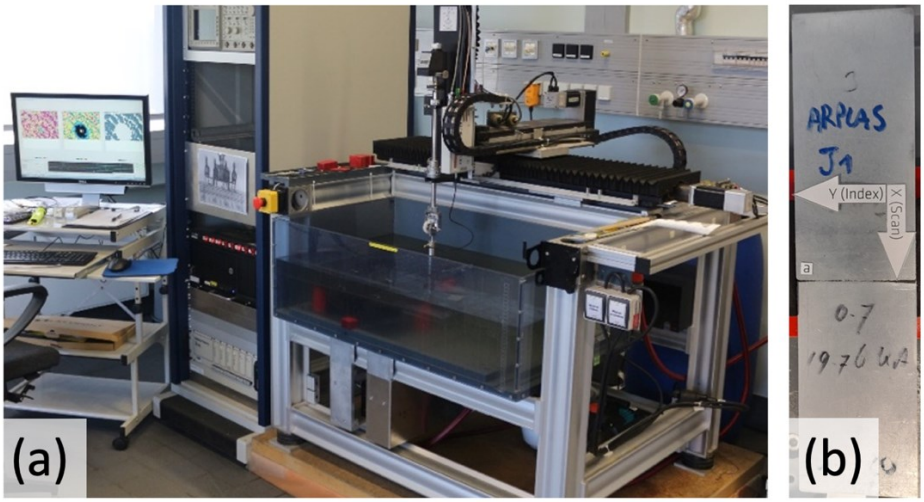

Figure 90. (a) Set-up for UT measurements in immersion thank system 7 DOF. (b) Sample with scan directions.

Micro Computed Tomography (µCT) measurements were carried out on a GE v|tome|x 180/300 L using experimental set-up showed in **Figure *91***. We used the reflection target and applied 200 kV acceleration voltage and 40 µA tube voltage resulting in 8W tube power. A flat panel detector (2024 x 2024 Pixel) was used with a pixel pitch off 200µm.

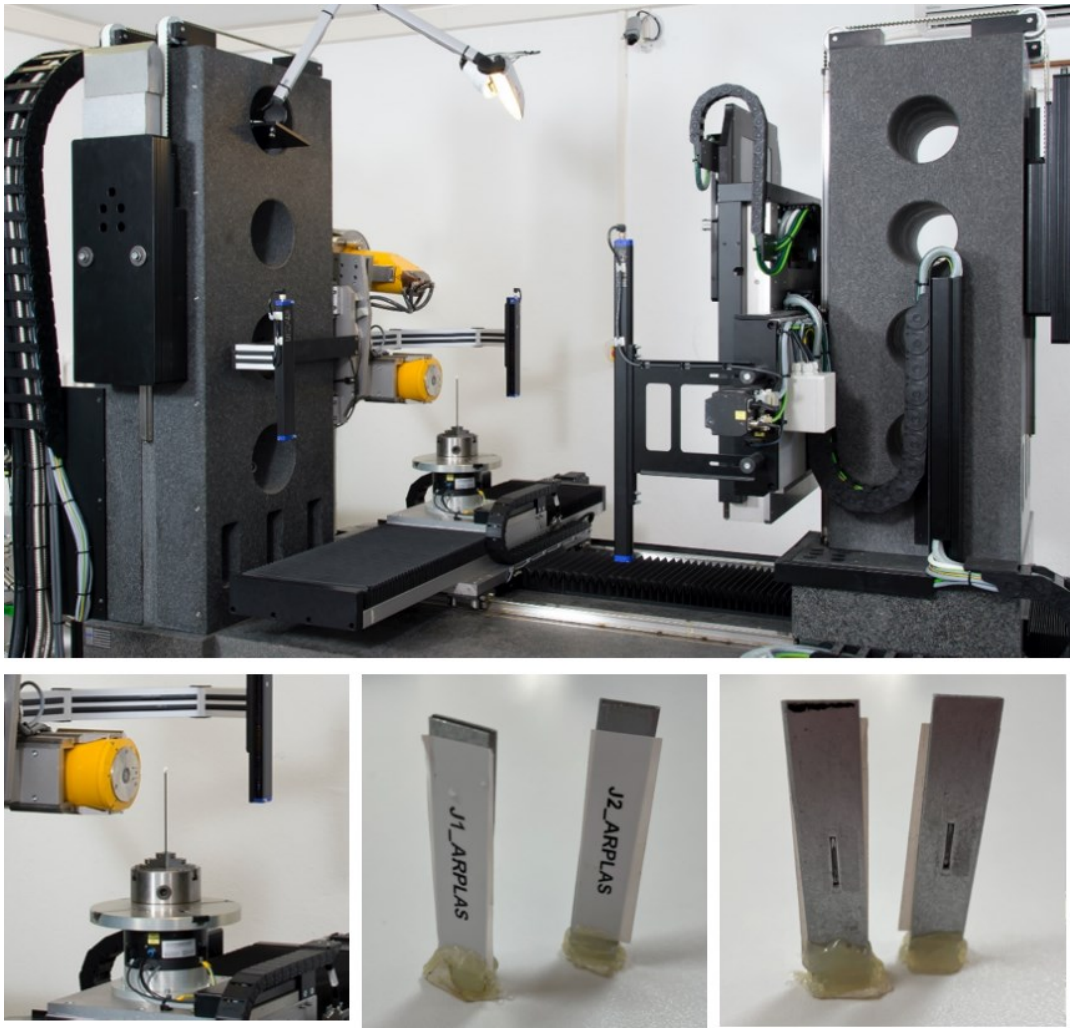

Figure 91. Set-up for µCT measurements with specimens and specimen positioning.

The source to object distance (SOD) was 20 mm and the source to detector distance (SDD) was 500 mm. This yielded a magnification of 25x and therefor a reconstructed voxel size of 8 µm and a field of view (FOV) of 16 mm x 16 mm. Transmission images at 2000 angles were acquired. For each angle, 3 projection, 1 s counting time were averaged. Including the motor movement, the scan time per sample was 2h.

3.3.2.3 Methods

In the first step, after the investigation of the specimen J1, the raw data must be processed to obtain binarized maps by using the slope algorithm, with the aim to measure the welded area by means of pulsed laser thermography. Then the recorded data has been analyzed by

using the slope algorithm. As it is known [17,177], considering the cooling curve over time, the slope is calculated by fitting a fixed number of data (time window). It is obvious that the value of the slope for each pixel is influenced by the considered time window, which is related with the inspected depth [22,34,171,173,176,178–181]. In this way, several time windows need to be considered to investigate the slope contrast over time (**Figure *92***). In this work, 1440 slope maps, one for each considered time window, have been considered for applying the proposed procedure, as described in this section.

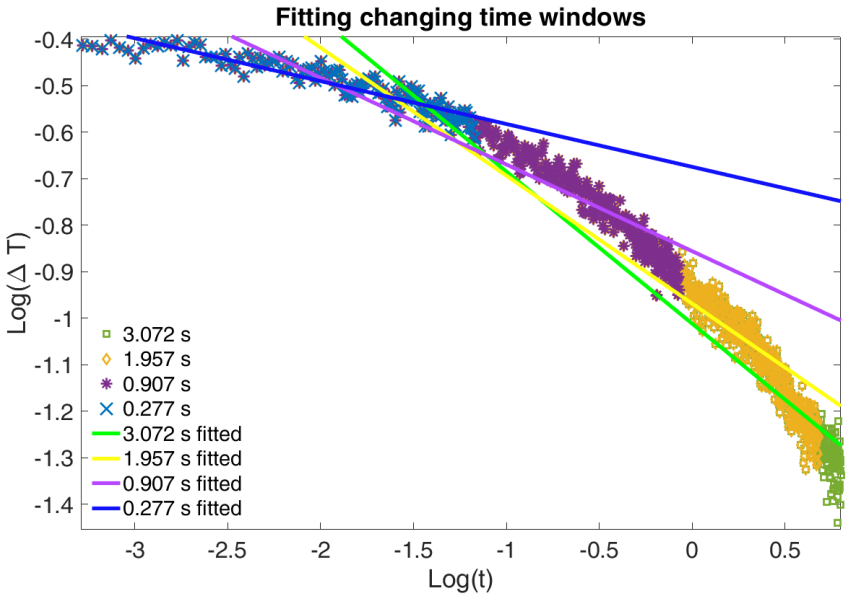

Figure 92. Changing in regression line considering different time windows.

The results have been compared considering the NSC [182] as written below:

$$NSC = \frac{S_{nw} - S_p}{\sigma_{nw}} \tag{35}$$

where S_{nw} and S_p are respectively the signal relative to a non-welded area and the signal in each pixel, and σ_{nw} is the standard deviation in non-welded areas. In this way a sequence with 1450 normalized signal contrast maps have been obtained.

In literature, especially for defect detection by thermography, an absolute value of 2 for the NSC is used as a threshold for classify an anomaly as a defect. Thus, the same concept has been used to proceed with binarization of each map, resulting in 1440 binarized maps which look like the one in **Figure *93*** (g). In this case, the threshold value of -2 for NSC has been used because, differently than for the defect detection, the welded area can be considered as a plate thicker than the not welded one and the sign of NSC is the opposite.

In **Figure *93*** is possible to see a scheme of the procedure used for data processing that describes each step. Starting from raw thermal data (a) a frame before the heating has been

subtracted resulting in ΔT curves(b). The base-10 logarithm of ΔT and time has been calculated (Figure 9 c) and a 1st grade polynomial fitting in Log-Log scale has been performed (Figure 9 d). Only the value of slope of each straight line, for each pixel, has been considered to obtain the slope map (Figure 9 e). As described before, through equation 4, a map of NSC has been obtained (Figure 9 f) and imposing the threshold of -2, the binarization has been performed. This procedure, as explained in the first part of this section, have been repeated for each of the 1440 considered maps.

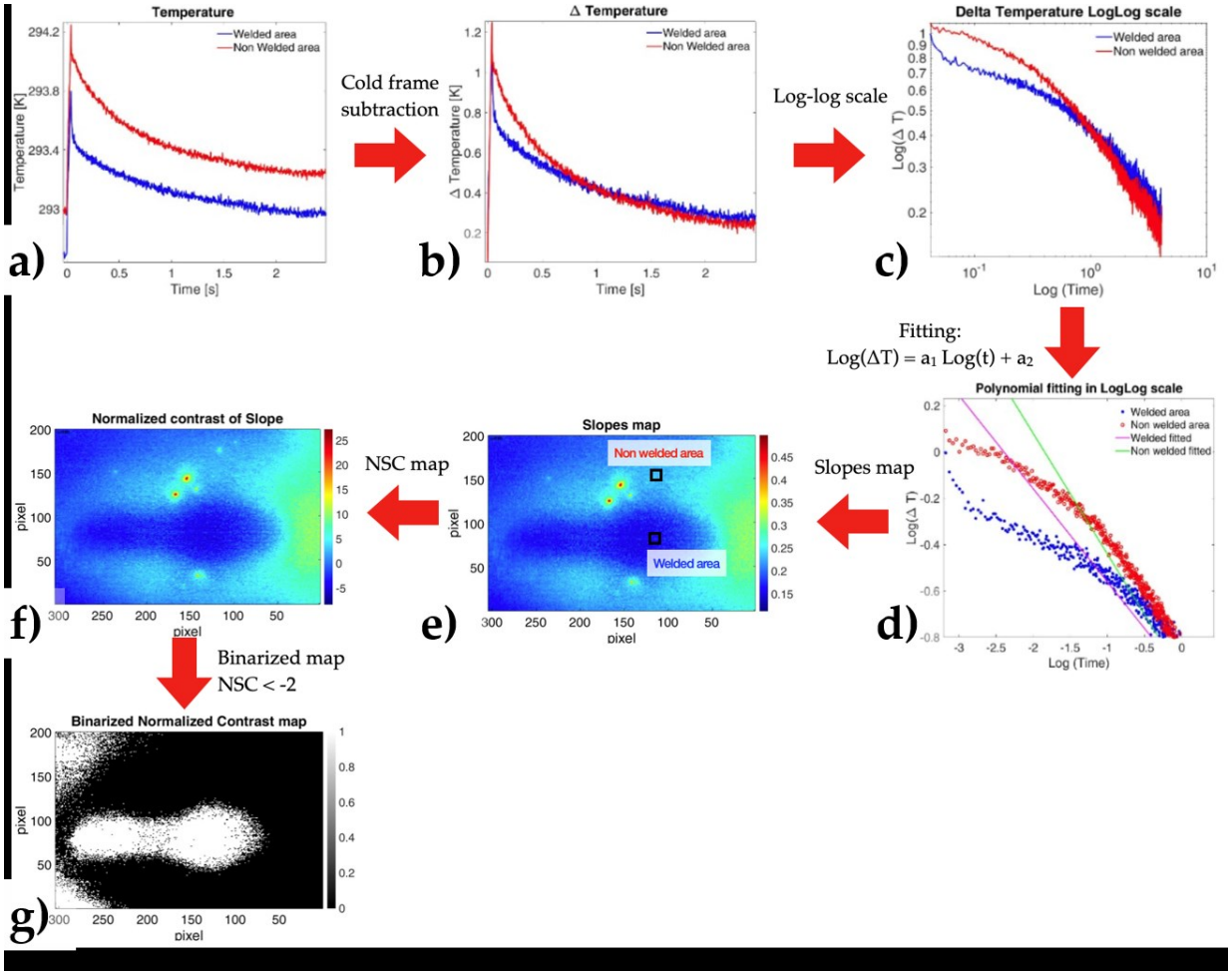

Figure 93. (a) As it is recorded signal for welded and non-welded area. (b) ΔT curves after cold frame subtraction. (c) Log (ΔT) vs Log (t) representation. (d) Example of fitting procedure with a 1st grade polynomial. (e) Example of slope map obtained and the selection of welded and non-welded area for the NSC calculation. (f) NSC map and (g) binarized map considering a threshold of -2.

For each binarized map, the longitudinal central axis has been considered as a reference to measure two profiles for each map: upper and lower profile as is possible to see in **Figure *94***). Hence, with a step size of 0.041 mm along the center line (dotted red line), a column of pixels (vertical direction) has been considered for counting the number of pixels by

starting from the center line; the count has been considered finished in presence of three consecutive pixels with value 0.

This procedure has been applied automatically by using a MATLAB© script, for each pixel of central axis, for both sides (upper and lower) and for each binarized map. The application of this procedure gives noisy data (**Figure *94*** c) hence, for each semi-profile, a 4th order polynomial fitting (**Figure *94*** d) has been applied to define the contour of welded area. In this way, is possible to describe continuously the boundaries of the area in which the NSC value is over the threshold.

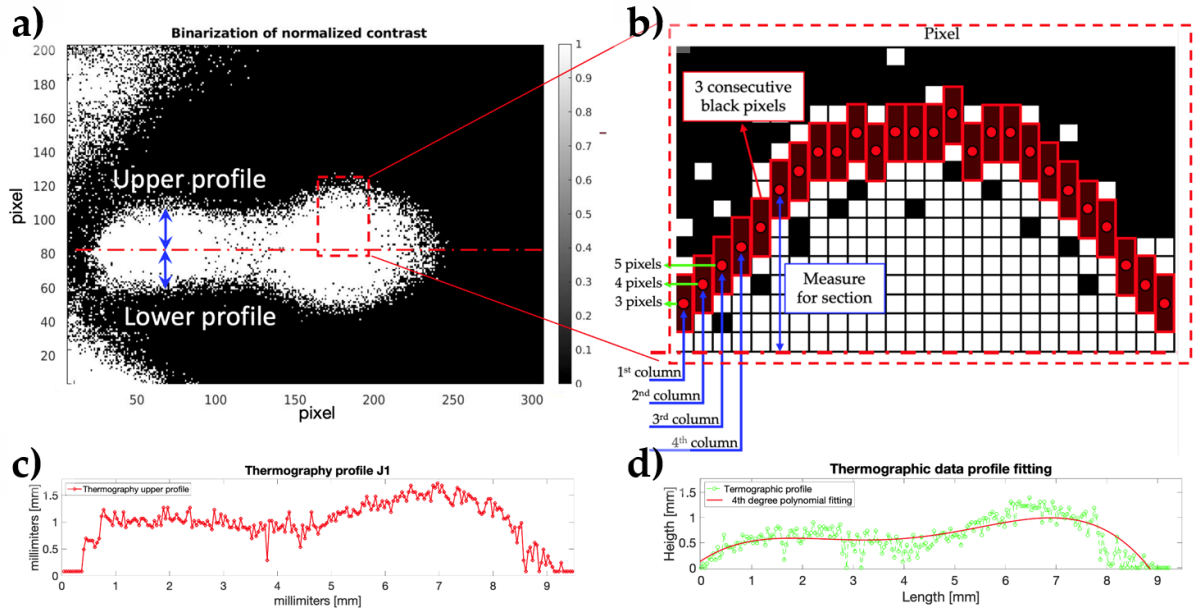

Figure 94. Representation of procedure used for the calculation of profiles for thermal analysis. (a) The binarized image with longitudinal axis that divides the map in "upper" and "lower" part. (b) A scheme of procedure that shows how it works the measure of profiles. Red dots represent the value of measure for that pixel column, and the red rectangular areas represents the three consecutive pixels with value 0. (c) Shows the profile obtained from the binarized image considered. (d) In green the same profile shown in (c) but with correspondent polynomial curve obtained by fitting procedure.

A suitable procedure is now necessary for detecting the best map among the 1440 collected binarized maps capable of correctly describing the welded area in terms of the shape and dimensions and to do that, a reference measurement of the welded area is necessary. To have a reference measurement of welded area there are two different possible ways. The first, it is to perform Chisel test destroying the specimens and obtaining a macrography of welded area that can be measured. It is clear that is the only way to have a definitive measure of welded area. Using this method, it is possible to obtain a real measurement of welded area, but the main cons is that it is not possible obtain information about mechanical properties of joints, which is the main aim of the assessment of the welded

joints. In fact, the quantification of welded area in RSW it is spreadly used, but only for the RSW joints a relation between welded area and mechanical resistance is widely known. The second one is to compare measurement of welded area obtained by thermographic method with well-established NDT as μCT and UT; the latter option has been preferred.

As output of UT, measurements D-scan (**Figure *95***) and C-scan (**Figure *96***) data have been obtained but only D-scans have been considered. The C-scan allows the detection of relative intensities at points in an x-y scan plane y and permits to investigate the entire volume of the analyzed component (**Figure *96***). The depth scan (D-Scan) shows the spatially resolved time of flight (**Figure *95***) and illustrates changes in the depth of the reflective back wall or just the thickness of the sample. Here, the connected zone appears as a region with certainly larger thickness than the original front plate. In **Figure *95***, an individual grey value corresponds to the time of flight or the corresponding wall thickness. In the considered case, it is difficult to define the boundaries of welded area from the C-scan, because a threshold value should be needed. Hence, the D-scan has been considered because of the clear distinction between welded and not-welded area.

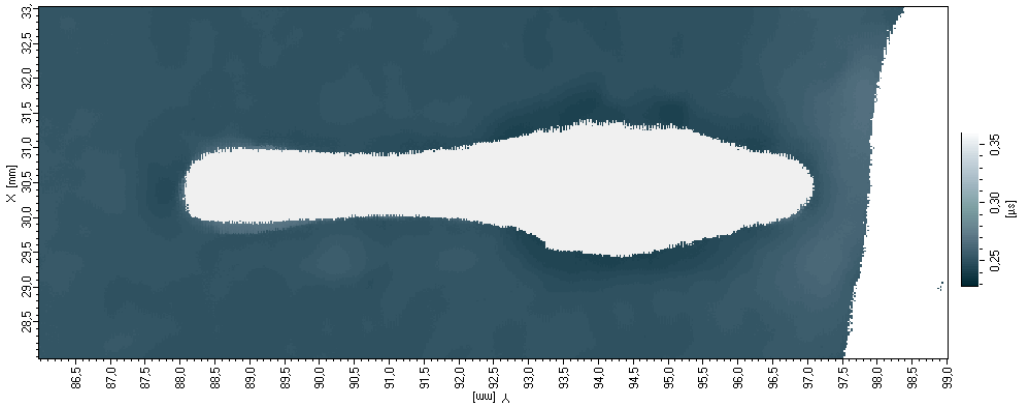

Figure 95. Example of D-Scan obtained for the specimen J1.

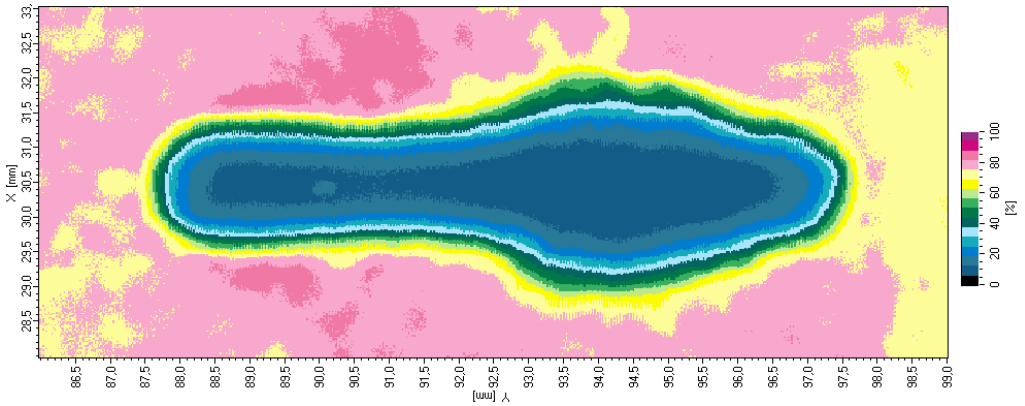

Figure 96. Example of C-Scan obtained for the specimen J1.

For the μCT results, projections obtained has been used to reconstruct the 3D volume using the filtered back-projection algorithm [Feldkamp L A, Davis L C and Kress J W 1984 Practical cone-beam algorithm vol 1] embedded in the reconstruction software of GE. Cross sections through the reconstructed volume are shown in **Figure *97*** b, for three different positions.

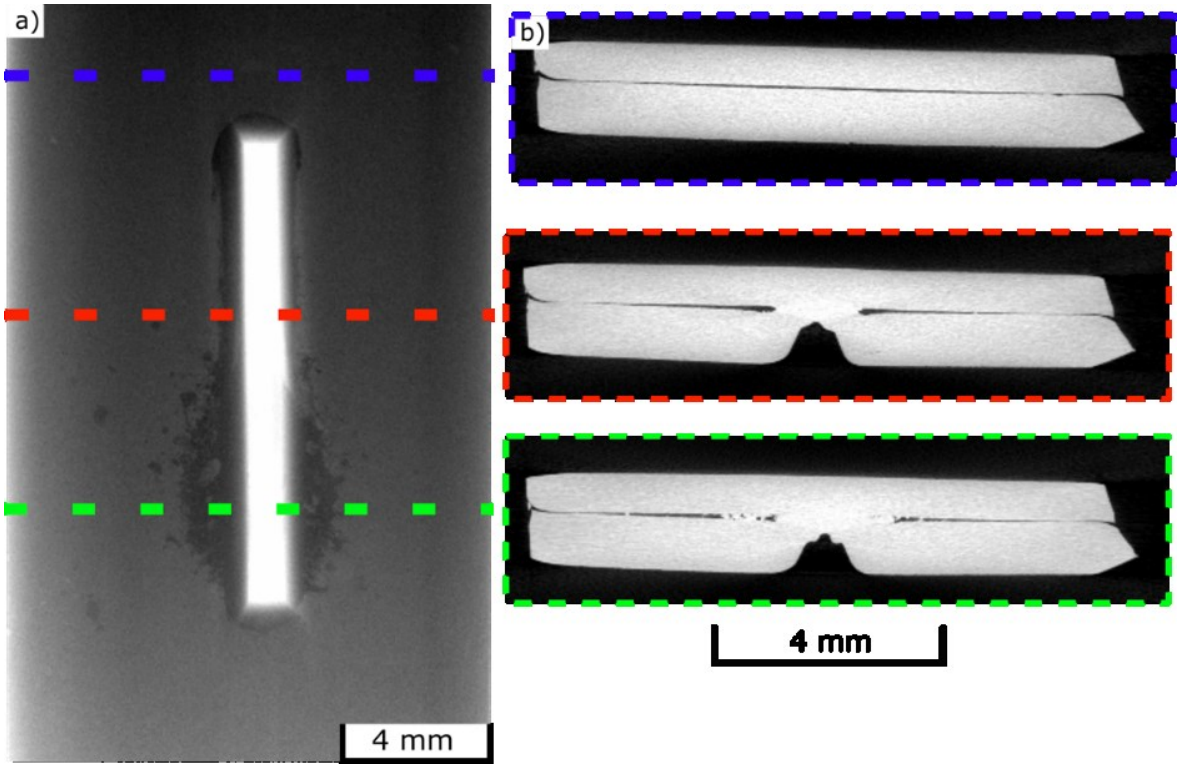

Figure 97. a) A single projection acquired during the CT-scan, and b) CT-slices through the reconstructed volume at three different cutting planes. The first slice (blue) shows the not heat affected area, the second (red) regular melted area and the third (green shows an over-melting of the material (many splatters).

If for the resistance spot welded joint the value of the area can be considered to characterize the quality of the joints, for the RPW it is not. In fact, considering the shape of embossing, it is evident that the welded area cannot be significant enough, but the distribution is needed: thus, the shape of the area. To compare the shape of the welded area, an approach in line with that used for the analysis of thermographic maps has been adopted.

The criterion considered to process UT and μCT is here described. Starting for central axis in the same plane considered for thermographic results, the length of welded area has been measured considering the external boundaries in D-scan and CT that clearly separate the welded area, from the non-welded area. In this way, it is possible to obtain, as for the thermographic data, two profiles: an upper and lower profile. Joining these two profiles on the central axis, a closed area is defined and considered the welded area. Contrary to thermographic results, for UT and CT is possible to obtain only one area because, in the

same plan of thermographic results, only one map for each method has been acquired. In order to compare the thermographic data with the other ones, the proposed procedure consists in the calculation of the percentage error as the relative error committed by thermographic data with respect to the UT and μCT data. Then, every column of pixels measured by thermographic results, with the correspondent measure from UT and μCT, must be compared and a percentage error must be calculated as follow:

$$Error_x\ [\%] = \left|\frac{M_{UT,\mu CT\ x} - M_{Therm_x}}{M_{UT,\mu CT_x}}\right| \cdot 100 \qquad (36)$$

where $M_{UT,\ \mu CT\ x}$ is the UT or μCT measurement and M_{Therm_x} is the correspondent thermographic ones.

This means that the percentage error can be calculated, for each considered profile (upper/lower) and then for each x value (total 225 values) for each binarized map. Thus, to identify the best slope binarized map, the map for which the average percentage error is minimum can be considered and then, in this way, it is possible to identify the best time window for the slope algorithm analysis.

Applying the same data evaluation to both samples considered (J1 and J2) with the same thickness of the front plate and the same experimental parameters, the obtained optimized period should be the same or very similar because the underlying physics is also the same.

Finally, the obtained contours were analyzed in terms of two geometrical parameters significant for the quality assessment of the welding: the length of welding and the value of welded area. In the D-Scan and μCT data, the length of welding has been measured on the longitudinal axis of the welded area. The length of the welded area has been measured considering the distance between the two intersection points along the longitudinal axis, obtained with the polynomial fittings. The welded area has been evaluated calculating the area between the two polynomial curves by using definite integrals between the two intersection points evaluated as extreme points.

3.3.3 Results and discussion

To apply the method discussed in previous section, the first step needed is to define the reference profiles from UT and μCT data.

Considering the μCT results, it is possible to see in the image obtained at the interface between the two welded plate (***Figure 98***) in a frontal view of welding that, especially in some areas, it is not clear how it is possible define the boundaries between welded and not-welded area. In fact, several splashes are present on the right side and, especially in the low

side, it is difficult from this view to understand if the area is welded or sticked. In **Figure *99***, it is clearly visible that the good welded area is present only in the center of section but, after some voids, it is not clear if the material is completely welded or not. In addition, in **Figure *99*** it is evident that voids can be created during the process especially because of splashes during the force application. In fact, these splashed parts derive from the embossing. Hence, considering the final thickness of welded zone and starting nominal thickness of plates, there is a volume of material that is expulsed during the process creating the splashed area. For these reasons, it has been impossible to identify the two profiles of welded area from the CT results which, on the other hands, provided other information about the process, as described.

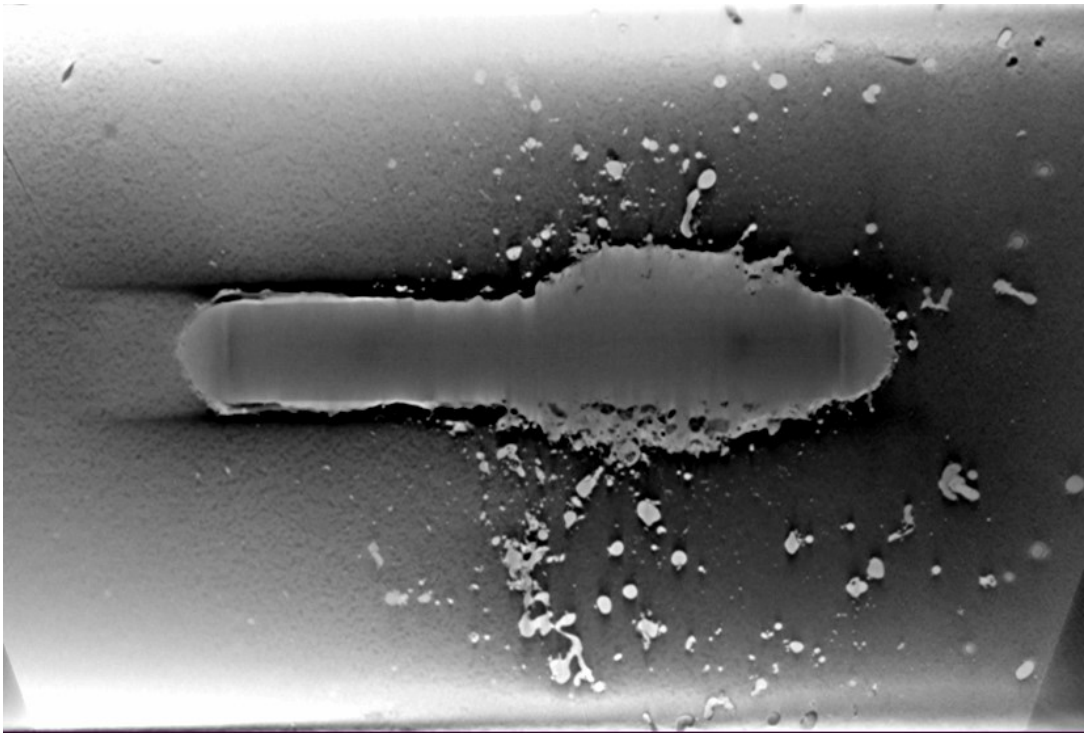

Figure 98. μCT data for specimen J1 on the plan at the interface between the two plates and in the same orientation of thermographic view.

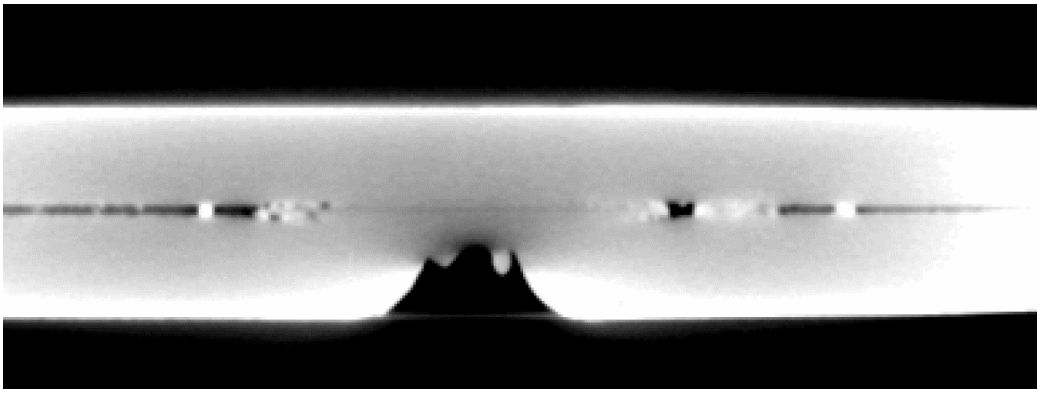

Figure 99. CT of cross section in splashed area for J1.

In **Figure *100*** (a,b), it is possible to see the normalized signal contrast maps and the correspondent binarized map.

Figure *100* (c) shows the average percentage measure error, evaluated as described in previous section as a function of the time window and then the cooling phase duration, considering as a reference the UT results. It is possible to see that there are two different curves: the red one for lower profile and the blue one for the upper profile. The behavior of these curves shows that there is a minimum in percentage error that is slightly different between the upper and lower profiles. To define the time window that minimizes both the errors, in this case, the intersection between the two curves has been considered because, obviously, the percentage error is slightly higher than the minimum for both individual profiles, but it has the advantage to have the same value of the error for both the profiles, which is easier to manage for measurement purposes.

As described in previous section, to obtain these profiles, only the boundaries of the area with higher time of flight in D-Scan has been chosen and no evaluation inside of this area has been done. Clearly, these profiles are not continuous but are made up of points with a spatial resolution that depends on the UT measurement system described in Section 3.3.2.2.

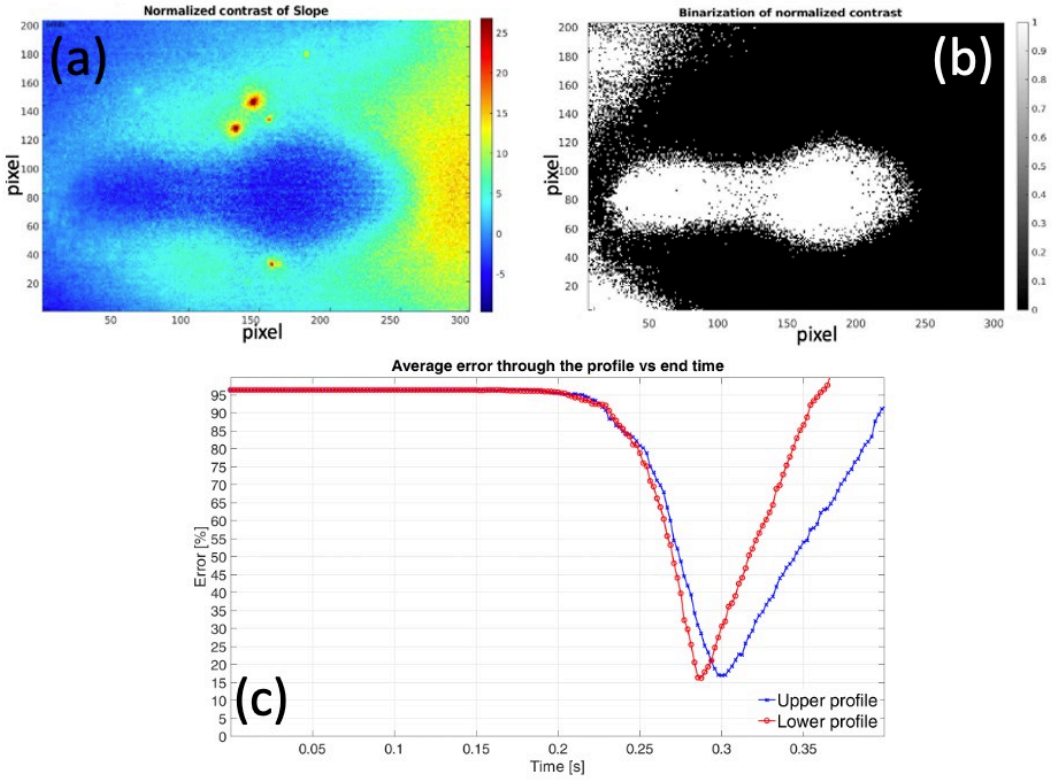

Figure 100. (a) Map of normalized contrast of slope (b) Binarized map of normalized contrast. (c) Average percentage error of measurements on upper (blue) and lower (red) profiles vs time window.

In **Figure 101** are showed the areas obtained from thermographic measurements compared with the ones obtained by UT measurements, used as reference. It is glaring that there are some parts in which the thermographic results agree very well with the UT results, but in some other parts, there are significant differences, especially at both ends of the welded area. Nevertheless, a consideration can be done: the spatial resolution of thermography is 0.041 mm/pxl but for UT is 0.02 mm that results in a higher number of points that describe each profile. At both the ends of the weld, the lateral heat flows are higher than the middle part, where the heat moves predominantly in one direction. These phenomena can influence the thermal signal in the edge parts of welded joint. As is visible in curves in **Figure *94***, the minimum average error for each profile is < 20%, when the profiles showed in **Figure 101** are compared.

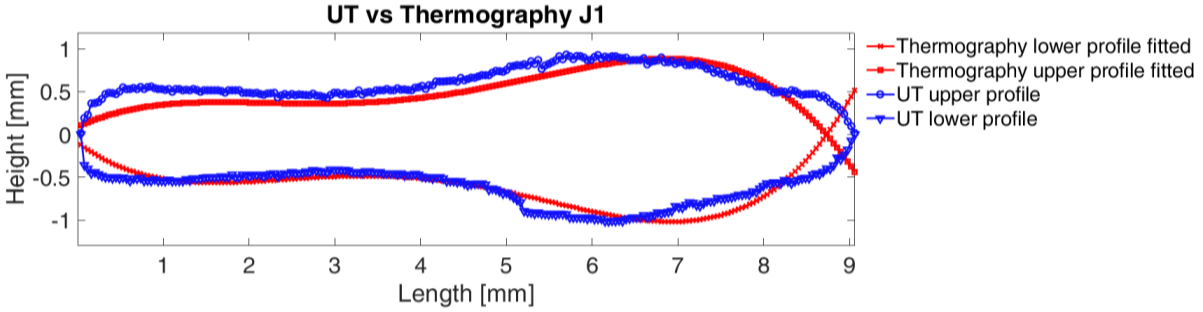

Figure 101. Profile of welded area obtained by UT and by thermography compared.

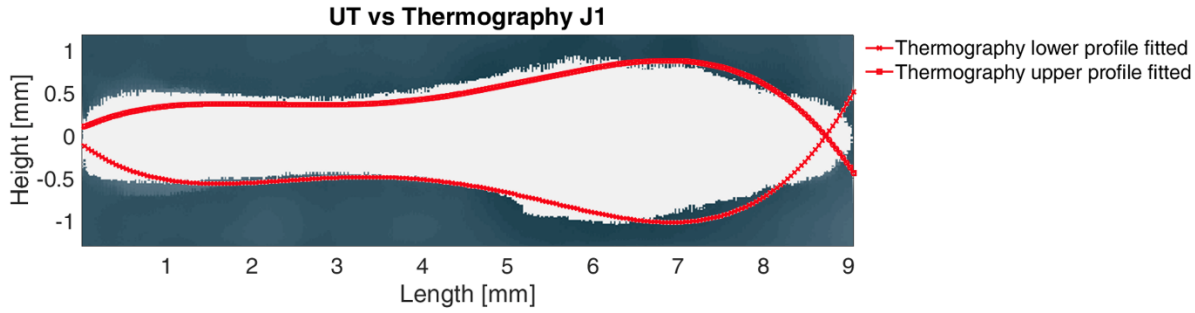

Figure 102. Profile of welded area obtain by thermography (t=0.294 s) compared overlapped on D-Scan image for specimen J1.

The same procedure has been used for the specimen J2, taking the same threshold to quantify the UT results in terms of spatial dimensions. Again, this size was used to estimate an optimized period for the binarization of the thermographic results. **Figure *104*** shows the direct comparison between TT and UT for the specimen. The agreement between both areas is not as well as in case of **Figure *101***, especially in the left half. To discuss this result, one should pay attention to the UT D-Scan in ***Figure 102***. It is possible to see that, differently from the D-Scan for J1 (**Figure *102***), the value of time of flight is not uniform

in the entire area inside the boundaries. Instead, there are some inhomogeneities, especially in the left side of **Figure *103***, that can represent some non-uniformity in the welded area.

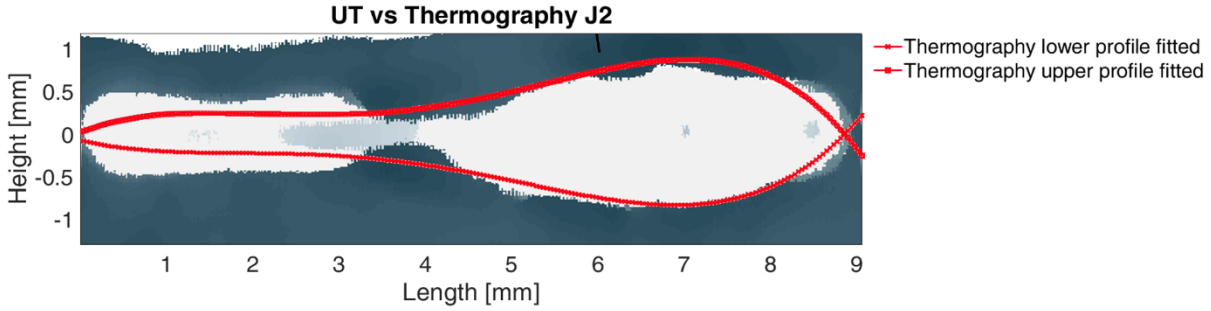

Figure 103. Profile of welded area obtain by thermography (t=0.312 s) compared overlapped on D-Scan image for specimen J2.

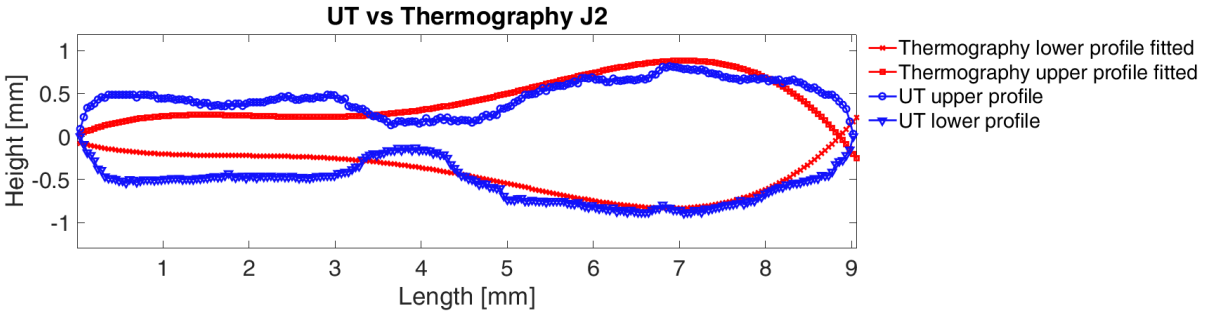

Figure 104. Profile of welded area obtain by UT and by thermography (t=0.312 s) compared for specimen J2.

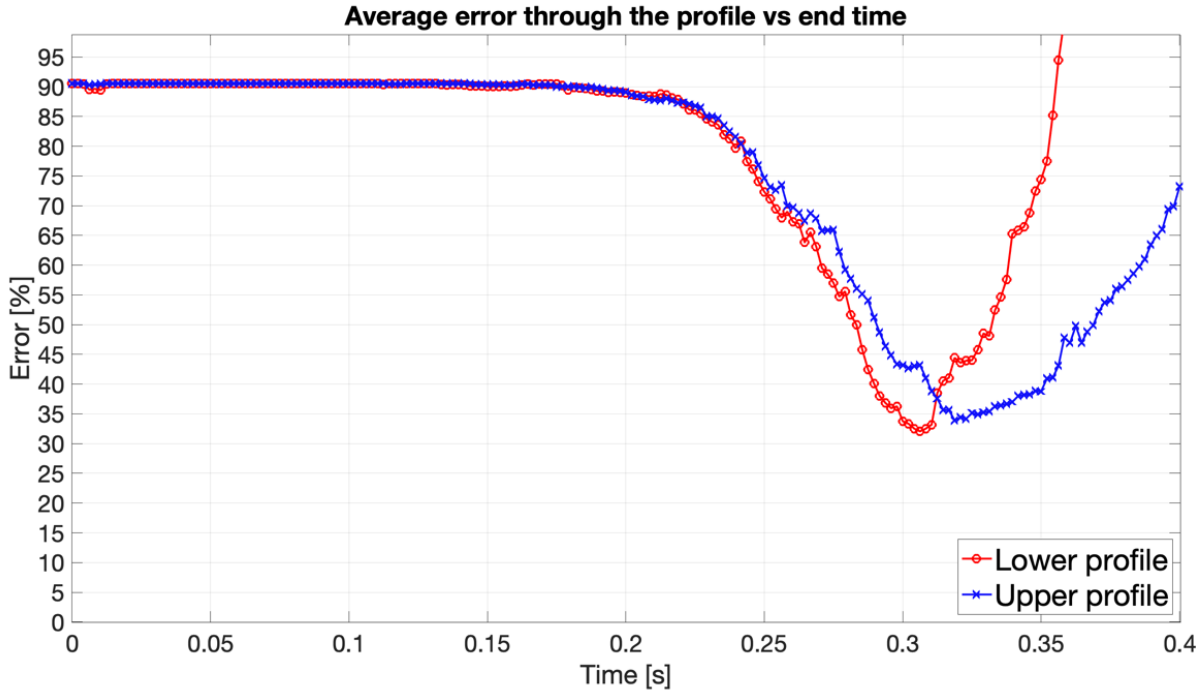

Figure 105. Average percentage error of measurements on upper (blue) and lower (red) profiles vs time window for specimen J2.

In **Figure *105***, the error curves are reported, where it is possible to see a similar trend to the previous ones, described above. The absolute value of the time window (0.312 s) is comparable with the one obtained for the specimen J1, that confirm as it is mainly dependent on the front plate thickness, considering the thermal source parameters constants.

CT results obtained for the specimen J2 reported in **Figure *106***, confirmed that is hard to define the boundaries between welded and not-welded area. In fact, the splashers are more evident than in the J1 results and are evident some voids and the irregularity of welded area contours. In **Figure *107*** voids and sticked parts are highlighted, and it is evident that, especially on the side of welded area, it is very difficult to distinctly define the end of the melted zone, making it impossible to unambiguously define a contour to be measured.

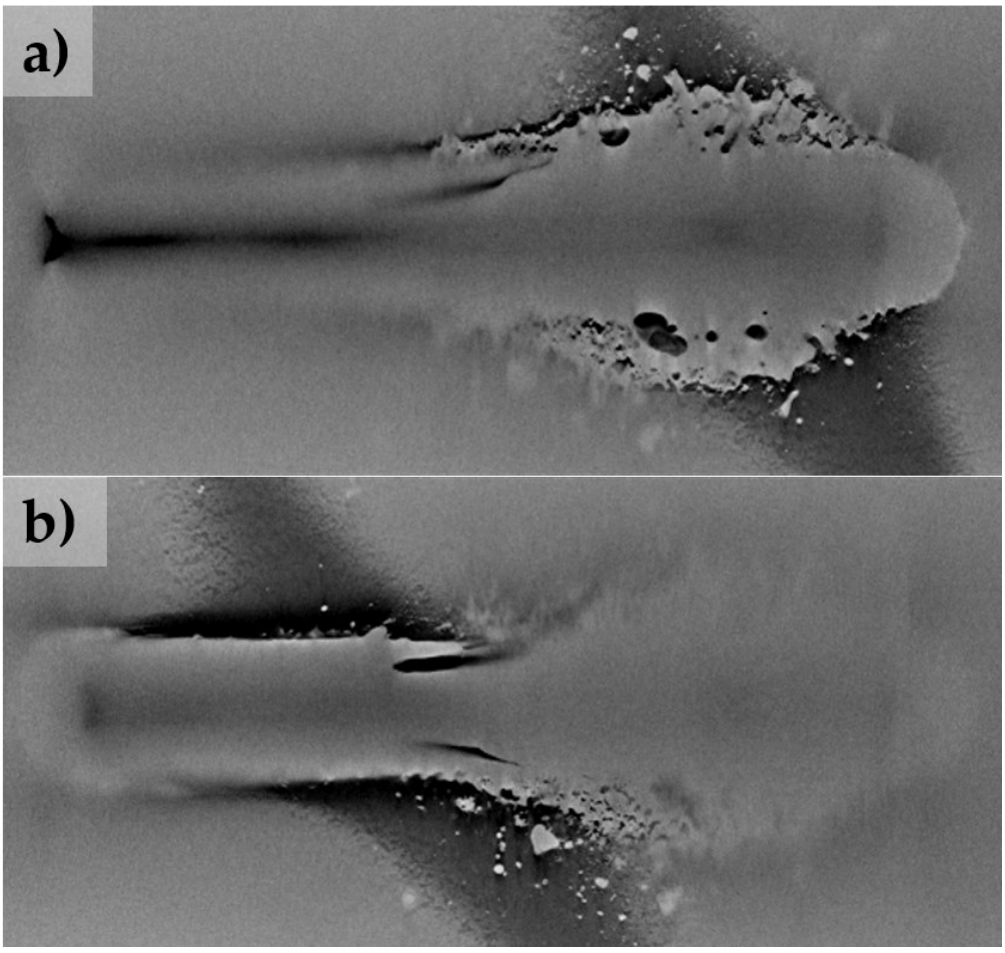

Figure 106. µCT data for specimen J2 on the plan at the interface between the two plates and in the same orientation of thermographic view.

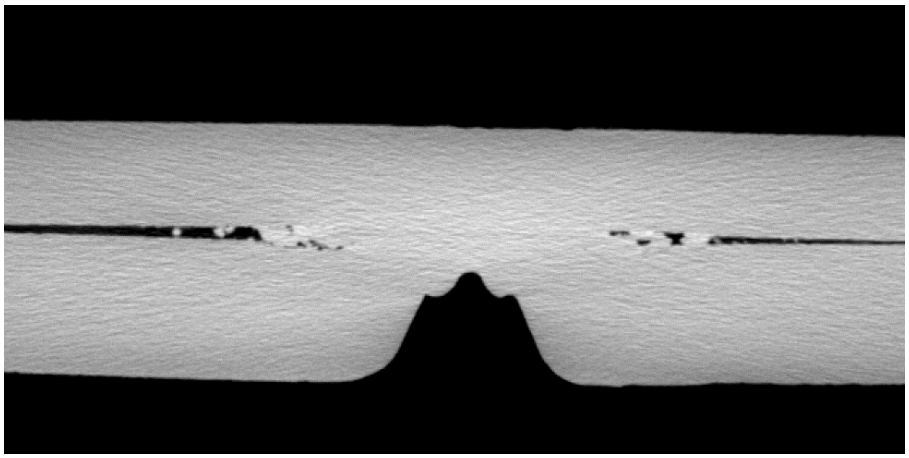

Figure 107. CT results for a section of the J2 specimen with voids and splashes details.

Considering a qualitative comparison between J2 CT and UT results, it is interesting to ascertain that, considering the D-Scan (**Figure *103***), in the center of welded area there is a reduction of height of welding footprint that suggest a reduction of welded area. The correspondent part in the CT results (**Figure *108***) shows two big lateral voids that suggest a complete welded area in the middle but two small sticked areas external to the two voids, which could explain the complete absence of that external part in D-Scan results.

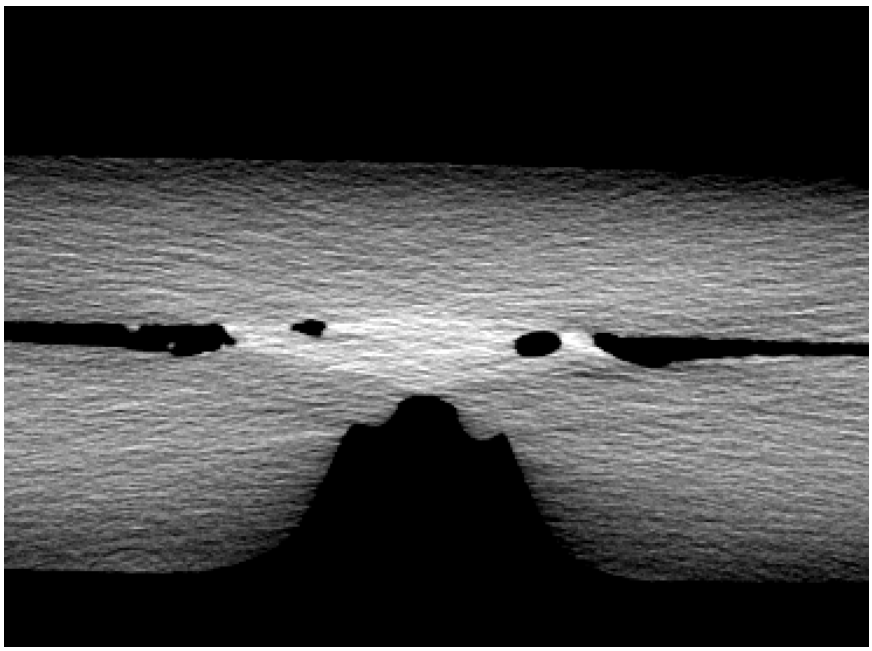

Figure 108. CT results detail of the central part of the J2 specimen

Therefore, after considerations about shape of the welded area, the CT results, and the comparison between thermographic and UT results, is possible to resume results about the main geometrical characteristics of RPW, that are: length along the major axis and the value of area enclosed between the profiles.

ID	Length UT (L_{UT})	Length TT (L_{TT})	Difference (%)	Area UT (A_{UT})	Area TT (A_{TT})	Difference (%)
J1	9.1 mm	8.9 mm	2.2 %	11.0 mm^2	10.0 mm^2	9.1 %
J2	9.0 mm	9.0 mm	0.0 %	9.1 mm^2	8.3 mm^2	8.8 %

Table 9. Measures obtained by the ultrasound (UT) and thermographic (TT) methods.

According with results showed in **Table *9***, is possible to see that for the measure of the welding length, the thermographic and UT results are in agreement with a difference that is 2.2%. For the welded area, that is a parameter commonly used for the resistance welding, for example in RSW, thermography underestimates the value for 9%. This is interesting because, for engineering applications, the underestimation of welded area in joints allows for safe operation and design. Compared to the previously illustrated methods present in the literature, the method presented allows for obtaining the dimensions of the melted area and a description of the shape comparable to that obtained with UT and CT in a semi-automatic manner. The advantage of this method is that it has significantly reduced operating times and does not require any contact or pre-treatment of the surface relative to the welded joint. Additionally, a testing procedure has been defined that enables obtaining repeatable measurement results.

3.3.4 Conclusions

In the present case study, a thermographic semi-automatic procedure for the quantitative evaluation of both the shape and dimensions of the welded area in RPW joints, has been presented. Laser pulsed thermography has been used and, with the goal of highlight the difference between welded and not-welded area, the slope algorithm has been used and the selection of the time window has been investigated. Normalized signal contrast maps, and binarized maps have been assessed to obtain the best time window through a suitable procedure based on the comparison between thermographic and well-established NDT methods as µCT and UT results.

As discussed in Section 3.3.3, considering the UT results as a reference, a good matching with UT results has been obtained and new data about the quality of RPW joints have been acquired through µCT analysis. Indeed, the higher error in shape evaluation is localized especially at the ends of welding or in areas where the shape changes rapidly. Considering the results obtained from µCT, this behavior can be caused by the presence of splashed materials outside the welded area but close to the boundaries, which can influence the heat flux beahviour. Usually, for resistance welding joints, the absolute value of welded area is

one of the most important parameters for the evaluation of quality of joint, and then, the value of areas obtained by UT and thermography have been compared. The thermographic results show a good agreement with D-Scan obtained by UT, with an error of ~10% for the welded area and ~2% for length of welding; that confirms the capability of thermography to assess adequately RPW, in according with a well-established technique as UT and μCT, but with an underestimation of the welded area compared with UT results. In conclusion, it is possible to assert that the developed thermographic semi-automatic procedure is capable to correctly quantify the shape and dimension of welded area in RPW joints, with localized errors for the shape obtained by UT and in good agreement with UT for area and length measurements, with a strong reduction of testing time compared with UT but especially with μCT. After a first calibration phase, the total testing time (test + analysis) is only ~6 s and can be performed without any contact, in-situ and with no preparation of inspected surface.

This procedure can be further improved in several ways: reducing analysis time, reducing the measurement error and using low-power laser to reduce the costs for laser and safety system too. To obtain these improvements the next planned activities are:

- Compare several algorithms for thermal data analysis in order to evaluate which is the faster and which one can guarantee the minimum measurement error;
- Evaluate the mechanical resistance of welded joints to study the influence of geometrical characteristics of welding on the mechanical properties;
- Develop a new procedure based on the long-pulsed heating to reduce the power of the laser;
- Design a system to full automatize the control and suitable for on-site applications.

CHAPTER 4

Microstructure evaluation through thermographic non-destructive methods

One of the present work aims is to verify the capability of active thermography to discern different microstructures through thermal diffusivity measurement. In the literature, several methods are present to measure thermal diffusivity by active thermography. Most of all will be presented and discussed in this chapter to define which could be suitable for the considered application. Developing a thermographic procedure to discern different microstructures is a fundamental step for achieving the final aim of measuring HAZ in welded joints.

4.1 Thermal diffusivity measurements by thermography

As described in the previous section, a critical goal for the welding assessment is to define and quantify the heat-affected zone (HAZ). It is essential to define and localize the boundaries of HAZ because, at the interface with the not-heat-affected zone, there is a higher probability of cracks and defects [39,183,184]. The HAZ is characterized by a different microstructure than the base material; hence, different mechanical properties can result in an interface surface, which may occur cracks because of different behavior under load conditions [185]. As discussed in section 2.3, in the literature, several works described the anti-correlation between thermal diffusivity and hardness in steels [186–194]; thus, the main idea is to correlate the microstructure to the thermal diffusivity and then to the mechanical properties to evaluate the limits of HAZ due to the difference of thermal properties between HAZ and base metal.

To obtain this result, an investigation of several non-destructive thermographic methods to measure thermal diffusivity is needed, and an evaluation of the resolution of the most suitable technique is necessary.

The next session will present an overview of principal non-destructive methods for measuring thermal diffusivity by thermography

4.1.1 Thermal diffusivity

The thermal diffusivity can be defined as the speed at which heat propagates. This is a material property and depends on: density, thermal conductivity and heat capacity defined as reported below:

$$\alpha = \frac{k}{\rho c_p} \tag{37}$$

In the expression above, α in the thermal diffusivity, measured as m^2/s, k the thermal conductivity, ρ the density of material and c_p the heat capacity of material. This thermal property it is very important in phenomena of non-stationary heat propagation as the thermal wave transmission in active thermography. In fact, in the case of thermal wave through a material, the k it is insufficient to describe the phenomena, but low density and specific heat values are needed.

This property is related to the direction of heat propagation, precisely as the thermal conductivity. Only in an isotropic and homogeneous material the thermal conductivity can be considered constant, which is suitable for most metallic materials; instead, for anisotropic materials, the thermal conductivity k and thermal diffusivity α, must be expressed through a tensor. This property is strictly related to the microstructure of the material and to the microscopic mechanism of heat transfer. In fact, as discussed in section 2.3, different microstructures and mechanical properties must result in different thermal diffusivity values [40–46].

There are several methods for measuring thermal diffusivity by thermographic techniques. However, only the most significative will be described in the next section and the methods will discussed separately discerning periodic heating and pulsed or long pulsed one.

4.1.2 Thermal diffusivity measurements by lock-in thermography

In 2009 Mendioroz at al. [195], presented a method for measurements of thermal diffusivity of thin plates and filaments using infrared thermography and laser heat source in transmission set-up configuration. In the work , calculations for this isotropic and an-isotropic plates are present, heated by a modulated and tightly focused laser beam, showing that the slope method is also valid for this kind of point-like heating.

Considering a slab of thickness l heated by a laser beam with a Gaussian profile of radius a, power P_0 and modulated heating with frequency f. The scheme of the problem is reported in ***Figure 109*** and, because of symmetry, can be written in Hankel space as

$$T_{ac}(r,z) = \int_0^\infty \delta J_0(\delta r)\left[Ae^{\beta z} + Be^{-\beta z}\right]d\delta \quad (38)$$

in which δ is the Hankel variable, J_0 is the Bessel function of the zeroth order and $\beta^2 = \delta^2 + \sigma^2$ being $\sigma = \sqrt{i\omega\alpha}$ the thermal wave vector. A and B are constants which depends on boundary conditions, heat flux continuity at the samples surface.

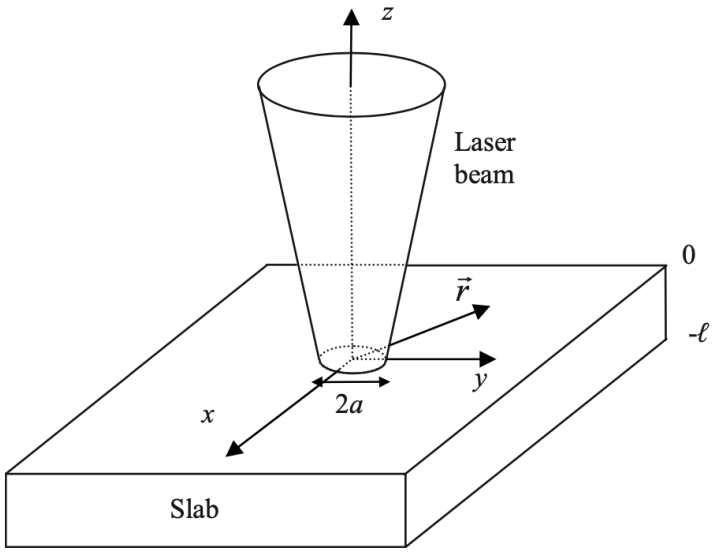

Figure 109. Diagram of a slab illuminated by a focused light beam [195].

Considering the Gaussian distribution of power in laser beam, it is possible to substitute the constants A and B and obtain:

$$T_{ac}(r,z) = \frac{P_0}{4\pi k}\int_0^\infty \delta J_0(\delta r)\frac{e^{-(\delta a)^2/8}}{\beta} \times \left[\frac{(1+H_1)e^{\beta l}e^{\beta z}+(1-H_1)e^{-\beta l}e^{-\beta z}}{(1+H_0)(1+H_1)e^{\beta l}-(1-H_0)(1-H_1)e^{-\beta l}}\right] d\delta \quad (38)$$

where $H_0=h_0/k\beta$ and $H_1=h_1/k\beta$. The heat conduction to the gas surrounding the slab is neglected due to its low thermal conductivity. Can be considered two main different cases: thermally thin (l<<μ) and thermally thick (l>>μ) slab for isotropic slab [195].

For thermally thin, with a tightly focused beam it is possible to reduce the equation to:

$$T_{ac}(r \to \infty, a = 0) \cong \frac{P_0}{4\pi kl}\sqrt{\frac{\pi}{2}}\frac{1}{\sqrt{\sigma_R' + i\sigma_I'}}\frac{e^{-\sigma_R' r}}{\sqrt{r}}e^{-i\sigma_I' r} \quad (39)$$

where σ_R' and σ_I' are the real and the imaginary parts of σ'. It is possible to see that the phase of the temperature has a linear dependance on r whose slope is $m_\Psi = -\sigma_I'$. Thus, the natural logarithm of the amplitude multiplied by the square root of r has a linear dependence on r too, whose slope is $m_{\ln(\sqrt{r}T)} = -\sigma_R'$. It can be noticed which both slopes are affected by heat losses so, to avoid the influence of losses in measurements, it is

necessary to consider the product $m_{\ln(\sqrt{r}T)} \times m_\psi = {}^{-\pi f}/_{\alpha}$ to obtain the thermal diffusivity for slab [195]. Finite laser spot sizes ($a \neq 0$) only affect the shape of the temperature amplitude and phase close to the laser spot, while at large *r* distances both slopes remain unchanged [195].

For thermally thick, the temperature can be described by the following relation:

$$T_{ac}(r, z=0) = \frac{P_0}{4\pi k}\int_0^\infty \delta\, J_0(\delta r)\frac{e^{-(\delta a)^2/8}}{\beta+\frac{h_0}{k}}\, d\delta \tag{40}$$

which has no analytical solution thus, from numerical simulations, several conclusions have been obtained. In the absence of heat losses, the natural logarithm of the amplitude multiplied by *r* and the phase shows a linear dependence on *r* with the slope $m = -\sqrt{{}^{\pi f}/_{\alpha}}$. The effect of heat losses is to change slopes in the same way as happens with thin slabs. However, this change in slope is not the same for the amplitude as for the phase and therefore their product does not give the thermal diffusivity of the sample $m_{\ln(\sqrt{r}T)} \times m_\psi \neq {}^{-\pi f}/_{\alpha}$. Anyway, it is worth mentioning that the effect of heat losses in thick samples is small even for samples of low thermal conductivity. Only at very low frequencies these losses should be taken in account [195].

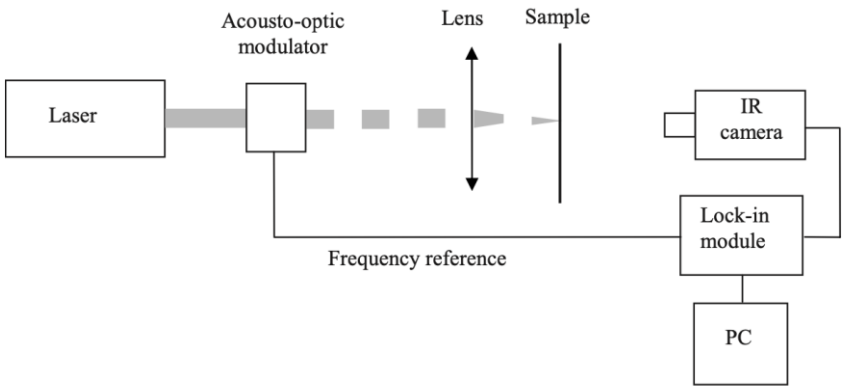

Figure 110. Scheme of experimental set-up adopted from Mendioroz et al [195].

In **Figure *110*** the scheme of experimental transmission set-up used in the described work [195].

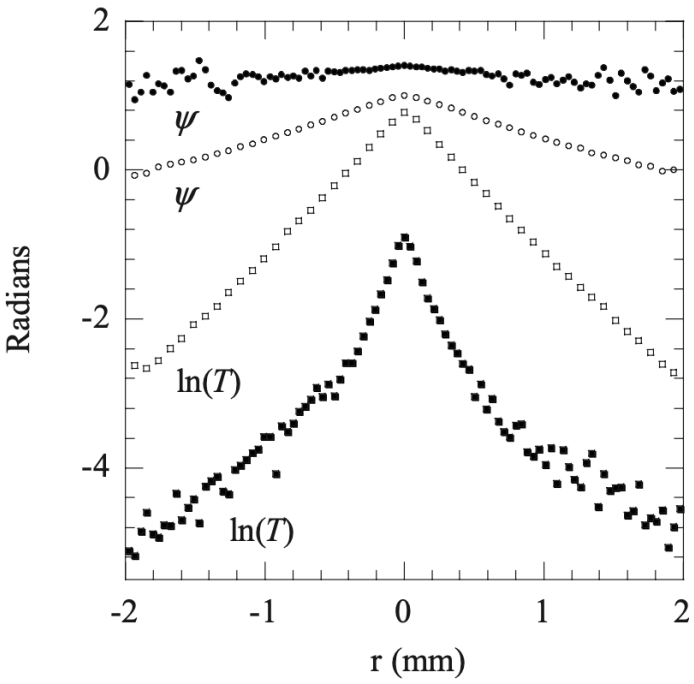

Figure 111. Example of results from Mendioroz et al. [195] work in which is reported the natural logarithm of the amplitude and phase of the surface temperature at a modulation frequency of 0.12 Hz.

In **Figure *111*** is depicted an example of the experimental results obtained by Mendioroz et al. [195], that shows the natural logarithm of the amplitude and phase of the surface temperature of a *34 μm* diameter PEEK filament measured in vacuum (open squares) and in air (solid squares) at a modulation frequency of 0.12 Hz.

One of the main advantages of the described method is that permits the evaluation of thermal diffusivity in isotropic and anisotropic materials, considering if it is thermally thin or not. The cons are that is in transmission and space and complex set-up is needed

In 2012, Bouè et al. [196], presented a protocol for measurement of thermal diffusivity and conductivity through the IR thermography. In the work ,a polymeric specimen has been investigated and a Peltier module has been adopted as heating source using a transmission set-up. Considering the equation of heat diffusion obtained applying the energy conservation to the Fourier equation, it is possible to obtain:

$$\rho c \frac{\partial T}{\partial t} - \nabla \cdot (\nabla T) = s \tag{41}$$

where ρ is the material density $[kg/m^3]$, c the specific heat $[J/kgK]$, s represents the heat source $[W/m^3]$, T the temperature and t the time instant considered. The solution to the equation above, considering hypothesis of homogeneous material, uniaxial heat flux in direction of thickness of the specimen and homogeneous heating distribution, can be written as [196]:

$$\rho c \frac{\partial T(z,t)}{\partial t} - k \frac{\partial^2 T(z,t)}{\partial z^2} = s(z,t) \tag{42}$$

It can be assumed that, for a finite body with thickness *d*, the temperature on the upper surface *(z=0)* is $T_m e^{i\omega t}$ with ω angular frequency. In addition, the flux is assumed to be zero for *z=d*, resulting in:

$$T(z,t) - T_0 = T_m \frac{cos\left(\frac{(i-1)(z-d)}{\mu}\right)}{cos\left(\frac{(i-1)d}{\mu}\right)} e^{i\omega t} \tag{43}$$

In the relation above, T_0 it is the starting temperature, $i = \sqrt{-1}$ and $\mu = \sqrt{2\alpha/\omega}$ that represent thermal length diffusivity. Thus, it is possible to define a phase contrast defined as the difference between the temperature signal on the heated surface and the opposite ones.

$$\Delta\varphi = \arg(T_{z=d}) - \arg(T_{z=0}) \cong \frac{d}{\mu} \tag{44}$$

This expression is all the more correct the more the thickness *d* is bigger than the thermal length diffusivity, thus the accuracy increases with higher values of the ratio d/μ, which can be considered suitable for values of ratio higher than 2[196].

It is possible to obtain the value of thermal diffusivity as:

$$\alpha = \frac{\omega}{2}\left(\frac{d}{\Delta\varphi}\right)^2 \tag{45}$$

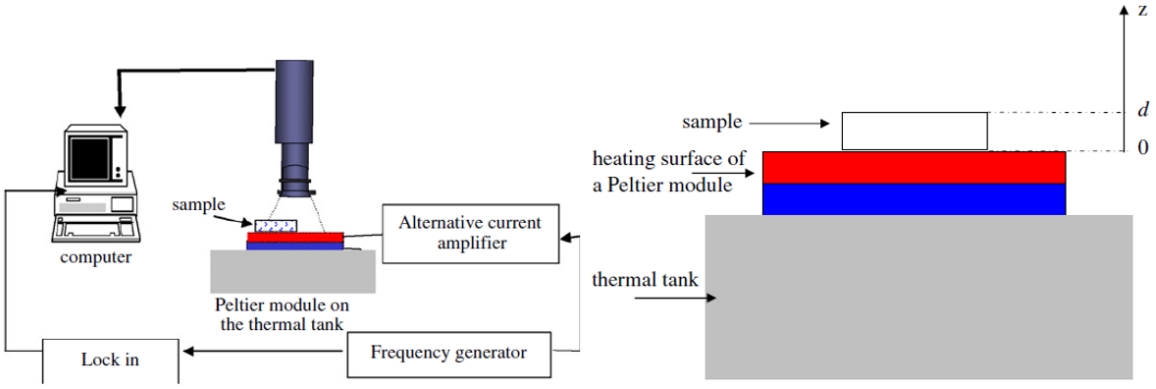

Figure 112. Set-up scheme of described test in reflection mode by Peltier module [196].

In the research work of Bouè et al. [196], to the Peltier module a current with frequency *f* has been applied. As showed in **Figure *112***, the back surface is in contact with the module while the opposite surface, the frontal one, it is recoded by camera. It must be observed that, in the recording window, the frontal surface is recorded but a part of Peltier module too, in order to evaluate, and hypnotize reasonably, that the phase of the Peltier module coincident with the back surface of plate. As values for φ_0 (for the module phase) and φ_1

(for the frontal surface), the average values are considered in inspected areas as highlighted in **Figure** ***113***.

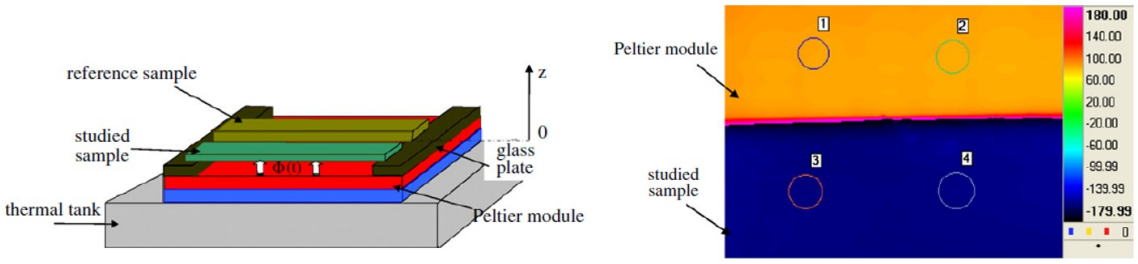

Figure 113. Scheme specimens positioning on Peltier module and indication of region if interest (circles on thermal image) [196]

Adopting the previous relations, it is possible to obtain the value of the material thermal diffusivity.

This method presents several cons as: the complexity of set-up, long time is needed for test, the transmission set-up needs space, and it is needed to have a Peltier module with dimension suitable with component to analyze.

Another method for measurement of thermal diffusivity by lock-in thermography has been developed in 2014 by Giri et al. [197], which consists in the heating of the component by a circular laser spot, generating a modulated thermal wave, than an analysis of phase map in one direction on the heated plan, must be done. Using several tests with different values of frequency for modulated heating, after the evaluation of slope of linear part of profiles, it is possible to estimate thermal diffusivity.

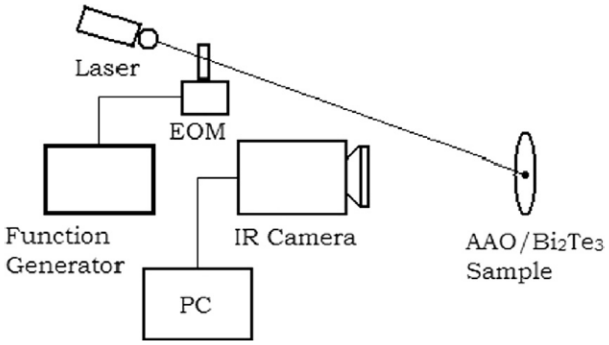

Figure 114. Scheme of reflection set-up used for thermal diffusivity evaluation in work of Giri er al [197].

Considering the hypothesis of a modulated thermal wave with a pint-shape source, unidimensional, in an isotropic and homogenous material, it is possible obtain the following expression which relates the thermal diffusivity value with heating frequency and with the value of the slope of phase profile in defined direction [197].

$$\alpha = \frac{\pi f}{\left(\frac{\varphi}{L}\right)^2} \tag{46}$$

In the relation above, f is the heating frequency, the ratio $\frac{\varphi}{L}$ is the slope of linear part of in-plane phase variation in the considered direction. A modulated heating is produced on the surface of the component analysing the phase profile along a diameter in-plane, as showed in **Figure *115***.

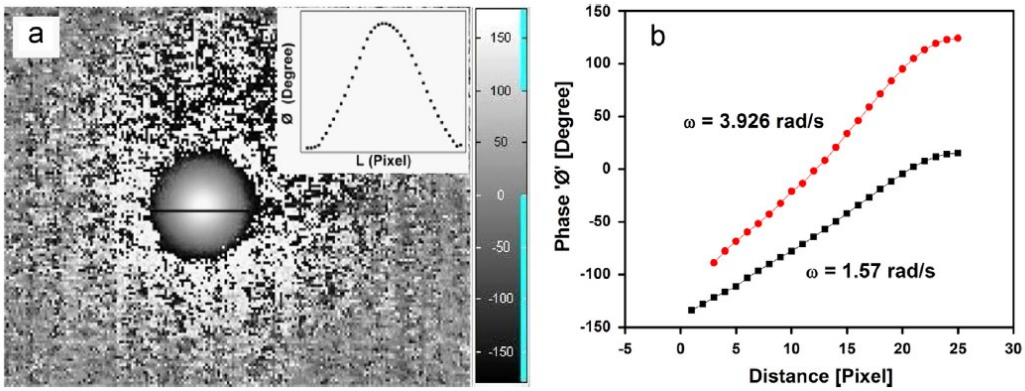

Figure 115. (a)Phase image of the experimental test conducted by Giri et al., (b) linear part of the in-plan phase [197]

It is possible to see in **Figure *115*** how the behavior of the phase can be described as a straight line in the area distant from the center of laser spot and how the slope of the signal is related to the heating frequency. It is necessary to perform several tests with different values of frequency to obtain relative phase values. Observing the values of the phase as a function of the square of the correspondent slope value, it is possible to measure thermal diffusivity through the relation reported above.

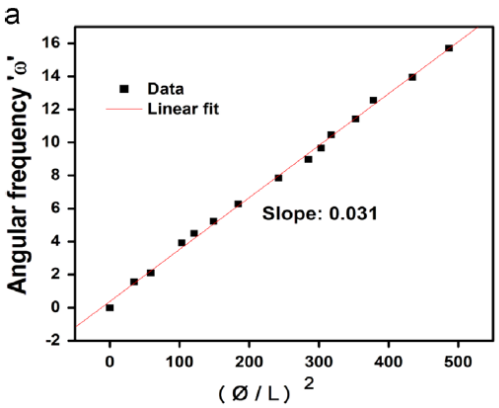

Figure 116. Modulation behaviour as a function of the square of the slope of the regression straight line. [197]

In the work of Strzał kowski et al. [198], a laser heat source has been used for the heating of surface in reflection mode. The phase value along the surface has been investigated and through an easy relation, the value of in-plane thermal diffusivity can be measured.

Through the heat diffusion equation 1D is possible to obtain the equation of thermal wave relative to a point-shape heating for an isotropic and homogeneous material:

$$T(x,t) = T_0 e^{i\left(\omega t - \sqrt{\frac{\pi f}{\alpha}}x\right)} \tag{47}$$

where x is the direction of propagation of thermal wave, the T_0 is the starting temperature on the surface, f the frequency of modulated thermal wave and α the value of thermal diffusivity in x direction. Considering the propagation of thermal wave in x direction, it is possible to write the relation that relates the thermal diffusivity with phase difference on the surface:

$$\Delta\varphi = -\sqrt{\frac{\pi f}{\alpha}}x = ax \tag{48}$$

Where a is the reciprocal of μ which is the thermal diffusion length.

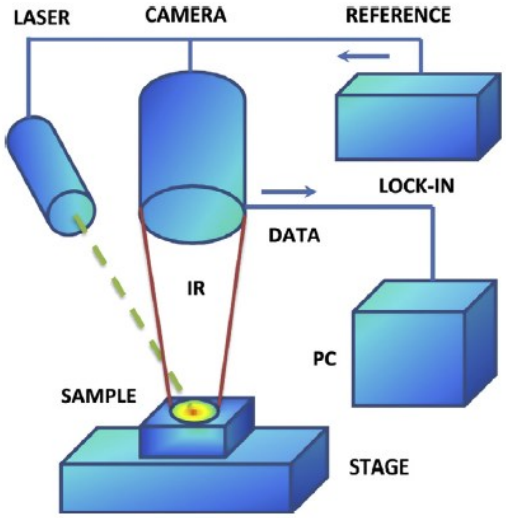

Figure 117. Reflection setup used for experimental phase in work of Strzalkowski et al. [198]

Considering the set-up in **Figure *117***, it is possible obtain thermal diffusivity analyzing the phase variation in a specific direction on the surface. In **Figure *118***, it is evident the symmetric behavior in side parts, thus a linear fitting of data can be used to obtain the value of thermal diffusivity by the regression straight line slopes applying the equation (48).

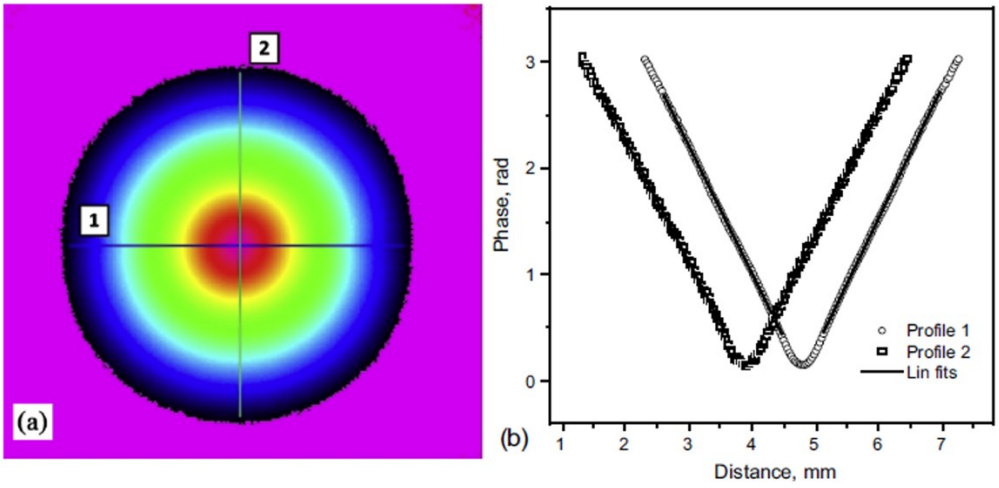

Figure 118. (a) Distribution of phase signal of thermal wave on surface (b) Values of phase along direction 1 and 2 with linear fitting of the curves obtained experimentally from Strzalkowski et al. [198].

An evaluation about the angle between laser source and optical axis of the IR camera it is important because can results in a measurement error of thermal diffusivity.

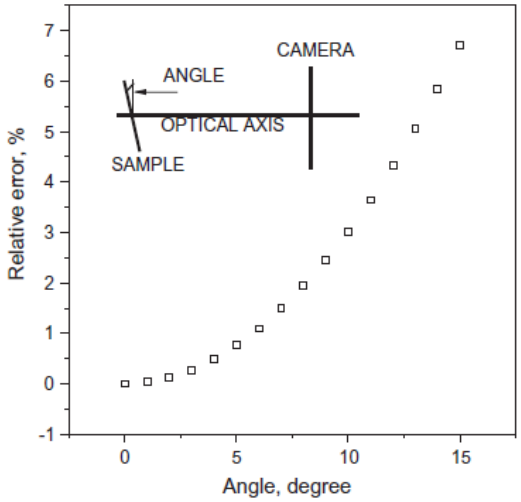

Figure 119. Measurement error in thermal diffusivity measurement as function of optical axis of IR camera and laser source obtained from Strzalkowski et al. [198].

In **Figure *119***, it possible to observe that for angle lower than 5% the measurement error estimated can be considered lower than 1%, although this value increases rapidly when the value of the angle grows [198].

The method presented is very easy to apply and permits to reduce space needed for setup, which is crucial especially for in-situ and on component applications. Another huge pro is that is possible to measure the thermal diffusivity in two different directions in-plane with only a measurement, which is interesting in case of anisotropic material.

In 2017 Nolte et al.[199], developed a laser method for the measurement of thermal diffusivity through thermographic non-destructive methods. This method uses the laser

heating on a specimen with a transmission set-up, thus heating a surface of specimen and recording the opposite ones. The described technique consists in producing a modulated heating on the specimen, considering several frequencies, and obtaining the behavior of phase contrast as function of heating frequencies. The slope of this curve is related to the thermal diffusivity.

Considering the solution to the heat diffusion equation:

$$\rho c \frac{\partial T(z,t)}{\partial t} - k \frac{\partial^2 T(z,t)}{\partial z^2} = s(z,t) \tag{49}$$

with hypothesis of homogeneous isotropic material, thermal flux 1D in the thickness direction and pulse $\omega = 2\pi f$, it is possible to use the following relation [199]:

$$T(z,t) = \frac{A}{d} e^{-\frac{d}{\mu}} \cdot e^{i\left(\omega t - \frac{d}{\mu}\right)} \tag{50}$$

In the relation 50, A is the amplitude of heating excitation, d the thickness of body, μ thermal diffusivity length. The phase shift in thermal wave $\Delta\varphi_{wave}$ on the back surface of specimen, the opposite ones to the heated surface by a point-shape heating source, can be expressed as the ratio between d and μ. The total phase contrast can be evaluated as the difference between the thermal heating wave and system ones. Hence it is possible to define b as showed below [199]:

$$b = d\sqrt{\frac{\pi}{\alpha}} \tag{51}$$

$$\varphi = \varphi_{system} - \varphi_{wave} = \varphi_{system} - {}^{d}/_{\mu} = \varphi_{system} - b \cdot \sqrt{f} \tag{52}$$

The frequency value has been varied in a specific range and the related value of phase shift has been plotted as function of heating frequency. Using a curve fitting on the obtained data, through the b value, a correspondent value of thermal diffusivity can be obtained.

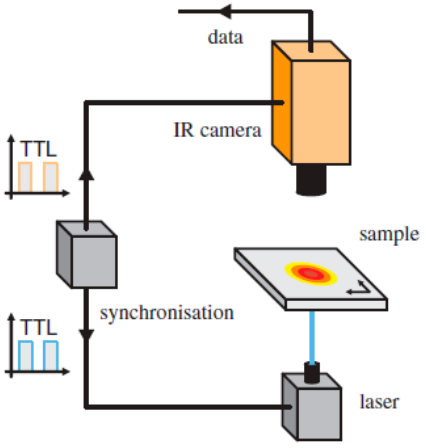

Figure 120. Scheme of experimental set-up adopted by Nolte et al [199].

In **Figure *120*** the experimental set-up scheme adopted by Nolte et al. [199] has been reported.

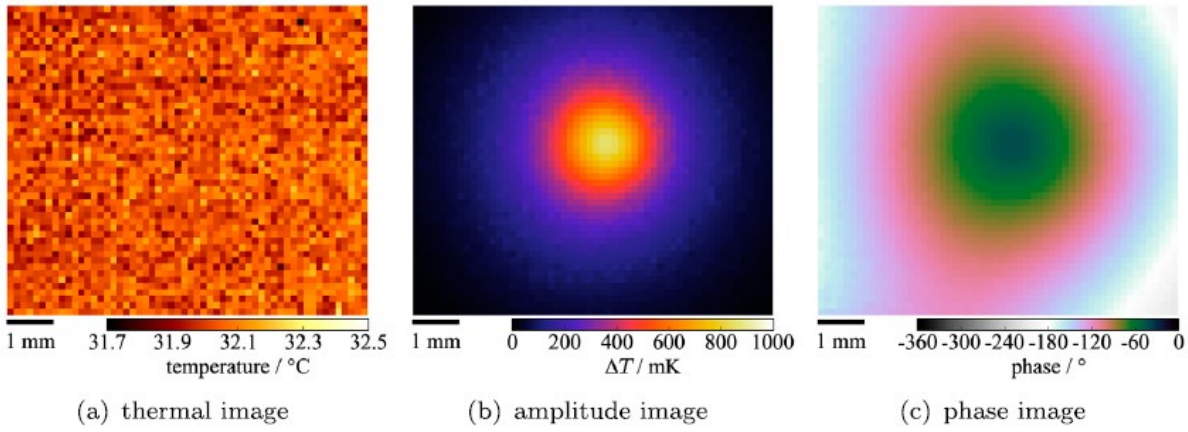

Figure 121. Images obtained for laser heating by Nolte et. al (a) of temperature, (b) amplitude and (c) phase [199]

In **Figure *121***, the results obtained by thermal, amplitude and phase images are reported. To evaluate the total phase contrast, an averaged value in the region with maximum amplitude value have to be considered.

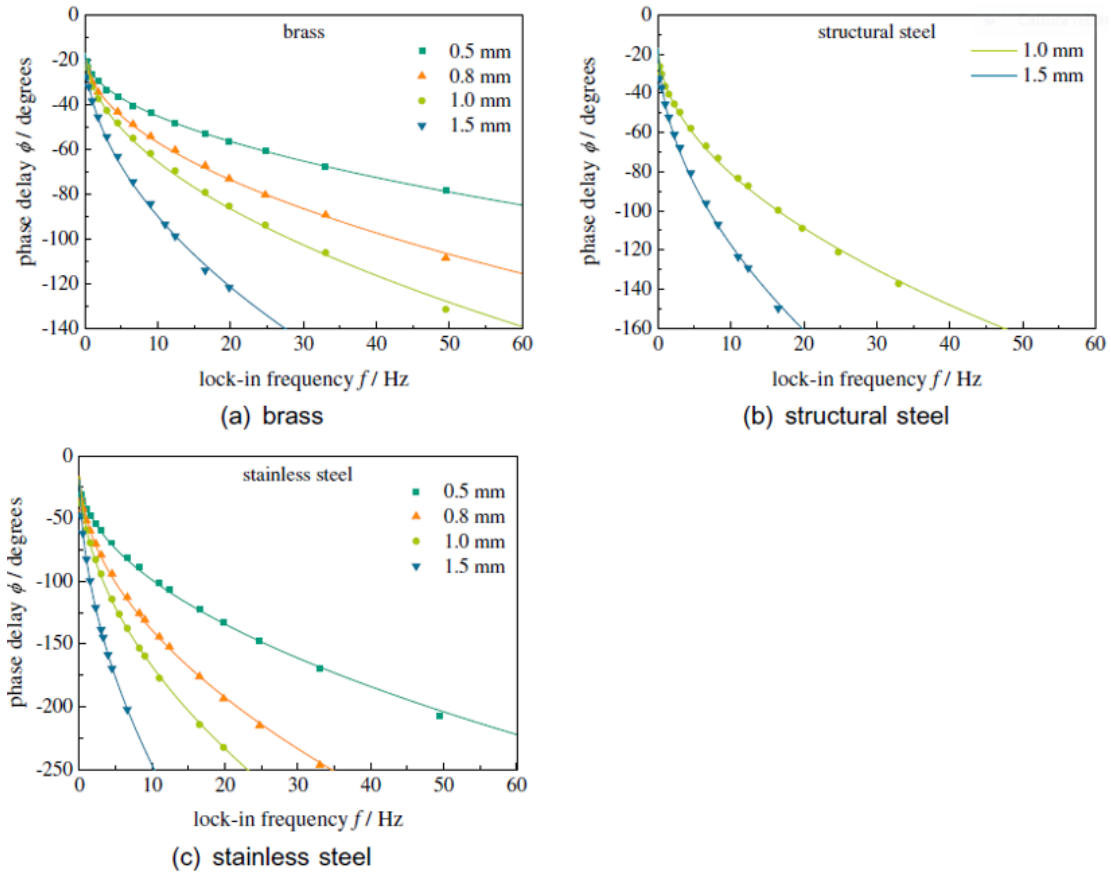

Figure 122. Phase shift curves normalized in respect of the thickness, as function of heating frequency. (a) brass, (b) structural steel and (c) stainless steel

To verify the method, in the cited study [199], this one has been applied to three different materials with results curves reported in **Figure *122***.

Observing the curves in **Figure *122***, it is possible to see how, through the experimental data fitting, it is possible to obtain the value of *b* connected to the value of thermal diffusivity. These values permit to have suitable measurements only if the value of thickness $d>2\mu$. Moreover, considering that the model adopted is a 1-D model, the value of thermal diffusivity obtained is the value in the thickness which is coincident with the value of α in all directions, only in case of isotropic material.

The main cons of the method described is that several measurements at different frequencies are needed to obtain a value of thermal diffusivity. Moreover, there is a big limitation about specimens with the value of *d* comparable with the μ ones.

The main advantage is in the use of laser which permits to manage efficiently and precisely the heat source power on the surface of specimen.

One of the most interesting and recent works about the thermographic lock-in methods to measure thermal diffusivity, has been presented by Salazar et al.[200,201] presented in 2020. In the cited work, a laser modulated spot heat source has been used but on a sample with a constant speed on a straight-line trajectory.

This procedure is based on the theoretical model below, under the hypotheses of semi-infinite opaque body, constant speed, Gaussian heat distribution in spot laser modulated with a frequency *f*. Considering the solution of heat diffusion equation, it is possible to write:

$$\nabla^2 T(\vec{r},t) - \frac{1}{\alpha}\frac{\partial T(\vec{r},t)}{\partial t} - \frac{v}{\alpha}\frac{\partial T(\vec{r},t)}{\partial x} = 0 \tag{53}$$

In the equation 53, α is the thermal diffusivity and v the relative speed between specimen and heating source. Under these conditions, it is possible to obtain the temperature as described below:

$$T(x,y,t) = \frac{P_0}{2\varepsilon\sqrt{\pi^3}}\int_0^t \frac{1}{\sqrt{t-\tau}}\frac{e^{-\frac{2\{[x-v(t-\tau)]^2+y^2\}}{a^2+8\alpha(t-\tau)}}}{a^2+8\alpha(t-\tau)}e^{i\omega t}d\tau \tag{54}$$

in which ε is the thermal effusivity, P_0 the laser power, *a* the radius of Gaussian profile evaluated as the distance from the center of spot in which the signal value is $1/e^2$. It is possible to re-arrange the equation and write it as:

$$T(x,y,t) = \theta(x,y)e^{i\omega t} = |\theta|e^{i\varphi}e^{i\omega t} \tag{55}$$

In the above equation, θ represents the component in space of superficial temperature, $|\theta|$ and φ the amplitude and angle, respectively.

Evaluating the amplitude and phase maps (**Figure *123***), it is possible, through the relations that will be described below, to obtain thermal diffusivity in direction of motion and in the perpendicular ones too [200,201].

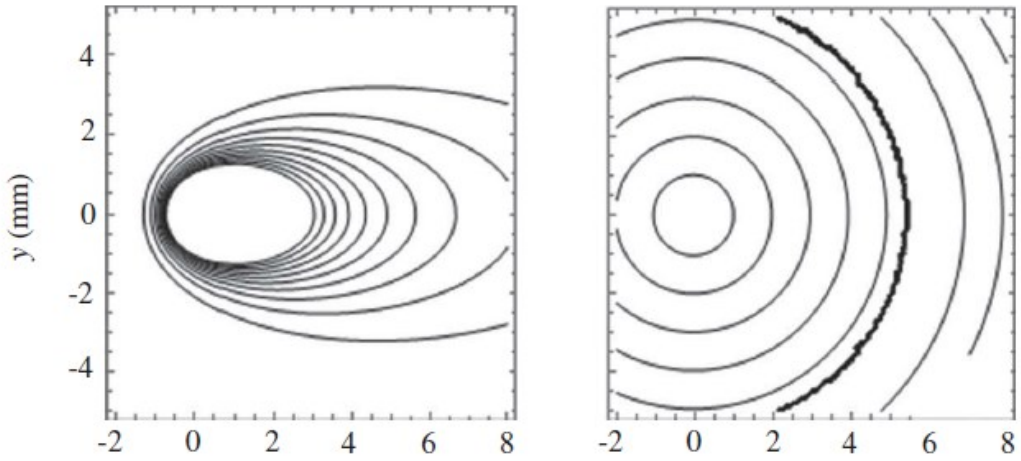

Figure 123. (a) Amplitude map on the surface after heating by described technique. (b) The relative phase map [200,201].

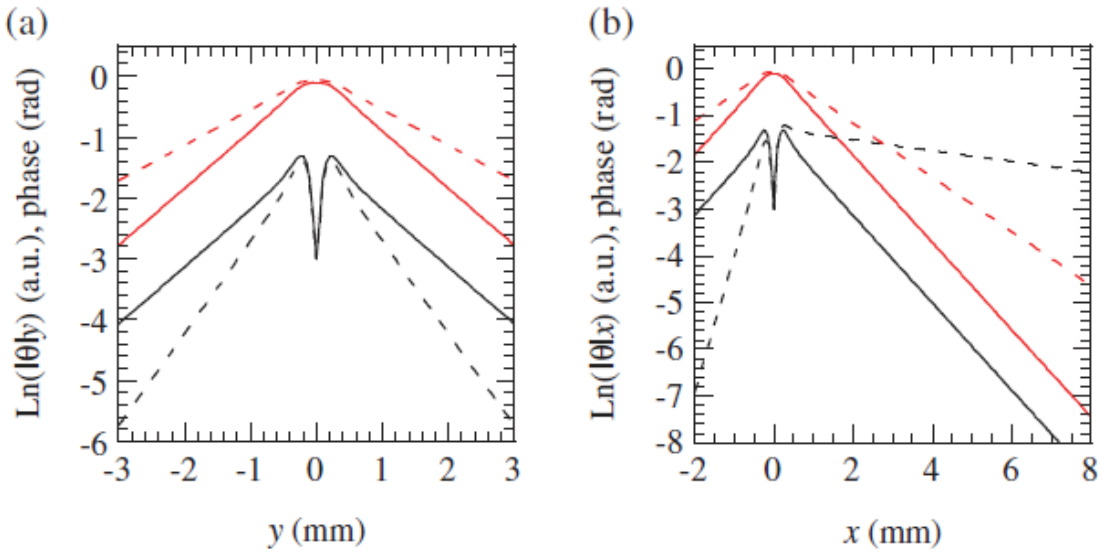

Figure 124. With solid line the LN of amplitude (black) and phase (red) for static test. With dashed lines results for moving sample obtained by Salazar et. al. [200,201].

In **Figure *124*** (a) can be observed that increasing the speed of specimen, the slope of linear part of curve increases for logarithm of amplitude and decreases for phase; thus, it is possible to relate the thermal diffusivity in this direction evaluating the product of slopes obtained from phase and amplitude signals.

$$m_{Ln(|\theta|y)} \times m_{\varphi} = \frac{\pi f}{\alpha} \tag{56}$$

In **Figure *124*** (b), the dashed red line retains an axial symmetry, instead of logarithm of amplitude. Hence, it is possible to obtain thermal diffusivity in direction of motion applying the relation below through the slopes obtained only from phase results:

$$m_{\varphi} = \sqrt{\frac{\pi f}{\alpha}} \sqrt{\frac{31.90}{31.90+\left(\frac{v^2}{\alpha f}\right)^{1.1813}}} \tag{57}$$

To evaluate the developed method, in the considered work, a comparison among values of thermal diffusivity obtained experimentally, applying the procedure described, and literature results for AISI 304 has been carried out.

The main advantage of the presented method is the possibility to investigate large parts and can be adopted in line, for example, during the motion of component in production line.

Among all the methods for thermal diffusivity measurement by lock-in thermography, only the most common have been reported and suitable with possible applications.

In the next section, pulsed and long pulsed method for measurement of thermal diffusivity by thermography, will be presented.

4.1.3 Thermal diffusivity measurement by pulsed thermography

The methods for evaluating the thermal diffusivity using pulsed thermography are more numerous than those that use lock-in, because they generally involve simpler instrumentation compared to that of LT and shorter test times, requiring only a thermal pulse.

The most common and well-established thermographic method to measure thermal diffusivity has been presented by Parker et al. in 1961 [127]. This method, based on flash thermography, is one of the reference methods; in fact, the standard ISO 22007-2 has been based on this procedure. Considering the solution of the Fourier heat equation, under the hypotheses of homogeneous body with thickness L, adiabatic heating after a Dirac pulse, considering a one-dimensional heat diffusion 1D, it is possible to obtain the expression for the temperature as a function of time t and the distance from the heated source in depth direction x.

$$T(x,t) = \frac{1}{L}\int_0^L T(x,0)\,dx + \frac{2}{L}\sum_{n=1}^{\infty} e^{\left(\frac{-n^2\pi^2\alpha t}{L^2}\right)} \times \cos\frac{n\pi x}{L}\int_0^L T(x,0)\cos\frac{n\pi x}{L}dx \tag{58}$$

in which the thermal diffusivity is reported with α. In case of pulsed heating with energy density *Q* homogeneously distributed in infinitesimal layer indicated by *g*, on the surface *(x=0),* it is possible to write [127]:

$$T(x,0) = {}^{Q}/_{\rho c g}\,, \qquad 0 < x < g$$

$$T(x,0) = 0\,, \qquad g < x < L$$

Considering initial conditions, it is possible re-write the equation as follows:

$$T(x,t) = \frac{Q}{\rho c L}\left[1 + 2\sum_{n=1}^{\infty} cos\frac{n\pi x}{L}\frac{sin\left({}^{n\pi g}/_{L}\right)}{\left({}^{n\pi g}/_{L}\right)} \times e^{\frac{-n^2\pi^2}{L^2}\alpha t}\right] \tag{59}$$

that, for the back surface of specimen *(x=L)*, because of the set-up in transmission mode, become:

$$T(L,t) = \frac{Q}{\rho c L}\left[1 + 2\sum_{n=1}^{\infty}(-1)^n \times e^{\frac{-n^2\pi^2}{L^2}\alpha t}\right] \tag{60}$$

Two dimensionless parameters can be defined as follows [127]:

$$V(L,t) = {}^{T(L,t)}/_{T_m}\,; \qquad \omega = \frac{\pi^2 \alpha t}{L^2}. \tag{61-62}$$

in which T_m is the maximum value of temperature after heating. Combining the relations reported above, after a few considerations, it is possible to obtain the value of thermal diffusivity in *x* direction [127].

$$V = 1 + 2\sum_{n=1}^{\infty}(-1)^n e^{-n^2\omega} \tag{63}$$

Thus, fixing the value of *V=0.5,* and the value of ω=1.38, it is possible to write the equation as function of thermal diffusivity *α* and the value $t_{0.5}$ that indicates the time instant for which the back surface reaches the value of temperature *0.5* T_m [127].

$$\alpha = \frac{1.38L^2}{\pi^2 t_{0.5}} = \frac{0.139L^2}{t_{0.5}} \tag{64}$$

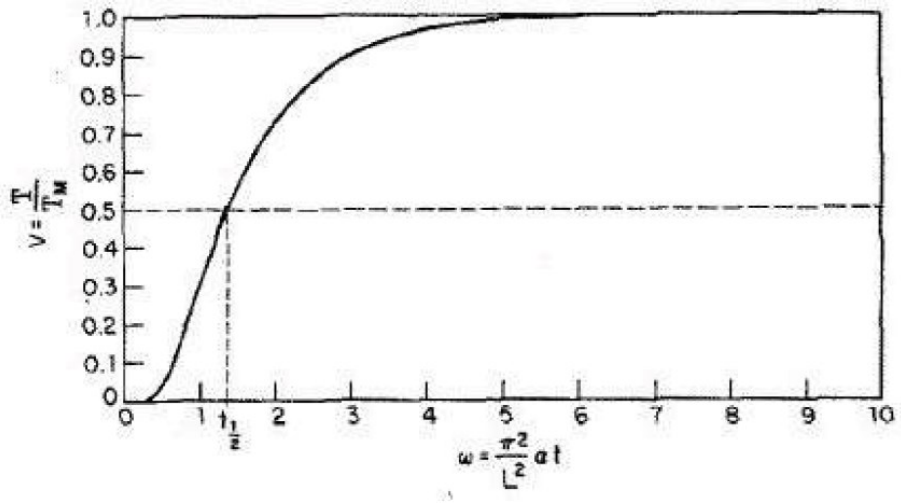

Figure 125. Behavior of V value as function of time. Dashed line is in correspondence of half-rising time necessary for thermal diffusivity estimation by Parker method [127]

The method is based on a flash test in transmission set-up, recording by IR camera the opposite surface as respect of the excited ones. In this case, the curve, as showed in **Figure *125***, has an asymptotic behavior (in adiabatic conditions) which is considered as the value T_m. Consequently, the curve must be normalized, thus it is necessary to divide by the maximum value of reached temperature, identifying the value of time for which the variable V reaches the value of 0.5. It is sufficient to know the thickness L of the plate to estimate a value of thermal diffusivity in x direction.

This method is spreadly used because it easy to apply and results are reliable, but some correction is needed to consider the finite pulse, especially in case of thin samples.

To obtain the correct thermal diffusivity values for flash measurements in transmission mode, a method has been developed by Azumi et al. [202]. This method consists of two steps: the first, adjustment for an "effective" irradiation time using the center of gravity pulse, and the second, the correction for the deviation in the parameter K from the ideal value of 0.139 reported in equation 65. In fact, instead of the relation used before for Dirac pulse, the following relation has been proposed:

$$\alpha = \frac{K_0 L^2}{t_{0.5}} \tag{65}$$

in which the value K_0 is a parameter that depends on heating shape and duration, and it is defined as $t_{0.5}/t_0$. Basing on different possible shapes investigated in several works [203–207], the relation among K_0, τ, that is the pulse duration and t_c that is the characteristic rise time defined as $t_c=L^2/\alpha$, can be represented as $K_0=0.1388 + b\,\tau/t_c$. Thus, the dependence of K_0 on τ/t_c, which is denoted as b, can be changed by introducing a new time axis having

the same scale but the different origin. After shifting the time axis, the parameter K_g can be considered as:

$$K_g = \frac{(t_{0.5} - t_g)}{t_c} = K_0 - \frac{t_g}{t_c} \tag{66}$$

where t_g is the value of shift that can be obtained as follow:

$$t_g = \frac{\int_0^\tau t' f(t') dt'}{\int_0^\tau f(t') dt'} \tag{67}$$

It is now possible to express thermal diffusivity by the following equation:

$$\alpha = \frac{K_g L^2}{(t_{0.5} - t_g)} \tag{68}$$

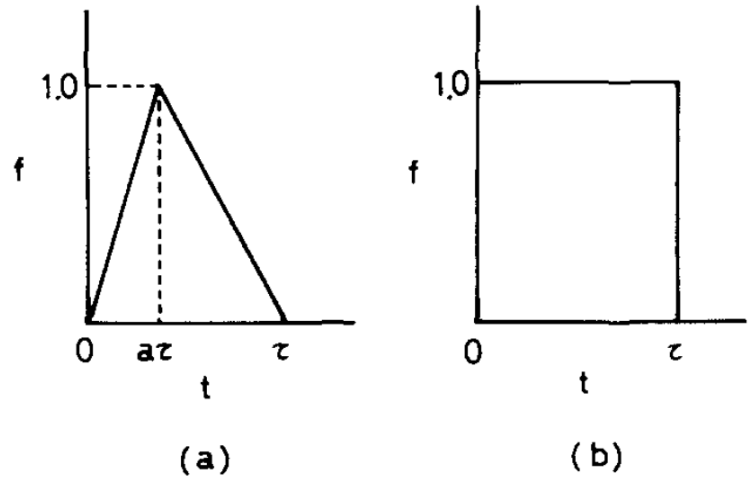

Figure 126. The pulse shaped assumed in calculations [202]

For shapes showed in **Figure *126***, the numerical values of K_0 and K_g normalized for the ideal case with *K=0.1388* have been calculated and resumed briefly in **Table *10***. With these values, it is possible to obtain the corrected values of thermal diffusivity, considering finite pulse, thus using a shift of the origin of time axis to take in account the relative duration of pulse, as respect of half rise time [202].

	Triangular pulse shape (a=0.25)		Rectangular pulse shape	
$t_{0.5}/\tau$	$K_0/0.1388$	$K_g/0.1388$	$K_0/0.1388$	$K_g/0.1388$
2	1.277	1.010	1.362	1.020
5	1.093	1.001	1.115	1.002
10	1.044	1.000	1.054	1.001
20	1.021	1.000	1.026	1.000

50	1.008	1.000	1.010	1.000

Table 10. Values of K_0 and K_g, normalized for the value of ideal case, K=0.1388 [202].

Using this procedure, it is possible to correct the value of the measurement for thermal diffusivity in transmission mode, considering a finite pulse width.

Based on the transmission set-up configuration, another method has been developed in 1996 by Brady et al.[208], which consists of the application of the finite difference method to solve the conduction problem in materials, considering the convective exchanges too.

Considering the problem of heat transmission in a thin plate thermally insulated with a surface heated by pulsed source, observing the opposite plate (**Figure *127***), the 1D model can be reported as:

$$\frac{1}{\alpha}\frac{\partial T}{\partial t} = \frac{\partial^2 T}{\partial x^2} \tag{69}$$

where T is the temperature at distance x from the heated surface, t indicates the instant after the start of heating pulse. Writing an energy balance between front and rear surfaces, it is possible to obtain the boundary conditions needed to solve the problem [208].

$$q'' = h(T - T_\infty) - k\frac{\partial T}{\partial x} \qquad \text{(rear surface)} \tag{70}$$

$$-k\frac{\partial T}{\partial x} = h(T - T_\infty) \qquad \text{(front surface)} \tag{71}$$

Thus:

$$q'' = \begin{cases} q''(t), & 0 < t \leq \tau \\ 0, & t \geq \tau \end{cases} \tag{72}$$

in which τ is the heating duration of flash lamps. Supposing to have, as the starting condition, the temperature of specimen equal to the ambient temperature T_∞ .

The parameters connected to the thermal phenomena *(q'', α, k* and *h)* are difficult to obtain, hence will be considered as unknown parameter in the relations which express q'' and divided for the product of density and specific heat of material [208]:

$$Q'' = \frac{q''}{\rho c_p}; \qquad H = \frac{h}{\rho c_p}; \qquad K = \frac{k}{\rho c_p} = \alpha \qquad (73 - 74 - 75)$$

After the substitution of described parameters, it is possible to solve di equations of heating transmission with numerical methods: in the presented work [208], the finite difference method. The solutions obtained through numerical methods are compared with experiments changing the values of Q'', H and K until a correspondence between experimental and numerical curves is obtained.

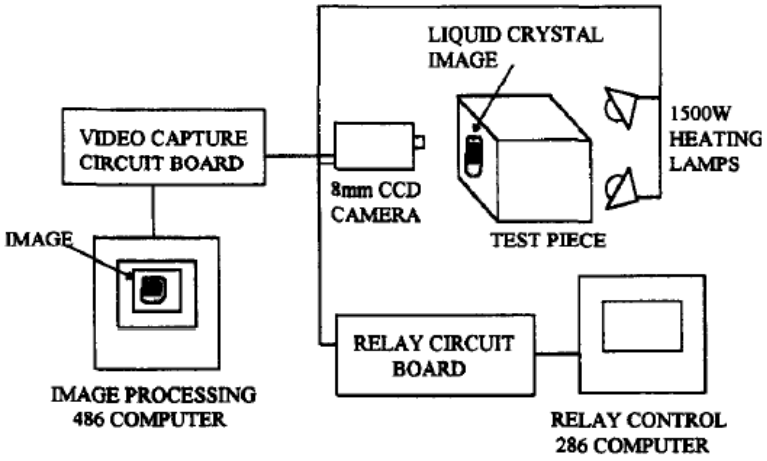

Figure 127. Experimental set-up adopted by Brady et al. [208]

Using the described procedure pixel by pixel, it is possible to obtain a map of thermal diffusivity in the component, although the finite difference method can be very computationally demanding. In the work presented by Brady et al. [208], three different materials have been considered, but only the map obtained for steel specimen has been reported in Figure **Figure *128***, as an example.

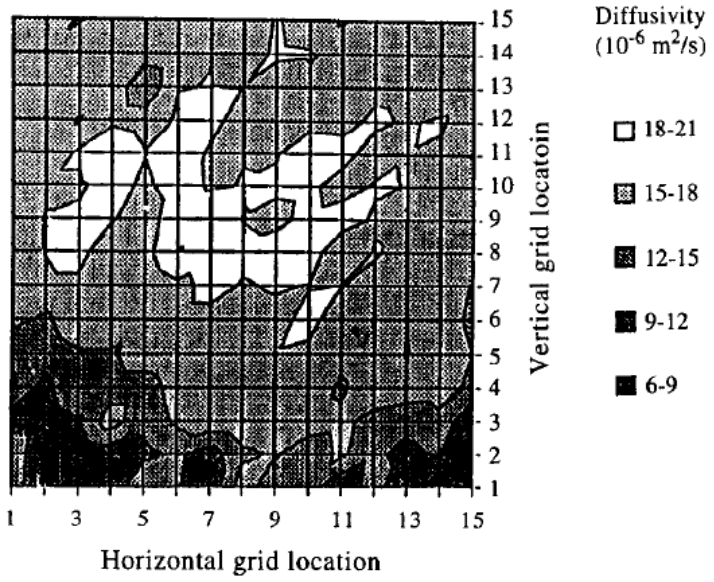

Figure 128. Example of thermal diffusivity map obtained for steel in research of Brady et al. [208]

An interesting method developed by Krapez in 2004 [209,210], after several works on the thermal properties of materials [211–214], is based on a pulse excitation in time but periodic in space, as well as in a work of Batsale (2005) [215], using a grid mask to generate a periodic illuminated pattern, in a specific direction of plate, as well represented in **Figure**

129. The method permits, through the application of the Fourier transform in space, to evaluate simultaneously the value of thermal diffusivity in z and x directions.

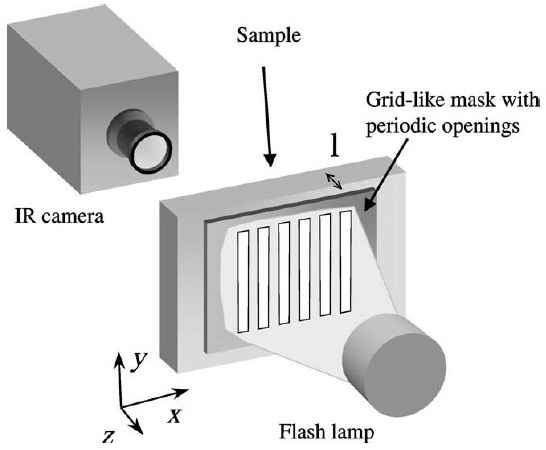

Figure 129. Setup scheme in transmission mode adopted to generate a periodic heating pattern on the surface in x direction [209].

To generate the space-periodic heating is possible to use a mask grid with specific geometry as showed in **Figure *129***.

The heat transmission model has been considered with the following hypotheses: planar infinite plate, thermally anisotropic, homogeneous, uniform thickness, uniform temperature at starting time, linear behavior of thermal losses on surfaces, Dirac pulse heating with a periodic spatial distribution (**Figure *130***).

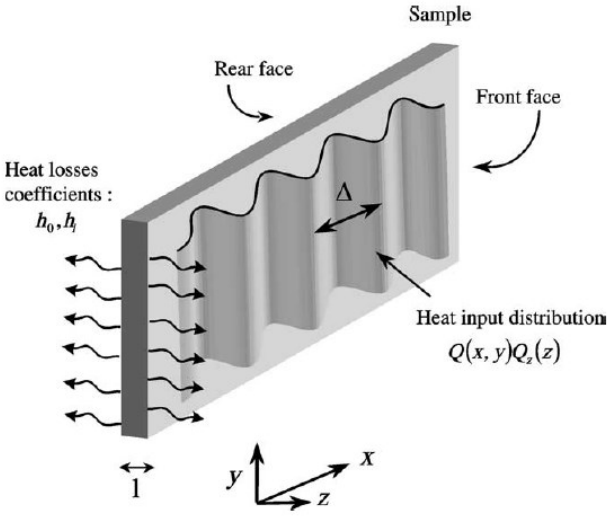

Figure 130. Representation of heating model considered by Krapez et al. [209]

The heat equations in the model, initial and boundary conditions are:

$$\rho C \frac{\partial T}{\partial t} = k_x \frac{\partial^2 T}{\partial x^2} + k_y \frac{\partial^2 T}{\partial y^2} + \frac{\partial}{\partial z}\left[k_z(z) \frac{\partial T}{\partial z}\right] \tag{76}$$

$$T(x,y,z,0) = \frac{Q(x,y)Q(z)}{\rho C} \tag{77}$$

$$-k_z \frac{\partial T}{\partial z}\Big|_{z=0} = -h_0 T(x,y,0,t) \tag{78}$$

$$-k_z \frac{\partial T}{\partial z}\Big|_{z=l} = -h_l T(x,y,l,t) \tag{79}$$

Through the Fourier-Laplace transform defined as following:

$$\tilde{\tilde{T}}(\omega_x,\omega_y,z,p) = \int_{t'=0}^{t'=\infty}\int_{x'=-\infty}^{x'=+\infty}\int_{y'=-\infty}^{y'=+\infty} T(x',y',z,t) \times e^{i\omega_x x'} e^{i\omega_y y'} e^{-pt'} dt'dy'dx' \tag{80}$$

it is possible to obtain:

$$\left(\rho C p + k_x\omega_x^2 + k_y\omega_y^2\right)\tilde{\tilde{T}} - \tilde{\tilde{Q}}Q_z(z) = \frac{\partial}{\partial z}\left[k_z(z)\frac{\partial \tilde{\tilde{T}}}{\partial z}\right] \tag{81}$$

in which, $T_z(z,t)$ is the solution in x and y to the diffusion heat problem in a plate uniformly heated with energy $Q_z(z)$ with 1D heat flux and thermal conductivity $k_z(z)$. The Laplace properties permits to write [209]:

$$\tilde{\tilde{T}}(\omega_x,\omega_y,z,t) = \tilde{\tilde{Q}}(\omega_x,\omega_y)T_z(z,t)e^{(-\alpha_x\omega_x^2 t - \alpha_y\omega_y^2 t)} \tag{82}$$

where α is the thermal diffusivity and the footnote expresses the direction. Hence, the double Fourier transform of temperature $(\omega_x, \omega_y) = (0, 0)$ for all depths, thus the spatial integral in x and y directions have the exact evolution of temperature induced by an uniform heating with a thermal contribution of $\tilde{\tilde{Q}}(0,0)Q_z(z)$, but it can be considered valid for a finite plate only in cases of insulated boundaries. It is possible to assume the thermal diffusivity in z direction and that $Q_z(z)$ is a Dirac pulse. In this way, it is possible to evaluate the thermal diffusivity in z direction through well-established algorithms [216]. Considering the relation 82 re-written without T_z, the relation becomes [209]:

$$\frac{\tilde{\tilde{T}}(\omega_x,\omega_y,z,t)}{\tilde{\tilde{T}}(0,0,z,t)} = \frac{\tilde{\tilde{Q}}(\omega_x,\omega_y)}{\tilde{\tilde{Q}}(0,0)}e^{(-a_x\omega_x^2 t - a_y\omega_y^2 t)} \tag{83}$$

This relation can be used for all depths, especially on the front and back surfaces, considering the thermal losses in both.

Hence, it can be used a periodical distribution in x direction with period Δ. The temperature is integrated in y direction between -Y and +Y, using the Fourier transform in x direction.

$$\tilde{\tilde{T}}(\omega_x, 0, z, t) = \frac{1}{n\Delta}\frac{1}{2Y}\int_{x'=0}^{x'=n\Delta}\int_{y'=-Y}^{y'=+Y} T(x', y', z, t)\cos\omega_x x'\, dy' dx' \tag{84}$$

Thus, the linear relation can be used to measure thermal diffusivity in *x* direction:

$$Ln\left[\frac{\tilde{\tilde{T}}(\omega_x, 0, z, t)}{\tilde{\tilde{T}}(0,0, z, t)}\right] = Ln\left[\frac{\tilde{\tilde{Q}}(\omega_x, 0)}{\tilde{\tilde{Q}}(0,0)}\right] - a_x\omega_x^2 t \tag{85}$$

This expression is valid for the back surface *(z=0)*. Therefore, because of the periodic heat distribution, it is particularly interesting the Fourier transform at angular frequency $\omega_x = {}^{2\pi}/_{\Delta}$. Using a linear regression in log-log scale, it is possible to obtain the thermal diffusivity in *x* direction from the slope of regression straight line. In *y* direction the value of thermal diffusivity can be evaluated, using the same mask rotated of 90° and it can be repeated for each direction, until the boundary conditions are valid [209].

A way to extract local thermal data obtained by grid method, is to reduce the dimensions of domain on which the analysis is conducted. Instead of Fourier transform on a time window multiple of period, it is possible to limit the area smallest as possible, thus the Δ of mask. The data analysis can be done in this period, hence the temperature is evaluated first as average in *y* direction, to execute the following operations:

- The average of temperature in *x* direction, in the considered time window: this value of $T_0(t) \equiv \tilde{\tilde{T}}(0,0,0,t)$ has been used to evaluate the value of thermal diffusivity through the thickness $\alpha_z(x)$;
- Calculate $T_1(t) \equiv \left|\tilde{\tilde{T}}(\omega_x, 0,0,t)\right|$. Through the relation $Ln\left[\tilde{\tilde{T}}(\omega_x, 0, z, t)/\tilde{\tilde{T}}(0,0,z,t)\right] = Ln\left[\tilde{\tilde{Q}}(\omega_x, 0)/\tilde{\tilde{Q}}(0,0)\right] - \alpha_x\omega_x^2$, it is possible to obtain an estimation of thermal diffusivity in *x* direction.

Through the described method, it is possible to obtain the thermal diffusivity value in two different directions, one on the surface dependent on the orientation of the mask-grid and the other one through the thickness. This method has the advantage to obtain thermal diffusivity in two different directions with only one experimental test, thus the possibility to be applied on anisotropic materials too. The main cons are the mask-grid use and the computational load to evaluate the spatial Fourier transform.

A well-known procedure which permits to measure thermal diffusivity by thermographic method has been developed by Mayr [217] in 2011 obtaining thermal diffusivity maps for all the surfaces. The hypotheses on which is based the developed procedure are: isotropic

phenomena, homogeneous material, 1D flux and Dirac pulse. Basing on these hypotheses, it is possible to write the relation in log-log scale reported below, in which has a sufficiently linear behavior:

$$T(L,t) = \frac{Q}{\rho c L}\left[1 + 2\sum_{n=1}^{\infty}(-1)^n \times e^{\frac{-n^2\pi^2}{L^2}\alpha t}\right] \quad (86)$$

Usually, it is represented in log-log scale as a function of $1/t$, as reported in ***Figure 131***.

$$\Delta T = T(L,t) + \frac{1}{2}ln(t) \quad (87)$$

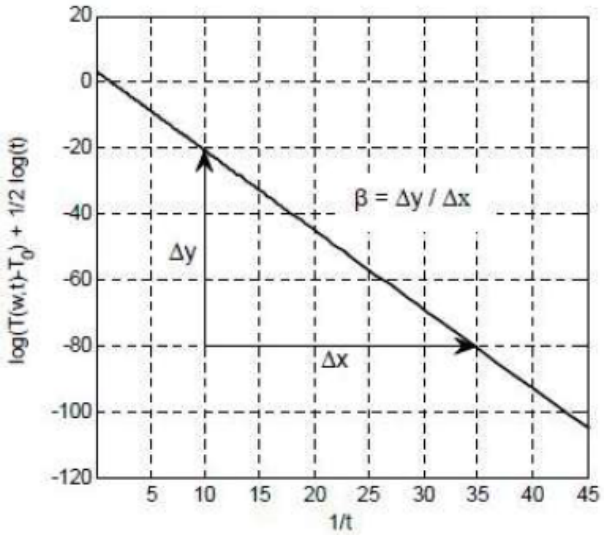

Figure 131. Linearization of described curve and related interval [217]

A central region of curve is considered to be sure about the linearity of curve, that is not present in extreme parts; in literature intervals of [$0.1\ T_{max}$; $0.9\ T_{max}$] or [$0.3\ T_{max}$; $0.8\ T_{max}$]. The slope of the considered line is used for the evaluation of the thermal diffusivity through the follow relation:

$$\alpha = -\frac{L^2}{4m} \quad (88)$$

in which m represents the slope of the regression straight line used for the curve fitting, for each considered pixel, that permits to obtain a map of thermal diffusivity as showed in **Figure *132*** [217].

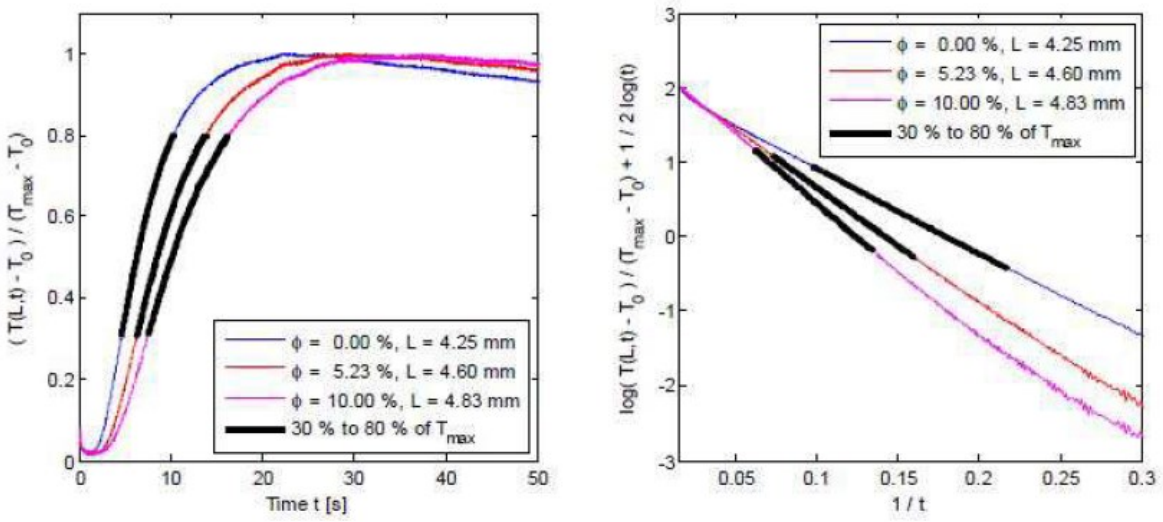

Figure 132. Curves obtained by experimental application of Mayr et al [217].

This method has the advantage to be slightly influenced by inhomogeneities of heating on surface and to results in a map of thermal diffusivity which permits evaluation of non-uniform distribution of thermal diffusivity.

On the same principle of Brady work [208] is based the method developed by Feuillet et al. [218] in which the analytical solution presented is more accurate, because the convective heat exchange on surfaces has been considered (**Figure *133***). Under the hypotheses of isotropic and homogeneous material, convective heat fluxes on surfaces and heating by a Dirac pulse, the solution can be written as:

$$\Delta T(z,t) = 2\Gamma \sum_{n=1}^{\infty} \frac{\xi_n \left[\xi_n \cos(\xi_n \delta) + B_0 \sin(\xi_n \delta)\right]}{\left({\xi_n}^2 + B_0^2\right)\left(1 + \frac{B_e}{{\xi_n}^2 + B_e^2}\right) + B_0} e^{\left(-\frac{\xi_n t}{\tau}\right)} \qquad (89)$$

in which:

$$B_0 = \frac{h_0 e}{k}; \qquad B_e = \frac{h_e e}{k}; \qquad \left(\xi_n^2 - B_0 B_e\right) tan\xi_n = (B_0 + B_e)\xi_n; \qquad (90-91-92)$$

thus ξ_n is the positive solution of the equation above [218].

The relations have been obtained for a transmission setup, to perform experimental data fitting partitioning the specimen surface in region of interest with dimensions 5x5 pixels. For each region, a value of thermal diffusivity can be obtained.

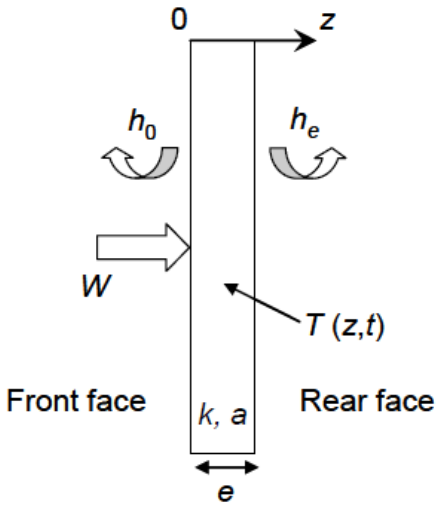

Figure 133. Model considered in work of Feuillet et al. [218]

In **Figure *134*** is represented an example of heating curve from a region of interest obtained experimentally and the related fitting. From this curveis possible to obtain values of thermal diffusivity for each region of interest and values of thermal conductivity too, both in depth [illegible]. This procedure can be very robust and adopted in reflection configuration too but, in that case, material must be isotropic [218].

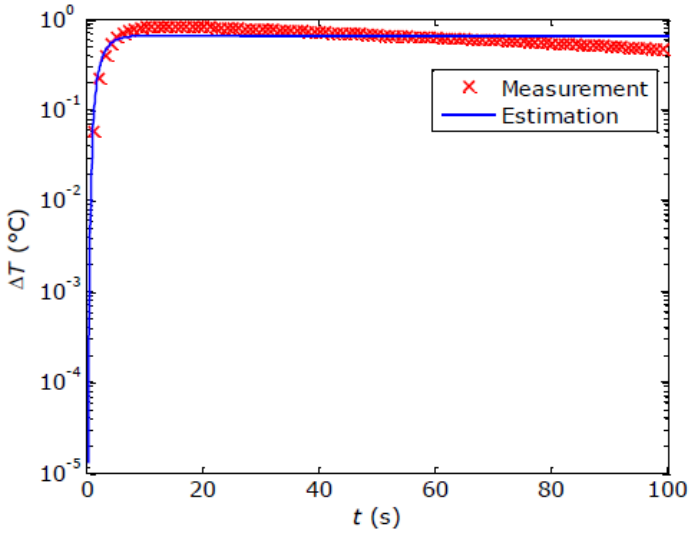

Figure 134. Example of experimental points and fitted curve obtained from work of Feuillet et al. [218].

In 2008 Laskar proposed a method based on the heating by a hot air flux with controlled temperature [219]. The used transmission set-up has been reported in **Figure *135*** and permits the evaluation of thermal diffusivity through the thickness direction.

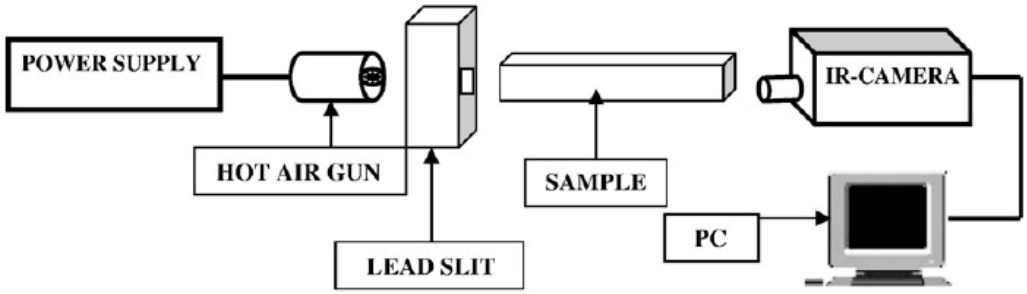

Figure 135. Experimental set-up scheme used by Laskar et al. using air-gun heating source [219].

To obtain the value of thermal diffusivity, a surface of specimen must be heated and the behavior of temperature on the opposite temperature must be observed by IR camera. To consider the heat losses, a correction term is included in the relation obtained for an isotropic and homogeneous material, subjected to continuous heating on a surface for a 1D heat flux:

$$T(l,t) = \frac{\dot{Q}}{kA}\sqrt{\pi(\alpha - l^2 h)t}\,\mathrm{erf}\left(\frac{l}{2\sqrt{(\alpha - l^2 h)t}}\right) \tag{93}$$

In which l is the thickness of the specimen, α the value of thermal diffusivity in thickness direction, h the heat losses. The correction term for thermal diffusivity is l^2h which introduces the heat losses. Usually, it is complicated to estimate the value of energy, although a few methods in literature are present[220,221], thus could be convenient to normalize the temperature respect to a temperature in a defined instant t_e [219].

$$\frac{T(l,t)}{T(l,t_e)} = \left[\frac{1}{\sqrt{t_e}\,erf\left(\frac{l}{2\sqrt{(\alpha - l^2 h)t_e}}\right)}\right]\sqrt{t}\,\mathrm{erf}\left(\frac{l}{2\sqrt{(\alpha - l^2 h)t}}\right) \tag{94}$$

The value of thermal diffusivity can be obtained by the best fitting of curve with the model described above, as showed in **Figure *136*** where are reported results obtained by Laskar et al. [219], from aluminum and copper plates.

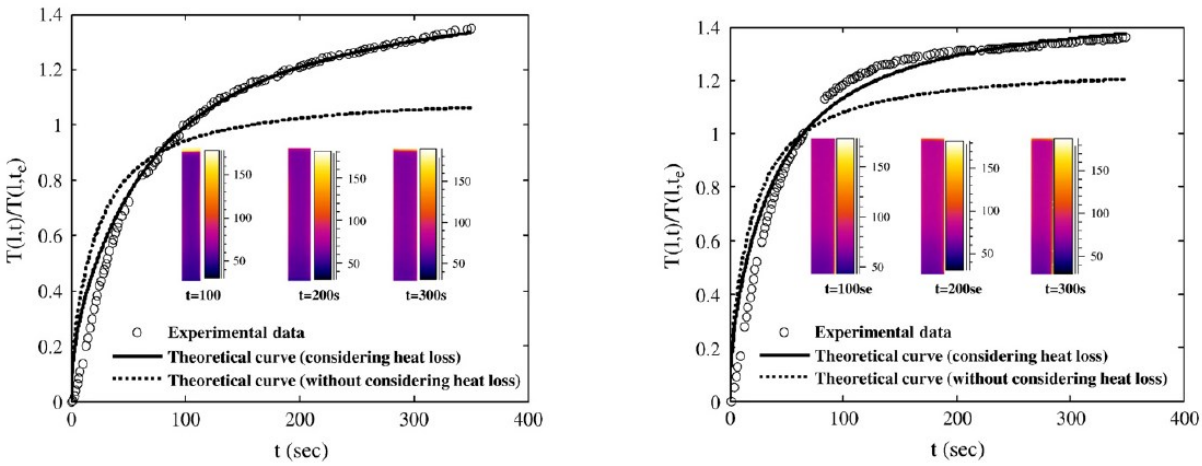

Figure 136. Theoretical curves and experimental data obtained by Laskar et al [219] for the evaluation of thermal diffusivity. To the left for aluminum and to the right for copper plates.

To apply this methodology, it is mandatory to know or estimate, considering some assumptions, the value of h before the fitting procedure to obtain the value of thermal diffusivity through the thickness.

The advantage of this procedure is that cheap equipment can be used, and heat losses can be included. The cons are the transmission configuration, which per the aim of this work is not convenient, and the steady state heat flux needed that can be increase the duration of thermographic test.

In the 2001 Albers et al. [222], used the laser heat source to apply pulsed thermography to measure thermal diffusivity. A study about the influence of the test parameters on the thermal diffusivity measurement has been presented by the authors. In fact, the test in transmission configuration, has been considered but two curves need to be analyzed: the first, named as VAL, which consider the start of heating of back surface coincident with the end of heating, the second, named as BEG, which consider the start of heating of front surface as the initial time closer to the real model. The used model is the one obtained using the hypotheses of 1D flux, homogeneous and isotropic material and a Dirac pulsed heating in adiabatic conditions. The formulation is the same used for the Parker method [127], discussed previously, but the difference is in the choice of starting time which is one of the main issues of this method.

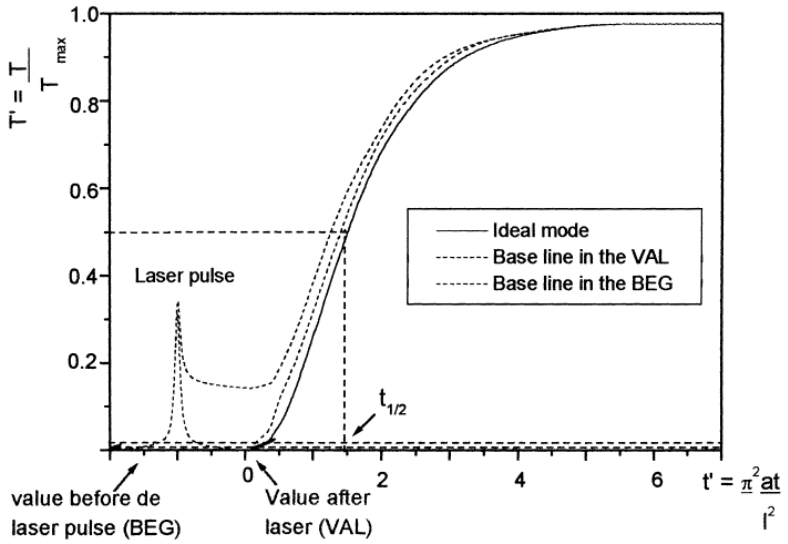

Figure 137. Heating curves used for transmission measurements by Albers et al. VAL, BEG and ideal curves are reported [222].

The choice between the two curves presented in **Figure *137*** influence the initial value, thus the value of half-rise time is influenced too with a difference in the value of thermal diffusivity obtained. Usually, the difference between the two curves can be considered neglectable in case of material with high values of thermal diffusivity, as the metals, but can influence the measurement if low thermal diffusivity materials are considered [222].

In 2016 Mayr et al.[223–225], proposed a method based on the flash pulsed thermography and reflection setup using the TSR method[226–229]. Considering the solution of heating equation in case of 1D heat flux, isotropic and homogeneous material, semi-infinite body and heated by a Dirac pulse in adiabatic conditions, it is possible to write, for the surface:

$$T(t,0) = T_0 + \frac{W}{e\sqrt{\pi t}} \tag{95}$$

in which T_0 is the initial value of temperature on the heated surface, W the value of energy incident on the surface and with e the thermal effusivity. Considering the logarithm of the relation and rearranging the terms, it is possible to obtain a straight line in log-log scale with a slope of value -0.5. As discussed previously, the presence of a defect or a discontinuity in material properties, a change in slope occurs. It is possible to fit the experimental curve by a n-grade polynomial which permits to reduce the noise and to have an analytical function to manage. The use of first and second derivative can be convenient to evaluate the stationary point of the temperature curve.

The procedure adopted for the evaluation of thermal diffusivity, is based on the evaluation of time t^* for which occurs the maximum value of the second derivative on the curve, thus an inflection point (**Figure *138***) and using the relation below.

$$\frac{L^2}{\alpha} = \pi t^* \tag{96}$$

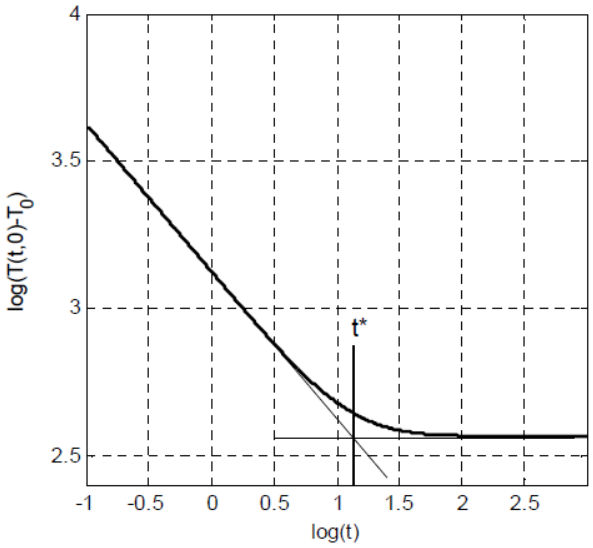

Figure 138. Cooling curve in log-log scale obtained with a reflection setup by Mayr et al. [223–225]

It is possible to obtain a map of thermal diffusivity for all the surface, knowing the thickness of the considered specimen. This method can be applied only if the energy value is high enough to penetrate all the thickness of specimen, which is hard for highly thermally diffusive materials, as metals.

From 2001 Cernuschi, Bison et al. [230–236], focused their works on the measurement of thermal diffusivity using laser spot pulsed method in reflection mode. Some difference in the works is about the energy distribution that in some cases has been modeled as a top hat, semi-circular and Gaussian distribution. The most common method, established used in other applications by several authors [230,232,233,237–240], is the one based on gaussian distribution of energy. The main advantage of the presented method is the capability to measure thermal diffusivity both in-plane and in-depth, that can be a huge pro considering the application to anisotropic materials. To measure thermal diffusivity, the solution of the heat equation in case of Gaussian distribution of energy, in adiabatic conditions, in a finite-body, in depth direction has been considered:

$$T(x,y,0,t) = \frac{2Q_0}{\pi}\frac{e^{-\frac{x^2+y^2}{\sigma_t^2}}}{\sigma_t^2}\left[\frac{1}{\rho CL}\left(1+2\sum_{n=1}^{\infty}e^{-\frac{n^2\pi^2\alpha_n t}{L^2}}\right)\right] \tag{97}$$

in which L is the thickness of plate, α_p the thermal diffusivity in-plane, Q_0 the value of energy density and σ_t the value of standard deviation of Gaussian temperature distribution which is related to α_n, the value of in-depth thermal diffusivity, by the following relation:

$$\sigma_t = \sqrt{R_0^2 + 8\alpha_p t} \tag{98}$$

where R_0 is the nominal radius of laser spot defined as the value for which the signal is $1/e$ of the maximum at the same t. In relation 97, two different terms can be considered. In the squared brackets there is the term that describes the in-depth heat diffusion while the other term is related to the in-plane heat diffusion. Integrating in space, the term to the left became a constant and the result decrease in accordance with the behavior of the term in squared brackets. Fitting of this curve as a function of time, it is possible to obtain the value of in-depth thermal diffusivity by the relation 97. To evaluate the in-plane thermal diffusivity, it is necessary to observe the Gaussian distribution of temperature in time. In fact, at the beginning after heat pulse, the Gaussian distribution of temperature has a defined standard deviation that is the minimum value as possible. In the cooling phase, the Gaussian profiles deserves the distribution but the value of standard deviation of Gaussian profile increases with time because of in-plane heat diffusion. As is possible to see from the relation 98, considering the variance of Gaussian profiles as function of time, it is possible to represent the curve as a straight line in which the slope it is strongly connected with in-plane thermal diffusivity. In **Figure *139***, it is possible to see the experimental data and correspondent fitting for measurements of in-depth and in-plane thermal diffusivity.

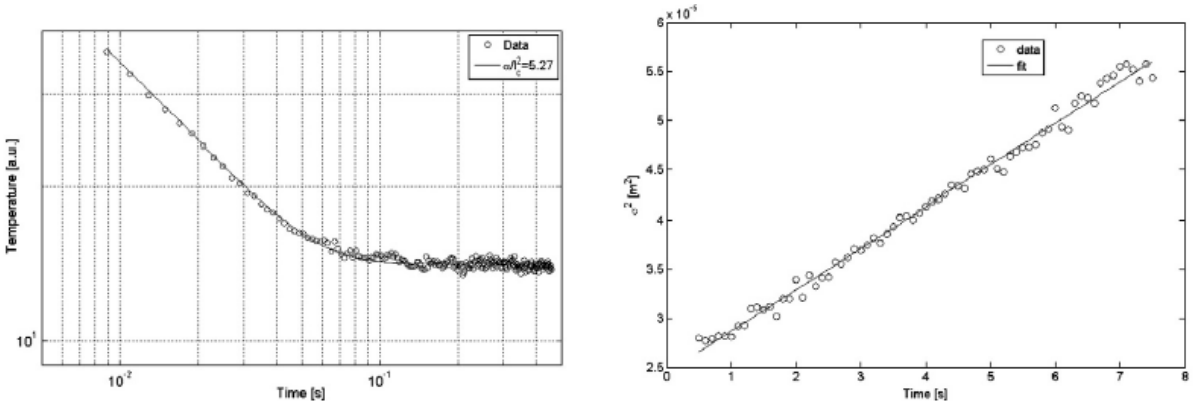

Figure 139. Results obtained by Bison et al. for the measurements of in-depth and in-plane thermal diffusivity[230].

This method can be powerful especially in case of coatings with characteristics different from the substrate, or in the anisotropic materials in which the measurement of thermal diffusivity in different directions can be done. In case of isotropic materials, the value of in-plane and in-depth thermal diffusivity must be coincident, hence can be used as method to confirm the thermal isotropy of materials. The main advantages of this method are the

possibility to measure simultaneously the in-depth and in-depth thermal diffusivity and to use a simple in reflection setup which can be suitable for on-line applications.

Basing on the same principle of the method presented before [230–236] in the 2017 Müller et al. [241], presented a method in which the pulsed heating by laser source has been obtained with a linear distribution. In fact, considering a Gaussian distribution in one direction and linear in the other, the thermal diffusivity in-plane in one direction has been evaluated. In this case, an average of signal in direction of laser line is performed to reduce the noise and a single averaged gaussian profile for each instant has been obtained. The next step is very easy and the difference of thickness of the Gaussian distribution in time is considered as reported below [241–243]:

$$\alpha \cdot t = \frac{w(t)^2 - w(0)^2}{4} \tag{99}$$

It is possible to plot the data obtained as a function of time and fit the data with a straight line in which the slope is related to thermal diffusivity in-plane, in the direction perpendicular to the laser line.

In **Figure *140***, the experimental set-up adopted for the application on a CFRP specimen has been reported. In the **Figure *140*** (b), the thermograms obtained from different times after heating, show the increasing of thickness of laser line. In **Figure *140*** c,d, the fitting procedure applied in two different directions for the same CFRP specimen.

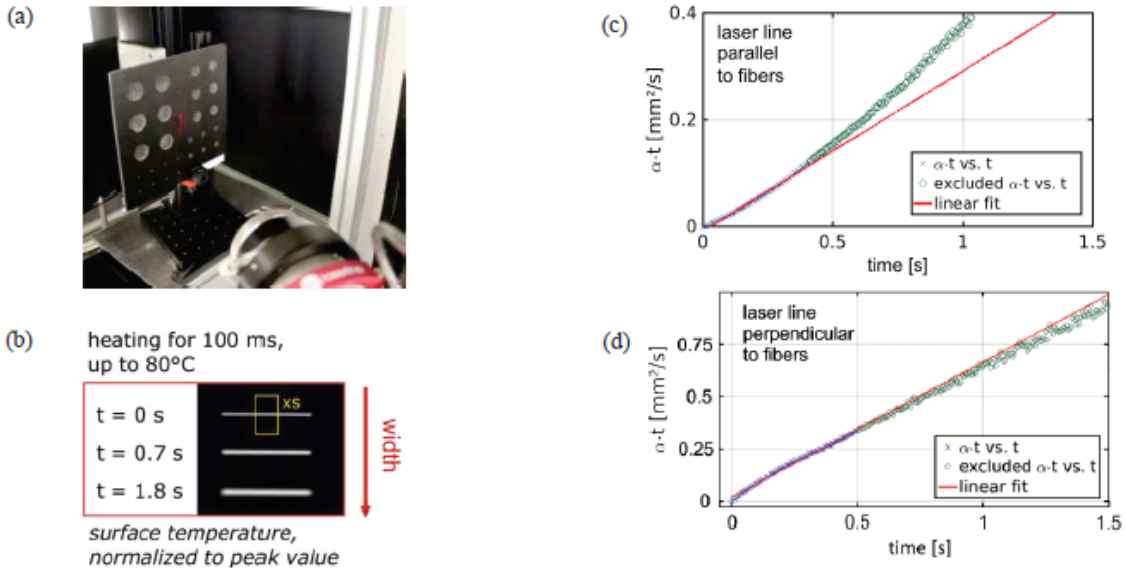

Figure 140. (a)Experimental setup used by Müller et al. (b) Variation of thickness of laser line in time. (c,d) Experimental data fitting and evaluation of thermal diffusivity in two directions for considered composite. [241]

This is a very fast method to measure thermal diffusivity and has the advantage to manage a very smooth signal because of averaging procedure in line direction. The main cons are that is not cheap and easy to obtain an equipment that permits to have a laser line Gaussian distribution and that only a specific direction for each test must be investigated.

From 2019 Bedoya, Gaverina, Mendioroz and Salazar [244–250], developed several works for measuring the thermal diffusivity with a laser method on moving samples. Considering a linear constant velocity relative motion between heat laser source and the surface in reflection mode, three different methods have been developed and presented. The first is based on the analysis of profile of logarithm of temperature in the center of laser spot in motion direction. The second one is based on the same profile but in perpendicular direction as respect of the motion ones. The last oneis based on the parabolic profile of logarithm of temperature as a function of distance from the laser spot, which is called parabola's method.

To better understand these procedures, it is necessary to describe the temperature on a surface of specimen after a Gaussian energy distribution with radius *a* ($1/e^2$), considering the heat losses on surface:

$$T(x,y,0,t) = \frac{2Q_0\eta}{\pi} A(t) \frac{e^{-\frac{2x^2}{a^2+8D_x t}}}{\sqrt{a^2+8D_x t}} \frac{e^{-\frac{2y^2}{a^2+8D_y t}}}{\sqrt{a^2+8D_y t}} \tag{100}$$

in which *A(t)* depends on the optical properties and thickness of the analyzed specimen. For thick and opaque materials, the function is:

$$A(t) = \frac{1}{\varepsilon_z}\left[\frac{1}{\sqrt{\pi t}} - \frac{h}{\varepsilon_z} e^{\left(\frac{h}{e_z}\right)^2 t} Erfc\left(\frac{h}{\varepsilon_z}\sqrt{t}\right)\right] \tag{101}$$

For thin and opaque , the function *A(t)* is:

$$A(t) = \frac{1}{\rho c L} e^{-\frac{2ht}{\rho c L}} \tag{102}$$

For semi-transparent and thick , it can be re-write as:

$$A(t) = \frac{1}{\rho c} \frac{\alpha\gamma}{\alpha+\gamma} \tag{103}$$

where η is the fraction of energy absorbed by specimen, α in this case is the coefficient of optical absorptivity at laser wavelength, γ is the effective absorption coefficient for wavelength (3-5 μm), D is the thermal diffusivity, ε the thermal effusivity, ρ the density, c the specific heat and L the thickness of specimen. With the assumption that there is a

slightly increase of temperature, the heat losses can be consideredas a linear function of temperature, where h is the coefficient of linear losses.

Considering the same specimen but adding the linear constant motion with a laser with power P_0 with Gaussian distribution with start heating at $t=0$, the temperature on surface can be described as:

$$T(x,y,0,t) = \frac{2P_0\eta}{\pi}\int_0^t A(t-\tau)\frac{e^{-\frac{2[x-v(t-\tau)]^2}{a^2+8D_x(t-\tau)}}}{\sqrt{a^2+8D_x(t-\tau)}}\times\frac{e^{-\frac{2y^2}{a^2+8D_y(t-\tau)}}}{\sqrt{a^2+8D_y(t-\tau)}}d\tau \qquad (104)$$

The proposed methods are based on the analysis of temperature distribution in logarithm scale. Also, these are valid in stationary conditions, thus the solution above permits a precise determination of needed time to reach the steady state (t_c) which is dependent on the velocity of specimen. In fact, for a fixed value of v and D, it is possible to determine the temperature on the surface until the stationary condition is achieved.

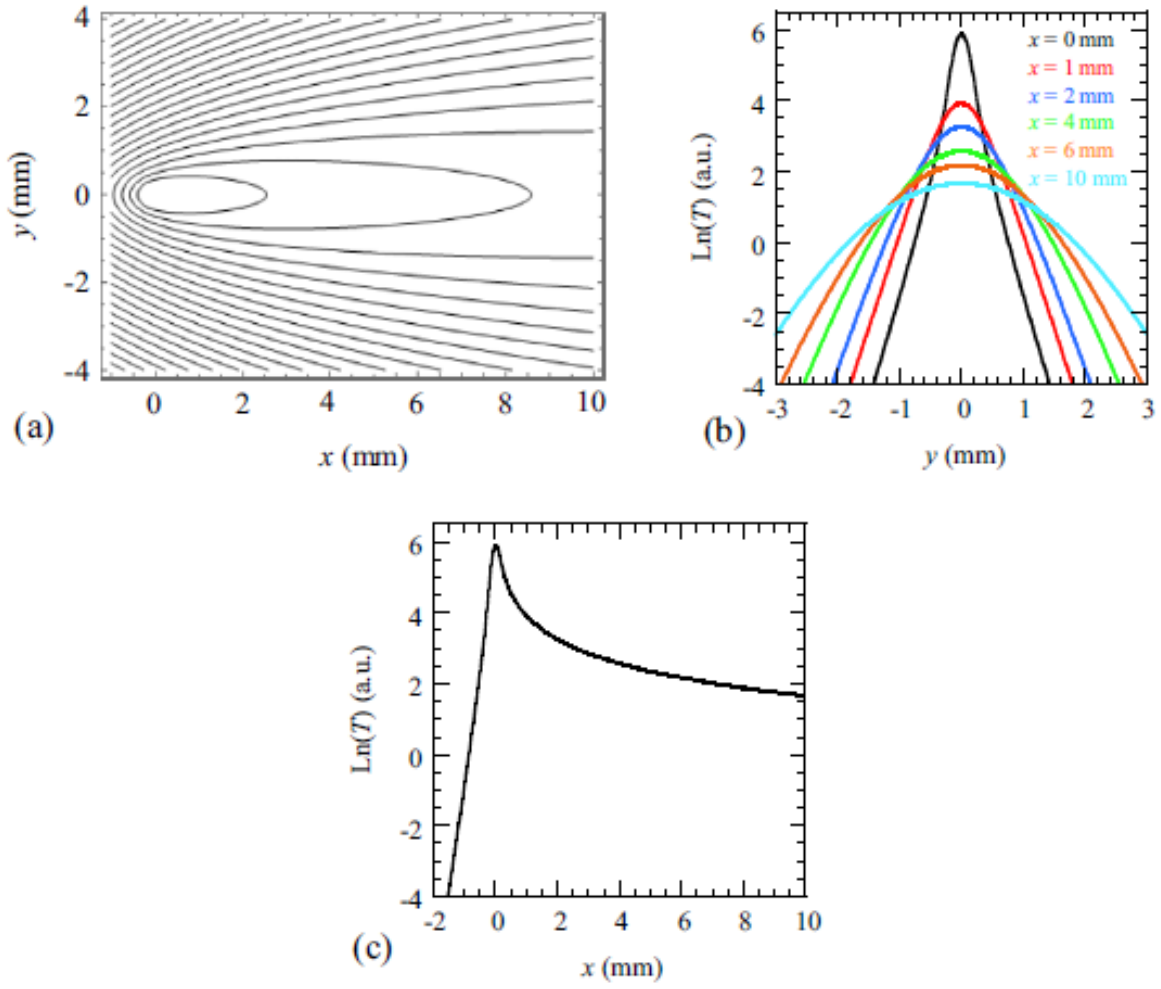

Figure 141. (a) Temperature distribution on the surface, (b) logarithm of temperature in y direction, (c) logarithm of ture in x direction [244–250].

In **Figure *141*** are showed the profiles analyzed for the application of the first two methods presented by Bedoya et al. [246] and the distribution of temperature on surface. The method of the transversal profiles based on the behavior of logarithm of temperature in *y* direction, fixed *x=0.* Multiplying the natural logarithm of temperature for a time function (for thick and opaque materials) or for the root square of time (thin and opaque specimens or thick and semi-transparent), a linear behavior can be obtainedin which the slope can be related to the thermal diffusivity in *y* direction by the relation:

$$m = \pm \frac{v}{2D_y} \tag{105}$$

This is slightly influenced by the heat losses and dimension of laser spot radius, as possible to observe in **Figure *142*** in which the linear region that must be considered has higher distance from the center of spot but has the same slope, thus the results will be not influenced by this parameter.

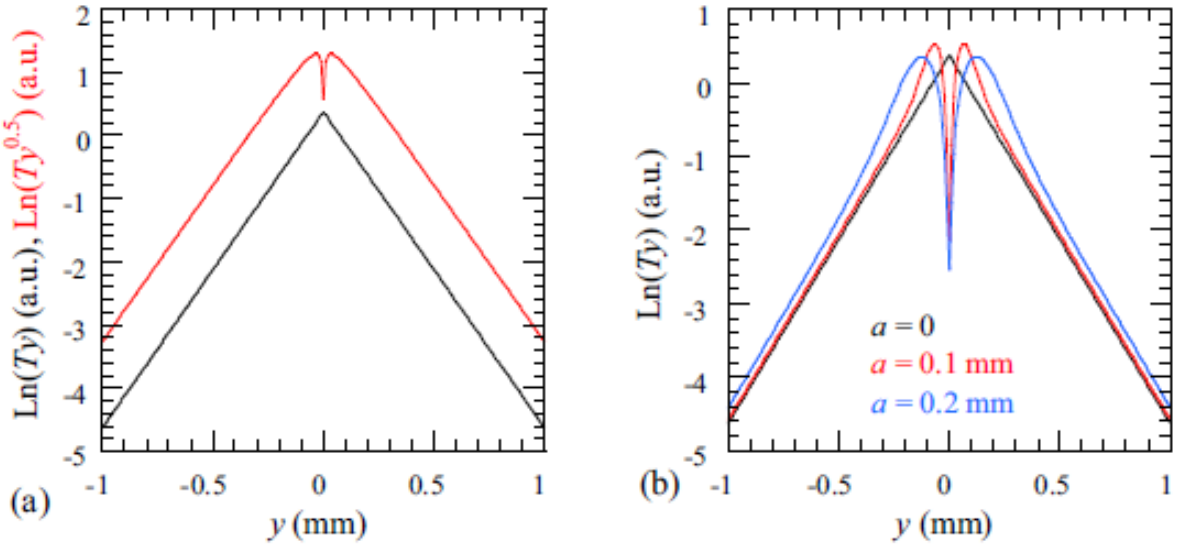

Figure 142.(a) Application of transversal profile method to opaque specimens. (b) Application of transverse profile method to semi-transparent specimen and the effect on profile of laser spot radius. [246]

he influence of heat losses on the central transversal profiles for different values of *h*has been obtained showing that the profile can be considered constant until the value of *h* reaches the very high value of *100* $Wm^{-2}K^{-1}$ [246].

In the case considered by Bedoya et al. [246], it must be considered that the diffusivity thermal length in transversal direction as respect of the motion, considering the logarithm of temperature, it is reduced by factor *e*:

$$\mu_i = \frac{2D_i}{v}, \qquad i = y \; e \; z. \tag{106}$$

In particular, in z direction, it defines the penetration of thermal energy in case of relative motion between heat source and specimen. The specimen can be considered thick for values of $L>2\mu_z$, and thin if $L<0.5\mu_z$.

The second method is based on the analysis of central longitudinal profile ($y=0$) of logarithm of temperature on the surface of specimen ($a=0$, $h=0$). This profile, as showed in **Figure *141*** (c), is not symmetric because the smooth part ($x>0$) hides the information about thermal diffusivity in that area that has been already heated by the laser. The other part ($x<0$) shows a linear relation which depends on the velocity and on thermal diffusivity in x direction. As in the previous method, two different cases have been analysed: the first for thick and opaque specimen and the other for thin opaque specimen. If the specimen is opaque and thick, the natural logarithm of temperature multiplied by the longitudinal distance, depends linearly on x. If the specimen is thin and opaque, the behavior of temperature multiplied for the square root of the x can be considered linear. The slope of these curves is related to the thermal diffusivity in x direction.

$$m = \frac{v}{D_x} \tag{107}$$

Exactly, as for the first method, the influence of the laser spot radius and of the losses have been considered. In **Figure *143***, it is possible to observe that the slope of the presented curves is not dependent on the spot radius or on the losses, thus the method can be considered robust for measurement of thermal diffusivity.

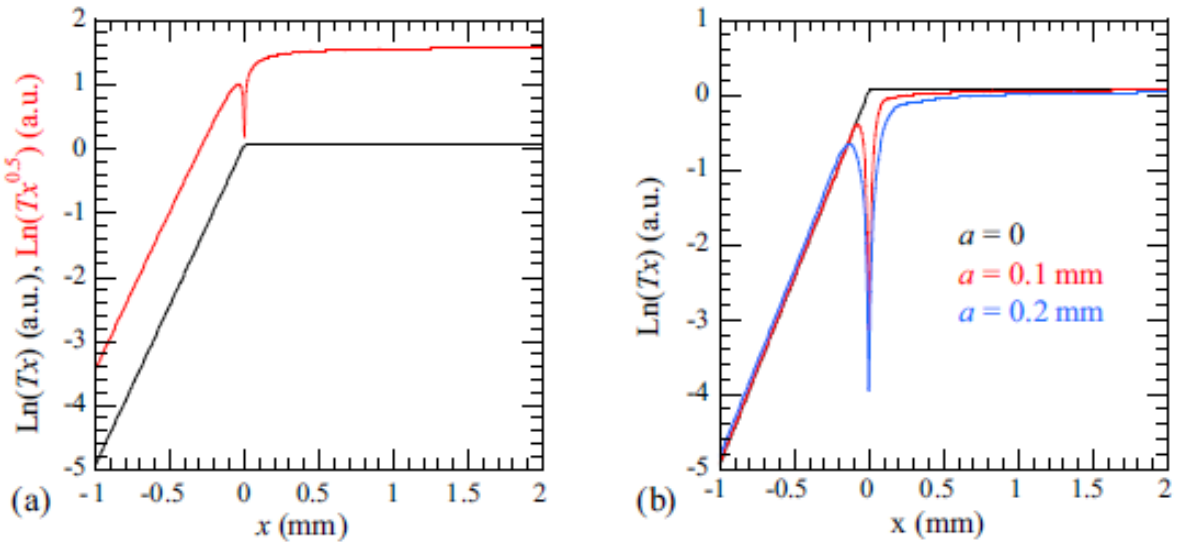

Figure 143. (a) Behavior of Ln(Tx) and Ln($Tx^{0.5}$) for thick materials (black) and thin (red) with a=0 and h=0. (b) The behavior of Ln(Tx) for thick materials with different radius values [246]

The third method is the *parabola's method* that is based on the hypotheses of surface heated by a Gaussian energy distribution obtained by a circular laser spot. In this case the logarithm of temperature on surface in the next instants after the pulsed heating, has a parabolic behavior.

$$Ln[T(x,0,0,t)] = A(t) - C_x(t)x^2; \quad Ln[T(y,0,0,t)] = A(t) - C_y(t)y^2. \qquad (108-109)$$

In the relations above, the second order inverse of parabola coefficient, has a linear dependency on time.

$$\frac{1}{C_j(t)} = \frac{a^2}{2} + 4D_j t; \quad j = x\ e\ y. \qquad (110)$$

The slope of this linear behavior is related with thermal diffusivity $m_j=4D_j$. It has been showed in **Figure *141***, that also for the moving sample, the transverse profile of logarithm of temperature presents a parabolic behavior considering a distance x from the spot center. Bedoya et al. [246], verified that the same relation, that is valid for the pulse heating, it is also true for the moving sample. Hence, it can be written as:

$$\frac{1}{C_y} = \frac{a^2}{2} + 4D_y t = \{x = vt\} = \frac{a^2}{2} + \frac{4D_y}{v}x. \qquad (111)$$

This result shows that the inverse of second order coefficient of parabola is a linear function of distance from the laser spot center, with slope

$$m = \frac{4D_y}{v} \qquad (112)$$

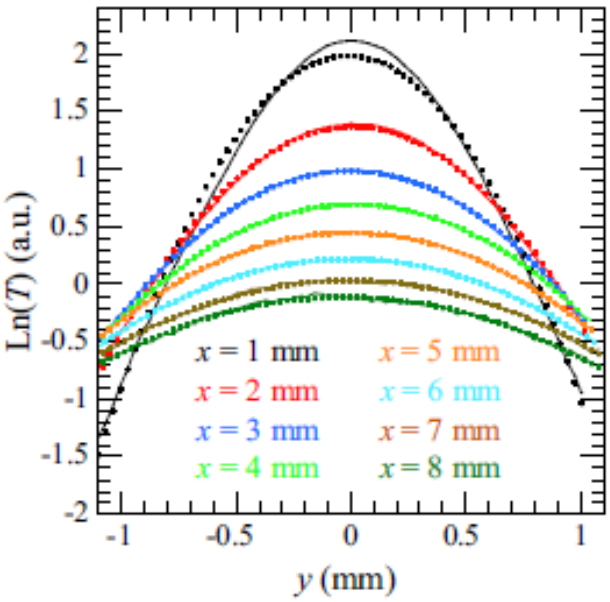

Figure 144. Profile of transversal logarithm of temperature for different values of distance from the center of laser spot obtained by Bedoya et al. for an application on steel AISI-304. The points are experimental data and the lines correspondent fitting [246].

These three methods are very robust because that the radius and losses have not influence on the thermal diffusivity measurements. The main advantage of the presented method is that can be used on-situ on a moving specimen or component, for example during the production line.

In 2021 Salazar et al. [251], proposed a method based on laser-spot step-heating to measure thermal diffusivity of solids.

The proposed method is based on a homogenous and isotropic plate of thickness *L,* infinite in both *OX* and *OY* directions, heated by a laser beam of Gaussian profile whose power density has the following spatial distribution

$$P(r) = \frac{2P_0}{\pi a^2} e^{-\frac{2r^2}{a^2}}, \tag{113}$$

where P_0 is the laser power and *a* is the radius at $1/e^2$ of peak intensity. The laser heating starts at *t=0* and the time dependence of the power satisfies a Heviside function: 0 for t<0 and P_0 for t>0. The scheme of the described model is in **Figure *145***

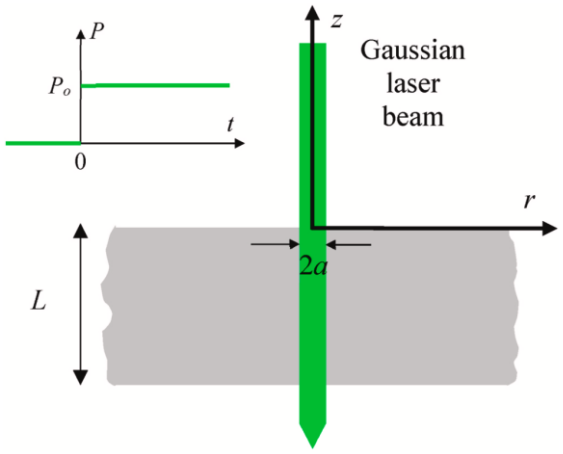

Figure 145. Cross section of a specimen heated by a laser beam of radius a. The inset shows the time profile of step-heating adopted [251]

To obtain the sample temperature as a function of *t, r* and *z,* it is necessary to solve the heat diffusion equation in which *Q* is the absorbed energy per unit volume while, *k* and *D* are the thermal conductivity and diffusivity of the specimen [251].

$$\nabla^2 T(r,z,t) - \frac{1}{D}\frac{\partial T(r,z,t)}{\partial t} = -\frac{Q(r,z,t)}{K} \tag{114}$$

To solve the above equation, considering that the laser beam follow the Beer-Lambert Law $Q(r,z,t) = \eta P(r) u(t) \alpha e^{\alpha z}$, where *u(t)* is the Heaviside unit step function and η the power fraction absorbed by sample, double transformation is needed: first a Laplace transform

and after, due to the cylindrical symmetry of problem, Hankel transform to achieve the general solution [251].

$$\tilde{\bar{T}}(\delta, z, s) = Ae^{-\beta z} + Be^{\beta z} + Ce^{\alpha z} \tag{115}$$

where $C = \frac{1}{k}\frac{\eta P_0}{2\pi} e^{-\frac{(\delta a)^2}{8}} \frac{1}{s}\frac{\alpha}{(\beta^2-\alpha^2)}$. Depth-independent factors *A* and *B* are obtained from the boundary conditions: flux continuity at the sample surfaces considering radiative and convective losses.

For opaque and thermally thick samples $\alpha \to \infty$ and $e^{-\alpha L} \approx 0$ the temperature behavior can be described, for *z=0* and in case of adiabatic conditions [251]:

$$T(r, 0, t) \approx \frac{\eta P_0}{2\pi K}\int_0^\infty J_0(\delta r)\,\mathrm{erf}\left(\delta\sqrt{Dt}\right) e^{-\frac{(\delta a)^2}{8}} d\delta \tag{116}$$

where J_0 is the Bessel function of order zero and *erf* the error function while δ is the conjugated variable to *r* in Hankel space.

For an opaque and thermally thin specimen $L \ll \mu$, so $e^{\pm\beta L} \approx 1 \pm \beta L$, the temperature distribution can be described by [251]:

$$T(r, t) \approx \frac{\eta P_0}{2\pi k L}\int_0^\infty \delta J_0(\delta r)\frac{1 - e^{-Dt\left(\delta^2 + \frac{2h}{kL}\right)}}{\delta^2 + \frac{2h}{kL}} e^{-\frac{(\delta a)^2}{8}} d\delta \tag{117}$$

which is independent of depth and it is interesting to observe that the thinner the sample the higher the effect of heat losses [251].

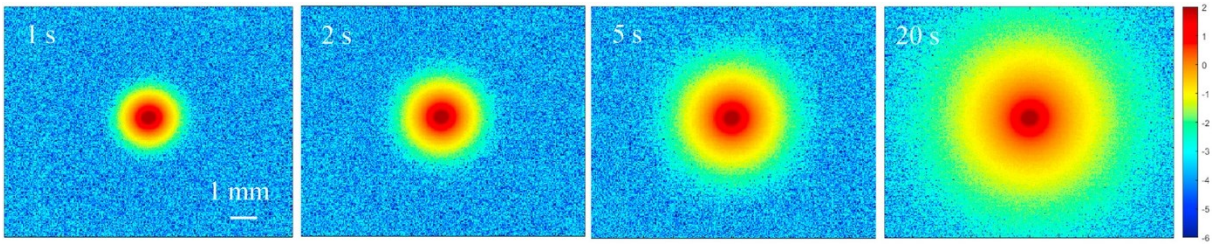

Figure 146. Sequence of thermograms of ln(T) obtained by Salazar et al. for PEEK. [251]

In **Figure *146*** a sequence of thermograms shows that, as predicted by theory, heat propagates radially with time, but the temperature at the laser spot remains almost constant after the first second. In **Figure *147***, in black dots are reported temperature profiles along the vertical axis after 1s and 5s heating. To reduce the high noise level in step-heating thermography, the cylindrical symmetry of the thermograms can be used to perform an average of the temperature along concentric circumferences around the laser spot. In this way, the longer the distances from the laser spot, where the noise is more pronounced, the

larger the number of pixels that are averaged, leading to cleaner temperature profiles. The red dots in **Figure *147***, correspond to such average profiles.

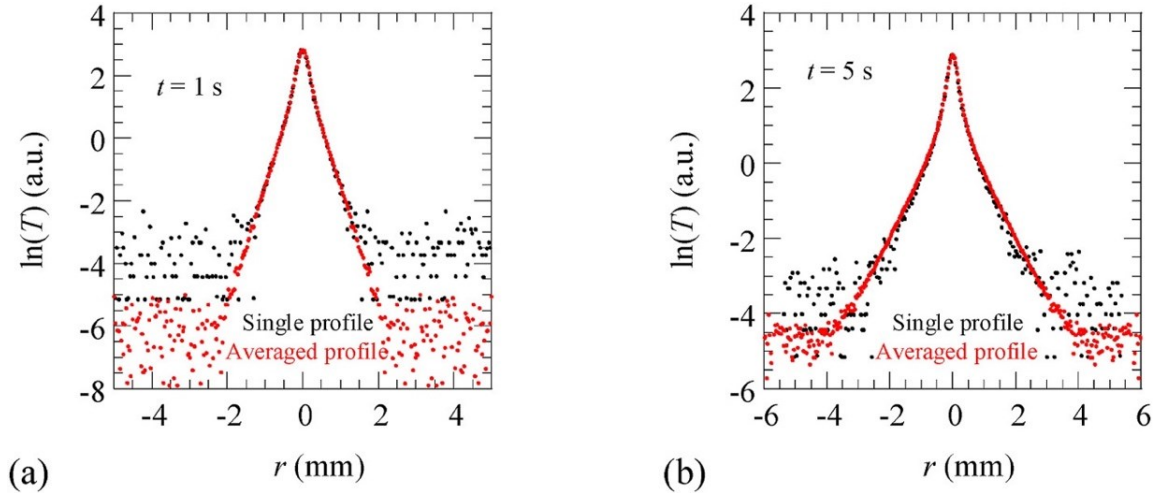

Figure 147. Comparison of single and averaged radial profiles of ln(T) obtained in a PEEK sample at two instants after the onset of the heating [251].

To obtain thermal diffusivity values a set of temperature profiles obtained at several instants after the start of heating, has been fitted by T (r,t) (**Figure *148***).

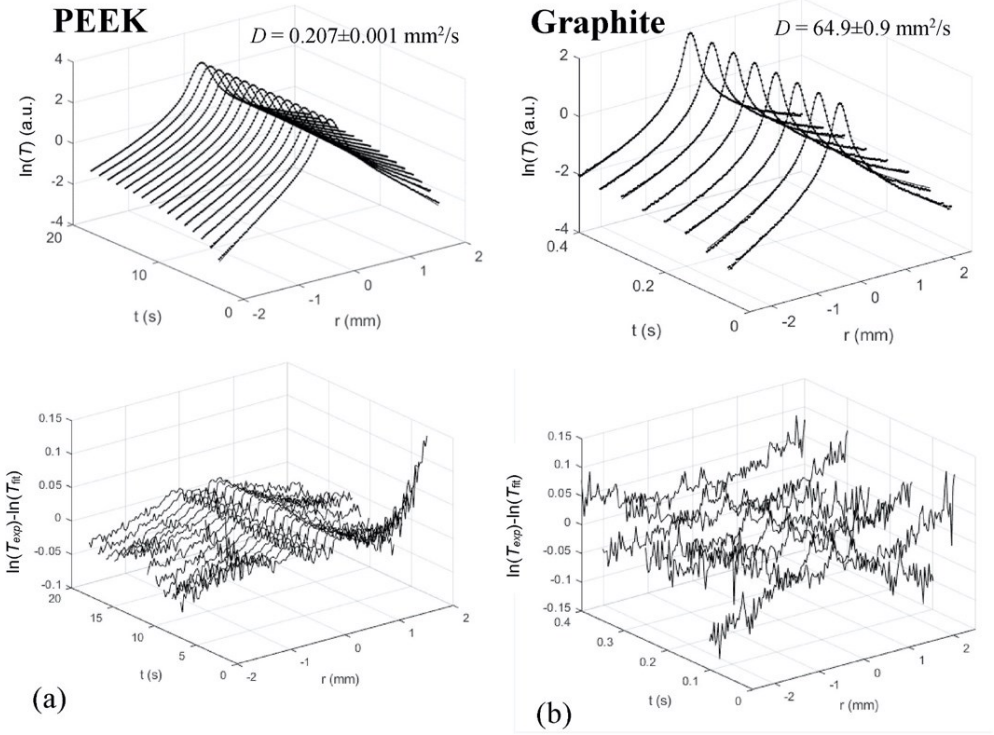

Figure 148. above: fittings of averaged profiles of ln(T) for two opaque and thermally thick samples. Below: residuals are plotted to highlight the quality of the fittings [251]

The method presented by Salazar et al. [251] has several advantages. Firstly, it is really easy to apply and, considering that the measurement has to be done in steady state conditions of heating, it can be applied with low power heat source too. Secondly, the

averaging procedure reduce the thermal noise significantly, and the fitting procedure is time-saving and easy to apply, considering the uncomplicatedness of the adopted setup.
Among all the considered methods for measure the thermal diffusivity [127,171,199,201,209,232,235–237,240,245,248,252–260], the following works have been focused on the pulsed-spot laser method [219,230–238,243,253,254] and have been considered as starting point. In fact, this method, presents an easy experimental set-up and a fast analysis process that can be easy to automatize.
The aim of the proposed approach is to verify the capability and resolution of the selected method to distinguish different microstructures in steel to develop a procedure that can be automatized to measure HAZ in welding. The first step, in direction of this final goal, is to study how the error of measurement in thermal diffusivity can be affected by test parameters. Then, developing a procedure to select the parameters in order to reduce this error and, in best condition of technique, defining a procedure that can be adopted to distinguish different microstructures and transition areas.
In this direction, a high strength boron steel[261–263] has been investigated and several microstructures have been considered to evaluate the capability of the thermographic technique to discern different microstructures and relate thermal properties to mechanical ones, in order to develop a non-destructive thermographic procedure to define boundaries of HAZ and estimate relative mechanical properties.

4.2 A non-destructive thermographic method to assess the microstructure changing in boron steel: a relation between thermal diffusivity and mechanical properties

4.2.1 Introduction

As a case study, eight boron steel (Usibor® 1500) plates with different structures (four with a ferritic-pearlitic and four with a 100% martensitic structure) have been considered to develop a laser thermographic method based on the anti-correlation between hardness and thermal diffusivity, to verify the effectiveness of heat treatments in boron steel in a non-destructive way and, also, a procedure to select the best experimental test parameters. In this application, the pulsed spot laser thermographic method [219,230–238,243,253,254] has been applied and a study about the influence of the test parameters on thermal diffusivity measurement has been conducted.

In particular, a finite element model has been developed and adopted, in conjunction with the response surface method (RSM), to study the resolution of the technique. After an evaluation about the test parameters that affect the measurement, the error in the measurement of thermal diffusivity as a function of test parameters has been investigated, obtaining information about the influence of main experimental test parameters: pulse length, acquisition frequency and spatial resolution.

Moreover, the described plates have been experimentally investigated to validate and verify the proposed method, which has also been verified in comparison with a well-established technique based on the use of a transient plane source [264].

After a validation of thermal diffusivity measurements, 1D tensile test have been conducted to measure the ultimate tensile strength of materials. In this way, a preliminary correlation between thermal diffusivity and ultimate tensile stress has been possible and, through the measurement of thermal diffusivity, an estimation of mechanical resistance of material has been possible.

4.2.2 Material and methods

4.2.2.1 Specimens

For this case, the boron steel Usibor® 1500 has been considered because it is an ultra-high-strength steel (UHSS) widely used in automotive body production due to crashworthiness improvements and part weight [261–263,265,266]. Frequently, UHSS are used for tailored welded blanks applications, in which are joined before the forming operation [267] thus, for this reason, it can be considered very interesting for thesis aims.

Eight rectangular different Usibor® 1500 plates with a ferritic-pearlitic structure have been investigated. With the aim of obtaining a martensitic microstructure, four of these plates have been heat-treated: for four minutes has been heated in the oven at a temperature of ~ 950 °C, then a rapid quenching in water has followed to have the desired microstructure [262,263,268]. After the application of the described thermal cycle, the quenching heat treatment involved the specimen volume, and the microstructure can be considered uniform through the thickness. This is important to guarantee homogenous properties of material hence, thermal and mechanical isotropic properties.

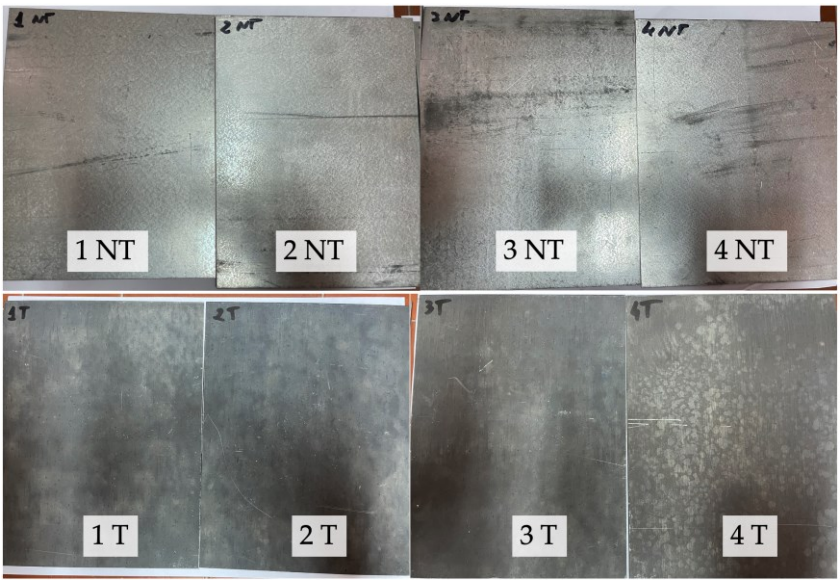

Figure 149. Anlaysed specimens. With ID 1/2/3/4 NT the specimens with ferritic-pearlitic structure and with ID 1/2/3/4 T the specimens that exhibits a martensitic structure.

ID	Dimensions [L x H]	Heat treatment	Micro-structure	Thickness
1/2/3/4 NT	150 x 195 mm	NO	Ferritic-pearlitic	1.03 mm
1/2/3/4 T	150 x 200 mm	YES	Martensitic	1.03 mm

Table 11. Geometrical dimensions and characteristics of investigated specimens.

The thermophysical properties of plates, before the heat treatment, have been measured by the transient plane source (TPS) method [264], which is established and adopted in standard ISO 22007-2, and resumed in **Table *12***. Values of thermal conductivity and heat capacity have been measured separately.

Micro-structure	Density *[kg/m³]*	Specific heat *[J/Kg·K]*	Thermal conductivity *[W/m·K]*	Thermal diffusivity *[mm²/s]*
Ferritic-pearlitic	7374 ± 14	443.9 ± 0.3	47.96 ± 0.03	14.65 ± 0.21

Table 12. Thermophysical properties of Usibor®1500 measured by TPS Method following standard ISO/FDIS 22007-2.

From the starting plates shown in ***Figure 150***, used for thermographic testing, ten specimens have been obtained according to ISO 6892-1:2019, then used for uniaxial tensile testing.

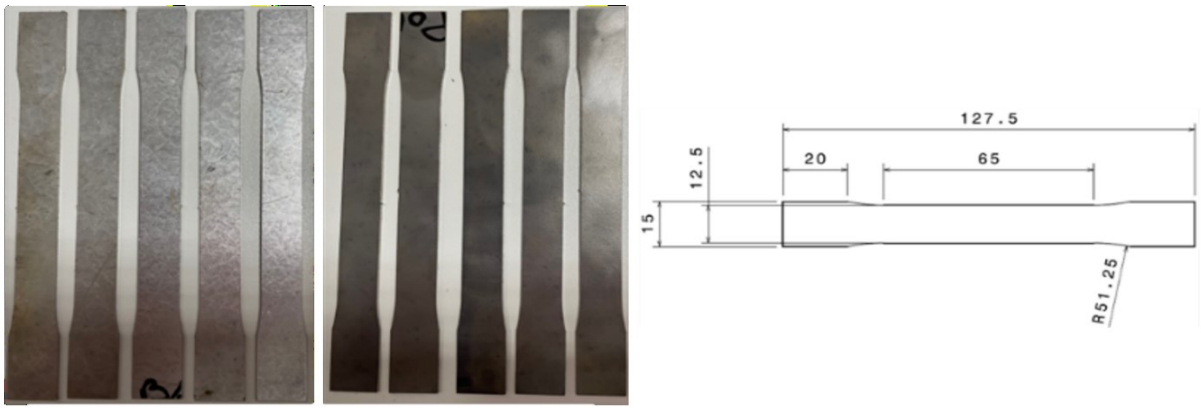

Figure 150. Uniaxial tensile test specimens obtained according to ISO 6892-1:2019.

4.2.2.2 FEM Model

To select the best parameters for experimental tests, a FEM model has been developed by COMSOL Multiphysics® software. Using the FEM model permits significantly reduces the number of preliminary tests for testing parameters selection, saving time. Considering the eq (97) that describes the temperature distribution as a function of time, after a pulsed heating with a Gaussian distribution, it is possible to define the best way to develop a FEM model. Since it is necessary to describe the behaviour of temperature profile on the surface and in depth, it is possible to simplify the model and consider it as a 2D axisymmetric problem. In fact, a 2D axisymmetric model has been created. Hence, a rectangular area has been modelled and, basing on the equipment specs (maximum laser power, laser beam diameter and minimum heating time), a surface heating has been modelled with the symmetry axis coincident with the *z* axis (**Figure 151**). In this way, considering as section a rectangular surface of 40 x 1 mm^2 and *z* as the rotation axis (**Figure 152**), the rotation solid obtained is a cylinder with a height of 1 mm and a basis diameter of 80 mm. A custom material has been applied to the geometry modelled with properties in **Table 13.** Thermal conduction and specific heat obtained by the TPS method have been considered the model's input values and measured values of density have been considered.

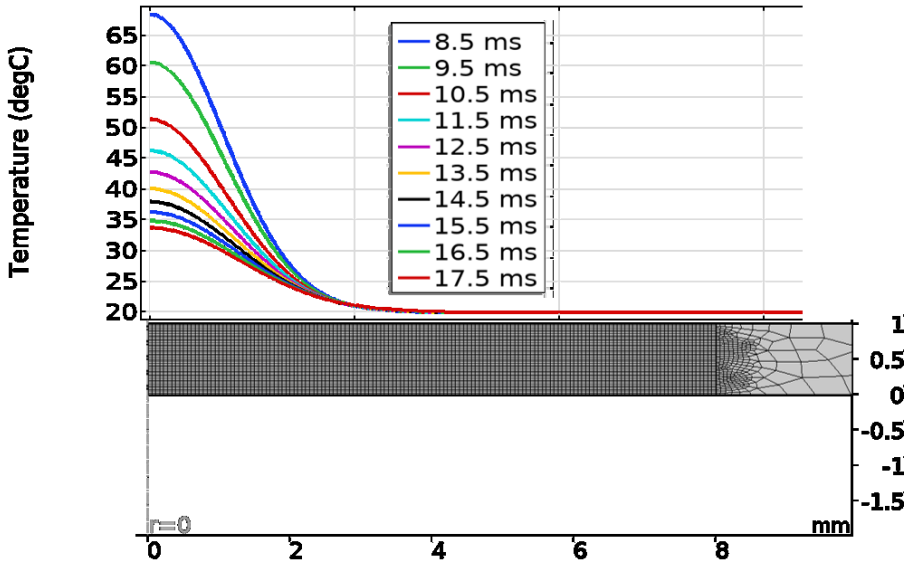

Figure 151. Scheme of relative position between Gaussian heating distribution and component surface.

Parameter	**Value**
Thermal conductivity (k)	47.96 W/m·K
Specific heat (Cp)	443 J/kg ·K
Density (ρ)	7374 kg/m^3
Emissivity (ε)	1
Power heating source (P)	20 W
Laser spot diameter (d)	6 mm
Energy source distribution	Gaussian
Heating pulse duration	8 ms
Convection losses coefficient (h)	8 W/m^2·K
Step solutions	0.01 ms
Simulated time	100 ms

Table 13. Thermophysical parameters adopted for 2D axisymmetric COMSOL® Multiphysics Model.

The exact initial temperature of 293.15 K has been set for the body and the ambient. The laser heat source has been simulated as a Gaussian energy distribution with a standard deviation $\sigma = d_{spot}/6$, where d_{spot} is the circular laser's nominal value. The Gaussian energy distribution has been centred with the rotation axis on the upper surface of the plate, with a power of laser of *20 W*. Natural convection heat flux has been considered using a heat transfer coefficient of $8\ W/m^2K$. The cooling phase has been observed for *100 ms* after a

heating duration of *8 ms.* All the considered parameters in the simulation have been based on the adopted lab equipment. For heating, a step function has been considered with amplitude 1 and duration coincident with heating pulse duration and, to avoid singularity in calculation in correspondence of the start of step, a transition zone of *0.05 ms* in heating and cooling has been considered as a ramp function but imposing the continuity of 1st and 2nd derivative (***Figure 153***).

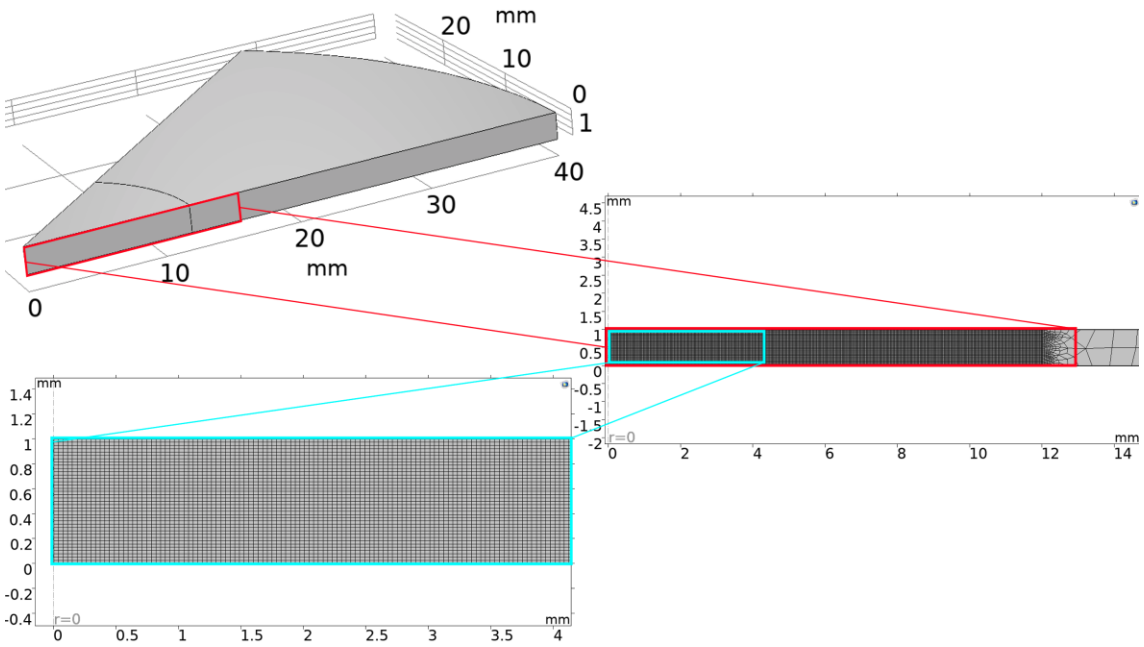

Figure 152. Mesh adopted for the domain discretization in the adopted FEM model. **a)** Section of the solid obtained after the revolution of section **b)** around the z axes. **c)** Detail of quadrangular fine mesh adopted through the thickness in the heated area.

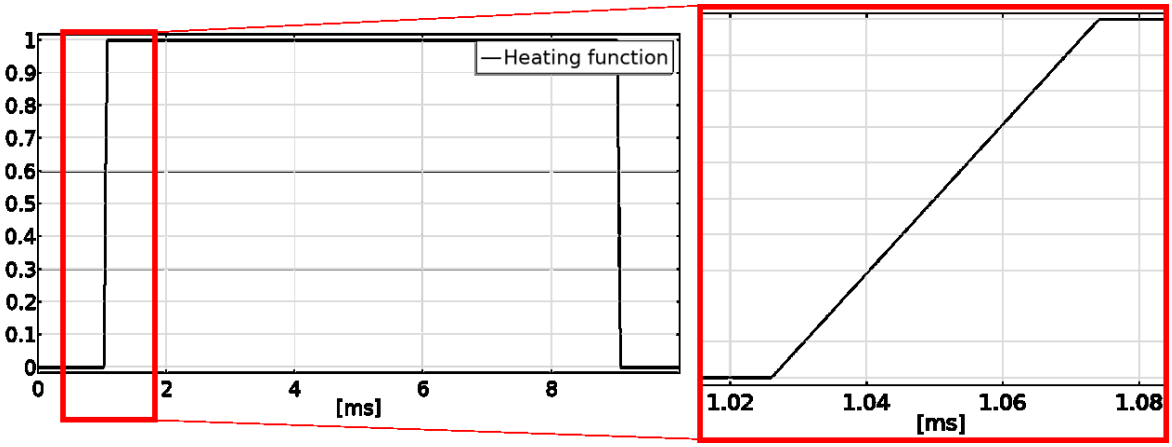

Figure 153. Step heating function adopted in FEM simulation with detail of heating ramp.

Quadrilateral elements have been selected to discretise the domain. **Figure 152** shows that a finer mesh in the area directly involved in heating and coarser ones for the remaining have been adopted.

As already described, a numerical model of spot pulsed laser thermography has been developed but, a comparison between experimental and FEM results is needed to validate the model. Hence, the pulsed laser method procedure has been applied to the FEM model results and compared to experimental preliminary test results to validate the numerical model. To analyse results obtained from FEM model, MATLAB® software has been used exporting results from COMSOL Multiphysics®. Observing a diameter of nominal laser spot of the FEM model, considering the temperature distribution in time and obtaining the straight line that represent the equation X, the measurement of thermal diffusivity has been done [219,230–238,243,253,254,268].

After the validation, the FEM model was used to identify and select the experimental test parameters that minimize the error in measurement of the thermal diffusivity and then understand the PLM technique's resolution, also considering the peculiar noise of the thermal camera.

4.2.2.3 Response Surface Method

In this section is described the adopted procedure to investigate the PLM technique's resolution. The first step was to identify the test parameters that can influence the measured value of thermal diffusivity. Considering the eq. 1, one of the main hypothesis regards the assumption of a Dirac's pulse and then it is evident that the heating duration can influence the results. On the other hand, the recording parameters such as, acquisition frequency and spatial resolution, can affect thermal diffusivity measurement too. Indeed, as already described, the method is based on the assessment of the Gaussian profile over time during the cooling phase after the heating pulse. Thus, the accuracy and precision in determining the thermal diffusivity value depend on both the number of considered Gaussian profiles and the number of points considered for fitting the profile. In particular, considering the fitting of temperature profile with a Gaussian profile, the higher the number of used points and the higher the chances of obtaining a high accuracy of the fitting. The number of points corresponds to the number of considered pixels, which strictly depends on the spatial resolution that, in turn, depends on the adopted experimental set-up (IR camera detector, lens, IR camera-specimen distance). Otherwise, the linear fitting of variance of Gaussian profiles as a function of time depends on the number of points, which depends on the acquisition frequency. In this regard, the present study has been focused on investigating the Influence of temporal frequency, spatial resolution, and heating time on measurement. In fact, these can be considered the main parameters that is needed to set for experimental

campaign and that are crucial for a suitable measurement. This investigation aims to evaluate the resolution of the PLM technique to measure thermal diffusivity in-plane and define test parameters for experimental measurements.

Another important issue to consider is the actual noise of the IR sensor that affects the uncertainty of the measurement. In fact, the noise of sensor affects both the reconstruction of the Gaussian temperature profile (spatial noise) and the fitting of the variance as a function of time (temporal noise). Thus, considering the PLM, the peculiar noise of the cooled sensor has been added to the FEM results to have reasonable results that can be used to evaluate the influence of noise on measurement procedure.

As described above, the spatial resolution is related to the adopted experimental set-up, and it depends essentially on the number of pixels contained in the diameter length. In this regard, an effective parameter that represents the spatial resolution is the parametrisation of the mm/pixel.

In the same way, also the other considered parameters can be parametrized to obtain a more generic characteristic parameter of the investigated physical phenomena. Both the heating time and the acquisition frequency are strictly related to the duration of phenomena in the cooling phase. In particular, the two considered parameters are the number of points/frames in cooling time and for the heating time, the ratio between heating time and cooling time.

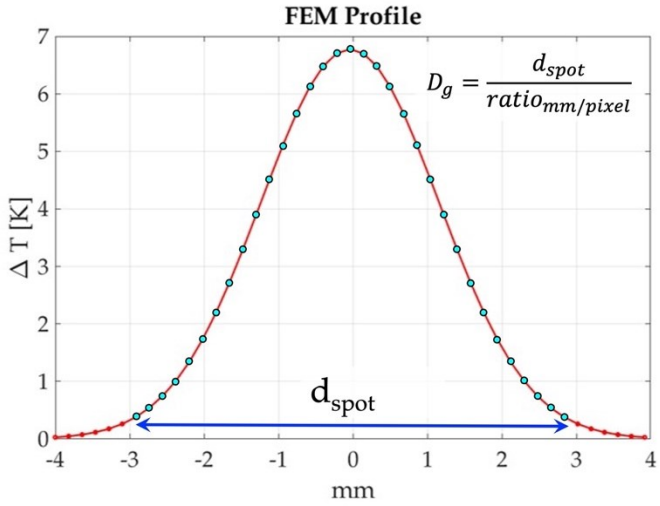

Figure 154. Gaussian temperature distribution with highlighted the pixels (cyan spot) contained in the nominal diameter of spot *(d_{spot}).*

A straightforward approach has been used to define the cooling down time: the syste''s settling time has been considered. The cooling phase is a step response of a first-order dynamic system, then the evaluation of time constant τ is possible, and the settling time is

defined as $T_s = 3\tau$, which is the time needed to reach 95% of the final value, as showed graphically in Figure 155. This value can be used to normalize the heat duration and the acquisition frequency considering in the first case, the ratio between heating time (t_h) and settling time (T_{heat}), as showed in Figure 156, and in the second one, the number of frames in the cooling time (N_{cool}), that can be obtained as the product between f_{acq} and T_s, as highlighted in Figure 157.

To estimate the value of T_s, a preliminary test is needed considering a heating time sufficient to have a ΔT in the centre of the laser spot detectable by the IR camera that permits to estimate τ (Figure 155.). Considering a fixed value of the energy, τ does not depend on the heating time but only on material properties and the volume of specimen, thus the thickness.

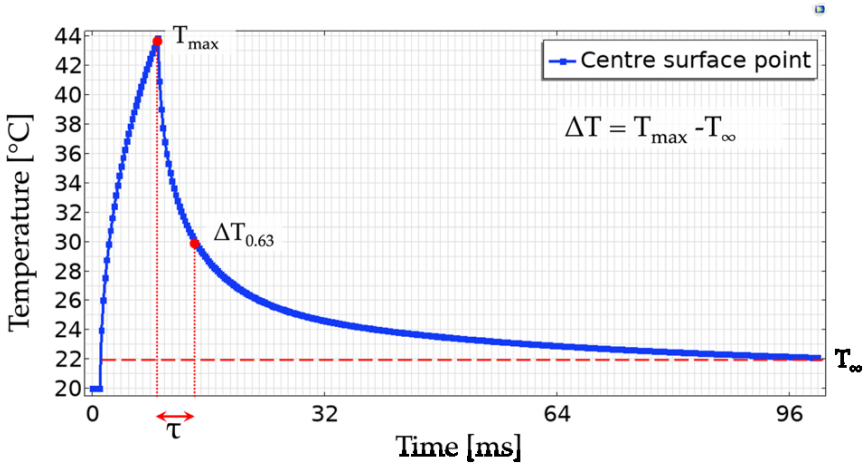

Figure 155. The temperature as a function of time in the center of laser spot from FEM model. Considering cooling down part, τ is the time constant.

The value of the settling time T_s, assessed for the not heat-treated boron steel plates was *15 ms.*

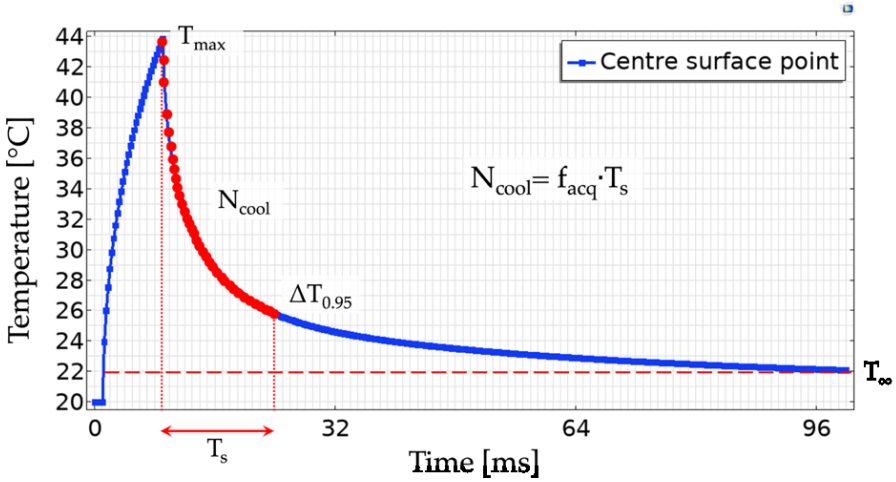

Figure 156. Cooling down part of curve, the number of red dots express the parameter N_{cool}.

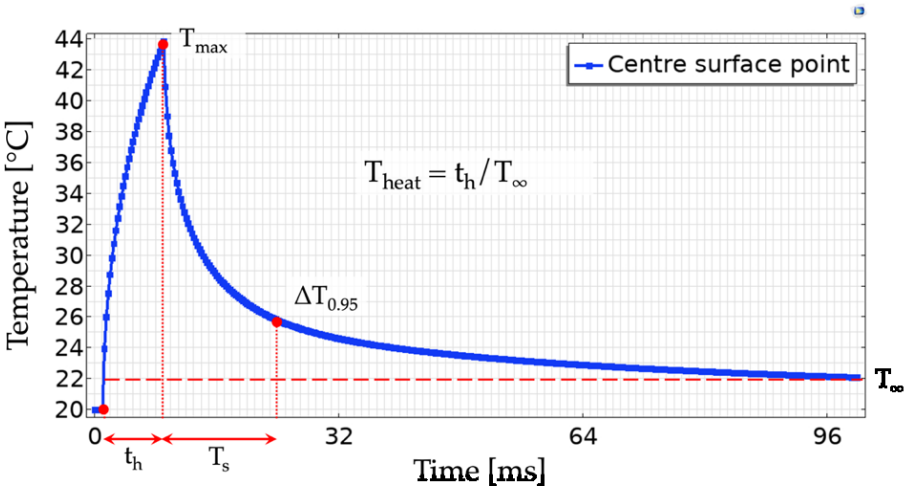

Figure 157. Temperature as a function of time in the center of laser spot obtained by FEM model. The ratio between t_h and T_s express the value of parameter T_{heat}.

Parameter	**-1**	**0**	**1**
N_{cool} (f_{acq})	3 (200 Hz)	7 (467 Hz)	11 (733 Hz)
T_{heat} (t_h)	0.07 (1 ms)	0.7 (10.5 ms)	1.33 (20 ms)
D_g	4	52	100

Table 14. Set of parameters adopted for the response surface method study.

Once defined the parametrised values resumed in Table 14, an advanced design of experiment technique named the response surface methodology (RSM) [269], has been used. In particular, the Box-Behnken design, which has parameter combinations at the midpoints of the edges of the experimental space, has been adopted and shown in Figure 158.

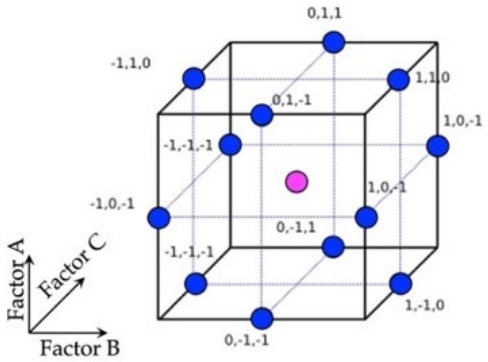

Figure 158. The Box-Behnken points scheme.

Hence, three parameters and three levels each have been considered, obtaining the simulation plan in **Table 15**.

Combination	N_{cool}	T_{heat}	D_g	Repetition
1	7	0.7	52	15
2	7	0.07	4	5
3	11	0.07	52	5
4	11	1.33	52	5
5	3	1.33	52	5
6	7	1.33	100	5
7	3	0.7	4	5
8	11	0.7	4	5
9	7	0.07	100	5
10	3	0.07	52	5
11	11	0.7	100	5
12	3	0.7	100	5
13	7	1.33	4	5

Table 15. Complete simulation plan for Box-Behnken methods with three parameters and five repetitions. Combination 1 is the central point with fifteen repetitions.

The FEM model has been used to simulate all the combinations of parameters, described in Table 15. FEM results have been exported in MATLAB® to apply the considered method, and, to simulate the actual behaviour of the thermal sensor, the peculiar noise of a cooled camera has been added for each simulated pixel (**Figure *159***).

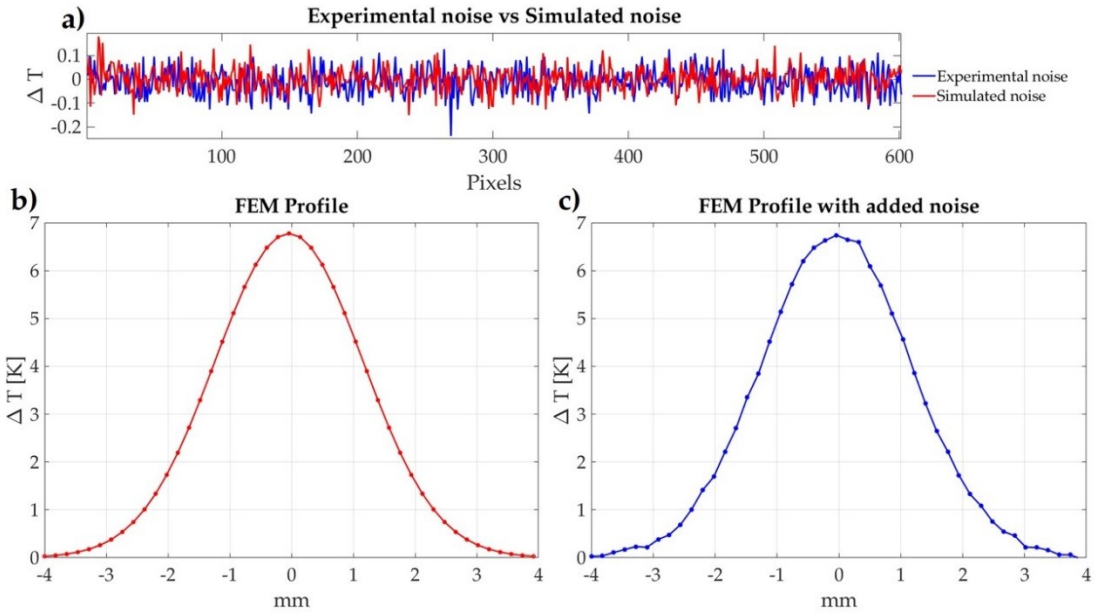

Figure 159. a) Experimental peculiar noise recorded by IR Camera with cooled sensor (blue line) and the simulated noise added to the FEM results. b) Gaussian temperature distribution obtained by the FEM model through a diameter of the laser spot. c) The same profile after adding peculiar noise of the thermal camera.

The output considered to evaluate the PLM technique's resolution and the influence of test parameters in the measurement value of thermal diffusivity is the percentage error of thermal diffusivity, described as reported in eq117.

$$\Delta\alpha\% = \left|\frac{\alpha_{in}-\alpha_{out}}{\alpha_{in}}\right| \cdot 100 \qquad (117)$$

where α_{in} is the value of thermal diffusivity used in input to the model, according to the TPS tests, and α_{out} is the value obtained after noise addition and application of PLM, as described in the previous section.

Using the resulting response surfaces, in accordance with equipment limits, the test parameters for the experimental test have been selected.

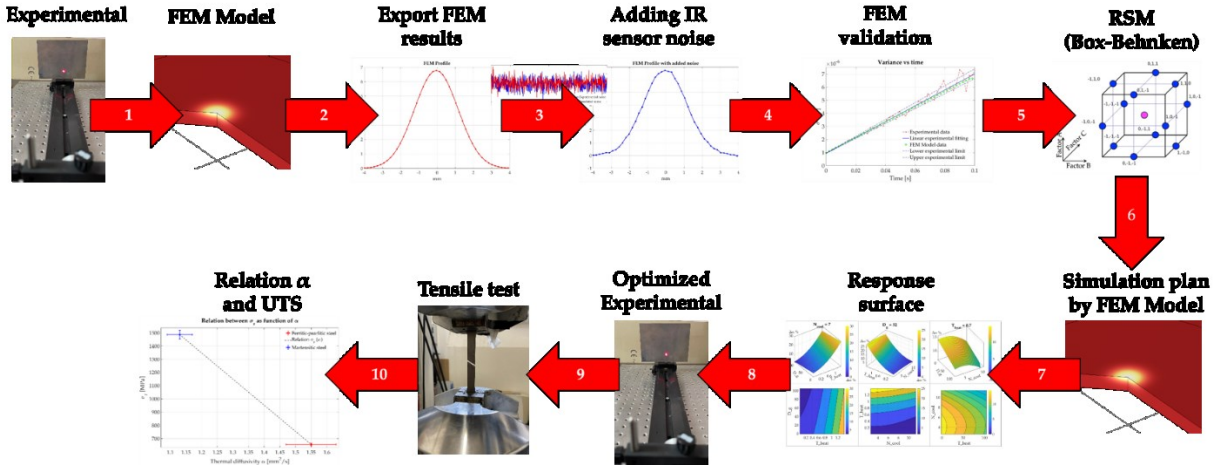

Figure 160. The scheme in picture describes the steps of the adopted procedure to select experimental test parameters

The proposed procedure adopted for the study of resolution of PLM and for the selection of the experimental parameters that minimize the error, has been resumed in **Figure *160***.

4.2.2.4 Experimental setup

For the experimental phase, a reflection setup is needed for applying the pulsed laser method. The Usibor® 1500 plates have been heated by an Ytterbium pulsed fibre laser (*YLP-V2 mJ series*) with a nominal power of 20 W and a circular 6 mm diameter spot for a heating time of 8 ms. Considering nominal power, heating time and nominal spot diameter, it is possible to state that the energy density is $Q = 5659\ {}^{J}/_{m^2}$. The thermal camera was an MWIR-camera *FLIR A6751sc*, equipped with a 50 mm lens. To permit a symmetrical Gaussian energy distribution, the laser has been placed frontally to the specimen's surface and the IR camera at the same height with an angle of ~20°, as shown

in **Figure *161***. A spatial resolution of 0.18 mm/pixel and a framerate of 400 Hz with an integration time of 2.3712 µs have been set. After the end of the heating phase, for 3 s, an IR sequence has been recorded.

Figure *161* shows the three points considered for each measurement repeated five times each. Each plate has been tested fifteen times; thus, considering eight plates, one hundred and twenty measurements have been carried out.

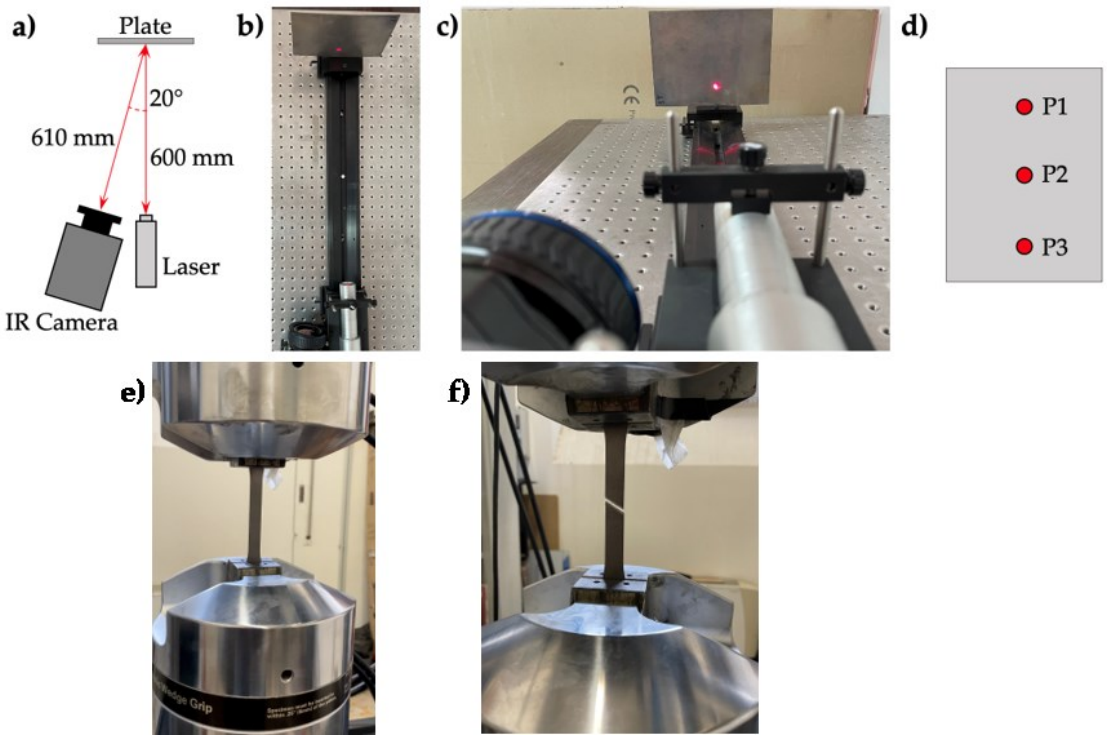

Figure 161. **a)** The scheme of the experimental setup. **b-c)** Experimental setup pictures with plate 1T, laser and FLIR A6751sc. **d)** Scheme of points of measurement on the specimens. Every point has been measured five times. **e-f)** Experimental setup for tensile tests.

The same setup and the same procedure for tests have been repeated with a heating time of 11 ms to verify the goodness of the surfaces obtained by RSM described in the previous section. Only the specimen with ferritic-pearlitic structure has been verified because, considered the parametrization of the surfaces obtained but, it will be possible to extend the application of the RSM to other materials.

For monoaxial tensile tests, a loading machine *MTS Model 370 Load Frame,* equipped with a ± 100 kN load cell has been used and the experimental tensile tests have been carried out through the procedure described in ISO 6892-1:2019. The load has been applied in

displacement control with a speed of 4 mm/min. The ISO 6892-1:2019 has been used to evaluate values of σ_r and $\Delta\varepsilon$ % (elongation at failure).

4.2.3 Results and discussion

To analyse the experimental tests, a vertical profile through the diameter has been considered, as shown in **Figure 162**. Indeed, as illustrated in **Figure *161*** a, an angle of 20° is present between the laser line and camera. Thus, to avoid any influence of the angle on the thermal diffusivity measurement procedure, only the vertical diameter profile has been considered for assessing the thermal diffusivity.

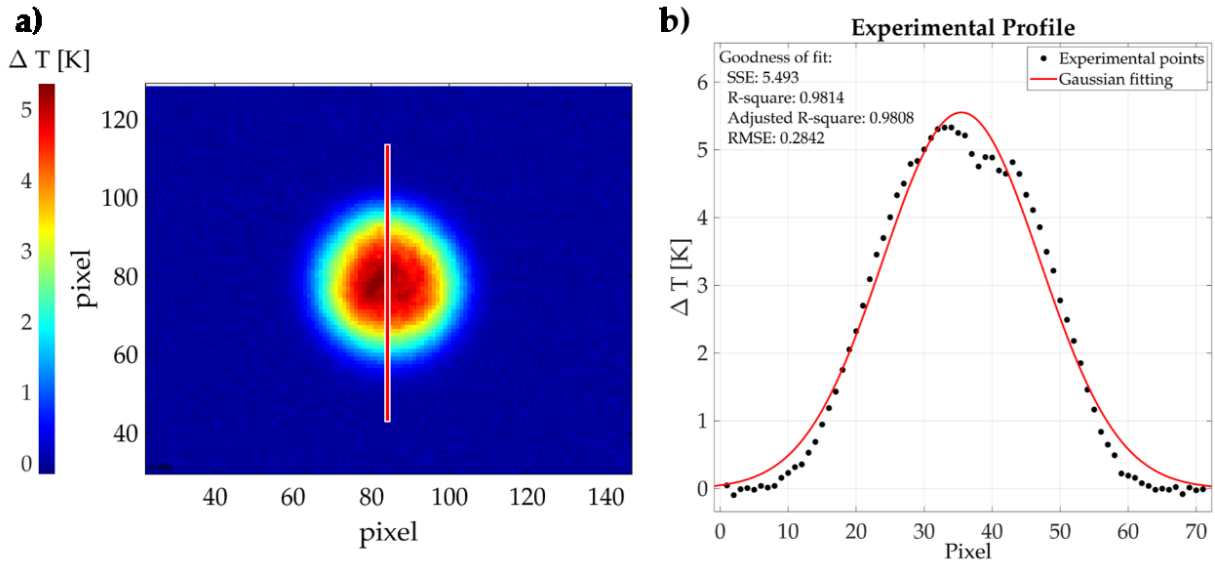

Figure 162. a) First cooling down frame after pulsed heating for plate T2 and the row of pixels considered as diameters for measurements. b) Experimental Gaussian profile measured for diameter in a).

Firstly, for validating the FEM model, a comparison with the experimental results from preliminary tests conducted on the plate NT1 (t_{heat}= *8 ms* – d_{spot}= *6 mm* – *mm/pixel ratio = 0.18 mm/pixel*) have been carried out (**Figure 162**).

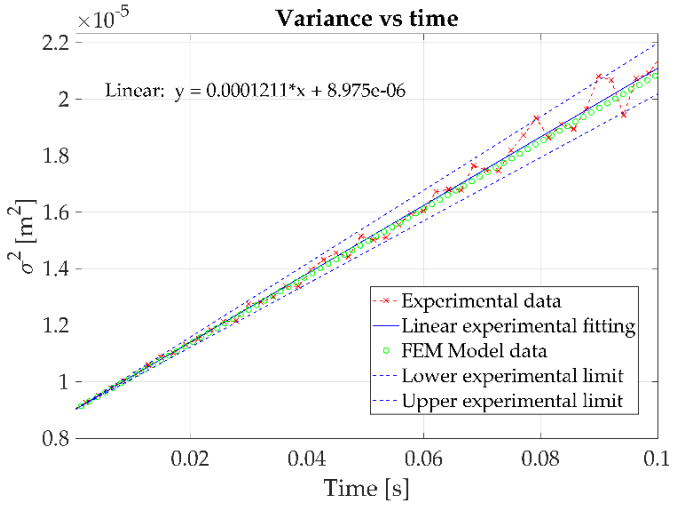

Figure 163. Variance vs time graph. The Red dashed line shows raw experimental data. The solid blue straight line is obtained through the linear fitting of experimental data. The Blue dashed lines are the superior and inferior limits of experimental results with 95% confidence. The Green dotted line is obtained from the analysis of FEM model results.

As shown in **Figure *163***, experimental results with two straight limit lines (blue dashed lines) have been considered to define a region of error with a confidence of 95%. The straight line representing the FEM results falls inside the experimental data region (green circles) and then the heat distribution over the time on the surface obtained with the FEM model matches the experimental heat distribution. This validation of model proofs that the temperature distribution for each time-step on the considered diameter of laser spot obtained from the FEM model, matches with the experimental data. Hence, the FEM model developed correctly describes the real phenomena and can be adopted for a study on the influence of test parameters on the thermal diffusivity measurement. This study, through FEM model application, it is timesaving compared with usual experimental procedure to define test parameters, based on empirical approaches.

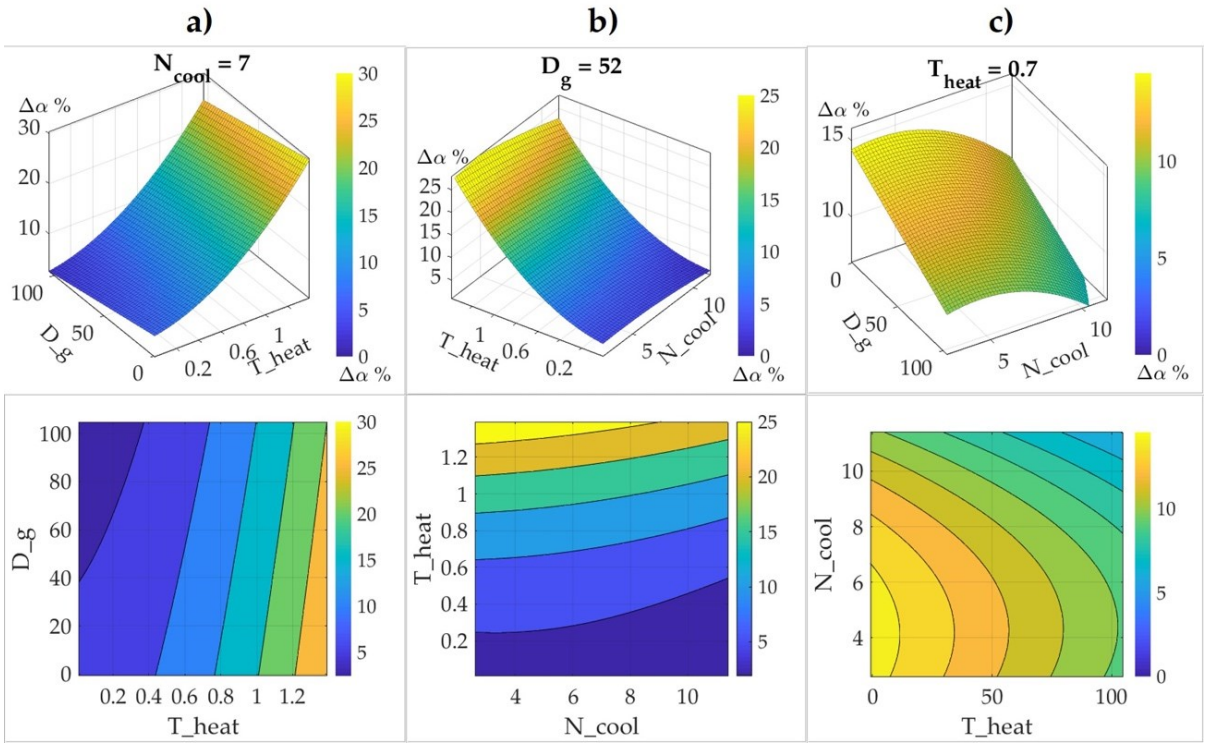

Figure 164. a) The surface obtained for the value of N_{cool} = 7 shows the error Δα % as a function of D_g and T_{heat} and with a relative contour plot. b) The surface obtained value of D_g = 52 shows the error Δα % as a function of N_{cool} and T_{heat} with the relative contour plot. c) The surface obtained for the value of T_{heat} = 0.7 shows the error Δα % as a function of T_{heat} and N_{cool} with the relative contour plot.

In **Figure 164**, the surfaces obtained by RSM are reported. Each surface represents the percentage error in thermal diffusivity measurement as a function of the considered parameters (N_{cool}, D_g, T_{pulse}) thus, the minimum value of error results in the best parameters. The surfaces represented in **Figure 164**, and correspondent contour plots, have been obtained for each one fixing the third parameter to a value in the middle of the considered interval.

As expected, considering the obtained surfaces, it is evident that the measured error in determining the thermal diffusivity reduces with high framerate, high spatial resolution (low mm/pixel ratio) and shorter pulse (close to the hypothesis of pulsed heating). The results show that in the best test condition, considering the analyzed ranges, the resolution of the technique can be assumed ~ 2 %. The surface obtained are a very useful and powerful tool for the application of PLM for thermal diffusivity measurements. In fact, the first use can be the described ones: the test parameters selection. In this case, it is possible, using the maps, select test parameters as a function of the error on thermal diffusivity

measurement, with the aim to minimize the error. To resume, considering as input the minimum value of error and obtaining as output tests parameters. The second use, can be the prediction of the error on thermal diffusivity measurement, considering the available equipment. Thus, it is possible to control and consider the order of error as a function of tests parameters that can be adopted, based on limits of the instruments. In this case, the input are the limits test parameters reachable and the output the percentage error that is expected with that combination of parameters. Nevertheless, with the described equipment, the minimum possible heating time has been *8 ms* with a value of $T_{pulse} \sim 0.5$. This means that considering the need to have a high framerate, high spatial resolution, and considering technological limits, it is necessary to have a trade-off solution. From the surfaces showed in Figure 164, an empirical model can be considered for evaluating the thermal diffusivity error as function of inspected parameters:

$$\Delta\alpha\,\% = 7.78 + 0.31N_{cool} + 4.25T_{heat} - 0.143D_g - 0.038N_{cool}^2 + 10.88T_{heat}^2 + \ldots$$

$$\ldots + 0.000978D_g^2 - 0.353N_{cool}T_{heat} + 0.00048N_{heat}D_g + 0.0067T_{heat}D_g \qquad (118)$$

where, in the experimental case, $D_g = 33$ and $N_{cool} = 6$. From the obtained surface, applying the eq 118, it is possible to see that the predicted error is 8%.

Summarizing, obtaining the response surfaces (Figure 164) and the model (eq 118), the selection of experimental test parameters can be done following the steps described below:

1. Carrying out one experimental preliminary test for measuring the value of T_s;
2. Using the response surface obtained to see the area that minimize the error;
3. Considering the corresponded values of D_g, T_{heat} and N_{cool} according with the limits of the equipment;
4. Obtaining the *mm/pixel* ratio, the acquisition frequency and the heating duration suitable for the application.

Considering as a reference the TPS measurement, the percentage difference between the value of thermal diffusivity obtained by PLM and TPS is ~ 5%, as resumed in Table 16, very close to the predicted value obtained from the RMS response. To verify the robustness of the obtained surface, another measurement with a longer pulse has been performed,

with a value of T_{pulse} ~ 0.7. The predicted error value in this case was ~ 11% while the experimental one is ~ 13 %, according, again, to the results of RMS.

N_{cool}	T_{heat}	D_g	Δα % (RSM)	Δα % (Experimental)
6	0.53	33	~ 8 %	~ 5 %
6	0.7	33	~ 11 %	~ 13%

Table 16. Values of parameters adopted for the validation of the model obtained by RSM and results of the error Δα% obtained from the model and experimentally, considering the TPS measurements as a reference.

Table 17 shows the values of thermal diffusivity obtained by the PLM and the TPS method for non-heat-treated plates (ferritic-pearlitic structure) and quenched steel plates (martensitic structure). It is possible to see that the relative difference between the values of thermal diffusivity obtained by the thermographic measurement is ~ 27 %, slightly different to the values obtained by the TPS method. These results confirm the goodness of the proposed procedure for assessing the effectiveness of the quenching process in the boron steel Usibor® 1500.

Micro-structure	Thermal diffusivity (PLM) *[mm^2/s]*	Thermal diffusivity (TPS) *[mm^2/s]*
Ferritic-pearlitic	15.53 ± 0.83	14.65 ± 0.21
Martensitic	11.34 ± 0.42	11.39 ± 0.23
Difference (%)	27%	23%

Table 17. Results of thermal diffusivity obtained from pulsed laser method and transient plane source for ferritic-pearlitic microstructure and martensitic ones. The last line shows the difference between the thermal diffusivity values for both ways.

With the aim to confirm the anti-correlation between thermographic results and hardness occurred because of changing in material microstructure, Vickers hardness tests were carried out, both on plates in the supplied state (ferritic-pearlitic microstructure) and on quenched plates (predominantly martensitic microstructure). Qness micro hardness tester Q10 A+ was adopted by setting a load of 1 kg and a dwell time of 5 s, after properly grinding and polishing specimens surface. This latter step is a metallographic preparation adopted to remove the superficial coating (Al-Si). The experimental setup is shown in *Figure 165*.

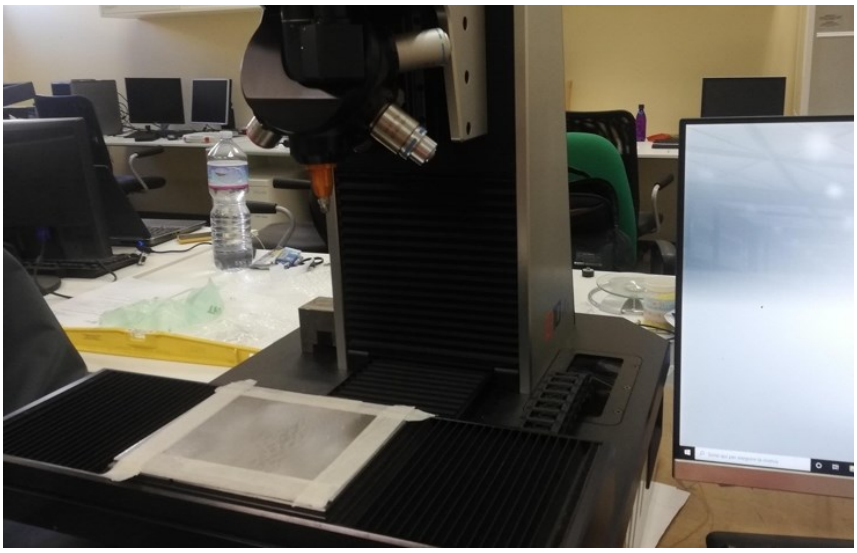

Figure 165. Experimental set-up used for hardness tests.

For each plate, five replications of hardness measurement were performed in the areas analyzed by thermography.

Micro-structure	**Thermal diffusivity (PLM)** ***[mm²/s]***	**Thermal diffusivity (TPS)** ***[mm²/s]***	**Hardness** ***[HV1]***
Ferritic-pearlitic	15.53 ± 0.83	14.65 ± 0.21	214.1 ± 3.4
Martensitic	11.34 ± 0.42	11.39 ± 0.23	548.5 ± 6.8
Difference (%)	27%	23%	~ 150%

Table 18. Experimental thermographic and hardness tests results

Consequently, the results of monoaxial tensile test have been analyzed trough the standard procedure reported in ISO 6892-1:2019 obtaining values of ultimate tensile strength (UTS) and percentage elongation. In Figure 166 are reported the representation with the definitions of peculiar quantities for tensile test specimens, that permits to obtain UTS and relative elongation. In Figure 166, the pictures of four specimens are reported: two before the (one for each micro-structure) and two after the tensile tests. It is possible to see the strong elongation before the fracture in sample with a ferritic-pearlitic structure that is indicative of greater ductility than the martensitic micro-structure, so the elongation is low.

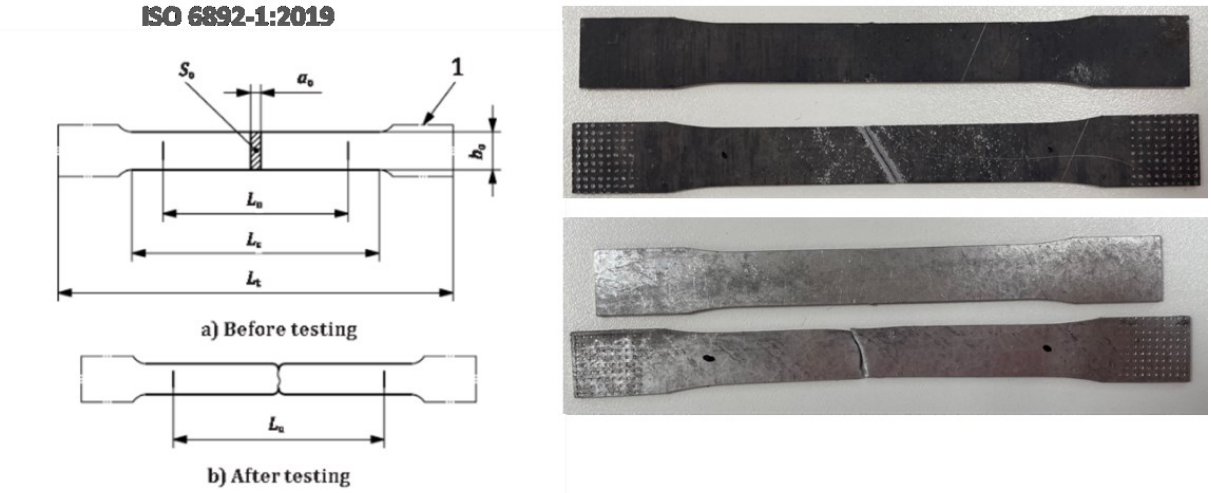

Figure 166. Specimens for monoaxial tensile test obtained in accordance with standard ISO 6892-1:2019.

After the tensile tests, values of σ_r and $\varepsilon(\%)$ have been obtained (Table 19) and a first correlation between thermal diffusivity and UTS have been supposed.

Micro-structure	**Thermal diffusivity (PLM)** *[mm²/s]*	**σ_r** **[MPa]**	**ε** **[%]**
Ferritic-pearlitic	15.53 ± 0.83	655.41 ± 8.69	9.11 ± 0.83
Martensitic	11.34 ± 0.42	1486.35 ± 33.41	2.02 ± 0.35

Table 19 Values of ultimate tensile strength and percentage elongation resulting from experimental tests.

A preliminary approach for the correlation between ultimate tensile stress of boron steel and thermal diffusivity has been supposed linear as showed in ***Figure 167*** with relative error bars. It is glaring that is possible distinguish between martensitic and ferritic-pearlitic structure trough the thermal diffusivity measurement by pulsed laser method in a completely non-destructive way. To have a statistical confirm of this result that can be evident observing the measurements point and error bars in ***Figure 167***, a t-test has been conducted. This test compares the average values of two data sets and determines if they came from the same population; hence, if it is not, it is reasonable to confirm that comes from different populations. Considering a significance level of 0.05, which corresponds to the 95% of confidence, and obtaining $|t| = 115.913 > t_c = 1.982$, it is possible to evaluate that the p-value = 0 < 0.05. Thus, it is possible to conclude that the two values obtained for thermal diffusivity for the two different micro-structures, belong to two different populations.

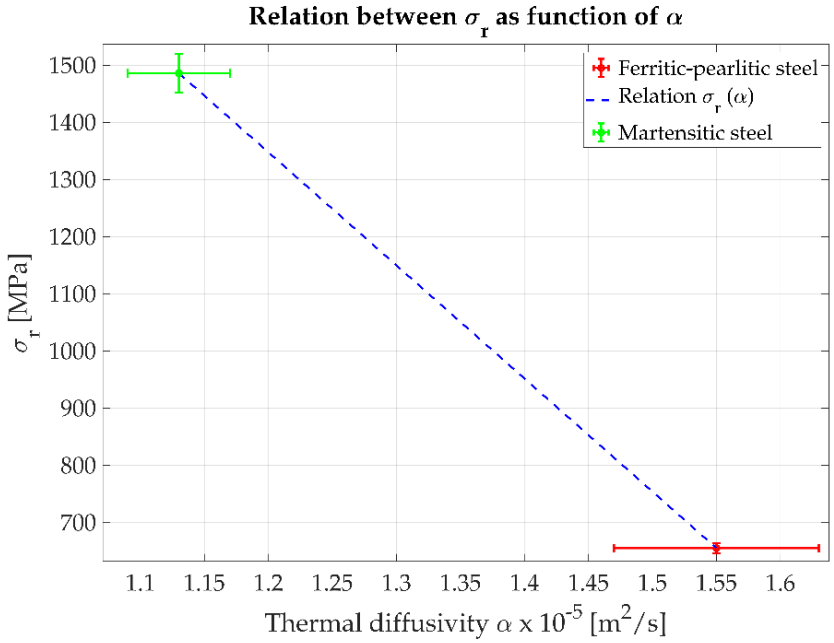

Figure 167. Relation between thermal diffusivity and UTS for boron steel.

It is self-evident that after a calibration for the material, it is possible to have a reliable estimation of material UTS, only through the thermal diffusivity measurement. It is possible to observe a significant error bar in measurement of thermal diffusivity obtained by PLM, especially for the ferritic-pearlitic structure. This is the effect of non-uniform surface condition that influence on the measurement significantly.

The discussed results confirms the anti-correlation between the mechanical properties and thermal diffusivity in steel. However, compared to existing literature, a law has been identified that relates thermal diffusivity to the ultimate tensile strength (UTS) of the material. A standard procedure has been identified for selecting optimal test parameters based on the measurement error of thermal diffusivity through the obtained response surfaces for the first time.

4.2.4 Conclusions

In the described application a non-destructive procedure for evaluating the effectiveness of the heat treatment in the boron steel Usibor 1500, through the thermal diffusivity measurement, has been presented. Additionally, an anti-correlation between thermal diffusivity values and σ_r of material has been found, that permits an estimation of mechanical properties of steel through thermographic technique. The pulsed laser method (PLM) has been applied to measure the in-plane thermal diffusivity and in addition, an investigation of the influence of test parameters on the measurement through the

development of a Finite Element Model and the design of experiment techniques (Response surface method) has been carried out.

Eight boron steel plates with a ferritic-pearlitic structure have been analysed. Four of these specimens have been subjected to a hardening heat treatment, obtaining a 100% martensitic structure. Thermal diffusivity has been considered as an index to characterise the microstructure considering the anticorrelation between hardness and thermal diffusivity. An FEM model of Pulsed laser method has been developed by COMSOL Multiphysics® to study how change the error $\Delta\alpha$ as a function of main test parameters: framerate, spatial resolution and heating duration which have been parametrized in order to obtain a general result. The response surface method (RSM) has been adopted, obtaining surfaces which describe the behaviour of error as a function of described parameters experimentally validated comparing results obtained by thermographic method with - established transient plane source (ISO/FDIS 22007-2). It is possible to confirm that the surfaces obtained by FEM and RSM are useful and powerful tools to have a good estimation of measurement error, for the considered thermographic metho.

The obtained surfaceshas been adopted for the evaluation of test parameters suitable for the experimental campaign, that demonstrates the capability of thermographic technique of discerning the two microstructures, resulting in a difference of 27% between ferritic-pearlitic structures and 100% martensitic ones. Following the ISO 6892-1:2019, five specimens for each microstructure have been obtained and monoaxial tensile test has been carried out, resulting in values of σ_r and percentage elongation. The values of ultimate tensile stress obtained for steel with martensitic microstructure are more than twice the values of steel in not treated state (ferritic-pearlitic). On the other hand, the average value of percentage elongation obtained for martensitic microstructure is one-fifth of the ferritic-pearlitic ones.

A first approach for the correlation between values of thermal diffusivity and ultimate tensile stress followed the first results, assuming a linear behaviour. In conclusion, it is possible to state that: for the Usibor 1500, the NDT proposed procedure is capable to recognize a ferritic-pearlitic microstructure to a completely martensitic ones and, through the resulting relation, it is possible to reliably estimate mechanical properties of boron steel, using thermal diffusivity measurements. To confirm and toughen up the procedure, an analysis of specimens with intermediate percentages of microstructures has been planned

to verify the hypothesis of linear relation between mechanical properties a thermophysical ones.

4.3 A thermographic method for the evaluation of percentage phase content in boron steel

4.3.1 Introduction

Following the activities of the previous case study, in which a procedure to select the experimental test parameters to reduce the error of measurement in thermal diffusivity have been discussed, in this one, a study of different microstructure has been investigated. Three different microstructures (100% bainitic – 50%-50% bainitic/martensitic - 100% martensitic) have been investigated to evaluate the capability of the thermographic technique to discern different microstructures with similar composition and to explore the limits of the presented thermographic technique.

To obtain these answers, nine specimens have been analysed with three different microstructures in order to quantify the limits of the techniques and the minimum number of repetitions needed to obtain the necessary resolution.

4.3.2 Material and methods

4.3.2.1 Specimens

To evaluate different level of phases, present in boron steel, nine specimens have been considered and analysed. These specimens were divided in three different groups which correspond to different phase percentage each, as described in **Table *20***. For each percentage of phase, three specimens have been produced, to consider replications too. To ensure the described percentage, the specimens have been obtained by a physical simulator with a procedure described in other works [262,263]. In the middle of the specimens, an area with total length of 1 cm presents nominal phase composition (***Figure 168***) hence, all the measurement of thermal diffusivity must be done in the area included in red square. To be sure about the uniformity of microstructure in the area in the middle of the specimen, the geometry of specimen has been optimized by FEM simulation, as described in other works [263].

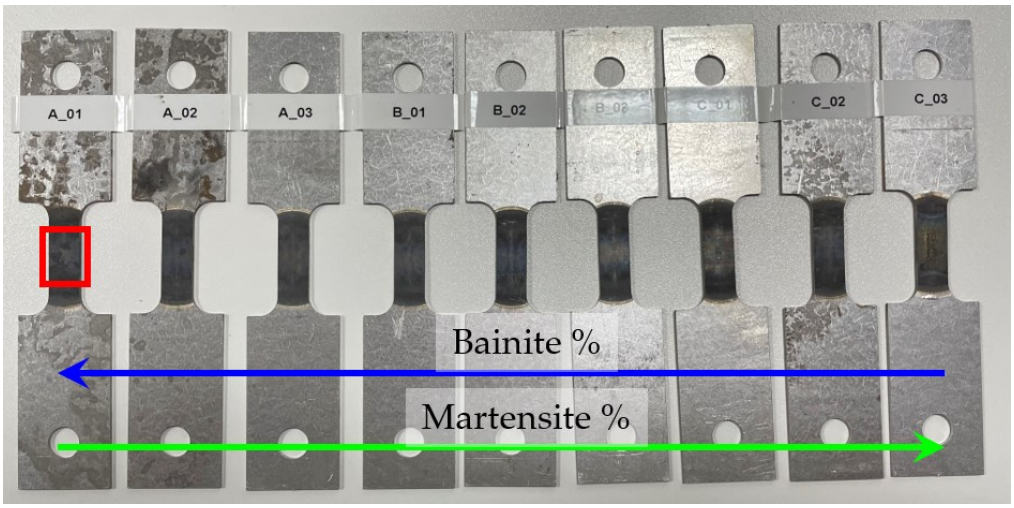

Figure 168. Specimens with several phase percentage. The red square highlights the area of specimens that has uniform microstructure and nominal phase percentage.

ID	Micro-structure	Thickness
A_01/02/03	100% Bainite	1.03 mm
B_01/02/03	50% Bainite – 50% Martensite	1.03 mm
C_01/02/03	100% Martensite	1.03 mm

Table 20. Geometrical dimesions and phase percentage composition of the inspected specimens.

4.3.2.2 Experimental setup

In the consequently experimental phase, a reflection setup has been realized for the application of PLM. The specimens described have been heated by an Ytterbium pulsed fibre laser (*YLP-V2 mJ series*) with a nominal power of 50 W and a circular 2 mm diameter spot for a heating time of 6 ms. A very small spot diameter has been used to avoid the influence of the edge of specimens. In fact, as it is possible to observe in **Figure *169***, the central part of specimen has a width of 10 mm and it is important that the edges of the specimen do not affect the diffusion of heat along the surface. Therefore, to do this, it was necessary to reduce the size of the laser spot as much as possible and place it as centrally as possible relative to the sides. The power of laser has been modulated and reduced after some preliminary tests in which strongly saturated thermograms were present. Thus, a value of 35% of nominal power, that corresponds to 17.5 W has been used. Considering a laser circular spot with nominal radius of 1 mm and the adopted heating time, it is possible to estimate an energy density of $Q = 33422\ {}^{J}/_{m^2}$. The thermal camera was an MWIR-

camera *FLIR A6751sc*, equipped with a 50 mm lens and extension ring to increase the spatial resolution, considered the small laser spot and the need to have more pixel as possible on the nominal spot diameter according with the maps obtained in ***Figure 164***. The laser has been placed frontally to the specimen's surface but on a different height. In fact, an angle of ~20° between specimen's surface and laser beam has been present. The IR camera has been positioned on the same axis of laser source with an angle of ~5° between the surface and the camera axis, as shown in **Figure *169***. A spatial resolution of 0.039 mm/pixel and a framerate of 540 Hz with an integration time of 2.3712 µs have been set. After the end of the heating phase, for 1.5 s, an IR sequence has been recorded.

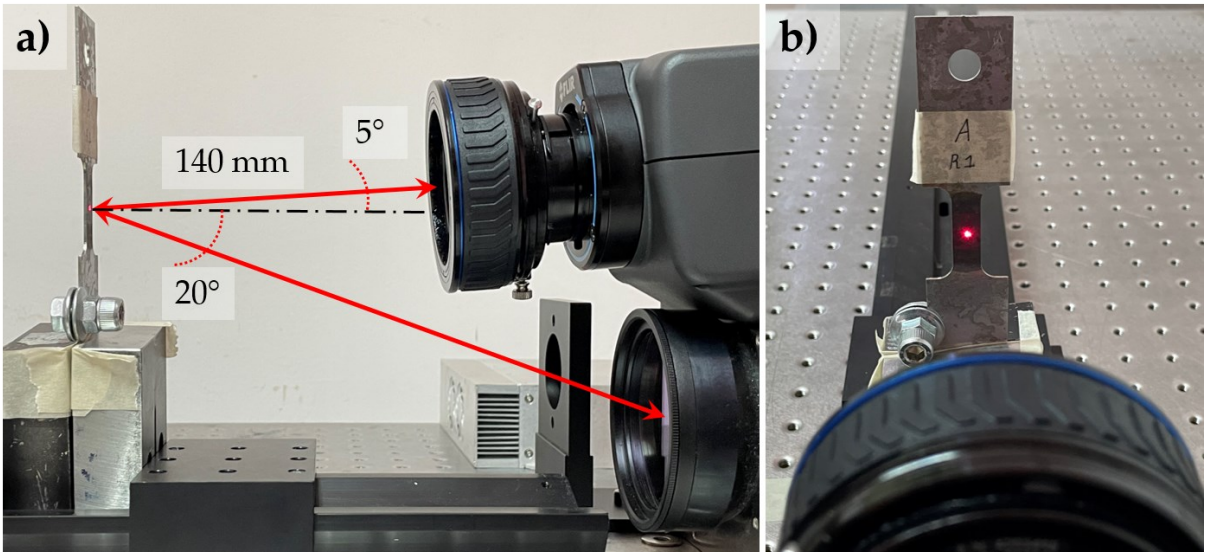

Figure 169. a) Experimental setup with dimensioned set-up scheme. b) Front view of specimen A_01 with detail on position of laser beam on specimen.

4.3.2.3 Time window selection

The pulsed laser method in reflection mode for the measure of thermal diffusivity is based, as well described previously, on the observation of standard deviation of gaussian temperature distribution, as a function of time. In the procedure, two fittings are present: the first, the fitting of temperature distribution on surface with a gaussian curve and the second, the linear fitting of values of variance of temperature distribution in time. It is reasonable to evaluate, considering a real phenomena and the noise of thermal sensor, that after a certain observation time, the fitting of gaussian profile is no longer possible because the temperature profile is not gaussian anymore, and the quality of fitting is very low. For this reason, if a long observation time is fixed, the value of the second linear fitting can be influenced from this behavior and an overestimation of the slope of the straight line is

possible and, in turn, an overestimation of thermal diffusivity. In the previous case study (section 4.2), the used criteria (section 4.2.2.3) adopted to parametrize the main parameters is based on the settling time of a first order response to a step input. In this case study, another approach has been adopted for the evaluation of time window, based on the goodness of gaussian fit and compared with the previous one.

To measure the goodness of fit of a model, the R^2 can be used. The R^2 coefficient of determination is a statistical measure of how well the regression predictions approximate the real data points because is a statistical measure in a regression model that determines the proportion of variance in the dependent variable that can be explained by the independent variable. An R^2 of 1 indicates that the regression predictions perfectly fit the data. Hence, a value too low of R^2 means that the considered model is not good to describes the fitted data. Therefore, the main idea is to define the time window as the time for which the fitting of gaussian temperature distribution results in $R^2>0.95$. Applying this procedure, it is possible to obtain for the second fitting a strong linearity in distribution with values of R^2 close to 1 (**Figure *170***).

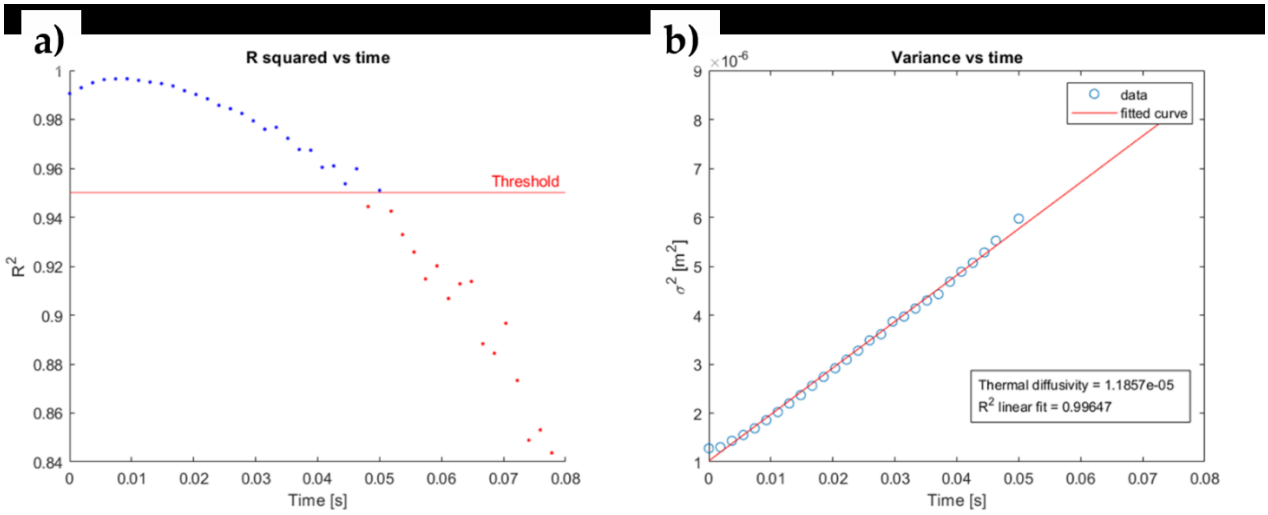

Figure 170. a) Representation of points considered to define the time-window. The blue dots represent the gaussian fitting with values of $R^2>0.95$, the red one fitting with $R^2<0.95$. b) Correspondent linear fitting of the values of variance obtained from the blue dots in a).

4.3.3 Results and discussion

To measure in-plan thermal diffusivity after the application of pulsed laser method, it is necessary to consider a suitable diameter for the laser spot and consider the evolution of temperature distribution over time. It has been previously discussed that the temperature profiles can be hardly distinguished from noise when the ΔT is lower than the background noise thus, the temperature profile shape can be influenced from spatial and temporal

noise. The spatial noise can be caused by the inhomogeneities on surface (scratches, oxides, etc…) influencing the signal and the quality of gaussian fitting. An approach to reduce the noise, can be to apply the just described procedure on the profile obtained from an average of three rows of pixels adjacent through the diameter, as showed in ***Figure 171*** c, resulting in smoother profiles, as showed in ***Figure 171*** d. With this procedure, it is possible to achieve high values of R^2 for an higher number of profiles increasing the available time window, so the number of points for the second linear fitting, to estimate the thermal diffusivity.

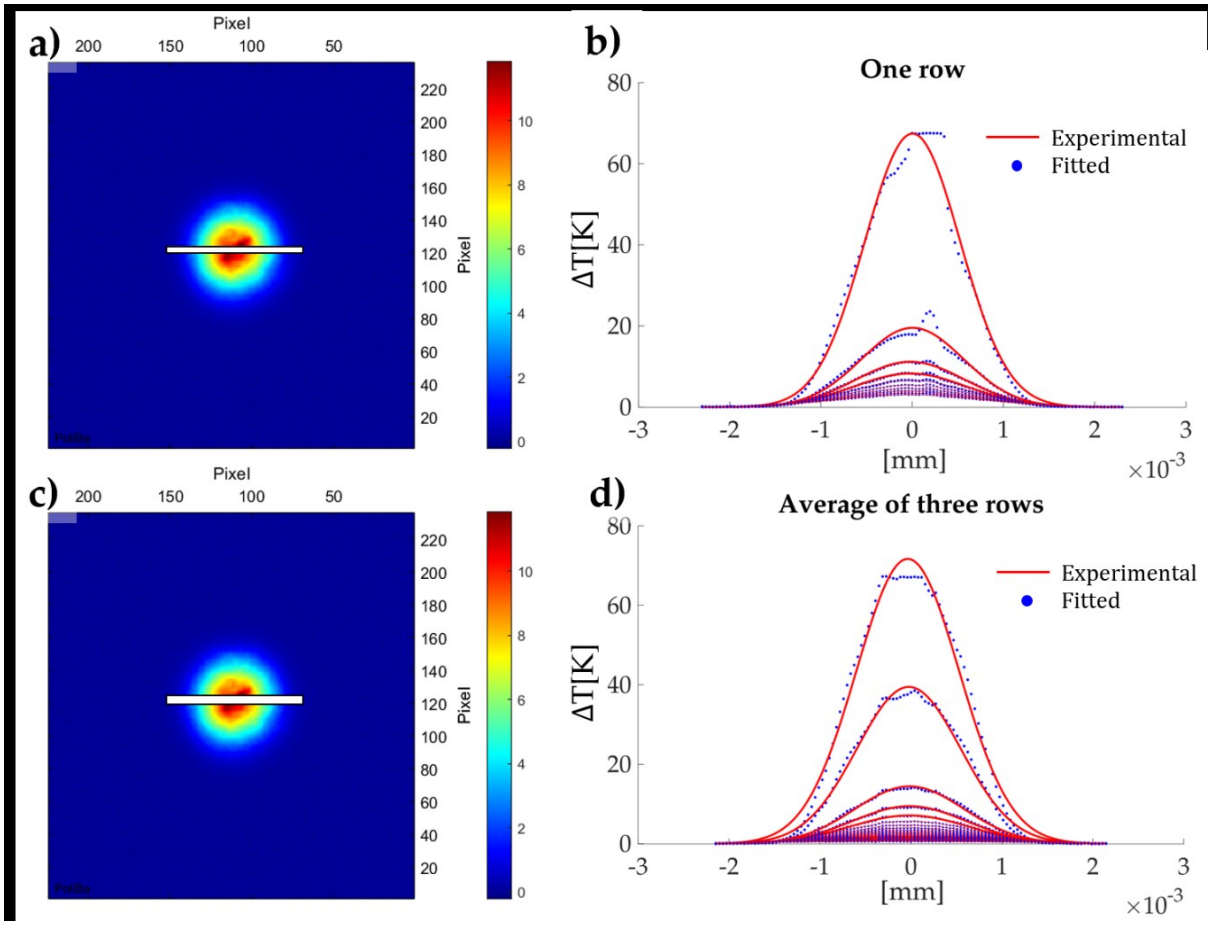

Figure 171 a) The single row pixel selection on a thermogram and b) relative temperature profiles. c) Pixel selection for three rows of pixels and d) correspondent averaged temperature profiles.

To evaluate the goodness of this proposed procedure, the results obtained with a time window fixed coincident with settling time has been compared with the ones obtained with the $R^2>0.95$ criteria (***Figure 172***).

To compare correctly the results obtained by the two different adopted methods, the measurements on the martensitic structure specimens have been considered. In fact, in the previous section 4.2, the value of thermal diffusivity measured for martensitic structure of Usibor® 1500 has been measured by TPS method [264]. Hence, to evaluate between the

two approaches presented which one results in a lower error in measurement of thermal diffusivity, a comparison between the values obtained by TPS and laser pulsed thermography has been considered.

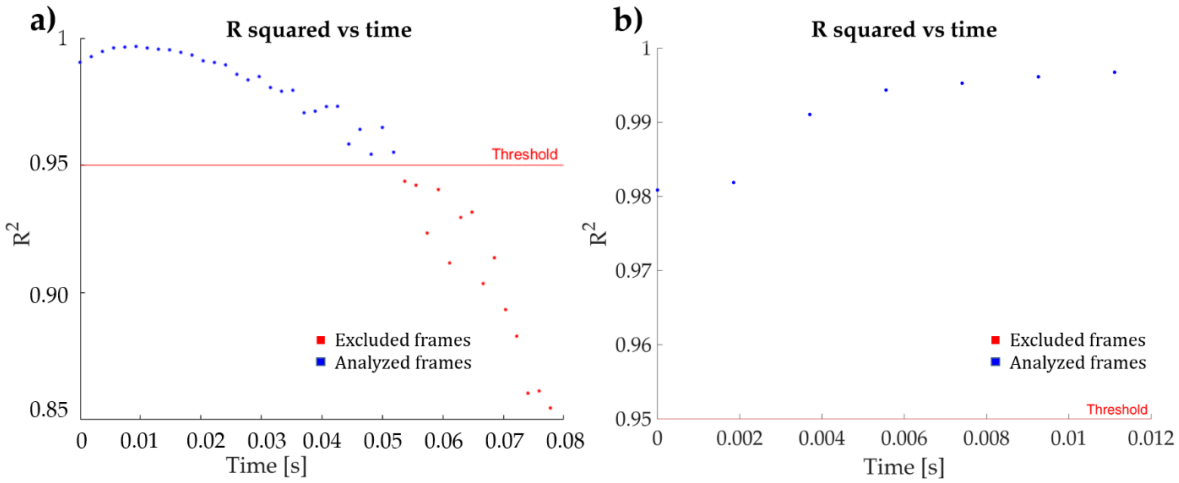

Figure 172. Value of R^2 as function of time. a) the number of frames analyzed applying the R^2>0.95 criteria. b) The frames analyzed applying the settling time criteria

In section 4.3.2.3, two different methods to evaluate the time window have been discussed. The measurement can also be affected by the time window, so the comparison between one-row diameter and averaged diameter has been conducted for both time window selection procedures.

Considering the settling time method to evaluate time window, the procedure to evaluate thermal diffusivity has been applied to single line pixel diameter and averaged diameter. Three measurements for each specimen with martensitic structure (C_01/02/03) have been carried out, to have three repetitions for each specimen and three specimen replications (C_01/02/03). The same measurements have been analyzed using the $R^2>0.95$ as time window selection criteria, then the results have been compared with results obtained from TPS method [264].

Micro-structure	**Time window selection**	**Thermal diffusivity (TPS)** ***[mm²/s]***	**Thermal diffusivity (single line)** ***[mm²/s]***	**Thermal diffusivity (averaged line)** ***[mm²/s]***
Martensitic	Settling time	11.39 ± 0.23	11.35 ± 0.32	11.13 ± 0.25
Martensitic	R^2>0.95	11.39 ± 0.23	11.23 ± 0.41	11.09 ± 0.28

Table 21. Values of thermal diffusivity of martensitic specimens obtained trough different procedures for time window selection (settling time or R^2>0.95) and analyzed diameter (single line or averaged line).

As it is possible to observe from values resumed in ***Table 21***, the application of measurement procedure to the averaged line results in an underestimation of thermal diffusivity value for both the procedures of time window selection. Considered the settling time procedure for time window selection, the difference among TPS values of thermal diffusivity and PLT is *0.35%* with single line diameter procedure and *2.28%* for the averaged pixel line. Using the $R^2>0.95$ criteria for the time window selection, for single line the difference is *1.40 %* and for averaged ones *2.63%*. It is possible to observe that there is always an underestimation of thermal diffusivity using the averaged line. All the uncertainty of measurements resumed in **Table *21*** are evaluated as the 1.96 the standard deviation of measurements, thus the 95% of confidence.

Taking into account the results obtained for the described preliminary analysis, all the other experimental tests have been analyzed applying the settling time criteria for the selection on time window and the single pixel approach for the selection of diameter. Hence, all specimens have been tested with the approach described before: three test repetitions for each specimen for a total number of 27 experimental tests, nine for each phase composition, have been obtained. All the results obtained are reported in **Table 22**.

Specimen	**Structure**	**Repetition**	**Thermal diffusivity** ***[mm²/s]***
A_01	100 % Bainite	1	12.53
A_01	100 % Bainite	2	12.53
A_01	100 % Bainite	3	12.40
A_02	100 % Bainite	1	12.31
A_02	100 % Bainite	2	12.37
A_02	100 % Bainite	3	12.36
A_03	100 % Bainite	1	12.30
A_03	100 % Bainite	2	12.29
A_03	100 % Bainite	3	12.26
B_01	50 % bainite – 50 % martensite	1	11.87
B_01	50 % bainite – 50 % martensite	2	11.94
B_01	50 % bainite – 50 % martensite	3	11.75
B_02	50 % bainite – 50 % martensite	1	12.07
B_02	50 % bainite – 50 % martensite	2	11.98
B_02	50 % bainite – 50 % martensite	3	12.14
B_03	50 % bainite – 50 % martensite	1	11.63
B_03	50 % bainite – 50 % martensite	2	11.74

B_03	50 % bainite – 50 % martensite	3	11.47
C_01	100 % martensite	1	11.49
C_01	100 % martensite	2	11.56
C_01	100 % martensite	3	11.49
C_02	100 % martensite	1	11.25
C_02	100 % martensite	2	11.28
C_02	100 % martensite	3	11.03
C_03	100 % martensite	1	11.42
C_03	100 % martensite	2	11.34
C_03	100 % martensite	3	11.31

Table 22. Results of thermal diffusivity measurement for each specimen.

To evaluate correctly the results obtained from experimental tests, it is needed to use statistical tools as the hypothesis test. To evaluate the replicability of production process, the first step is to understand if the values of thermal diffusivity obtained for the replications of the same nominal phase percentage (01/02/03) are part of the same population thus, if the mean value of thermal diffusivity is the same for the three replications. The test that permits to compare the mean values of thermal diffusivity obtained is the T-test based on the t-Student distribution. To apply the test correctly, it is needed to know if the value of variance can be considered constant for the measurements hence, to obtain this information, the F-test based on the Fisher-Snedecor distribution has been used. Results of F-test applied on results obtained confirm that the variance among the three different nominal phase percentage can be considered the same thus, a T-test considering variance constant can be applied. As first step, the replicability of the production process has been verified applying T-test among the three replications comparing the values of thermal diffusivity obtained. The statistical tests adopted confirmed the hypothesis that the mean value of thermal diffusivity measured for the three specimens with the same phase percentage belong to the same population; thus, the mean value of thermal diffusivity obtained is representative of that population.

Specimen	**Structure**	**Repetition**	**Thermal diffusivity** ***[mm²/s]***
A_01/02/03	100 % Bainite	9	12.37 ± 0.19
B_01/02/03	50 % Bainite – 50 % Martensite	9	11.84 ± 0.42
C_01/02/03	100 % Martensite	9	11.35 ± 0.32

Table 23. Results of thermal diffusivity measurements obtained for three different phase percentage.

As resumed in ***Table 23***, it is possible to distinguish three different values of thermal diffusivity, each one correspondent to a specific steel micro-structure. To understand if it is statistically correct to define the values obtained as three different measurements, a Student t-test has been used among the three values and results are resumed below. The question the test answer is: "Are the mean values of measured thermal diffusivity,different?" and the answer is in last line of ***Table 24*** obtained from the comparison between critical t and statistics-t.

Specimen	**A vs B**	**B vs C**	**A vs C**
α	0.05	0.05	0.05
Statistics-t	6.67	5.47	16.18
Critical t	2.20	2.13	2.16
Evaluation	6.67 > 2.20	5.47 > 2.13	16.18 > 2.16
Answer	yes	yes	yes

Table 24. Values relative to the student t-test applied to the measured values of thermal diffusivity.

From this test, it is possible to confirm that there is a variation in thermal diffusivity that corresponds to a variation in microstructure composition of considered boron steels.

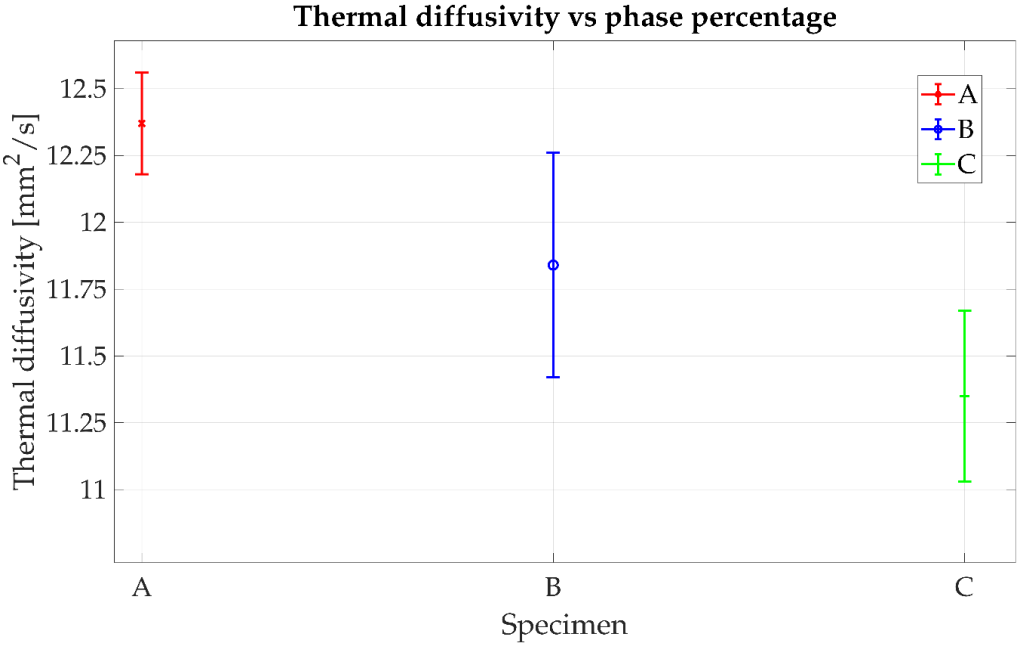

Figure 173. Representation of mean thermal diffusivity measurements correspondent to the three phase percentages of specimens with relative error bars that represent ±1.96 σ.

As it is possible to see in **Figure *173***, the mean values of thermal diffusivity are different, but the error bars present an overlap because of high values of standard deviation that can be reduced increasing the number of repetition of measurements. An estimation of the

number of repetitions that is necessary to obtain a fixed value of standard deviation has been done by the following equation:

$$n > 2\left[\frac{(z_\alpha + z_\beta)\sigma}{\delta}\right]^2 \quad (119)$$

in which: z_α depends on the value of α (α=0.05), z_β depends on the power of the test thus, the β error, σ is the standard deviation obtained for preliminary tests, δ is the minimum difference between two values of thermal diffusivity that it is possible consider significative and n is the number of repetitions needed to be able to discern a difference of δ. To estimate the value of repetition needed (n), the values of $z_\alpha = 1.96$ and $z_\beta = 1.645$ (Power=95%) have been assumed, and a δ=*0.20* mm^2/s has been fixed. The value of standard deviation has been fixed to σ=*0.22* mm^2/s because is the higher obtained from test thus, the evaluation of the number n can be considered conservative. After the application of equation 119, results show that, to increase the resolution of technique, to be capable to resolve a difference of *0.20* mm^2/s in thermal diffusivity, with the 95% of confidence and test power, 32 repetitions should be considered. At first glance, 32 repetitions may seem a very high number but, considering the time needed for the current controls of microstructure and the time needed for each measurement by PLM, the procedure proposed it is still time saving and easier than the traditional controls. In fact, with a defined set-up, the total time can be estimated as: the sum of heating time, cooling time and analysis time that results in less than 1.5 seconds overall. Thus, to achieve the 32 repetitions, the total time needed can be estimated to ~45 s. It must be considered that, at the moment, the proposed method competes with hardness semi-destructive measurements and metallography, which need definitely more time and cannot be automatized.

4.3.4 Conclusions

In the case study considered, a non-destructive procedure for evaluating the microstructure in the boron steel Usibor 1500, through the thermal diffusivity measurement, has been presented.

The anti-correlation between thermal diffusivity values and hardness, so microstructure, of material has been used to permits an estimation of phase percentage composition of steel through thermographic technique. The pulsed laser method (PLM) has been applied to

measure the in-plane thermal diffusivity and a discussion about the influence of truncation time window on the thermal diffusivity measurement has been conducted.

Nine boron steel specimens with three different microstructures have been analyzed. All these specimens have been subjected to three different hardening heat treatments, obtaining: 100% bainitic, 100% martensitic and 50% bainitic – 50% martensitic structures. The thermal diffusivity has been considered as an index to identify the phase percentage composition in boron steels and a statistical approach for the evaluation of the influence of analysed time window and the pixel line, has been adopted. To set the number of frames needed for the application of PLM to measure thermal diffusivity in reflection mode, two different approaches have been used. The first one, based on the settling time of the system considered as a response to a step cooling function, the second one based on the value of R^2 of the gaussian fitting. The influence of considered pixels for the analysed diameter has been indagated too, considering the error of measurement on thermal diffusivity between the diameter composed by a single pixel line and by the average of 3 pixels lines. These analyses confirm that the lower measurement error on thermal diffusivity, compared with the value obtained from TPS method, occurs when a single line ad settling time approach are applied.

Consequently, three measurements for each specimen have been made to have a statistically significant result. After the F-test, to verify that the standard deviation among measurements can be considered the same, a Student t-test approach has been applied to verify two conditions. The first, that the three replications are part of the same population and, the second, that the three mean values of thermal diffusivity obtained for three different phases (A/B/C) are reasonably different. It is possible to see that between the average values of measurements obtained for 100% bainitic and 100% martensitic structure, the percentage difference in terms of thermal diffusivity is around 8%. On the other hand, a difference of ~4% is present between the phase A and B and between B and C.

Considering values of standard deviation obtained for each measurement, it is statistically possible to see that the specimens can be considered different but there is an overlap among uncertainty intervals. To reduce this superposition and further the resolution of technique, 32 measurements has been calculated as a suitable number that results in ~45 s of control

process, with the 95% of confidence to distinguish a difference in thermal diffusivity of 0.20 $mm^2/_s$ with a power of test of 95%.

Next steps will include:

- The mechanical traditional tests to correlate the thermal diffusivity to mechanical properties;
- Analyse more levels of phase percentage to identify the capability of the technique;
- Apply flying spot to compare results and resolution of flying spot with PLM technique;
- Apply the flying spot method to identify the HAZ in welded joints through measurements of thermal diffusivity.

CONCLUSIONS

This work evaluated the possibility of developing automatic or semi-automatic non-destructive thermal imaging control procedures for verifying joints. Specifically, the goal was to use active thermal imaging techniques to assess the quality and measure the fused zone of welds and to evaluate the technique's ability to distinguish microstructure variations.

For the measurement of the fused region, the analysis has been focused on joints obtained through an innovative resistance projection welding (RPW) process. Firstly, 12 joints obtained through RPW with different process parameters were analyzed to identify their influence on joint quality. Flash thermal imaging was then used on coated joints, analyzing the phase results obtained after applying the PPT algorithm. Specifically, the phase profile along the top axis of each weld was analyzed to identify significant indices. Two different thermal imaging features were then identified that, after an ANOVA, were found to be indicative of two of the three process parameters, force (F) and current (I). With a confidence of 95%, it can be stated that the minimum phase value in the low-frequency profile (greater depths) is sensitive to the variation of I and the slope of the profile in the high-frequency map (shallow depths) is sensitive to the variation of F. Therefore, the ability of the thermal imaging technique to distinguish between joints obtained with suitable process parameters and those that are not suitable was verified.

The work was continued with the second case study in which two welded joints obtained with RPW were examined through pulsed laser thermal imaging techniques. The slope algorithm was used to perform a quantitative analysis of the fused zone, also evaluating the influence of the suitable truncation window, identified by comparison with well-established techniques such as UT and μCT. The developed procedure was then applied to the first and confirmed on a second test specimen, confirming the ability of the thermal imaging technique to quantify the weld fusion zone with an error of ~10% on the measurement of the area and ~2% on the length of the major axis, always with an underestimation of the same, thus allowing a safe evaluation.

To evaluate the ability of the thermal imaging technique to evaluate microstructure variations, eight boron steel plates were analyzed, four of which were subjected to quenching heat treatment resulting in two different microstructures (ferritic-perlite / martensite). To do this, the pulsed laser spot thermal imaging technique was used. After

measuring the thermal diffusivity with standard methods (TPS), a FEM model was developed to simulate the thermal test and evaluate, through the use of response surfaces, the influence of test parameters on the diffusivity measurement, thus evaluating the trend of the measurement error as a function of the main test parameters (frame rate, heating duration, spatial resolution). A procedure for the selection of test parameters was then identified. Subsequently, the two different microstructures were analyzed, confirming the ability of the developed procedure to distinguish the two different microstructures through the measurement of thermal diffusivity. Subsequently, ten tensile specimens were obtained from the analyzed plates according to standards to obtain the UTS for the two microstructures. A preliminary correlation was then identified between the ultimate tensile stress of the material and the thermal diffusivity, thus allowing the value of UTS to be estimated through the thermal imaging technique.

Continuing along the same line, nine different specimens with three different microstructures (100% bainite - 50% bainite/50% martensite - 100% martensite) were analyzed to investigate the sensitivity of the variation in thermal diffusivity to the variation of microstructure. After verifying the proposed procedure, the sensitivity of the thermal imaging technique to different degrees of microstructural variations was verified. A statistical analysis was also carried out to verify the goodness of the results and identify the minimum number of repetitions that would guarantee a reduction in the measurement uncertainty. In conclusion, it can be said that the thermal imaging technique has proven effective in measuring the fused zone in thin resistance welded joints, demonstrating competitiveness with well-established techniques such as UT and μCT. In addition, unlike these, the measurements were made without the need for contact with the surface and with total times (test + analysis) of ~6 s, compared to times of more than two orders of magnitude higher for UT and well beyond for μCT. Intending to recognize microstructure variations, the thermal imaging technique has proven adequate and capable of distinguishing, through thermal diffusivity measurements, at least four different microstructures (100% martensite - 100% bainite - 50% bainite / 50% martensite - ferrite/perlite), demonstrating the potential to be used to detect microstructural variations due to welding processes (HAZ). For the broader goal of developing an automatic thermal imaging procedure that allows for the verification of welded joints (fused zone, defects and HAZ), the subsequent developments are:

- Compare several algorithms for thermal data analysis in order to evaluate which is the faster and which one can guarantee the minimum measurement error;
- Evaluate the mechanical resistance of welded joints to study the influence of geometrical characteristics of welding on the mechanical properties;
- Develop a new procedure based on long-pulsed heating to reduce the power of the laser;
- Analyze more levels of phase percentage to identify the capability of the technique;
- Carring out traditional mechanical tests to correlate the thermal diffusivity to mechanical properties for more levels of phase percentage;
- Apply flying spot to compare results and resolution of flying spot with PLM technique;
- Apply the flying spot method to identify the HAZ in welded joints through thermal diffusivity measurements.
- Design a system based on the procedures developed to automatize the control and be suitable for on-site applications fully.

LIST OF PUBLICATIONS

1. **Dell'Avvocato G**., Palumbo D., Galietti U."A non-destructive thermographic procedure for the evaluation of heat treatment in Usibor®1500 through the thermal diffusivity measurement", **NDT & E International**, Volume 133, 2023, 102748, ISSN 0963-8695, https://doi.org/10.1016/j.ndteint.2022.102748.
2. **Dell'Avvocato G**., Gohlke D., Palumbo D., Krankenhagen R., Galietti U." "Quantitative evaluation of the welded area in Resistance Projection Welded (RPW) thin joints by pulsed laser thermography" Proc. SPIE 12109, Thermosense: Thermal Infrared Applications XLIV, 121090J (27 May 2022); https://doi.org/10.1117/12.2618806
3. **Dell'Avvocato G.,** Palumbo D., Palmieri M.E., Galietti U "Non-destructive thermographic method for the assessment of heat treatment in boron steel", Proc. SPIE 12109, Thermosense: Thermal Infrared Applications XLIV, 1210906 (27 May 2022); https://doi.org/10.1117/12.2618810
4. **Dell'Avvocato G.,** Palumbo, D., Palmieri, M.E., Galietti, U. "Evaluation of Effectiveness of Heat Treatments in Boron Steel by Laser Thermography". Eng. Proc. 2021, 8, 8. https://doi.org/10.3390/engproc2021008008

5. **Dell'Avvocato G**., Palumbo D., Pepe R., Galietti U "Non-destructive evaluation of resistance projection welded joints (RPW) by flash thermography" 2021 IOP Conf. Ser.: Mater. Sci. Eng. 1038 012003, http://doi.org/10.1088/1757-899X/1038/1/012003

AWARDS

- ***"Ermanno Grinzato"*** **Under 35 years best paper award** of 16th International Workshop on Advanced Infrared Technology & Applications 2021 – AITA Conference with the work: *"Evaluation of Effectiveness of Heat Treatments in Boron Steel by Laser Thermography"*, **Dell'Avvocato G.**, Palumbo, D., Palmieri, M.E, Galietti, U.

LITERATURE

[1] Faulkner LL, Hablanian MH, Piotrowski J, Keating EL. Blake's Design of Mechanical Joints Mechanical Engineering A Series of Textbooks and Reference Books PUBLISHED TITLES High-Vacuum Technology: A Practical Guide, Second Edition Shaft Alignment Handbook, Third Edition Applied Combustion, Second Edition Introduction to the Design and Behavior of Bolted Joints, Fourth Edition: Non-Gasketed Joints. n.d.

[2] Guo W, Li L, Dong S, Crowther D, Thompson A. Comparison of microstructure and mechanical properties of ultra-narrow gap laser and gas-metal-arc welded S960 high strength steel. Opt Lasers Eng 2017;91:1–15. https://doi.org/10.1016/j.optlaseng.2016.11.011.

[3] Consonni M, Wee CF, Schneider C. Manufacturing of welded joints with realistic defects. Insight: Non-Destructive Testing and Condition Monitoring, vol. 54, 2012. https://doi.org/10.1784/insi.2012.54.2.76.

[4] Dumont V, Badulescu C, Stamoulis G, Adrien J, Maire E, Lefèvre A, et al. On the effect of the curing cycle on the creation of pores in structural adhesive joints by means of X-ray microtomography. Journal of Adhesion 2021;97:1073–106. https://doi.org/10.1080/00218464.2020.1728257.

[5] Halmshaw R. Visual methods. Introduction to the Non-Destructive Testing of Welded Joints, Elsevier; 1996, p. 1–4. https://doi.org/10.1533/9781845698829.1.

[6] Maldague X, Galmiche F, Ziadi A. Advances in pulsed phase thermography. n.d.

[7] S Carslaw BH, Jaeger JC, Owmie P, Technologia c. conduction of heat in solids Bfbffothek FB7 Technfsche Hocbschule Darmstadt Car oxford at the clarendon press contents. n.d.

[8] Vavilov VP, Shiryaev V v., Kuimova M v. Time- and phase-domain thermal tomography of composites. Photonics 2018;5. https://doi.org/10.3390/photonics5040031.

[9] Vavilov VP, Pawar SS. A novel approach for one-sided thermal nondestructive testing of composites by using infrared thermography. Polym Test 2015;44:224–33. https://doi.org/10.1016/j.polymertesting.2015.04.013.

[10] Vavilov VP, Burleigh DD. Review of pulsed thermal NDT: Physical principles, theory and data processing. NDT and E International 2015;73:28–52. https://doi.org/10.1016/j.ndteint.2015.03.003.

[11] Spiessberger C, Gleiter A, Busse G. Data Fusion of Lockin-Thermography Phase Images. n.d.

[12] Ibarra-Castanedo C, Maldague X. Pulsed phase thermography reviewed. Quant Infrared Thermogr J 2004;1:47–70. https://doi.org/10.3166/qirt.1.47-70.

[13] Pitarresi G. Thermal NDE of thick GRP panels by means of a Pulse modulated lock-in thermography technique. EPJ Web Conf, vol. 6, EDP Sciences; 2010. https://doi.org/10.1051/epjconf/20100638014.

[14] Krapez JC, Krapez J-C. Compared performances of four algorithms used for modulation thermography. n.d.

[15] Krapez JC, Krapez J-C. Thermal Modulation Transfer Function (TMTF). n.d.

[16] Wu S, Gao B, Yang Y, Zhu Y, Burrascano P, Laureti S, et al. Halogen optical referred pulse-compression thermography for defect detection of CFRP. Infrared Phys Technol 2019;102. https://doi.org/10.1016/j.infrared.2019.103006.

[17] Palumbo D, Galietti U. Damage Investigation in Composite Materials by Means of New Thermal Data Processing Procedures. Strain, vol. 52, Blackwell Publishing Ltd; 2016, p. 276–85. https://doi.org/10.1111/str.12179.

[18] D'accardi E, Palumbo D, Galietti U. A comparison among different ways to investigate composite materials with lock-in thermography: The multi-frequency approach. Materials 2021;14. https://doi.org/10.3390/ma14102525.

[19] Pech-May NW, Paul A, Ziegler M. Pulse-compression laser thermography using a modified Barker code: enhanced detection of subsurface defects, SPIE-Intl Soc Optical Eng; 2021, p. 17. https://doi.org/10.1117/12.2586078.

[20] Laureti S, Ricci M, Burrascano P, Hutchins DA, Tian GY, Gao B. Complementary Barker Code excitation for Pulse-compression Thermography, QIRT Council; 2020. https://doi.org/10.21611/qirt.2020.105.

[21] Ibarra-Castanedo c. quantitative subsurface defect evaluation by pulsed phase thermography : depth retrieval with the phase. N.d.

[22] Wang Z, Tian GY, Meo M, Ciampa F. Image processing based quantitative damage evaluation in composites with long pulse thermography. NDT and E International 2018;99:93–104. https://doi.org/10.1016/j.ndteint.2018.07.004.

[23] Pilla M, Klein M, Maldague X, Salerno A. New Absolute Contrast for pulsed thermography, QIRT Council; 2002. https://doi.org/10.21611/qirt.2002.004.

[24] Krapez JC, Lepoutre F, Balageas D. Early detection of thermal contrast in pulsed stimulated thermography. Journal De Physique IV : JP 1994;4. https://doi.org/10.1051/jp4:1994712.

[25] Alvarez-Restrepo CA, Benitez-Restrepo HD, Tobón LE. Characterization of defects of pulsed thermography inspections by orthogonal polynomial decomposition. NDT and E International 2017;91:9–21. https://doi.org/10.1016/j.ndteint.2017.05.003.

[26] Pavlopoulou S, Grammatikos SA, Kordatos EZ, Worden K, Paipetis AS, Matikas TE, et al. Continuous debonding monitoring of a patch repaired helicopter stabilizer: Damage assessment and analysis. Compos Struct 2015;127:231–44. https://doi.org/10.1016/j.compstruct.2015.03.014.

[27] Rajic N. Principal component thermography for flaw contrast enhancement and flaw depth characterisation in composite structures. n.d.

[28] Shepard SM. Advances in Pulsed Thermography. 2001.

[29] Shepard SM, Lhota JR. Flash duration and timing effects in thermographic NDT. Thermosense XXVII, vol. 5782, SPIE; 2005, p. 352. https://doi.org/10.1117/12.606122.

[30] Oswald-Tranta B, Shepard SM. Comparison of pulse phase and thermographic signal reconstruction processing methods. Thermosense: Thermal Infrared Applications XXXV, vol. 8705, SPIE; 2013, p. 87050S. https://doi.org/10.1117/12.2017899.

[31] Shepard SM. Introduction to active thermography for non-destructive evaluation. Anti-Corrosion Methods and Materials 1997;44:236–9. https://doi.org/10.1108/00035599710183199.

[32] Shepard SM, Lhota JR, Ahmed T. Measurement limits in flash thermography. Thermosense XXXI, vol. 7299, SPIE; 2009, p. 72990T. https://doi.org/10.1117/12.820062.

[33] Shepard SM. Reconstruction and enhancement of active thermographic image sequences. Optical Engineering 2003;42:1337. https://doi.org/10.1117/1.1566969.

[34] D'Accardi E, Palumbo D, Tamborrino R, Galietti U. Quantitative analysis of thermographic data through different algorithms. Procedia Structural Integrity, vol. 8, Elsevier B.V.; 2018, p. 354–67. https://doi.org/10.1016/j.prostr.2017.12.036.

[35] Palumbo D, Cavallo P, Galietti U. An investigation of the stepped thermography technique for defects evaluation in GFRP materials. NDT and E International 2019;102:254–63. https://doi.org/10.1016/j.ndteint.2018.12.011.

[36] Vavilov VP, Pawar SS. A novel approach for one-sided thermal nondestructive testing of composites by using infrared thermography. Polym Test 2015;44:224–33. https://doi.org/10.1016/j.polymertesting.2015.04.013.

[37] Press WH, Teukolsky SA, Vetterling WT, Flannery BP. Numerical Recipes in C ++ The Art of Scientific Computing Second Edition. n.d.

[38] Lomozik M. Effect of the welding thermal cycles on the structural changes in the heat affected zone and on its properties in joints welded in low-alloy steels. Welding International 2000;14:845–50. https://doi.org/10.1080/09507110009549281.

[39] Mičian M, Winczek J, Gucwa M, Koňár R, Málek M, Postawa P. Investigation of welds and heat affected zones in weld surfacing steel plates taking into account the bead sequence. Materials 2020;13:1–17. https://doi.org/10.3390/ma13245666.

[40] Liu Y, Baddour N, Mandelis A, Beingessner C. Photothermal depth profilometry of heat-treated hardened 0.15%-0.2% C, 0.6%-0.9% Mn Steels. J Appl Phys 2004;96:1521–8. https://doi.org/10.1063/1.1765868.

[41] Qu H, Wang C, Guo X, Mandelis A. Reconstruction of depth profiles of thermal conductivity of case hardened steels using a three-dimensional photothermal technique. J Appl Phys 2008;104. https://doi.org/10.1063/1.3035831.

[42] Xie G, Zhang J, Liu L, Wang C, Mandelis A. Thermal conductivity depth-profile reconstruction of multilayered cylindrical solids using the thermal-wave Green function method. J Appl Phys 2011;109. https://doi.org/10.1063/1.3595674.

[43] Celorrio R, Mendioroz A, Apiñaniz E, Salazar A, Wang C, Mandelis A. Reconstruction of radial thermal conductivity depth profile in case hardened steel rods. J Appl Phys 2009;105. https://doi.org/10.1063/1.3106662.

[44] Qu H, Wang C, Guo X, Mandelis A. Reconstruction of depth profiles of thermal conductivity of case hardened steels using a three-dimensional photothermal technique. J Appl Phys 2008;104. https://doi.org/10.1063/1.3035831.

[45] Munidasa M, Tian-Chi M, Mandelis A, Brown SK, Mannik L. Non-destructive depth profiling of laser-processed Zr-2.5Nb alloy by IR photothermal radiometry. vol. 159. 1992.

[46] Fivez J, Glorieux C. Case-hardening inspection of steel using photothermal phase maxima. J Appl Phys, vol. 108, 2010. https://doi.org/10.1063/1.3506522.

[47] Hao M, Osman KA, Boomer DR, Newton CJ. Sponsored by the American Welding Society and the Welding Research Council Developments in Characterization of Resistance Spot Welding of Aluminum A monitoring system analyzes data and correlates the information to parameters for spot welding aluminum. 1996.

[48] Murashov V v. Nondestructive testing of glued joints. Polymer Science - Series D 2009;2:58–63. https://doi.org/10.1134/S1995421209010122.

[49] Patil DD, Chougule PG, Morale MA, Salunkhe SD. Review of Failure of Grinder Wheel. IARJSET 2017;4:120–3. https://doi.org/10.17148/iarjset/ncdmete.2017.28.

[50] Yilmaz B, Smagulova D, Jasiuniene E. Model-assisted reliability assessment for adhesive bonding quality evaluation with ultrasonic NDT. NDT and E International 2022;126. https://doi.org/10.1016/j.ndteint.2021.102596.

[51] Yilmaz B, Ba A, Jasiuniene E, Bui HK, Berthiau G. Comparison of different non-destructive testing techniques for bonding quality evaluation. 2019 IEEE International Workshop on Metrology for AeroSpace, MetroAeroSpace 2019 - Proceedings, Institute of Electrical and Electronics Engineers Inc.; 2019, p. 92–7. https://doi.org/10.1109/MetroAeroSpace.2019.8869692.

[52] Derusova D, Vavilov V, Sfarra S, Sarasini F, Krasnoveikin V, Chulkov A, et al. Ultrasonic spectroscopic analysis of impact damage in composites by using laser vibrometry. Compos Struct 2019;211:221–8. https://doi.org/10.1016/j.compstruct.2018.12.050.

[53] Pineda Allen JC, Ng CT. Debonding detection at adhesive joints using nonlinear Lamb waves mixing. NDT and E International 2022;125. https://doi.org/10.1016/j.ndteint.2021.102552.

[54] Hean Gan T, Kanfoud J, Ramagiri S, Christopoulos A, Kanterakis G, Kitsianos K, et al. Evaluation of NDT techniques for the detection of kissing bond defects in composite joints. n.d.

[55] Wood M, Charlton P, Yan D. Ultrasonic Evaluation of Artificial Kissing Bonds in CFRP Composites. n.d.

[56] Deepak JR, Bupesh Raja VK, Srikanth D, Surendran H, Nickolas MM. Non-destructive testing (NDT) techniques for low carbon steel welded joints: A review

and experimental study. Mater Today Proc, vol. 44, Elsevier Ltd; 2021, p. 3732–7. https://doi.org/10.1016/j.matpr.2020.11.578.

[57] Amza G. Ultrasound effect on the mechanical properties of parts loaded by welding n.d.

[58] Provencal E, Laperrière L. Identification of weld geometry from ultrasound scan data using deep learning. Procedia CIRP, vol. 104, Elsevier B.V.; 2021, p. 122–7. https://doi.org/10.1016/j.procir.2021.11.021.

[59] Neumann AWE. On the State of the Art of the Inspection of Austenitic Welds with Ultrasound. vol. 39. 1989.

[60] Cruz FC, Simas Filho EF, Albuquerque MCS, Silva IC, Farias CTT, Gouvêa LL. Efficient feature selection for neural network based detection of flaws in steel welded joints using ultrasound testing. Ultrasonics 2017;73:1–8. https://doi.org/10.1016/j.ultras.2016.08.017.

[61] Cruz FC, Simas Filho EF, Albuquerque MCS, Silva IC, Farias CTT, Gouvêa LL. Efficient feature selection for neural network based detection of flaws in steel welded joints using ultrasound testing. Ultrasonics 2017;73:1–8. https://doi.org/10.1016/j.ultras.2016.08.017.

[62] Thomä M, Gester A, Wagner G, Straß B, Wolter B, Benfer S, et al. Application of the hybrid process ultrasound enhanced friction stir welding on dissimilar aluminum/dual-phase steel and aluminum/magnesium joints. Materwiss Werksttech 2019;50:893–912. https://doi.org/10.1002/mawe.201900028.

[63] Summerville C, Adams D, Compston P, Doolan M. Nugget Diameter in Resistance Spot Welding: A Comparison between a Dynamic Resistance Based Approach and Ultrasound C-scan. Procedia Eng, vol. 183, Elsevier Ltd; 2017, p. 257–63. https://doi.org/10.1016/j.proeng.2017.04.033.

[64] Summerville C, Adams D, Compston P, Doolan M. Nugget Diameter in Resistance Spot Welding: A Comparison between a Dynamic Resistance Based Approach and Ultrasound C-scan. Procedia Eng, vol. 183, Elsevier Ltd; 2017, p. 257–63. https://doi.org/10.1016/j.proeng.2017.04.033.

[65] Sun X, Zeng K, He X, Zhang L. Ultrasonic C-scan imaging and analysis of the mechanical properties of resistance spot-welded joints of stainless steel. Nondestructive Testing and Evaluation 2017;32:242–54. https://doi.org/10.1080/10589759.2016.1241251.

[66] Vértesy G, Tomáš I. Nondestructive magnetic inspection of spot welding. NDT and E International 2018;98:95–100. https://doi.org/10.1016/j.ndteint.2018.05.001.

[67] Tsukada K, Miyake K, Harada D, Sakai K, Kiwa T. Magnetic nondestructive test for resistance spot welds using magnetic flux penetration and eddy current methods. J Nondestr Eval 2013;32:286–93. https://doi.org/10.1007/s10921-013-0181-0.

[68] Harada D, Sakai K, Kiwa T, Tsukada K. Analysis of the internal structure of a spot-weld by magnetic measurement. n.d.

[69] Ma N, Gao X, Tian M, Wang C, Zhang Y, Gao PP. Magneto-Optical Imaging of Arbitrarily Distributed Defects in Welds under Combined Magnetic Field. Metals (Basel) 2022;12. https://doi.org/10.3390/met12061055.

[70] Tsukada K, Yoshioka M, Kiwa T, Hirano Y. A magnetic flux leakage method using a magnetoresistive sensor for nondestructive evaluation of spot welds. NDT and E International 2011;44:101–5. https://doi.org/10.1016/j.ndteint.2010.09.012.

[71] Allag A, Drai R, Benammar A, Boutkedjirt T. X-rays tomographic reconstruction images using proximal methods based on L1 norm and TV regularization. Procedia Comput Sci, vol. 127, Elsevier B.V.; 2018, p. 236–45. https://doi.org/10.1016/j.procs.2018.01.119.

[72] Halmshaw R. Radiographic methods. Insight: Non-Destructive Testing and Condition Monitoring 2000;42:199–201. https://doi.org/10.1533/9781845698829.5.

[73] Halmshaw R. Penetrant methods. Introduction to the Non-Destructive Testing of Welded Joints, Elsevier; 1996, p. 104–10. https://doi.org/10.1533/9781845698829.104.

[74] Gould JE. Vehicle Lightweighting and the Need for Aluminum in Body-in-White Construction Joining Aluminum Sheet in the Automotive Industry-A 30 Year History Resistance welding, mechanical fasteners, and ultrasonic welding are examined in this overview of joining technology KEYWORDS Aluminum Alloys Body-in-White Resistance Welding Mechanical Fastening Ultrasonic Welding. n.d.

[75] Xia YJ, Su ZW, Li YB, Zhou L, Shen Y. Online quantitative evaluation of expulsion in resistance spot welding. J Manuf Process 2019;46:34–43. https://doi.org/10.1016/j.jmapro.2019.08.004.

[76] Zhang W. Design and Implementation of Software for Resistance Welding Process Simulations. vol. 112. 2003.

[77] Valaee-Tale M, Sheikhi M, Mazaheri Y, Malek Ghaini F, Usefifar GR. Criterion for predicting expulsion in resistance spot welding of steel sheets. J Mater Process Technol 2020;275. https://doi.org/10.1016/j.jmatprotec.2019.116329.

[78] Ambroziak A, Korzeniowski M. Using resistance spot welding for joining aluminium elements in automotive industry. Archives of Civil and Mechanical Engineering 2010;10:5–13. https://doi.org/10.1016/s1644-9665(12)60126-5.

[79] Martín Ó, Tiedra P de, López M, San-Juan M, García C, Martín F, et al. Quality prediction of resistance spot welding joints of 304 austenitic stainless steel. Mater Des 2009;30:68–77. https://doi.org/10.1016/j.matdes.2008.04.050.

[80] Zhang H, Qiu X, Bai Y, Xing F, Yu H, Shi Y. Resistance spot welding macro characteristics of the dissimilar thickness dual phase steels. Mater Des 2014;63:151–8. https://doi.org/10.1016/j.matdes.2014.05.060.

[81] den Uijl N, Smith S, Rd&t C. Resistance Spot Welding of Advanced High Strength Steels for the Automotive Industry. n.d.

[82] Zhao D, Ren D, Song G, Zhao K, Liu L, Zhang Z. Comparison of mechanical properties and the nugget formation of composite ceramic-centered annular welding and traditional resistance spot welding. Int J Mech Sci 2020;187. https://doi.org/10.1016/j.ijmecsci.2020.105933.

[83] Kimchi M, Phillips DH. Resistance Spot Welding Fundamentals and Applications for the Automotive Industry Synthesis Lectures on Mechanical Engineering Synthesis Lectures on Mechanical Engineering Resistance Spot Welding Fundamentals and Applications for the Automotive Industry. n.d.

[84] Hua L, Wang B, Wang X, He X, Guan S. In-situ ultrasonic detection of resistance spot welding quality using embedded probe. J Mater Process Technol 2019;267:205–14. https://doi.org/10.1016/j.jmatprotec.2018.12.008.

[85] Capezza C, Centofanti F, Lepore A, Palumbo B. Functional clustering methods for resistance spot welding process data in the automotive industry. Appl Stoch Models Bus Ind 2021;37:908–25. https://doi.org/10.1002/asmb.2648.

[86] Martín Ó, de Tiedra P. Advances in the Control and Improvement of Quality in the Resistance Spot Welding Process. Metals (Basel) 2022;12:1810. https://doi.org/10.3390/met12111810.

[87] Thornton M, Han L, Shergold M. Progress in NDT of resistance spot welding of aluminium using ultrasonic C-scan. NDT and E International 2012;48:30–8. https://doi.org/10.1016/j.ndteint.2012.02.005.

[88] Martín Ó, Pereda M, Santos JI, Galán JM. Assessment of resistance spot welding quality based on ultrasonic testing and tree-based techniques. J Mater Process Technol 2014;214:2478–87. https://doi.org/10.1016/j.jmatprotec.2014.05.021.

[89] Liu J, Xu G, Ren L, Qian Z, Ren L. Defect intelligent identification in resistance spot welding ultrasonic detection based on wavelet packet and neural network. International Journal of Advanced Manufacturing Technology 2017;90:2581–8. https://doi.org/10.1007/s00170-016-9588-y.

[90] Zhao D, Wang Y, Liang D. Correlating variations in the dynamic power signature to nugget diameter in resistance spot welding using Kriging model. Measurement (Lond) 2019;135:6–12. https://doi.org/10.1016/j.measurement.2018.11.025.

[91] Deepati AK, Alhazmi W, Benjeer I. Mechanical characterization of AA5083 aluminum alloy welded using resistance spot welding for the lightweight automobile body fabrication. Mater Today Proc, vol. 45, Elsevier Ltd; 2021, p. 5139–48. https://doi.org/10.1016/j.matpr.2021.01.646.

[92] Wan X, Wang Y, Zhao D, Huang YA. A comparison of two types of neural network for weld quality prediction in small scale resistance spot welding. Mech Syst Signal Process 2017;93:634–44. https://doi.org/10.1016/j.ymssp.2017.01.028.

[93] Palumbo D, D'Accardi E, Galietti U. A new thermographic procedure for the non-destructive evaluation of RSW joints, SPIE-Intl Soc Optical Eng; 2019, p. 23. https://doi.org/10.1117/12.2518979.

[94] Chen Z, Shi Y, Jiao B, Zhao H. Ultrasonic nondestructive evaluation of spot welds for zinc-coated high strength steel sheet based on wavelet packet analysis. J Mater Process Technol 2009;209:2329–37. https://doi.org/10.1016/j.jmatprotec.2008.05.030.

[95] Rupin F, Blatman G, Lacaze S, Fouquet T, Chassignole B. Probabilistic approaches to compute uncertainty intervals and sensitivity factors of ultrasonic simulations of a weld inspection. Ultrasonics 2014;54:1037–46. https://doi.org/10.1016/j.ultras.2013.12.006.

[96] Martín O, López M, Martín F. Artificial neural networks for quality control by ultrasonic testing in resistance spot welding´Oscar. J Mater Process Technol 2007;183:226–33. https://doi.org/10.1016/j.jmatprotec.2006.10.011´O.

[97] Hua L, Wang B, Wang X, He X, Guan S. In-situ ultrasonic detection of resistance spot welding quality using embedded probe. J Mater Process Technol 2019;267:205–14. https://doi.org/10.1016/j.jmatprotec.2018.12.008.

[98] Wang X, Guan S, Hua L, Wang B, He X. Classification of spot-welded joint strength using ultrasonic signal time-frequency features and PSO-SVM method. Ultrasonics 2019;91:161–9. https://doi.org/10.1016/j.ultras.2018.08.014.

[99] Qiuyue F, Guocheng X, Xiaopeng G. Ultrasonic Nondestructive Evaluation of Porosity Size and Location of Spot Welding Based on Wavelet Packet Analysis. J Nondestr Eval 2020;39. https://doi.org/10.1007/s10921-019-0650-1.

[100] Moghanizadeh A. Evaluation of the physical properties of spot welding using ultrasonic testing. International Journal of Advanced Manufacturing Technology 2016;85:535–45. https://doi.org/10.1007/s00170-015-7952-y.

[101] Amiri N, Farrahi GH, Kashyzadeh KR, Chizari M. Applications of ultrasonic testing and machine learning methods to predict the static & fatigue behavior of spot-welded joints. J Manuf Process 2020;52:26–34. https://doi.org/10.1016/j.jmapro.2020.01.047.

[102] Lindner S, Deike R. Detection Method for Liquid Metal Embrittlement Cracks Inside the Intermediate Sheet Zone of Dissimilar Resistance Spot Welds. Steel Res Int 2020;91. https://doi.org/10.1002/srin.202000044.

[103] Liu F, Wang H, Meng X, Tan C, Chen B, Song X. Effect of magnetic field orientation on suppressing porosity in steady-magnetic-field-assisted aluminum alloy deep-penetration laser welding. J Mater Process Technol 2022;304. https://doi.org/10.1016/j.jmatprotec.2022.117569.

[104] Waugh RC, Dulieu-Barton JM, Quinn S. Pulse phase thermography and its application to kissing defects in adhesively bonded joints. Applied Mechanics and Materials, vol. 70, 2011, p. 369–74. https://doi.org/10.4028/www.scientific.net/AMM.70.369.

[105] Schroeder JA, Ahmed T, Chaudhry B, Shepard S. Non-destructive testing of structural composites and adhesively bonded composite joints: pulsed thermography. n.d.

[106] Wu X, Zhou B, Huang F, Lin P, Cao R. Super-Resolution Thermal Imaging Using Uncooled Infrared Sensors for Non-Destructive Testing of Adhesively Bonded

Joints. IEEE Sens J 2022;22:14415–23. https://doi.org/10.1109/JSEN.2022.3183868.

[107] Palumbo D, Tamborrino R, Galietti U, Aversa P, Tatì A, Luprano VAM. Ultrasonic analysis and lock-in thermography for debonding evaluation of composite adhesive joints. NDT and E International 2016;78:1–9. https://doi.org/10.1016/j.ndteint.2015.09.001.

[108] Kostroun T, Dvořák M. Application of the pulse infrared thermography method for nondestructive evaluation of composite aircraft adhesive joints. Materials 2021;14:1–20. https://doi.org/10.3390/ma14030533.

[109] Yi Q, Tian GY, Yilmaz B, Malekmohammadi H, Laureti S, Ricci M, et al. Evaluation of debonding in CFRP-epoxy adhesive single-lap joints using eddy current pulse-compression thermography. Compos B Eng 2019;178. https://doi.org/10.1016/j.compositesb.2019.107461.

[110] Barus M, Welemane H, Collombet F, Pastor ML, Cantarel A, Crouzeix L, et al. Bonded repair issues for composites: An investigation approach based on infrared thermography. NDT and E International 2017;85:27–33. https://doi.org/10.1016/j.ndteint.2016.10.003.

[111] Barus M, Welemane H, Nassiet V, Pastor ML, Cantarel A, Collombet F, et al. NDT-based design of joint material for the detection of bonding defects by infrared thermography. NDT and E International 2018;93:157–63. https://doi.org/10.1016/j.ndteint.2017.10.005.

[112] Sreedhar U, Krishnamurthy C v., Balasubramaniam K, Raghupathy VD, Ravisankar S. Automatic defect identification using thermal image analysis for online weld quality monitoring. J Mater Process Technol 2012;212:1557–66. https://doi.org/10.1016/j.jmatprotec.2012.03.002.

[113] Lee S, Nam J, Hwang W, Kim J, Lee B. A study on integrity assessment of the resistance spot weld by infrared thermography. Procedia Eng, vol. 10, Elsevier Ltd; 2011, p. 1748–53. https://doi.org/10.1016/j.proeng.2011.04.291.

[114] Garcia La Yedra A de, Echeverria A, Beizama A, Fuente R, Fernández E. Infrared Thermography as an Alternative to Traditional Weld Inspection Methods thanks to Signal Processing Techniques. n.d.

[115] Jonietz F, Myrach P, Suwala H, Ziegler M. Examination of Spot Welded Joints with Active Thermography. J Nondestr Eval 2016;35:1–14. https://doi.org/10.1007/s10921-015-0318-4.

[116] Li X, Liu W, Liu H, Zhang Z, Bao P. Microstructure and thermal cracking susceptibility of dissimilar resistance spot welded austenitic and mild steels. Welding in the World 2022. https://doi.org/10.1007/s40194-022-01440-z.

[117] Omar M, Hassan M, Donohue K, Saito K, Alloo R. Infrared thermography for inspecting the adhesion integrity of plastic welded joints. NDT and E International 2006;39:1–7. https://doi.org/10.1016/j.ndteint.2005.04.008.

[118] Serio LM, Palumbo D, Galietti U, de Filippis LAC, Ludovico AD. Monitoring of the friction stir welding process by means of thermography. Nondestructive Testing and Evaluation 2016;31:371–83. https://doi.org/10.1080/10589759.2015.1121266.

[119] Kastner L, Ahmadi S, Jonietz F, Jung P, Caire G, Ziegler M, et al. Classification of Spot-Welded Joints in Laser Thermography Data Using Convolutional Neural Networks. IEEE Access 2021;9:48303–12. https://doi.org/10.1109/ACCESS.2021.3063672.

[120] Villar M, Garnier C, Chabert F, Nassiet V, Samélor D, Diez JC, et al. In-situ infrared thermography measurements to master transmission laser welding process parameters of PEKK. Opt Lasers Eng 2018;106:94–104. https://doi.org/10.1016/j.optlaseng.2018.02.016.

[121] Kotovshchikov IO, Yakovlev JO, Prohorovich VE. Development of methodological approaches for non-destructive testing of welded joints of steel finned panels by the active thermography method. IOP Conf Ser Mater Sci Eng 2021;1093:012016. https://doi.org/10.1088/1757-899x/1093/1/012016.

[122] Naksuk N, Nakngoenthong J, Printrakoon W, Yuttawiriya R. Real-time temperature measurement using infrared thermography camera and effects on tensile strength and microhardness of hot wire plasma arc welding. Metals (Basel) 2020;10:1–14. https://doi.org/10.3390/met10081046.

[123] Leicht H, Heilig M, Pommer C, Kraus E, Baudrit B. Active and passive thermography for defect detection in polymer joints. n.d.

[124] Wu D, Busse G. Lock-in thermography for nondestructive evaluation of materials. Revue Generale de Thermique 1998;37. https://doi.org/10.1016/S0035-3159(98)80047-0.

[125] Wandelt M, Roetzel W. Lock-in thermography as a measurement technique in heat transfer, QIRT Council; 1996. https://doi.org/10.21611/qirt.1996.031.

[126] Springer Series in advanced microelectronics 10. n.d.

[127] Parker WJ, Jenkins RJ, Butler CP, Abbott GL. Flash method of determining thermal diffusivity, heat capacity, and thermal conductivity. J Appl Phys 1961;32:1679–84. https://doi.org/10.1063/1.1728417.

[128] Ciampa F, Mahmoodi P, Pinto F, Meo M. Recent advances in active infrared thermography for non-destructive testing of aerospace components. Sensors (Switzerland) 2018;18. https://doi.org/10.3390/s18020609.

[129] Marini M, Bouzin M, Sironi L, D'Alfonso L, Colombo R, di Martino D, et al. A novel method for spatially-resolved thermal conductivity measurement by super-resolution photo-activated infrared imaging. Materials Today Physics 2021;18. https://doi.org/10.1016/j.mtphys.2021.100375.

[130] Ahmadi S, Thummerer G, Breitwieser S, Mayr G, Lecompagnon J, Burgholzer P, et al. Multi-dimensional reconstruction of internal defects in additively manufactured steel using photothermal super resolution combined with virtual wave based image processing. IEEE Trans Industr Inform 2021. https://doi.org/10.1109/TII.2021.3054411.

[131] Burgholzer P, Berer T, Gruber J, Mayr G. Super-resolution thermographic imaging using blind structured illumination. Appl Phys Lett 2017;111. https://doi.org/10.1063/1.4995410.

[132] Ahmadi S, Burgholzer P, Mayr G, Jung P, Caire G, Ziegler M. Photothermal super resolution imaging: A comparison of different thermographic reconstruction techniques. NDT and E International 2020;111. https://doi.org/10.1016/j.ndteint.2020.102228.

[133] Krstulovic-Opara L, Klarin B, Neves P, Domazet Z. Thermal imaging and Thermoelastic Stress Analysis of impact damage of composite materials. Eng Fail Anal 2011;18:713–9. https://doi.org/10.1016/j.engfailanal.2010.11.010.

[134] Carteron L, Doudard C, Calloch S, Levieil B, Beaudet J, Bridier F. Naval welded joints local stress assessment and fatigue cracks monitoring with quantitative thermoelastic stress analysis. Theoretical and Applied Fracture Mechanics 2020;110. https://doi.org/10.1016/j.tafmec.2020.102792.

[135] Palumbo D, de Finis R, Demelio GP, Galietti U. Study of damage evolution in composite materials based on the Thermoelastic Phase Analysis (TPA) method. Compos B Eng 2017;117:49–60. https://doi.org/10.1016/j.compositesb.2017.02.040.

[136] Johnson S. Thermoelastic stress analysis for detecting and characterizing static damage initiation in composite lap shear joints. Compos B Eng 2014;56:740–8. https://doi.org/10.1016/j.compositesb.2013.09.014.

[137] Di Carolo F, de Finis R, Palumbo D, Galietti U. A thermoelastic stress analysis general model: Study of the influence of biaxial residual stress on aluminium and titanium. Metals (Basel) 2019;9. https://doi.org/10.3390/met9060671.

[138] Pitarresi G, Patterson EA. A review of the general theory of thermoelastic stress analysis. n.d.

[139] Palumbo D, de Finis R, Galietti U. Thermoelastic stress analysis as a method for the quantitative non-destructive evaluation of bonded CFRP T-joints. NDT and E International 2021;124. https://doi.org/10.1016/j.ndteint.2021.102526.

[140] Moradi M, Safizadeh MS. Detection of edge debonding in composite patch using novel post processing method of thermography. NDT and E International 2019;107. https://doi.org/10.1016/j.ndteint.2019.102153.

[141] Heutling B, Prints E, Mund M, Srajbr C, Heutling B, Prints E, et al. Qualification of active thermographic methods for testing welded joints. n.d.

[142] Guo X. Ultrasonic Infrared Thermography of Aluminium Thin Plates for Crack Inspection in Friction Stir Welded Joints. IEEE Sens J 2020;20:6524–31. https://doi.org/10.1109/JSEN.2020.2976144.

[143] Runnemalm A, Broberg P, Henrikson P. Ultraviolet excitation for thermography inspection of surface cracks in welded joints. Nondestructive Testing and Evaluation 2014;29:332–44. https://doi.org/10.1080/10589759.2014.941842.

[144] Chen J, Feng Z. IR-based spot weld NDT in automotive applications. Thermosense: Thermal Infrared Applications XXXVII, vol. 9485, SPIE; 2015, p. 948513. https://doi.org/10.1117/12.2177124.

[145] Runnemalm A, Ahlberg J, Appelgren A, Sjökvist S. Automatic inspection of spot welds by thermography. J Nondestr Eval 2014;33:398–406. https://doi.org/10.1007/s10921-014-0233-0.

[146] Verspeek S, Ribbens B, Maldague X, Steenackers G. Spot Weld Inspections Using Active Thermography. Applied Sciences (Switzerland) 2022;12. https://doi.org/10.3390/app12115668.

[147] Feuillet V, Ibos L, Fois M, Dumoulin J, Candau Y. Defect detection and characterization in composite materials using square pulse thermography coupled

with singular value decomposition analysis and thermal quadrupole modeling. NDT and E International 2012;51:58–67. https://doi.org/10.1016/j.ndteint.2012.06.003.

[148] Furlanetto V, Stocco D, Batalha GF, Szabados FR. inspection of projection welded automotive nuts through b-scan ultrasonic acoustic imaging. 2012.

[149] Schwenk EB, Shearer GD. Measuring projection weld strength by acoustic emission. n.d.

[150] Yetilmezsoy K, Erhuy CG, Ates F, Bilgin MB. Implementation of fuzzy logic approach to estimate the degree of expulsion and spattering index and weld strength in projection welding. Journal of the Brazilian Society of Mechanical Sciences and Engineering 2018;40. https://doi.org/10.1007/s40430-018-1210-9.

[151] Shojaee M, Midawi ARH, Barber B, Ghassemi-Armaki H, Worswick M, Biro E. Mechanical properties and failure behavior of resistance spot welded third-generation advanced high strength steels. J Manuf Process 2021;65:364–72. https://doi.org/10.1016/j.jmapro.2021.03.047.

[152] Hong KM, Shin YC. Prospects of laser welding technology in the automotive industry: A review. J Mater Process Technol 2017;245:46–69. https://doi.org/10.1016/j.jmatprotec.2017.02.008.

[153] Figueredo B, Ramachandran DC, Macwan A, Biro E. Failure behavior and mechanical properties in the resistance spot welding of quenched and partitioned (Q&P) steels. Welding in the World 2021;65:2359–69. https://doi.org/10.1007/s40194-021-01179-z.

[154] Pouranvari M, Marashi SPH. Critical review of automotive steels spot welding: Process, structure and properties. Science and Technology of Welding and Joining 2013;18:361–403. https://doi.org/10.1179/1362171813Y.0000000120.

[155] Summerville C, Adams D, Compston P, Doolan M. Nugget Diameter in Resistance Spot Welding: A Comparison between a Dynamic Resistance Based Approach and Ultrasound C-scan. Procedia Eng, vol. 183, Elsevier Ltd; 2017, p. 257–63. https://doi.org/10.1016/j.proeng.2017.04.033.

[156] Nielsen C v., Zhang W, Martins PAF, Bay N. 3D numerical simulation of projection welding of square nuts to sheets. J Mater Process Technol 2015;215:171–80. https://doi.org/10.1016/j.jmatprotec.2014.08.017.

[157] Ambroziak A, Korzeniowski M. Using resistance spot welding for joining aluminium elements in automotive industry. Archives of Civil and Mechanical Engineering 2010;10:5–13. https://doi.org/10.1016/s1644-9665(12)60126-5.

[158] Fatmahardi I, Mustapha M, Ahmad A, Derman MN, Lenggo Ginta T, Taufiqurrahman I. An exploratory study on resistance spot welding of titanium alloy Ti-6Al-4V. Materials 2021;14. https://doi.org/10.3390/ma14092336.

[159] Rajarajan C, Sivaraj P, Sonar T, Raja S, Mathiazhagan N. Investigation on microstructural features and tensile shear fracture properties of resistance spot welded advanced high strength dual phase steel sheets in lap joint configuration for automotive frame applications. J Mech Behav Mater 2022;31:52–63. https://doi.org/10.1515/jmbm-2022-0006.

[160] Zeng W, Cai M, Wang P, Lu T, Yao F. Application of laser ultrasonic technique for detecting weld defect based on FDST method. Optik (Stuttg) 2020;221. https://doi.org/10.1016/j.ijleo.2020.165366.

[161] Xu W, Li X, Zhang J, Xue Z, Cao J. Ultrasonic signal enhancement for coarse grain materials by machine learning analysis. Ultrasonics 2021;117. https://doi.org/10.1016/j.ultras.2021.106550.

[162] Martín Ó, Pereda M, Santos JI, Galán JM. Assessment of resistance spot welding quality based on ultrasonic testing and tree-based techniques. J Mater Process Technol 2014;214:2478–87. https://doi.org/10.1016/j.jmatprotec.2014.05.021.

[163] Lalithakumari S, Pandian R. Effect of topology changes of neural network in classification of weld defects. Mater Today Proc, vol. 33, Elsevier Ltd; 2020, p. 2656–9. https://doi.org/10.1016/j.matpr.2020.01.222.

[164] Metwally K, Lubeigt E, Rakotonarivo S, Chaix JF, Baqué F, Gobillot G, et al. Weld inspection by focused adjoint method. Ultrasonics 2018;83:80–7. https://doi.org/10.1016/j.ultras.2017.08.009.

[165] Kerscher PJP, Schmith J, Martins EA, Figueiredo RM de, Keller AL. Steel type determination by spark test image processing with machine learning. Measurement (Lond) 2022;187. https://doi.org/10.1016/j.measurement.2021.110361.

[166] Provencal E, Laperrière L. WeldNet: From 3D phased-array ultrasound scans to 3D geometrical models of welds and defects. CIRP Annals 2022;71:445–8. https://doi.org/10.1016/j.cirp.2022.04.033.

[167] Yang Q, Xu W, Xiao Y, Xie W, Xiong J, Zhang T. Microstructures and Mechanical Properties of 304 Stainless Steel Joints by Focused Ultrasound-Assisted TIG Welding. Metallography, Microstructure, and Analysis 2022;11:141–9. https://doi.org/10.1007/s13632-022-00826-1.

[168] Schramkó M, Nyikes Z, Tóth L, Kovács TA. Investigation of the ultrasonic welded stainless steel corrosion resistance. J Phys Conf Ser, vol. 2315, Institute of Physics; 2022. https://doi.org/10.1088/1742-6596/2315/1/012028.

[169] Jesus, Mucsi ;, Lara ;, Nogueira ;, Furlanetto ;, Rossi ; Analysis of the mechanical performance of spot welding on PHS 22MnB5 steel. n.d.

[170] Vrana J, Meyendorf N, Ida N, Singh R. Introduction to NDE 4.0. Handbook of Nondestructive Evaluation 4.0, Springer International Publishing; 2021, p. 1–28. https://doi.org/10.1007/978-3-030-48200-8_43-1.

[171] Ospina-Barras JE, Florez-Ospina JF, Benitez-Restrepo HD, Maldague X. Thermal diffusivity estimation with quantitative pulsed phase thermography. Thermosense: Thermal Infrared Applications XXXVII, vol. 9485, SPIE; 2015, p. 948512. https://doi.org/10.1117/12.2178886.

[172] Waugh RC, Dulieu-Barton JM, Quinn S. Modelling and evaluation of pulsed and pulse phase thermography through application of composite and metallic case studies. NDT and E International 2014;66:52–66. https://doi.org/10.1016/j.ndteint.2014.04.002.

[173] Ibarra-Castanedo C, Maldague XPV. Interactive methodology for optimized defect characterization by quantitative pulsed phase thermography. Research in Nondestructive Evaluation 2005;16:175–93. https://doi.org/10.1080/09349840500351846.

[174] Oswald-Tranta B. Comparison of time and frequency behavior in TSR and PPT evaluation. Thermosense: Thermal Infrared Applications XXXVIII, vol. 9861, SPIE; 2016, p. 98610P. https://doi.org/10.1117/12.2228864.

[175] Oswald-Tranta B. Time and frequency behaviour in TSR and PPT evaluation for flash thermography*. Quant Infrared Thermogr J 2017;14:164–84. https://doi.org/10.1080/17686733.2017.1283743.

[176] Ibarra-Castanedo C. QUANTITATIVE SUBSURFACE DEFECT EVALUATION BY PULSED PHASE THERMOGRAPHY : DEPTH RETRIEVAL WITH THE PHASE. n.d.

[177] D'Accardi E, Palumbo D, Tamborrino R, Galietti U. The influence of the truncation window size on the quantitative thermographic results after a pulsed test on an aluminium sample: comparison among different post-processing algorithms, SPIE-Intl Soc Optical Eng; 2019, p. 22. https://doi.org/10.1117/12.2518984.

[178] Zeng Z, Li C, Tao N, Feng L, Zhang C. Depth prediction of non-air interface defect using pulsed thermography. NDT and E International 2012;48:39–45. https://doi.org/10.1016/j.ndteint.2012.02.008.

[179] Moskovchenko A, Švantner M, Vavilov V, Chulkov A. Analyzing probability of detection as a function of defect size and depth in pulsed IR thermography. NDT and E International 2022;130. https://doi.org/10.1016/j.ndteint.2022.102673.

[180] de Angelis G, Meo M, Almond DP, Pickering SG, Angioni SL. A new technique to detect defect size and depth in composite structures using digital shearography and unconstrained optimization. NDT and E International 2012;45:91–6. https://doi.org/10.1016/j.ndteint.2011.07.007.

[181] Ibarra-Castanedo C, Genest M, Servais P, Maldague XPV, Bendada A. Qualitative and quantitative assessment of aerospace structures by pulsed thermography. Nondestructive Testing and Evaluation 2007;22:199–215. https://doi.org/10.1080/10589750701448548.

[182] Vavilov V. Evaluating the efficiency of data processing algorithms in transient thermal NDT. Thermosense XXVI, vol. 5405, 2004. https://doi.org/10.1117/12.537604.

[183] Chen KC, Chen TC, Shiue RK, Tsay LW. Liquation cracking in the heat-affected zone of IN738 superalloy weld. Metals (Basel) 2018;8. https://doi.org/10.3390/met8060387.

[184] Raza T, Hurtig K, Asala G, Andersson J, Svensson LE, Ojo OA. Influence of heat treatments on heat affected zone cracking of gas tungsten arc welded additive manufactured alloy 718. Metals (Basel) 2019;9. https://doi.org/10.3390/met9080881.

[185] Liu SD, Zhu ML, Zhou HB, Wan D, Xuan FZ. Strain visualization of growing short fatigue cracks in the heat-affected zone of a Ni–Cr–Mo–V steel welded joint: Intergranular cracking and crack closure. International Journal of Pressure Vessels and Piping 2019;178. https://doi.org/10.1016/j.ijpvp.2019.103992.

[186] Mandelis A, Munidasa M. Depth Profilometry of Near-Surface Inhomogeneities Via Laser-Photothermal Probing of the Thermal Diffusivity of Condensed Phases. vol. 15. 1994.

[187] Liu Y, Baddour N, Mandelis A. Transverse depth-profilometric hardness photothermal phase imaging of heat treated steels. J Appl Phys 2003;94:5543–8. https://doi.org/10.1063/1.1613808.

[188] Nicolaides L, Mandelis A, Beingessner CJ. Physical mechanisms of thermal-diffusivity depth-profile generation in a hardened low-alloy Mn, Si, Cr, Mo steel reconstructed by photothermal radiometry. J Appl Phys 2001;89:7879–84. https://doi.org/10.1063/1.1373698.

[189] Qu H, Wang C, Guo X, Mandelis A. Reconstruction of depth profiles of thermal conductivity of case hardened steels using a three-dimensional photothermal technique. J Appl Phys 2008;104. https://doi.org/10.1063/1.3035831.

[190] Liu Y, Baddour N, Mandelis A, Beingessner C. Photothermal depth profilometry of heat-treated hardened 0.15%-0.2% C, 0.6%-0.9% Mn Steels. J Appl Phys 2004;96:1521–8. https://doi.org/10.1063/1.1765868.

[191] Celorrio R, Mendioroz A, Apiñaniz E, Salazar A, Wang C, Mandelis A. Reconstruction of radial thermal conductivity depth profile in case hardened steel rods. J Appl Phys 2009;105. https://doi.org/10.1063/1.3106662.

[192] Munidasa M, Tian-Chi M, Mandelis A, Brown SK, Mannik L. Non-destructive depth profiling of laser-processed Zr-2.5Nb alloy by IR photothermal radiometry. vol. 159. 1992.

[193] Klein S, Weber S, Theisen W. Effect of heat treatment on phase structure and thermal conductivity of a copper-infiltrated steel. J Mater Sci 2015;50:3586–96. https://doi.org/10.1007/s10853-015-8919-y.

[194] Klein S, Mujica Roncery L, Walter M, Weber S, Theisen W. Diffusion processes during cementite precipitation and their impact on electrical and thermal conductivity of a heat-treatable steel. J Mater Sci 2017;52:375–90. https://doi.org/10.1007/s10853-016-0338-1.

[195] Mendioroz A, Fuente-Dacal R, Apianiz E, Salazar A. Thermal diffusivity measurements of thin plates and filaments using lock-in thermography. Review of Scientific Instruments 2009;80. https://doi.org/10.1063/1.3176467.

[196] Boué C, Holé S. Infrared thermography protocol for simple measurements of thermal diffusivity and conductivity. Infrared Phys Technol 2012;55:376–9. https://doi.org/10.1016/j.infrared.2012.02.002.

[197] Giri LI, Tuli S, Sharma M, Bugnon P, Berger H, Magrez A. Thermal diffusivity measurements of templated nanocomposite using infrared thermography. Mater Lett 2014;115:106–8. https://doi.org/10.1016/j.matlet.2013.10.042.

[198] Strzałkowski K, Streza M, Pawlak M. Lock-in thermography versus PPE calorimetry for accurate measurements of thermophysical properties of solid samples: A comparative study. Measurement (Lond) 2015;64:64–70. https://doi.org/10.1016/j.measurement.2014.12.040.

[199] Nolte PW, Malvisalo T, Wagner F, Schweizer S. Thermal diffusivity of metals determined by lock-in thermography. Quant Infrared Thermogr J 2017;14:218–25. https://doi.org/10.1080/17686733.2017.1329777.

[200] Salazar A, Zamanillo L, Colom M, Mendioroz A, Galietti U, Sommier A, et al. Lock-in thermography on moving samples: amazing mismatch between amplitude and phase. Quant Infrared Thermogr J 2020;17:279–86. https://doi.org/10.1080/17686733.2019.1655248.

[201] Colom M, Bedoya A, Mendioroz A, Salazar A. Measuring the in-plane thermal diffusivity of moving samples using laser spot lock-in thermography. International Journal of Thermal Sciences 2020;151. https://doi.org/10.1016/j.ijthermalsci.2020.106277.

[202] Azumi T, Takahashi Y. Novel finite pulse-width correction in flash thermal diffusivity measurement. Review of Scientific Instruments 1981;52:1411–3. https://doi.org/10.1063/1.1136793.

[203] Taylor RE, Cape JA. Finite pulse-time effects in the flash diffusivity technique. Appl Phys Lett 1964;5:212–3. https://doi.org/10.1063/1.1723593.

[204] Heckman RC. Finite pulse-time and heat-loss effects in pulse thermal diffusivity measurements. J Appl Phys 1973;44:1455–60. https://doi.org/10.1063/1.1662393.

[205] Cape JA, Lehman GW. Temperature and finite pulse-time effects in the flash method for measuring thermal diffusivity. J Appl Phys 1963;34:1909–13. https://doi.org/10.1063/1.1729711.

[206] Larson KB, Koyama K. Correction for finite-pulse-time effects in very thin samples using the flash method of measuring thermal diffusivity. J Appl Phys 1967;38:465–74. https://doi.org/10.1063/1.1709360.

[207] Maglic KD, Taylor RE. The Apparatus for Thermal Diffusivity Measurement by the Laser Pulse Method. n.d.

[208] Brady RI, Kulkarni MR. Determination of thermal diffusivity distribution for three types of materials by transient thermography. vol. 29. 1996.

[209] Krapez JC, Spagnolo L, Frieß M, Maier HP, Neuer G ünter. Measurement of in-plane diffusivity in non-homogeneous slabs by applying flash thermography. International Journal of Thermal Sciences 2004;43:967–77. https://doi.org/10.1016/j.ijthermalsci.2004.02.003.

[210] Krapez J-C. Diffusivity measurement by using a grid-like mask Modeling of the infrared remote sensing signal View project leak detection in water transmission systems by multispectral remote sensing with airplane and uav View project Diffusivity measurement by using a grid-like mask. 2017.

[211] Krapez J-C. R solution spatiale de la camera thermique source volante. vol. 38. 1999.

[212] Krapez J-C. Measurements without contact in heat transfer: multiwavelength radiation thermometry. Principle, implementation and pitfalls Infrared thermography of fatigue View project Modeling of diffusion-based phenomena and wave-like phenomena in graded materials View project Measurements without contact in heat transfer: multiwavelength radiation thermometry. Principle, implementation and pitfalls. n.d.

[213] Balageas DL, Krapez JC, Cielo P. Pulsed photothermal modeling of layered materials. J Appl Phys 1986;59:348–57. https://doi.org/10.1063/1.336690.

[214] Krapez LC, Balageas D, Deom A, Lepoutre F. early detection by stimulated infrared thermography. comparison with ultrasonics and holo/shearography earl y detection by stimulated infrared thermography. comparison with ultrasonics and holo/shearography. 1994.

[215] Fudym O, Battaglia JL, Batsale JC. Measurement of thermophysical properties in semi-infinite media by random heating and fractional model identification. Review of Scientific Instruments 2005;76. https://doi.org/10.1063/1.1877012.

[216] Degiovanni A, Laurent M, Lemta AD. Une nouvelle technique d'identification de la diffusivité thermique pour la méthode " flash " Une nouvelle technique d'identification de la diffusivité thermique pour la méthode « flash ». Revue de Physique Appliquée 1986;21:229–37. https://doi.org/10.1051/rphysap:01986002103022900ï.

[217] Mayr G, Plank B, Sekelja J, Hendorfer G. Active thermography as a quantitative method for non-destructive evaluation of porous carbon fiber reinforced polymers.

NDT and E International 2011;44:537–43. https://doi.org/10.1016/j.ndteint.2011.05.012.

[218] Feuillet V, Dujardin N, Fois M, Ibos L, Poilâne C, Candau Y. Pulsed thermography: a useful tool to determine porosity in composite materials ? n.d.

[219] Laskar JM, Bagavathiappan S, Sardar M, Jayakumar T, Philip J, Raj B. Measurement of thermal diffusivity of solids using infrared thermography. Mater Lett 2008;62:2740–2. https://doi.org/10.1016/j.matlet.2008.01.045.

[220] Krankenhagen R, Maierhofer C. Measurement of the radiative energy output of flash lamps by means of thermal thin probes. Infrared Phys Technol 2014;67:363–70. https://doi.org/10.1016/j.infrared.2014.07.012.

[221] Krankenhagen R, Worzewski T, Maierhofer C. Cooling-down of thermal thick probes after flash excitation - A measure for the real energy density? Infrared Phys Technol 2015;72:258–65. https://doi.org/10.1016/j.infrared.2015.07.014.

[222] Paula A, Albers F, Restivo TAG, Pagano L, Äo J, Baldo B. Effect of testing conditions on the laser ¯ash thermal diffusivity measurements of ceramics. n.d.

[223] Mayr G, Plank B, Gruber J, Sekelja J, Hendorfer G. Thermal diffusivity measurements of porous CFRP specimens with different number of plies using pulsed thermography in transmission and reflection mode. n.d.

[224] Mayr G, Hendorfer G. Porosity Determination by Pulsed Thermography in Reflection Mode. n.d.

[225] Mayr G, Plank B, Sekelja J, Hendorfer G. Active thermography as a quantitative method for non-destructive evaluation of porous carbon fiber reinforced polymers. NDT and E International 2011;44:537–43. https://doi.org/10.1016/j.ndteint.2011.05.012.

[226] Shepard SM. Reconstruction and enhancement of active thermographic image sequences. Optical Engineering 2003;42:1337. https://doi.org/10.1117/1.1566969.

[227] Shepard SM, Lhota JR, Ahmed T, Rubadeux BA, Wang D. Quantification and Automation of Pulsed Thermographic NDE. 2001.

[228] Shepard SM. Flash Thermography of Aerospace Composites. n.d.

[229] Shepard SM, Lhota JR, Ahmed T. Measurement limits in flash thermography. Thermosense XXXI, vol. 7299, SPIE; 2009, p. 72990T. https://doi.org/10.1117/12.820062.

[230] Cernuschi F, Bison P. The influence of the laser energy on the thermal diffusivity evaluation of TBC by Laser Flash. Journal of Thermal Spray Technology 2008;17:465–72. https://doi.org/10.1007/s11666-008-9199-8.

[231] Bison P, Cernuschi F, Capelli S. A thermographic technique for the simultaneous estimation of in-plane and in-depth thermal diffusivities of TBCs. Surf Coat Technol 2011;205:3128–33. https://doi.org/10.1016/j.surfcoat.2010.11.013.

[232] Bison P, Cernuschi F, Grinzato E. In-depth and in-plane thermal diffusivity measurements of thermal barrier coatings by IR camera: Evaluation of ageing. Int J Thermophys 2008;29:2149–61. https://doi.org/10.1007/s10765-008-0421-1.

[233] Cernuschi F, Bison P, Marinetti S, Campagnoli E. Thermal diffusivity measurement by thermographic technique for the non-destructive integrity assessment of TBCs coupons. Surf Coat Technol 2010;205:498–505. https://doi.org/10.1016/j.surfcoat.2010.07.024.

[234] Bison PG, Cernuschi F, Grinzato E, Marinetti S, Robba D. Ageing evaluation of thermal barrier coatings by thermal diffusivity. Infrared Phys Technol 2007;49:286–91. https://doi.org/10.1016/j.infrared.2006.06.019.

[235] Cernuschi SAF, Bison PG, Figari A, Marinetti S, Grinzato E. Thermal Diffusivity Measurements by Photothermal and Thermographic Techniques 1. vol. 25. 2004.

[236] Cernuschi F, Russo A, Lorenzoni L, Figari A. In-plane thermal diffusivity evaluation by infrared thermography. Review of Scientific Instruments 2001;72:3988–95. https://doi.org/10.1063/1.1400151.

[237] Bison P, Cernuschi F, Capelli S. A thermographic technique for the simultaneous estimation of in-plane and in-depth thermal diffusivities of TBCs. Surf Coat Technol 2011;205:3128–33. https://doi.org/10.1016/j.surfcoat.2010.11.013.

[238] Pech-May NW, Mendioroz A, Salazar A. Simultaneous measurement of the in-plane and in-depth thermal diffusivity of solids using pulsed infrared thermography with focused illumination. NDT and E International 2016;77:28–34. https://doi.org/10.1016/j.ndteint.2015.10.001.

[239] Dell'Avvocato G., Palumbo D, Palmieri E. M., Galietti. org/conference-proceedings-of-spie 2022:1210906. https://doi.org/10.1117/12.2618810.

[240] Krankenhagen R, Jonietz F, Zirker S. Determination of Thermal Parameters of Concrete by Active Thermographic Measurements. J Nondestr Eval 2022;41. https://doi.org/10.1007/s10921-022-00861-6.

[241] Müller JP, Götschel S, Maierhofer C, Weiser M. Determining the material parameters for the reconstruction of defects in carbon fiber reinforced polymers from data measured by flash thermography. AIP Conf Proc, vol. 1806, American Institute of Physics Inc.; 2017. https://doi.org/10.1063/1.4974671.

[242] Winfree WP, Cramer KE, Zalameda JN, Howell PA. Numerical simulations of thermographic responses in composites. AIP Conf Proc, vol. 1706, American Institute of Physics Inc.; 2016. https://doi.org/10.1063/1.4940597.

[243] Welch CS, Heath DM, Winfree WP. Remote measurement of in-plane diffusivity components in plates. J Appl Phys 1987;61:895–8. https://doi.org/10.1063/1.338140.

[244] González J, Mendioroz A, Sommier A, Batsale JC, Pradere C, Salazar A. Fast sizing of the width of infinite vertical cracks using constant velocity Flying-Spot thermography. NDT and E International 2019;103:166–72. https://doi.org/10.1016/j.ndteint.2019.03.003.

[245] Gaverina L, Bensalem M, Bedoya A, González J, Sommier A, Battaglia JL, et al. Constant Velocity Flying Spot for the estimation of in-plane thermal diffusivity on anisotropic materials. International Journal of Thermal Sciences 2019;145. https://doi.org/10.1016/j.ijthermalsci.2019.106000.

[246] Bedoya A, González J, Rodríguez-Aseguinolaza J, Mendioroz A, Sommier A, Batsale JC, et al. Measurement of in-plane thermal diffusivity of solids moving at constant velocity using laser spot infrared thermography. Measurement (Lond) 2019;134:519–26. https://doi.org/10.1016/j.measurement.2018.11.013.

[247] Salazar A, Mendioroz A, Oleaga A. Flying spot thermography: Quantitative assessment of thermal diffusivity and crack width. J Appl Phys 2020;127. https://doi.org/10.1063/1.5144972.

[248] Gaverina L, Batsale JC, Sommier A, Pradere C. Pulsed flying spot with the logarithmic parabolas method for the estimation of in-plane thermal diffusivity fields on heterogeneous and anisotropic materials. J Appl Phys 2017;121. https://doi.org/10.1063/1.4978919.

[249] Rodríguez-Aseguinolaza J, Colom M, González J, Mendioroz A, Salazar A. Quantifying the width and angle of inclined cracks using laser-spot lock-in thermography. NDT and E International 2021;122. https://doi.org/10.1016/j.ndteint.2021.102494.

[250] Mendioroz A, Colom M, Salazar A. Assessing the thermal diffusivity and principal directions of moving samples by infrared thermography: towards fiber orientation monitoring in production chains, SPIE-Intl Soc Optical Eng; 2022, p. 36. https://doi.org/10.1117/12.2618278.

[251] Salazar A, Colom M, Mendioroz A. Laser-spot step-heating thermography to measure the thermal diffusivity of solids. International Journal of Thermal Sciences 2021;170. https://doi.org/10.1016/j.ijthermalsci.2021.107124.

[252] Cielo P, Utracki LA, Lamontacne DM. Thermal-diffusivity measurements by the converging-thermal-wave technique. n.d.

[253] dos Santos WN, Mummery P, Wallwork A. Thermal diffusivity of polymers by the laser flash technique. Polym Test 2005;24:628–34. https://doi.org/10.1016/j.polymertesting.2005.03.007.

[254] Laskar JM, Bagavathiappan S, Sardar M, Jayakumar T, Philip J, Raj B. Measurement of thermal diffusivity of solids using infrared thermography. Mater Lett 2008;62:2740–2. https://doi.org/10.1016/j.matlet.2008.01.045.

[255] Basheer CM, Krishnamurthy C v., Balasubramaniam K. Hot-rod thermography for in-plane thermal diffusivity measurement. Measurement (Lond) 2017;103:235–40. https://doi.org/10.1016/j.measurement.2017.02.022.

[256] Perkowski Z. A thermal diffusivity determination method using thermography: Theoretical background and verification. Int J Heat Mass Transf 2011;54:2126–35. https://doi.org/10.1016/j.ijheatmasstransfer.2010.12.015.

[257] Salazar A, Colom M, Mendioroz A. Laser-spot step-heating thermography to measure the thermal diffusivity of solids. International Journal of Thermal Sciences 2021;170. https://doi.org/10.1016/j.ijthermalsci.2021.107124.

[258] Salazar A, Mendioroz A, Apiñaniz E, Pradere C, Noël F, Batsale JC. Extending the flash method to measure the thermal diffusivity of semitransparent solids. Meas Sci Technol 2014;25. https://doi.org/10.1088/0957-0233/25/3/035604.

[259] Bedoya A, González J, Rodríguez-Aseguinolaza J, Mendioroz A, Sommier A, Batsale JC, et al. Measurement of in-plane thermal diffusivity of solids moving at constant velocity using laser spot infrared thermography. Measurement (Lond) 2019;134:519–26. https://doi.org/10.1016/j.measurement.2018.11.013.

[260] Ryu M, Batsale JC, Morikawa J. Quadrupole modelling of dual lock-in method for the simultaneous measurements of thermal diffusivity and thermal effusivity. Int J

Heat Mass Transf 2020;162. https://doi.org/10.1016/j.ijheatmasstransfer.2020.120337.

[261] Contuzzi N, Palmieri ME, Angelastro A. Study on properties and microstructure of laser beam butt welded joints of Al-Si coated USIBOR® 1500 steel. Manuf Lett 2022;33:38–41. https://doi.org/10.1016/j.mfglet.2022.07.008.

[262] Palmieri ME, Lorusso VD, Tricarico L. Investigation of material properties of tailored press hardening parts using numerical and physical simulation. Procedia Manuf, vol. 50, Elsevier B.V.; 2020, p. 104–9. https://doi.org/10.1016/j.promfg.2020.08.019.

[263] Palmieri ME, Galetta FR, Tricarico L. Study of Tailored Hot Stamping Process on Advanced High-Strength Steels. Journal of Manufacturing and Materials Processing 2022;6. https://doi.org/10.3390/JMMP6010011.

[264] Gustafsson SE. Transient plane source techniques for thermal conductivity and thermal diffusivity measurements of solid materials. Review of Scientific Instruments 1991;62:797–804. https://doi.org/10.1063/1.1142087.

[265] Güler H. Investigation of usibor 1500 formability in a hot forming operation. Medziagotyra 2013;19:144–6. https://doi.org/10.5755/j01.ms.19.2.1484.

[266] Zhang P, Zhu L, Xi C, Luo J. Study on phase transformation in hot stamping process of USIBOR® 1500 high-strength steel. Metals (Basel) 2019;9. https://doi.org/10.3390/met9101119.

[267] Sharma RS, Molian P. Weldability of advanced high strength steels using an Yb: YAG disk laser. J Mater Process Technol 2011;211:1888–97. https://doi.org/10.1016/j.jmatprotec.2011.06.009.

[268] Dell'Avvocato G, Palumbo D, Galietti U. A non-destructive thermographic procedure for the evaluation of heat treatment in Usibor®1500 through the thermal diffusivity measurement. NDT & E International 2023;133:102748. https://doi.org/10.1016/j.ndteint.2022.102748.

[269] Verspeek S, Gladines J, Ribbens B, Maldague X, Steenackers G. Dynamic line scan thermography optimisation using response surfaces implemented on PVC flat bottom hole plates. Applied Sciences (Switzerland) 2021;11:1–15. https://doi.org/10.3390/app11041538.